

Faculty of Aerospace Engineering | Delft University of Technology

Analysis Strategies for As-Manufactured Composite Pressure Vessels

Master of Science Thesis

A. Soriano Sutil

TU Delft

Analysis Strategies for As-Manufactured Composite Pressure Vessels

Master of Science Thesis

by

A. Soriano Sutil

to obtain the degree of Master of Science in Aerospace Engineering
at the Delft University of Technology,
to be defended publicly on Friday August 14, 2020 at 9:30 AM.

Student number:	4875303	
Project duration:	November 2019 – August 2020	
Thesis committee:	Prof. Dr. C. Kassapoglou,	TU Delft, chair
	Dr. Ir. J.M.J.F. van Campen,	TU Delft, supervisor
	Dr. D. Zarouchas,	TU Delft
	Dr. B. Chen,	TU Delft
	Dipl.-Ing. M. Nebe,	Daimler AG, supervisor

This thesis is confidential and cannot be made public until August 14, 2023.

An electronic version of this thesis is available at `http://repository.tudelft.nl/`.

TU Delft

God is in the detail
The devil is in the detail

Abstract

Commercial development of gaseous hydrogen storage in fuel cell electric vehicles (FCEVs) is inherently subjected to the reliable and cost-effective design of Type IV pressure vessels. These shall comply with strict safety requirements, as long as the high cost of carbon fiber demands weight minimization to limit production costs. Sound structural conceptions thus require a comprehensive understanding of the vessel mechanical response, wherever non-uniformity in the material stiffness and strength prevails as one of the main obstacles.

This research aims to build strategies for the accurate analysis of composite pressure vessels (CPVs) under internal pressure by connecting the outcome of their manufacturing process to their structural performance. First, the manufacturing product is comprehensively related to the vessel design, its resulting geometry, and the corresponding material characteristics. The final vessel geometry is estimated from the revision of the original predictions made by the filament winding software and the correlation with experimental data. Likewise, the mechanical response of the material is determined from experimental testing on specimens that representatively depict the filament winding process.

Thereupon, the detailed definition of the vessel configuration permits the development of faithful three-dimensional finite element (FE) models, featuring a discretization of each composite ply and its interaction with the neighboring layers. In the first term, the constitutively elastic analysis illustrates the mechanical response of the CPV, depicting its deformational behavior and allowing the estimation of the pressure stages of damage onset. Final collapse is determined by the evaluation of failure criteria in the fiber constituent, which, besides disregarding load redistribution because of the existence of damage, provides a quick estimation of the burst pressure.

The degree of complexity is increased by accounting for the progression of damage in the material and, ultimately, also by the heterogeneity of the material properties. A continuum damage mechanics (CDM) model developed by Leone et al. [1] is implemented to reproduce cracks embedded within the continuum element as cohesive surfaces. Material degradation is represented during the loading process by conveniently diminishing stiffness in the damaged constituents and, therefore, depicting the vessel collapse more realistically.

The generality of the analysis strategy is demonstrated by modeling, discussing, and experimentally correlating three vessel designs of distinct anticipated behavior. These feature two extreme asymmetric layups of low angle helical and circumferential layers, whereas the third features the two layer types in a staggered, intercalated version. The deformational behavior of the investigated vessels is illustrated through the outer surface strain measurement obtained using digital image correlation (DIC), while the recording of acoustic emissions (AEs) correspondingly permit to correlate the progression of damage.

The increased sophistication of the modeling results shows a noteworthy agreement with the experimental data, where the trends and magnitudes there observed are fundamentally reproduced. Withal, modest discrepancies exist concerning the deformational response in the dome transition region, justified in the insufficiently accurate, albeit still realistic, depictions of the groups' tapering shape.

The directional stiffness distribution in the cylinder-dome transition region shows to influence the distinct response at this location intensely. Accordingly, a gradual stiffness change from cylinder to the dome is presented to result in a smooth strain variation, a steady progression of failure, and a final collapse in the cylindrical region. However, when the directional stiffness changes abruptly, a protrusion grows, generating premature material degradation and an early burst event.

Lastly, the precision of the burst pressure estimation is linked to the type of failure experienced. When failure in the cylinder occurs, discrepancy against the average experimental result is minimum, both for the constitutively elastic result ($\sim$4.8 %) and the analysis with damage progression ($\sim$2.2 %). If the existence of a protrusion decidedly controls the burst, the mismatch is larger, non only because of the more complex representation of reality, but also because of the larger scatter in the corresponding experimental response. Therefore, deviations with experimental tests are significant both for the constitutively elastic result ($\sim$27.1 %) and the analysis with damage progression ($\sim$12.3 %).

Preface

Studying a second master's degree at the TU Delft became a real idea a little more than two years ago. It sounded ambitious and, perhaps, not even necessary. Yet, now that it is coming to an end, I can confidently look back and say that it has been quite an enjoyable journey. Moving from Spain to the Netherlands introduced me to a great crowd, proposed new challenges, showed new ways of thinking, and got to a pinnacle with me moving again to Germany to write my thesis at Daimler AG.

The work that follows deals with the numerical analysis of composite pressure vessels, thus bringing together two key aspects I revere as an engineer. On the one hand, I support the commercial development of fuel cell electric vehicles (FCEVs), a potentially game-changing approach to transportation, energy storage, and the way we deal with climate change. On the other hand, I show the capabilities of structural simulations to create knowledge, shorten product development times, and save costs. This report is a precise mirror of my approach to these two challenges, trustfully showing an insightful contribution, although still lacking my weaknesses.

Nonetheless, none of this would have been possible without the financial support of 'la Caixa' Foundation, granting me one of its highly competitive fellowships. Your trust in me allowed this personal 'Dutch voyage' while covering my expenses during the last two years. You also opened the door to a group of excellence, of which now I am proud to be part. I thank Dr. Jacobo Díaz and Dr. Miguel Costas for encouraging and upholding me in applying to this program.

Thinking of how my work at Daimler started, I sincerely express my gratitude toward my academic supervisor Julien van Campen. You looked to me as a thesis candidate and accompanied it with healthy doses of criticism and openness.

Withal, the daily routine could not have been more stimulating than the always fresh and bright guidance of Martin Nebe and Clemens Braun. I have appreciated your thriving and genuine attitude, and I cannot but wish you all the best for the future. My wishes can be extended to Alex Kasses and Antonio Johman; colleagues, classmates, and friends. Also, to Tom Aisjee, Eleonora Cesari, and Chiara Ardemani.

Last but not for that less important, thanks to my closest friends, family, and fellow student colleagues. You had the patience to see me disappear long hours while working in this project.

A. Soriano Sutil
Stuttgart, August 2020

Contents

Table of Contents xi

List of Abbreviations xiii

1 Introduction 1

2 Types and Manufacturing Processes of Pressure Vessels 5
2.1 Introduction to the Normative Framework . . . 5
2.2 Structural Definition of Cylindrical Vessels with Domed Heads . . . 7
2.3 Composite Filament Winding of Pressure Vessels . . . 9
2.4 Description of Filament Paths . . . 11
2.5 Coupled Definition of Layer Thickness and Non-Geodesic Filament Paths . . . 12

3 Background to the Analysis of Composite Pressure Vessels 17
3.1 Analytical Analysis of Cylindrical Composite Shells . . . 17
3.2 Fundamental Work in the Analysis of Pressure Vessels . . . 18
3.3 Applications of The Classical Lamination Theory to the Analysis of CPVs . . . 20
3.4 Thick-wall FE Analysis Solutions and Failure Modeling of CPVs . . . 22
3.4.1 Mesoscale Solutions . . . 23
3.4.2 Multiscale Solutions . . . 25
3.4.3 Material Variability . . . 25
3.5 Foresight in the Analysis of CPVs and Research Questions . . . 26

4 Analysis Methdology Overview 29

5 Geometrical Definition of the CPV 33
5.1 Introduction to the Vessel Thickness Characterization Techniques . . . 33
5.2 Methodology for the Ply Thickness Adjustment . . . 34
5.2.1 Readjustment of the Circumferential Tow Drops . . . 34
5.2.2 Generation of the Liner Manufacturing Gap . . . 35
5.2.3 Correction for Layer Confinement . . . 36
5.2.4 Extrapolation of the Boss Ply End . . . 36
5.3 Experimental Analysis of the Vessel Geometry . . . 37
5.3.1 Description of the Vessel Manufacturing and Stacking Sequence . . . 37
5.3.2 Discussion on the Liner Deformation during Winding and Curing . . . 38
5.3.3 Discussion on the Wall Thickness of the Composite Reinforcement . . . 39
5.3.4 Discussion on the Vessel Outer Contour . . . 40
5.4 Results and Discussion of the Geometry Prediction for Various Stacking Sequences . . . 42
5.4.1 Prediction on the Liner Manufacturing Gap . . . 42
5.4.2 Prediction on the Layer Group and Vessel Boundaries . . . 42
5.5 Concluding Remarks . . . 44

6 Experimental Characterization of Material Properties 49
6.1 Overview of the Material Properties Determination . . . 49
6.2 Design and Manufacturing of Test Specimens . . . 52
6.2.1 Design of Testing Plates . . . 52
6.2.2 Manufacturing of Specimens . . . 52
6.2.3 Discussion on the Manufacturing Results . . . 55
6.3 Results and Discussion of Material Stiffness and Strength . . . 57
6.3.1 Longitudinal Tensile Tests . . . 57
6.3.2 Transverse Tensile Tests . . . 59
6.3.3 in-plane Shear Tensile Tests . . . 59

6.4 Results and Discussion of Material Fracture Toughness . . . 63
6.4.1 Mode I Fracture Toughness . . . 63
6.4.2 Mode II Fracture Toughness . . . 64
6.5 Concluding Remarks . . . 68

7 Constitutively Elastic Analysis 71
7.1 Introduction to the Correlation of Results . . . 71
7.2 Definition of the FE Model . . . 73
7.3 Results and Discussion of the Dome Transition Region Behavior . . . 78
7.3.1 Prediction on the Behavior of a Homogeneous Orthotropic Vessel . . . 78
7.3.2 Prediction on the Deformed Shapes of the W1A, E+ and B* Stacking Sequences . 78
7.3.3 Prediction on the Outer Surface Strain of the W1A, E+ and B* Stacking Sequences . . . 82
7.4 Results and Discussion of the Through-the-Thickness Response along a Meridional Path 84
7.4.1 Prediction on the W1A Stacking Sequence . . . 84
7.4.2 Prediction on the E+ and B* Stacking Sequences . . . 85
7.5 Results and Discussion of the Cylinder Expansion . . . 89
7.5.1 Prediction on the Tangential Stress and Strain . . . 89
7.5.2 Prediction on the Meridional and Tangential Strain with Increasing Pressure . . . 91
7.6 Results and Discussion of the Boss Axial Displacement . . . 92
7.7 Concluding Remarks . . . 97

8 Prediction of First-Ply-Failure 101
8.1 Introduction to Failure in Composite Materials . . . 101
8.2 Criteria for Failure Prediction . . . 103
8.2.1 Fundamental Failure Criteria . . . 103
8.2.2 Puck's Failure Criteria . . . 103
8.2.3 LaRC04 Failure Criteria . . . 105
8.3 Results and Discussion on Failure Prediction . . . 107
8.3.1 Prediction on the W1A Stacking Sequence . . . 109
8.3.2 Prediction on the E+ and B* Stacking Sequences . . . 110
8.3.3 Correlation with Experimental Results . . . 112
8.4 Concluding Remarks . . . 117

9 Modeling of Damage Progression 119
9.1 Implementation of the CDM Model . . . 119
9.1.1 Modeling of Transverse Damage . . . 120
9.1.2 Modeling of Longitudinal Damage . . . 122
9.2 Results and Discussion of Damage Progression . . . 123
9.2.1 Prediction on the Damage Progression of the W1A Stacking Sequence . . . 123
9.2.2 Prediction on the Deformational Behavior of the W1A Stacking Sequence . . . 129
9.2.3 Prediction on the Damage Progression of the B* Stacking Sequence . . . 133
9.2.4 Prediction on the Deformational Behavior of the B* Stacking Sequence . . . 139
9.3 Concluding Remarks . . . 142

10 Modeling Heterogeneous Material Properties 145
10.1 Experimental Analysis of the Vessel Material Characteristics . . . 145
10.2 Results of Vessel Behavior with a Heterogeneous Material Definition . . . 150
10.2.1 Prediction on the Damage Progression of the W1A Stacking Sequence . . . 150
10.2.2 Prediction on the Deformational Behavior of the W1A Stacking Sequence . . . 152
10.3 Concluding Remarks . . . 155

11 Conclusions 157

12 Future Work 163

A Vessel Stacking Sequence Description 165

B Influence of the Circumferential Ply Drop Location on the B* Stacking Sequence Deformation 169

C Sensitivity of the Deformational Behavior to the Numerical Setup **173**

Bibliography **177**

List of Abbreviations

A

AE acoustic emission. v, 4, 27, 32, 73, 95, 96, 112, 114, 124–127, 134–138, 142, 143, 148, 151, 156, 157, 161

C

CC compliance calibration. 65–67
CDM continuum damage mechanics. v, 23–26, 119, 121, 139, 142, 158, 160, 163
CFRP carbon fiber reinforced polymer. 2, 3, 104
CLT classical lamination theory. 11, 17, 18, 20–22, 26, 73
CNG compressed natural gas. 5
CPV composite pressure vessel. v, 2–5, 8–12, 14, 17, 18, 20–33, 35, 37, 49–54, 56, 68, 71–74, 78, 92, 97, 99, 101, 102, 107, 116, 117, 119, 123, 145, 155, 157, 158, 160–164
CT computerized tomography. 24, 31, 34–37, 39, 40, 42–48, 51, 73, 94, 96, 114, 137, 145–148, 157, 158, 161, 165

D

DCB double cantilever beam. 52, 55, 63, 64, 66
DIC digital image correlation. v, 4, 27, 32, 72, 73, 82, 84, 91, 94, 139, 157, 169, 173
DVC digital volume correlation. 73

E

ENF end notch flexure. 52, 55, 63, 64, 66, 68

F

FBG fiber bragg grating. 72
FCEV fuel cell electric vehicle. v, 1, 2
FE finite element. v, 4, 12, 17, 18, 21–25, 27, 29, 31, 32, 52, 56, 71–74, 101, 119, 145, 157, 164, 165, 173, 176
FPF first ply failure. 4, 26, 71, 101, 103, 107, 117, 119, 142, 157
FSDT first-order shear deformation theory. 18, 21

G

GA genetic algorithm. 22

I

ICE internal combustion engine. 1, 2
ISO International Standards Organization. 5

L

LHS linear shear loading law. 106
LVDT linear variable differential transducer. 72

M

MMF micromechanics of failure. 25
MPDM micromechanics progressive damage modeling. 25

N

NWP nominal working pressure. 5, 6, 82

O

OEM original equipment manufacturer. 1

P

PSO particle swarm optimization. 21

R

RHS shear material response law. 106
RVE representative volume element. 25

S

SA simulated annealing. 22
SEM scanning electron microscope. 26, 51
SG strain gauges. 72

T

TSDT third-order shear deformation theory. 21

W

WCM Wound Composite Modeler. 12, 24

1 Introduction

Industry Context

It is observed from the main original equipment manufacturers (OEMs) strategies, that hybridization and electrification of vehicle fleets is a critical shift towards industry's survivability. This reality is not only motivated by the volatile oil market prices, but also by a broader social mindset change that demands speedy action against a manifested human-induced climate change. Within the European context, this is, for instance, illustrated by the effort towards the reduction of greenhouse gas emissions. It comprises, among others, the decarbonization of the power supply system, its substitution for renewable energy sources, and, of particular interest for the automotive industry, the electrification of the transportation drivetrains.

Concerning road transportation, the most significant technological development towards this change of paradigm can be arguably attributed to the proliferation of battery electric vehicles. These, being able to transform chemical energy into electricity, provide a drivetrain with a practically immediate power supply that, in a like manner, tolerates in terms of performance as much demanding driving conditions as any other internal combustion engine (ICE) vehicle. Nevertheless, commercial batteries appear to be limited because of their weight and volume, to provide comparable driving ranges to those of conventional ICE ranges. Batteries on commercial vehicles render an energy density of approximately 0.15 kWh per kg, meaning that a 650 kg battery is needed to achieve a 500 km range on a 180 Wh per km average consumption. Furthermore, battery electric vehicles are restricted to reasonably slow charging times that inevitably condition their usage in long-range applications. For instance, the 2019 75 kWh battery of the Tesla Model S requires approximately 20 hours to charge on a conventional 3.7 kW household plug, while it reduces to about 1 hour on a rapid 150 kW socket.

TThe intrinsic limitations of battery electric vehicles motivate the development of alternative technologies that better fit their long-haul transportation usage. Hybrid vehicles close the gap between full battery-electric and conventional ICE systems by featuring a tentatively reduced scale combustion engine. The use of hybrid engines emerges as a transitional solution in the transformation of the transportation sector. Their implementation is almost immediate because the otherwise robust development of ICEs directly covers any shortfalls in the electric powertrain design. Nevertheless, hybrid vehicles do not eliminate greenhouse gas emissions from within the vehicle. On the contrary, fuel-cell electric vehicles present themselves as an increasingly feasible alternative based on fast refueling possibilities and an almost ready-for-production development level.

Fuel Cell Technology

The principle on which FCEVs work is, as introduced by Ehsani et al. [2], an electrical powertrain fed by the output of the electromechanical processes taking place in a galvanic cell. The anode of the galvanic cell is continuously provided by fuel, releasing electrons from it, and generating a steady potential difference that results in a voltage similar to that of a chemical battery. FCEVs are possibly the fuel-cell vehicle concept furthest matured, which has also already been introduced in the commercial models Toyota Mirai, Hyundai Nexo, Honda Clarity, and Mercedes-Benz GLC F-Cell. These vehicles feature pressurized hydrogen vessels that, in a similar manner to the conventional ICE car refueling process, are refilled by pumping in the propellant.

Hydrogen FCEVs may be regarded as zero-emission, considering that the byproduct of a hydrogen-air fuel cell is just water, [2]. Nevertheless, the real environmental impact of a hydrogen FCEV resides in the production, storage, and transportation of the hydrogen itself. From the reporting of Holladay et al. [3], the most mature hydrogen production technologies are based on the reforming of hydrocarbons, the gasification of biomass, and the electrolysis of water. The reforming and gasification-based technologies are greenhouse gases emitting techniques, whereas the use of biomass and water is intrinsically renewable. Of these three, the electrolysis of water appears as the most sustainable solution, mainly because it is not a direct greenhouse emitting activity. Still, this process is highly energy demanding, meaning that it would only be economically feasible if the temporary renewable energy production surplus is possibly redirected to this purpose. Then, as Chi and Yu [4] asserts, one of the critical features for the success of FCEVs is that a robust power supply management policy exists to allow the production of hydrogen in a cleanly manner.

Hydrogen Storage and CPVs

The use of hydrogen as a vehicle propellant entails, among others, multiple challenges regarding the cell design and operation, the vehicle architecture, the fuel storage, and the refueling process, meaning that the various feasible technical solutions are still defining their market shares. Regarding fuel storage, this can be exemplified by alternative stashing hydrogen in pressurized, cryogenic, or chemical conditions. Withal, pressurized hydrogen gas appears as a more qualified solution for road transportation; its setup is technologically the simplest, while knowledge exists in other pressurized propellant systems, like compressed natural gas.

The idea of pressurizing hydrogen gas arises from the low density of the fuel at atmospheric conditions, which is approximately 0.09 g/L, while an average fuel cell consumption of a family car is about 1 kg of hydrogen per 100 km. Hence, comparable ranges to those of an ICE vehicle can only be achieved if the gas density is increased sufficiently to fit the required amount of fuel within the vehicle architecture. The working pressure of these vessels has been targeted as the result of standardization efforts, consequently setting the value of 700 bar as the reference specification, [5]. However, the conception at this working pressure, of vessels made out of metallic materials would lead to unacceptably heavy components. So-called CPVs, vessels produced by filament winding carbon fiber reinforced polymer (CFRP) have been, instead, the design approach adopted by major players in the development of FCEV architectures. The configuration of these is presented generally to be that of a cylinder with domed heads, like the one presented in fig. 1.1, corresponding to one of the hydrogen vessels of the Toyota Mirai.

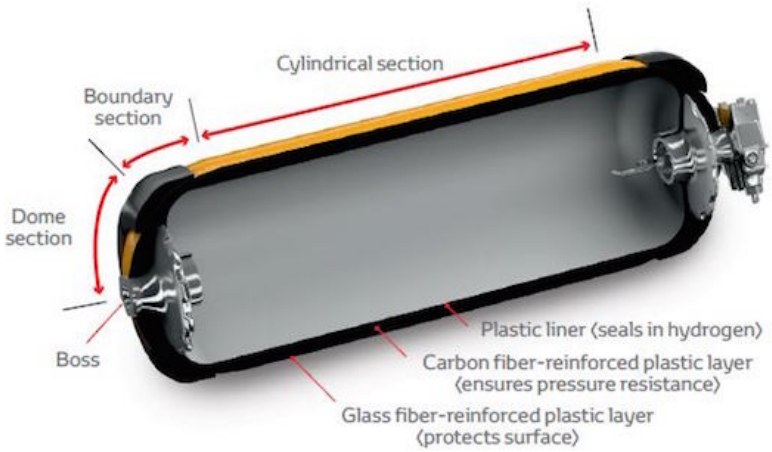


Figure 1.1: Filament wound CPV for a Toyota Mirai commercial vehicle (taken from The Official Blog of Toyota GB [6])

It can then be easily inferred from the geometrical configuration of the vessel that while loaded with internal pressure, it expands, and tensile stresses dominate its mechanical response. By presenting CFRP a tensile strength to weight ratio of about tenfold of that of steel, it looms as a competent material choice in the production of pressure vessels. However, its elevated price causes the final manufacturing figures to be composed on about 60 to 70 % solely on the cost of materials, [7]. This circumstance

undoubtedly promotes the optimization of material used on the premise that increased design robustness has a direct impact on tolerating less conservative manufacturing safety factors. Consequently, a refined design would reduce the amount of material used to achieve the required level of product reliability that, in turn, has a direct impact on the production cost.

Vessel Mechanical Response

In this context, the CPV reliability is determined by how confidently the pressure threshold above which burst occurs is ascertained. Additionally, the design reliability is complemented by predicting the mechanical response and damage evolution of the component during a single event and cycling loadings. Transferring this definition to the presented configuration of a cylinder and domed ends, the design's reliability may be interpreted within which region is burst triggered. This result emerges from the fact that failure taking place in the cylinder shows less scatter than failure taking place in the domes. The cylindrical region of a CPV generally presents a constant winding angle, resulting in a uniform subsection thickness, fiber-volume, and void contents.

On the contrary, towpaths gradually change orientation in the domes to wrap around the dome boss's end opening. This winding pattern causes the thickness to increase because of the successive winding of CFRP bands, while fiber-volume and porosity contents vary according to the normal force applied on the winding surface. Additionally, the orientation change of the filament tows in the domes allows for gaps and resin-rich areas to form where consecutive bands shift to each other.

Whether cylinder or dome failure prevails is, as a consequence, closely connected with the sequence of layer orientations with which a vessel is manufactured. The layup impacts the uniformity of the material properties and dominates the creation of the manufacturing induced defects such as the inter-band porosity and resin-rich areas. Furthermore, the defined stacking sequence precisely defines the directional stiffness distribution within the vessel and, consequently, the resulting load distribution scheme, the generation of local bending moments because of the through-the-thickness stiffness gradient and the appearance of stress concentrations. The compound effect of all these characteristics governs the predictability of the burst pressure and, thus, is the focus of investigations leading to broader commercial use of this type of vessels, [8–11].

In light of the complex mechanical response of CPVs, the comprehensive understanding of the sensitive design and manufacturing variables of these vessels transcends conventional physical tests' reach. The prediction of a particular vessel design burst pressure requires the procurement of mechanical response data at locations, like the inner plies or the ply interfaces, that are not generally accessible. Furthermore, this required data includes the deformational state of the component and the monitoring of its damage evolution. As a result, computational simulations can bring valuable product development insights where experimental data acquisition systems are limited. Simultaneously, simulations limit the test specimen production needs, which considerably reduces development costs.

Research Focus

The goal of this research project is to contribute to the safe design of CPVs by investigating how to incorporate computational simulations into the manufacturing-induced features that impact the prediction of vessel burst pressures. The core of this investigation resides in the correlation of numerical and experimental results at different levels of sophistication. This effort allows verifying the soundness of the followed approach at different stages of the methodology development, while in the meantime providing intermediate results that are directly useful for their industry usage. For instance, burst pressure estimations can be made based on first-ply-failure criteria results, granted that the mechanical response of the vessel in the elastic range had been validated against experimental data. To present the generality of approach, three different vessel stacking sequences are studied on which distinct deformational responses are predicted. Throughout this process, it is expected that new insights will arise in the mechanical response of these components, hence benefiting the development of future designs and introducing a methodology on which to frame it.

This investigation is realized with the support of Daimler AG in its facilities in Untertükheim, Stuttgart. At this location, some stages of the fuel cell stack production occur, whereas research and development are also performed on some of their related components. Concerning CPVs, the facilities at Daimler AG comprise a winding cabin capable of producing full-scale vessels and a specially designed pressure test chamber. This chamber, depicted in fig. 1.2, can pressurize with rates from 0.1 to 200 bar s^{-1}, featuring an array of portholes through which a digital imaging system monitors the outer deformational state of

the specimen. Additionally, the chamber includes a collection of sound pressure sensors used to record the acoustic emissions during pressurization.

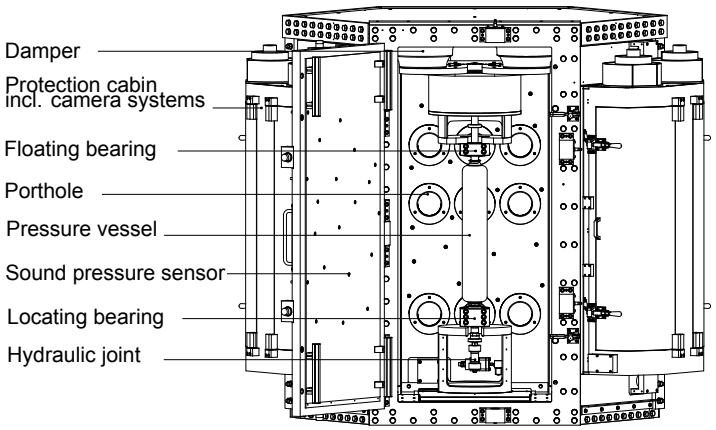


Figure 1.2: CPV testing chamber for the combined acquisition of DIC surface strain and AE data (taken from [12])

Report Structure

To start with this report, a review is presented on the critical aspects that lead to an in-depth analysis of CPVs, hence concluding with the research objective that drives the subsequent thesis work. This review is structured throughout the first chapters, wherein chapter 2 CPVs are introduced from the perspectives of the normative framework, the structural concept, and the manufacturing process, while background to the most relevant approaches for analysis is provided in chapter 3. Next, the analysis methodology followed to account for the influence of the manufacturing process in the mechanical response of CPVs is outlined in chapter 4, which is used to establish a concise framework for the further detailed work. Results are presented and discussed for various vessel stacking sequences by adding levels of complexity to the analysis involved with them.

The construction of the FE model and the mechanical response for a constitutively elastic analysis are then presented in chapter 7. Resulting from these, estimations on the burst pressure are preliminary made from the evaluation of first ply failure (FPF) criteria in chapter 8, whereas modeling of damage progression and its impact in the component strength determination is added subsequently in chapter 9. Ultimately, the variability of material properties along the vessel geometry is considered by, first, characterizing the filament wound material characteristics for changing void contents in chapter 6, and second, implementing this variability in the mechanical analysis in chapter 10. This report finalizes by drawing a set of conclusions in chapter 11 on the accomplishments and limitations of the methodology implemented, which furthermore concretizes in some practical comments on the generalization of the presented strategy. In this regard, aspects that remain open during this investigation are reported and projected into future work considerations in chapter 12.

2

Types and Manufacturing Processes of Pressure Vessels

The design of CPVs for their application in the transportation sector stands as a holistic process that involves reliability regarding the normative framework compliance, the fitting of suitable geometrical vessel configurations within the vehicle architecture, the sufficient design strength in the range of loading cases, scalability and economy of the manufacturing process. In this convoluted context, the available design variables regarding vessel shape and its production methods counterbalance the outcome of strength and safety assessments. This tendency results from the boxed-shapes that maximize enclosed volume in a component boundary container, being relevantly weakened by their sharp edges while also hard to produce, hence making CPV development a somewhat convoluted task.

One of the complexities in the analysis of CPVs is that the composite filament paths gradually change orientation in the dome regions due to the winding process. These filaments show high directional stiffness because of the distinct elastic properties of fiber and matrix, meaning that the load paths in the dome are determined directly from their placement. Furthermore, this directional stiffness pattern is influenced by the local thickness profile that results from the successive stackup of composite bands.

This chapter approaches some of the aspects of the conception of CPVs. It starts by introducing in section 2.1 the currently approved normative framework that sets the requirements for the use of hydrogen pressure vessels in the automotive industry. Following, the most common vessel configuration of the cylinder with dome heads is presented in section 2.2, where its geometrical definition is justified from the work of various authors. The manufacturing process of filament winding is described in section 2.3 by identifying the influence on the final product of various of the multiple production parameters. The definition of filament paths in CPVs is approached next by considering the fiber orientation, the associated thickness increase, and the corresponding winding patterns. Therefore, the compound effect of filament paths and dome shapes is described in section 2.4 in the context of the general vessel mechanical response. Lastly, the filament path definition is coupled in section 2.5 with the thickness increase experienced during layer winding to show the impact of these in the dome profile characterization.

2.1. Introduction to the Normative Framework

The storage of hydrogen gas in pressurized conditions within the automotive industry evolves consistently from the matured technology for the stocking of compressed natural gas (CNG). Because of this reason, the already established certification framework that determines the technical specifications of hydrogen pressure tanks, the ISO 19881 [13], presents numerous similitudes with the one previously defined for CNG, the ISO 11439 [14]. Particularly to hydrogen storage, the International Standards Organization (ISO) standard complements with the regulatory framework settled by the Economic Commission for Europe of the United Nations (UN/ECE) [5], thus creating a compelling scheme that defines the tank service conditions, the material and component design qualification tests, the manufacturing processes, the inspection methods and the peripherals specifications (check, shut-off valves, and pressure relief devices).

According to this regulatory scheme, [5], the nominal working pressure (NWP) of a pressurized hydrogen tank is established in 700 bar. This NWP is subsequently verified for baseline static and cyclic pressure loading tests, as well as several other pressure cycles involving various durability conditions. Specifically, the static burst pressure requirement is set to be above 225 % NWP within a scatter of ±10 % percent on three containers, whereas three tested tanks shall resist 22 000 cycle sets to 125 % NWP at ambient temperature without failure. Following, verification tests for performance durability are carried according to the series presented in fig. 2.1, where failure shall not happen. It consists of a proof pressure test to 150 % NWP held for 30 s, after which the vessel is subjected to a drop impact and surface damage. The container is then exposed to chemicals found in the on-road environment and cycled to 125 % NWP, where the last 10 cycles are increased to 150 % NWP. After the vessel is pressurized to 125 % NWP at 85 °C for 1000 hours, it is cycled to 80 % NWP at −40 °C and a combined 85 °C and 95 % humidity. Finally the residual strength is verified by pressurizing to 180 % NWP for four minutes, and reaching an 80 % of the static burst pressure BP_0 without failure.

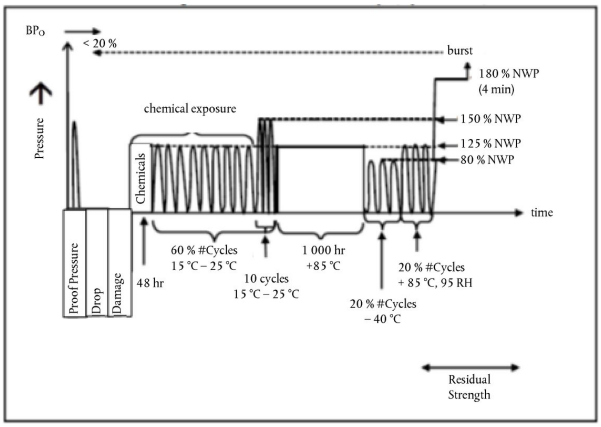


Figure 2.1: Verification cycle for performance durability testing of hydrogen pressure vessels (taken from [5])

In a like manner, on-road performance is verified by carrying the test cycle presented in fig. 2.2 where leak shall occur. The series consists of a proof pressure test to 150 % NWP for 30 s, followed by a 500 hydrogen gas cycle. The cycle loading is interrupted by a permeation test and finalized with a residual strength verification equivalent to the performance durability series. During the cycle loading, alternative combinations of pressure, cycle number, temperature, and humidity are defined as indicated in fig. 2.2.

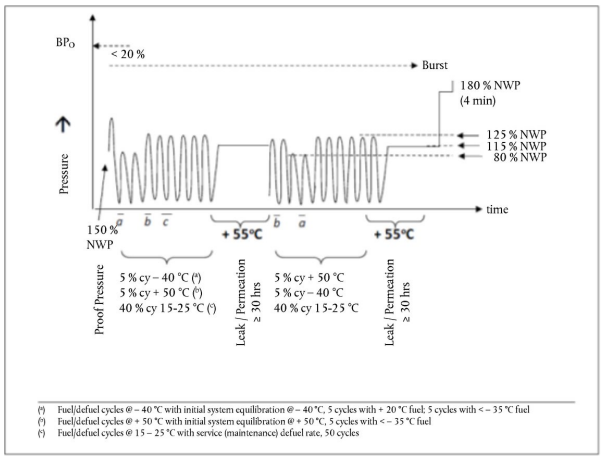


Figure 2.2: Verification cycle for on-road performance testing of hydrogen pressure vessels (taken from [5])

The comprehensiveness of these tests is motivated by the risk that a bursting vessel poses to the integrity of the vehicle and occupants. Therefore, high reliability is required from the tank production that results from a conservative design in light of a complex mechanical response. The choice of

materials is closely related to the accuracy with which burst is predicted as, for instance, metal-based solutions show a more predictable mechanical response than composites. This behavior motivates that the international specification [13] classifies pressure vessels according to their material construction, which range from full metal to full composite. This classification is illustrated in fig. 2.3 for a cylinder tank configuration with domed heads, and is specified as follows:

- Type I: Full-metal vessel.
- Type II: Metal vessel with a hoop-wrapped composite reinforcement in the cylindrical section.
- Type III: Metal liner that is fully overwrapped by composite reinforcement.
- Type IV: Full-composite vessel wrapped over a plastic liner served as mandrel during the manufacturing process and as seal during service.
- Type V: Full liner-less composite vessel.

The presented vessel configurations progressively increase the use of composite materials, as it also reflects from their standardization and generalization. A parallel trend can be observed on the progressively reducing vessel weight and its arguably increasing strength. However, associated costs also increase because of the less productive manufacturing processes and the pricey acquisition of materials.

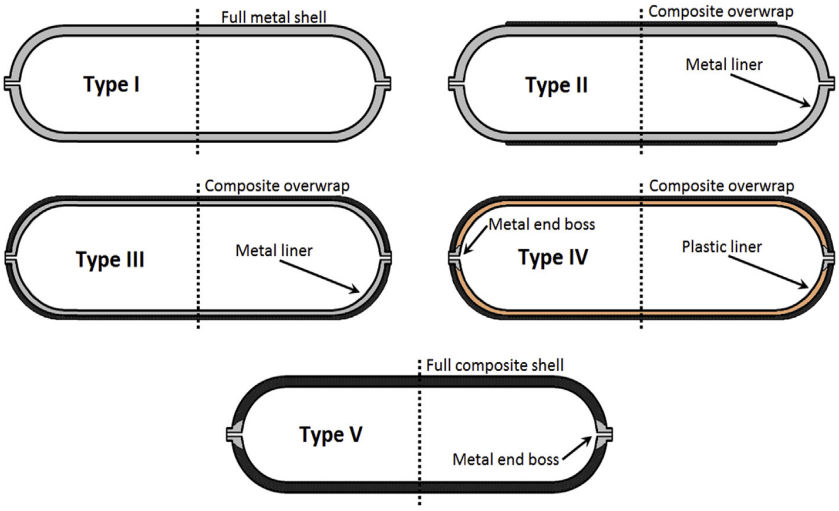


Figure 2.3: Identified pressure vessel types according to their structural design (taken from [15] after [14])

2.2. Structural Definition of Cylindrical Vessels with Domed Heads

The cylindrical vessels with domed heads in fig. 2.3 appears to be the preferred geometrical concept in the currently available pressure tanks. It can be argued to be based on the effective volume extension of the spherical vessel concept, that naturally distributes membrane loads uniformly because of their infinite axes of symmetry, [15]. However, the large bulk volume of spheres makes them fit poorly within vehicle architectures while also storing comparatively small quantities of gas. Instead, cylindrical shapes can be laid on flat areas while taking much smaller useful volumes. Nevertheless, the convenience in the geometric setup comes from a moderately more complex dome construction that requires the dome shape to find the right balance between maximum capacity and minimum wall material thickness. In this regard, Błachut and Magnucki [16] present the dome shapes that generate isotensoid states on isotropic vessels of various radius-to-depth ratios to be close to those of ellipsoids. Correspondingly, Vasiliev et al. [17] conclude in their work that ellipsoidal and tropospheric dome shapes are the convenient choices in the production of commercial vessels made out of orthotropic materials.

Optimum dome shapes of vessels made of filament wound composite materials are obtained in their most elemental form from the isotensoid solution to unidirectionally reinforced components, [18].

However, the influence of failure criteria in finding dome solutions for orthotropic materials has already been investigated by Fukunaga and Uemura [19]. Correspondingly, Hojjati et al. [20] studied the uniform stress dome solution, where the dome material thickness shows to have a direct impact on the results. It is concluded that the thickness is not straightforwardly estimated due to its coupling with the defined dome material orientations. Further work in this matter is introduced by Liang et al. [21], who conclude that an ellipsoidal shape is close to optimal in minimizing the results of a Tsai-Wu failure criterion when the material orthotropy is considered. In fig. 2.4, the results of their dome shape optimization are presented against previous optimum shape results, which, although subject to the limitations of thin wall assumptions, appear to be considered a baseline of more recent vessel optimization works, [9, 11, 22]. Nevertheless, these show to instead focus on the definition of fiber orientations and stacking sequences and do not seem to consider the compound effect of the thick-wall composite and its corresponding mandrel shape.

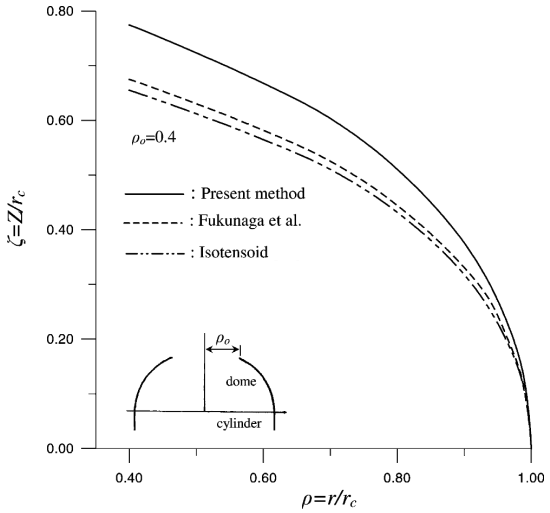


Figure 2.4: Comparison of optimum dome shapes of Fukunaga and Uemura [19] and Liang et al. [21], where ρ and ζ are normalized parameters with respect to the cylinder radious r_c (adapted from [21])

The use of composite materials in the production of pressure vessels is presented by Vasiliev et al. [17] to be an advantageous choice based on the driving tensile membrane forces that emerge from the vessel when subjected to internal pressure. Hence, as their tensile strength to weight ratios outperform those of steel, composite materials have a relevant potential in meeting the demanding regulatory requirements illustrated in section 2.1. The equipment of peripherals is generally achieved by placing metallic bosses at the domes, which additionally have a twofold advantage. First, they substitute the pole areas on which composite bands easily slip with a robust metallic component. Second, the boss shape accommodates the composite material in the vicinity of the pole regions, allowing them to keep adequate geometrical control of the filament path alignment. The influence of the boss in the composite fiber orientation definition is further explained in section 2.4, where their impact on the design flexibility of the tank is also introduced.

The internal pressure state of the vessel leads to two different types of plies that are relevant for its design, namely circumferential and helical. Circumferential plies are formed by fibers that wrap the tangential direction of the cylindrical region of the tank, where stress in the hoop direction outpaces the meridional components. In pipes where thin-wall assumptions hold, the factor of the hoop to meridional stress tends to two, even though concerning CPVs this guess is rather non-realistic because of the general high thickness to diameter ratios. Helical plies are formed by fibers mostly aligned with the vessel meridional direction, draping and turning in a continuous form at the dome ends. The alternating change of course of the helical layers at the vessel poles generates an interwoven $\pm\alpha$ orientation pattern where the α angle is constant in the cylinder and varying in the domes according to either geodesic or non-geodesic descriptions. The helical dome paths are responsible for carrying the axial components of the pressure load and are further described in section 2.4 according to their load-carrying capability. Despite balancing the axial load component transferred to the cylinder, helical layers also bear the hoop component of the dome region load. This change of optimum directional s

It is resolved that even for the most sophisticated cylindrical CPV designs, relevant factors limit their reliability. These are mostly related to the structural strength in the dome regions compared with the cylindrical section, the suitability of the domed shapes for filament winding, and the resulting material characteristics that derive from the latter.

2.3. Composite Filament Winding of Pressure Vessels

The production of composite pressure vessels can be conveniently accomplished through the winding of composite filaments over a rotating mandrel. This process allows the drape of the composite material on relatively high curvature shapes by permitting differential positioning of progressive bands. Internal shear stresses that create wrinkles are thus prevented, producing a composite reinforcement that truly follows the shape of the mandrel. This process also evades for the most part from the most severe material imperfections that would arise from a conventional lamination, such as severe fiber misalignments, resin-rich areas, and gaps.

Thence, the idea behind filament winding consists of a rotating mandrel over which a moving bundle delivery eye wraps a composite material roving, [23]. For the production of CPVs, the filament feeder is generally capable of moving axially (along the vessel longitudinal direction), as well as radially (transversely to the vessel longitudinal axis). Additionally, the delivery eye features a rotational degree of freedom at its head, that permits to fit the composite tow to its desired orientation in the dome regions as depicted in fig. 2.5. During the winding process, a mandrel is needed to maintain the geometric control of the final product. However, it is derived from the vessel classification in fig. 2.3 that depending on whether the mandrel is made out metal, plastic, or it will be reused, it contributes in different extents to the structural characteristics of the manufactured vessel. Metallic mandrels significantly increase the strength while having a significant impact on the total weight, whereas plastic ones serve principally as seals. Removable mandrels are generally presented as dissoluble sands or as inflatable molds. These, either eliminate unnecessary material usage in performance-driven applications or allow the reuse of manufacturing components for reduced costs per component in mass production.

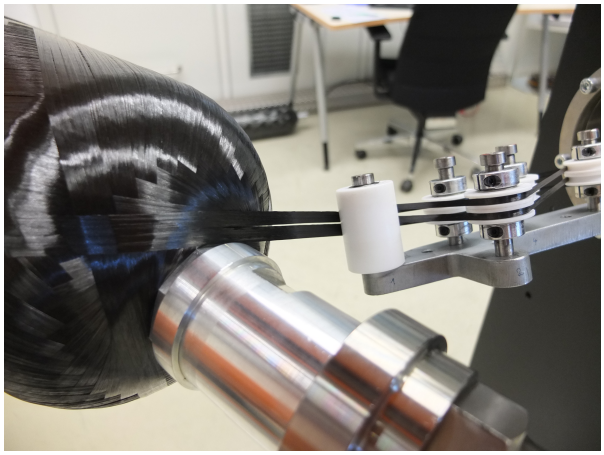


Figure 2.5: Rotation of a delivery eye during winding of the dome regions of a CPV

The schematics of a filament winding configuration is presented in fig. 2.6, on which a system that winds dry rovings with a multi-axis robot is depicted. In this configuration, preimpregnated rovings are gathered in a band from spools and fed into the delivery eye. As the vessel rotates, the multi-axis robot moves axially, and the delivery eye adjusts its inclination angle as presented in fig. 2.5. Therefore, it places the material band following normal directions to the mandrel surface at each location, reducing its slip potential and preventing the formation of wrinkles when the filament orientation changes. The vessel is wound in a continuous form, where the change of layer pattern is achieved using connecting circuits. Alternatively to dry winding, a wet process is set up if fibers are gathered and bathed with resin.

Wet winding requires a precise definition of the amount and viscosity of the resin to be fed, which leads to an intrinsic scatter in the resulting material fiber volume contents. Nevertheless, being the shelf life simply limited by the degradation of fiber sizing derives in relatively low operational costs. Dry

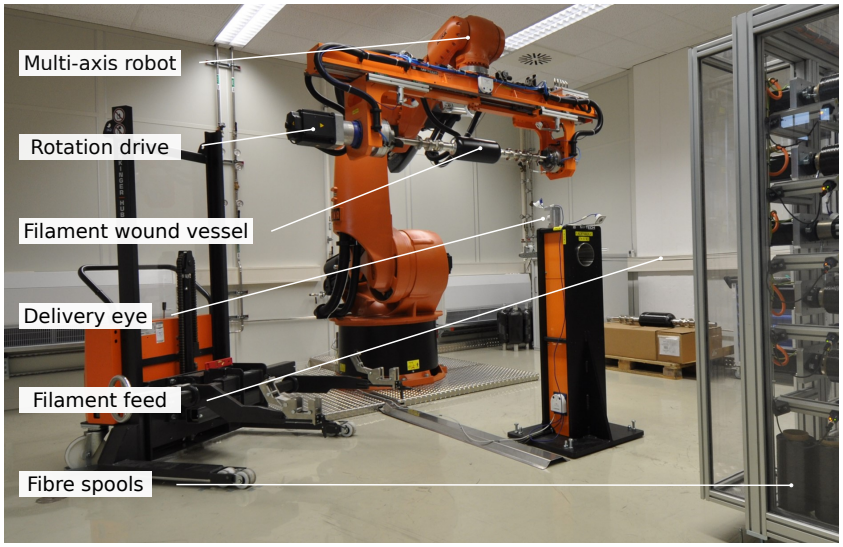


Figure 2.6: Schematics of a multi-axis filament winding equipment

winding employs preimpregnated tows where the resin content is consistently controlled at the bundle production stage. However, as a result of the reactive impregnated resin compound, the storage life is somewhat restricted and limited to reduced temperature conditions. Regarding the material quality outcome, the low viscosity of the resin during wet winding makes it more prone to its accumulation in pockets, whereas high porosity values can be expected if the impregnation stage entraps excessive air. On the contrary, the more exhaustive quality control of prepregs results in lower porosity contents, although inter-band voids can be generated because of the more limited resin flow before full crosslinking.

The friction generated during winding of successive tows appears as a relevant variable in the definition of the dome filament paths. This potential of slippage determines the rate to which the fiber orientations can deviate from their geodesic trajectory, i.e., the shortest trajectory that connects two points of the dome, and as shown by Wang et al. [24], it is connected with multiple manufacturing parameters. From the results of this investigation, the most relevant variables are the roving width and the resin viscosity, which is likewise influenced by the winding type (dry vs. wet).

The resulting quality of the filament wound material is additionally controlled by the tension with which the composite rovings are fed to the winding delivery eye. It has a twofold influence, as the filament tension prevents the roving from wrapping and wrinkling, while it also generates normal traction towards the underlying mandrel surface, [25]. If the fiber tension is low, small compaction of the inner layers results, leading to high porosities and smaller fiber volume contents. Instead, high fiber tension induces some of the uncured roving filaments to fail and bloop, reducing the strength and creating material imperfections during subsequent winding. High tow tension leads to excessive resin infusion in the presence of low viscosity resin, which ultimately causes undesirably high fiber volume contents. In this case, an insufficient resin content in the composite material prevents the load from being carried collaboratively between fiber and matrix, therefore detrimentally impacting its strength.

Ovens and radiating heaters are presented as the preferred options for curing the wound product whenever the material compaction achieved during the filament winding process results in low porosities, [25]. Correspondingly, the alternatives of autoclave and vacuum bag assisted curing induce a predefined pressure cycle that assists the degassing and the infusion of excessive resin. However, the problematic compatibility of these processes with economic mass production emerged as one of the reasons the automotive industry does not consider them in the manufacturing of CPVs, [26]. Still, the sustained moderately high temperatures applied during the curing process directly impact the geometric stability of the final product. When metallic liners are used, the thermal expansion mismatch between liner and reinforcement appears to cause a small gap between the two. This effect is explained from the temperature increase that causes the metallic liner to expand and viscously deform the uncured composite while matrix crosslinking is not fully developed. As the resin cures and acquires its final state, the deformed configuration is preserved when the liner contracts to its original ambient

temperature geometry. In the case a plastic liner is used, a similar outcome results from the necessity of applying a sustained internal pressure during the manufacturing process. It prevents the liner from collapsing due to the winding induced normal loading until the resin is fully cured. However, as the uncured composite material is loaded with a mild constant internal load, a viscous deformation is induced, which likewise generates a gap when the liner is depressurized.

Altogether, filament winding suits well the manufacturing of composite surfaces of revolution by producing geometrically consistent components. Nevertheless, the quality of the final product is presented to be sensitive to a high degree on the process variables. An adequate selection of the tow tension, the roving impregnation method, and the resin viscosity and tackiness appear to have a definite impact on the porosity, fiber volume contents, layer thickness, and fiber misalignment. Concerning this matter, it is relevant to define whether a fixed set of manufacturing parameters improves the quality of the domed regions while diminishing that of the cylinder or, correspondingly, improving the quality of the inner layers while weakening the outer ones.

2.4. Description of Filament Paths

The production of CPVs through the filament winding process requires the composite tows to drape around the dome ends to achieve full surface coverage and ensure material continuity. Thus, the wrapping of bands on the domes creates a fiber orientation variation for the meridional vessel direction and, as such, has a direct impact on the stiffness and load distribution [27]. As presented in the work of Zu et al. [28], this characteristic also couples with the intrinsic thickness increase towards the vessel pole openings, having a substantial impact on the structural strength in the domes. During the filament winding process, the thickness increases towards the dome poles because successive composite bands overlap with each other in their turnaround locations. This effect happens because material continuity requires the thickness to increase where the diameter reduces, i.e., towards the poles, thus leading to a successive laying of bands until full coverage of the cylindrical region is achieved. The specific choice of material architecture (layers sequence and orientations) has a significant effect in the stiffness pattern of the vessel and the confinement effect induced by the winding of successive layers.

Being the compound effect of the filament path definitions and the dome shape an aspect of clear relevance towards the strength of CPVs, several studies have been found to explore their design and optimization possibilities [17, 19–22, 27–34]. The earliest works are found to be based on the rather rudimentary netting analysis, [18, 19, 29]. In contrast, this approach is also used in more recent works because of its convenient simplicity, [31, 32]. From then on, the CLT appears to be a much more general approach because of the possibility of accounting for material orthotropy. Initially, the CLT is presented to show its applicability over the netting theory, [20, 21, 30], while in the subsequent studies, it is directly regarded as a reasonably accurate and cost-effective solution, [17, 27, 28, 34]. The use of thick wall analysis for layup simulation through finite elements has only been possible with the widespread of modern computational capabilities where, nevertheless, axisymmetrical simplifications appear to be enforced, [22, 33].

The netting theory is based on sole contribution of the fibers to the strength and stiffness of the material. Loading other than membrane is neglected and, as no contribution of the resin content is accounted, the interaction between layers is likewise disregarded. Correspondingly, the CLT considers the full orthotropy of the material and allows showing the relevance of the matrix strength in the definition of the optimum fiber paths, [20]. Notwithstanding, in the more recent works of Park et al. [33] and Leh et al. [8], the composite layer thickness is shown to have a major role in the CPVs mechanics. These studies indicate that, on the one hand, the thickness increase of the inner layers has a significant effect on the path definition of the successive ones.

On the other hand, as Baličević et al. [35] argue, for the hydrostatic loading state, meridional moments and out-of-plane shear loads appear in the dome transition regions because of the change of geometry curvature. The existence of these internal loads in a component that has a relatively thick wall implies that the assumption of plane sections remaining plane after deformation is not generally acceptable. As a result, authors like Park et al. [33], Leh et al. [8], and Zu et al. [28], indicated the necessity of coupling methods for the fiber path definition with the estimation of the layer thickness after each circuit winding. Such a methodology for the coupled filament path prediction and layer thickness is illustrated in fig. 2.7 after the results of Leh et al. [8]. In this figure, the predicted layer thickness following a non-geodesic path description is compared with that of the produced dome cross-section

to show the complex stack of layers taking place in a vessel dome. The presented layup comprises a non-thin stacking sequence with multiple ply end features that fall out of the scope of the classical lamination theory (CLT), thus justifying the use of more sophisticated analysis methods.

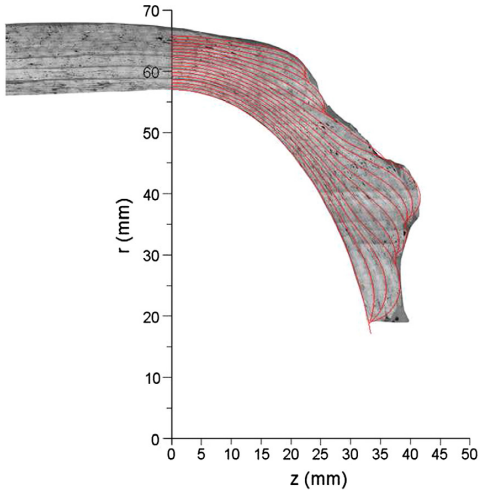


Figure 2.7: Comparison of calculated layer thickness at the dome region of a CPV by coupling of non-geodesic fiber path and a roving thickness estimation (taken from [8])

Geodesic fiber paths refer to the shortest line that connects two points of the dome, where their definition is solely based on the initial fiber angle and the underlying surface. The use of geodesic paths is relatively simple, although, from the work of Zu et al. [27], it does not necessarily provide a solution uniformly distributing stress along the dome surface. Correspondingly, non-geodesic fiber paths deviate from the geodesic definition by introducing a controlled lateral displacement of the roving based on its lateral slippage resistance. Through this refined path definition, the load distribution in the dome can be designed to make more efficient use of the material, which, as a result, has a direct impact on the vessel strength. Non-geodesic paths also tolerate the design of non-symmetric CPVs, like the ones encountered when a pole opening is defined in only one of the sides, and which the work of Zu et al. [32] further develop by characterizing the equations that control the path non-symmetry. All in all, it is observed that the works of authors in the topic of CPVs have made use of geodesic filament paths mostly during their earlier stages of development, [17, 19–21, 29–31, 36], whereas non-geodesics seem normalized in more recent investigations, [22, 27, 28, 32–34].

The filament behavior definition at the turnaround points is a relevant variable for the subsequent winding pattern description. Turnaround points refer to the position of the pole opening where the filament is wound tangentially to the opening circumference. At these points, the relative winding angle between meridian and filament path is approximately orthogonal and following; the filament describes a symmetrical trajectory over the dome surface. In the work of Zu et al. [28], during the winding process, the total number of tow tangential points at the pole opening has a significant influence on the uniformity of the layer end thickness increase. Moreover, the resulting pole opening of a defined layer is mostly controlled by the initial winding angle in the cylindrical region. Non-geodesic filament paths permit to vary, to an extent, the pole opening for fixed cylindrical winding angles, although limited by the maximum allowed slippage potential.

A stacking sequence that features multiple winding angles for helically wound layers results in a staggered pole opening configuration that generates a non-uniform dome thickness profile of the type depicted in fig. 2.7. Such a non-uniformity influences the dome stiffness pattern and, because of it, its load distribution and strength characteristics. Therefore, the effect of the combined vessel design and resulting geometry emerges to be a relevant variable in the robust and reliable production of CPVs.

2.5. Coupled Definition of Layer Thickness and Non-Geodesic Filament Paths

Based on the general idea that the thickness dome profile is influenced by the stacking of successive layers of different orientations, multiple approaches are proposed in the literature and the engineering

practice to estimate the dome profile. One of the most fundamental approaches is the one from the Wound Composite Modeler (WCM), [37], of the Abaqus FE software, [38], that uses a geometrically derived equation dependent solely on the winding angles. Not considering the bandwidth in the calculation implies that the thickness tends to infinite at the pole, which is arbitrarily tackled by truncating the thickness profile at a specified pole distance. Similar approaches are proposed by Knoell [39] and Gramoll et al. [40], whereas Wang et al. [41, 42] introduce a new method based on the approximation of the thickness profile by cubic spline functions.

The strong correlation between the defined winding pattern and the resulting vessel dome thickness profile is illustrated by Zu et al. [27], and studied in its coupled form by Park et al. [33] and Leh et al. [8]. Specifically, Leh et al. [8], develop a methodology based on the cubic spline function thickness prediction of Wang et al. [41, 42] and non-geodesic filament paths. These trajectories significantly increase the design space but require the enforcement of derivative path continuity between the dome and cylindrical regions. The geodesic and non-geodesic paths are defined by the following equation, [27],

$$\frac{d\alpha}{dz} = \lambda\left[\frac{\sin\alpha\tan\alpha}{r} - \frac{r''}{1+r'^2}\cos\alpha\right] - \frac{r'\tan\alpha}{r}, \tag{2.1}$$

where α refers to the angle between the filament path and the meridian direction shown in fig. 2.8, λ indicates the coefficient of slippage between the tow and the underlying surface, r and z indicate the radial and axial coordinates of the dome, and serve to define the thickness at which the stacking of tows is taking place. The variable $r = r(\theta, z)$ is a function of the circumferential angle θ and the dome axial depth z, whose derivative detailed definition is presented in [28].

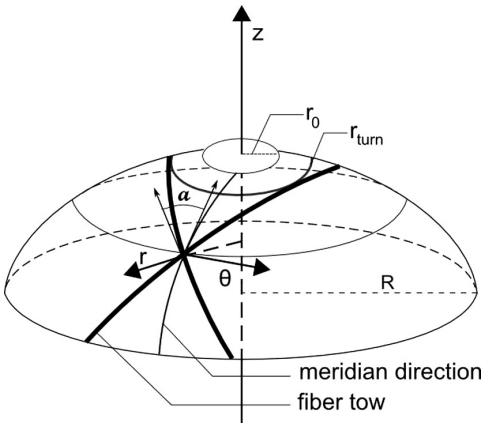


Figure 2.8: Schematic representation of the filament path in the dome region (taken from [8])

The concept of slippage potential is introduced by De Carvalho et al. [43] and refers to the ratio of transverse (f_b) to normal (f_n) forces acting on the filament:

$$\lambda = \frac{f_b}{f_n}. \tag{2.2}$$

The normal force acts perpendicularly to the dome surface and is balanced by the mandrel reaction, while the transverse force is canceled out by friction. Correspondingly, the filament path is stable insofar the lateral force is smaller than the friction force which, if defined by a Coulombian description, can be written as

$$|f_b| \leq |f_w| = |\mu_s f_n|, \tag{2.3}$$

being f_w the friction force and μ_s the static coefficient of friction between roving and surface. The condition of stability for non-geodesic paths can thus be regarded as the need to define a lower slippage factor than the local coefficient of friction. In the case the coefficient of slippage λ is 0 in eq. (2.1), the solution to the corresponding equation results in a geodesic path and is simplified to the law of Clairaut for surfaces of revolution $R\sin\alpha = K$ (constant), [27]. Whether the slippage coefficient is positive or negative controls the location of the turnaround point for the geodesic solution, either displacing it to

the pole or towards the cylindrical region. Likewise, for the same turnaround position as in the geodesic solution, positive and negative slippage coefficients result in lower and higher initial winding angles in the cylindrical region, [8].

The continuity condition ensures a smooth transition between the cylindrical and dome region fiber orientations is enforced according to Zu et al. [27] as

$$\lambda = \lambda_{max} \cos\left(\frac{\pi}{2}\frac{(r - r_{turn})}{(R - r_{turn})}\right), \tag{2.4}$$

where R refers to the radius of the cylindrical section (equator of the domed head) including the thickness build-up with successive plies, r_{turn} is the dome radius at the turnaround point and λ_{max} is an arbitrarily chosen maximum value of the coefficient of slippage that respects the friction-limited critical coefficient condition. Friction between consecutive tows is identified from the work of Wang et al. [24] to be mostly dependent on the resin viscosity and the roving width, while the winding speed and the tow tension have a much less relevant effect. In this investigation, the slippage coefficients are measured over specifically designed mandrels to linearly relate the cross-section radius with the transverse tow forces before slippage. As a result, it is noted that for engineering purposes, the slippage coefficients generally range from 0.1 (wet winding) to 0.5 (dry winding).

In the work of Leh et al. [8] the thickness description is defined after the spline function method presented by Wang et al. [41, 42], and formulated as

$$t(r) = \frac{n_R m_R t_p}{\pi}\left[\arccos\left(\frac{r_{turn}}{r}\right) - \arccos\left(\frac{r_b}{r}\right)\right] \text{ for } r_{2b} \le r \le R \tag{2.5}$$

and

$$t(r) = A + B \times r + C \times r^2 + D \times r^3 \text{ for } r_{turn} \le r \le r_{2b}, \tag{2.6}$$

being n_R and m_R the number of helical plies and their count in the cylindrical section of the CPV. Correspondingly, the values of r_b and r_{2b} refer to the pole radius at one and two tow-width distances from the turnaround point, r_{turn}, that can be located either at the pole opening or at a conveniently staggered position. The constants A, B, C and D are the fitting coefficients that define the layer end thickness, which are determined from the helical ply thickness at the turnaround point, the continuity of thickness and curvature in r_{2b} and a constant material volume between r_{turn} and r_{2b}. A layer is then defined as the group of helical plies that have the same winding angle ($\pm\alpha$) in the cylindrical section. The parameters n_R and m_R are described as,

$$n_R = \frac{t_R}{2t_p} \tag{2.7}$$

$$m_R = \frac{2\pi R \cos\alpha_R}{b}, \tag{2.8}$$

where t_p and b are the thickness and the width of the filament band, t_R and α_R are the thickness and the initial winding angle of that layer in the cylindrical region.

The method introduced by Leh et al. [8] is solved by calculating the first two derivatives of the liner shape contour, which correspondingly allow finding its shape normals. The dome head is then divided into an arbitrarily chosen number of points in its axial direction for which the corresponding cylindrical coordinates are defined (radial and axial). The turnaround position for the helical ply is calculated from eq. (2.1), which permits to obtain the thickness profile from eqs. (2.5) and (2.6). After a B-spline smoothing, the thickness solution to the first ply defines the base shape contour of the subsequent one. Then, with the new shape contour, a new turnaround point is calculated, leading to an updated thickness profile.

Among the relevant considerations of the filament path determination methodology is the fact that the initial winding angle of the helical layer is limited as a function of the tow width. This constraint is necessary to avoid the variable r_{2b} to be larger than the cylinder radius, thus leading to the divergence of eq. (2.1). Correspondingly, the maximum winding angle of the circumferential layers is limited to allow surface coverage with a minimum overlapping. Regarding the influence of the filament path definition on the helical ply thickness, the only considered effect is its impact on the determination of the turnaround point. Moreover, the confinement experienced by the inner layers can only be accounted for in the

presented approach by the empirical definition of the parameter t_R. The confinement is related to the winding angle in the form that higher angles concerning the meridional direction generate a higher compression, and vice versa.

The approach presented by Leh et al. [8] appears to be primarily subjected to the complexity of the underlying surface shapes over which the composite layers are wound, wherefrom the configuration depicted in fig. 2.7 a right prediction is observed for an arguably complex stacking sequence. A high potential of this dome thickness definition appears from its coupling with the winding pattern influence on the thickness. This topic has been further studied by Zu et al. [28], who depict the importance of the number of tangential points and tow widths in achieving dome thickness uniformity.

3

Background to the Analysis of Composite Pressure Vessels

The variable with the most significant industrial applicability in the design process of CPVs is the pressure above which the tank can be predicted reliably to burst. In the attempt to forecast it, authors in the topic have applied different mechanical analysis methodologies that, in the first term, allow to determine the material stress state when the CPV is subjected to increasing internal pressure. Then, the likelihood of failure can be estimated based on the existing knowledge regarding composite material strength. In more advanced studies, this is extended to the progression of damage description that, from its triggering, leads to the final structural collapse.

This chapter provides a background to the CPVs analysis by reviewing the work that authors have made on the topic. In section 3.1, the analytical tools for the analysis of composite pipes are first considered because of their potential in accounting for the thick-wall shell definitions. Following, some fundamental works are reported in section 3.2 to present the analysis of isotropic and unidirectionally reinforced vessels. The scope is extended in section 3.3 to the composite material orthotropy of the CLT and its usefulness as a preliminary design tool of the following more detailed FE analysis. These are introduced in section 3.4 by examining the potential of broad FE usage and the possibility of modeling material damage triggering and progression. The chapter concludes in section 3.5 with the analysis opportunities review of the current state of the art CPVs and the considered research questions.

Altogether, the focus is set on the contribution of these investigations to the robust understanding of the mechanical response of the components. Thus, it is generally noted whether the presented studies account for the triggering of material damage if they model boss and liner yielding, their material characterization steps, and the extent to which they validate their results with experimental and analytical investigations.

3.1. Analytical Analysis of Cylindrical Composite Shells

The sole study of pipes appears to be of relevance in the development of analysis techniques of CPVs inasmuch their cylindrical section shows the mildly high length to diameter ratios. Analytical solutions that consider either thin or thick wall assumptions can be developed, which results in favorably fast calculation methods. Nevertheless, their applicability is diminished if the mechanical response becomes more complex, for instance, because of the application of boundary conditions.

The thin composite pipes analysis appears to be equivalent to that of conventional laminates when its reference system is transformed from Cartesian to cylindrical. It is for this reason that, although the elementary netting composite analysis theory is only regarded for preliminary analysis, [44], the classical lamination theory (CLT) serves as an accessible generally acceptable analytical tool, [45]. As a result of the high-pressure loading of CPVs, the cylinder wall definition soon falls within a thick-wall range, meaning that theories that account for its non-linear through-the-thickness deformation are required.

An approximation to the full 3D elasticity theory is presented by Xia et al. [46] for thick composite cylinders. This work presents the stress and strain distribution variation for various stacking sequences

and the effect these have on the hoop ratio to axial stresses. Following, the investigation of Zu et al. [47], further develops this approach by accounting for the in-plane twisting due to helical layer orientation unbalance. The effect of a metallic liner in smoothing the through-the-thickness stress gradients is reported, as well as the sensitivity of these to the various liner and composite laminate thickness combinations. In the work of Asadi et al. [48], a 3D elasticity approach is coupled with two different first-order shear deformation theory (FSDT) alternatives to show their suitability for different thickness to diameter ratios. Correspondingly, Parnas and Katirci [49] use the CLT and a generalized plane strain model to account for a detailed gradient of stresses through-the-thickness. It is shown from this investigation that, for ratios of outer to inner radius larger than 1.1, the burst pressure determined by a quadratic failure criterion starts to become overly conservative if the thin wall assumption is in use.

Recently, Ramos et al. [50] have introduced a generalized approach to 3D elasticity theory for thick composite pipes subjected to multiple mechanical loadings. This methodology allows calculating the stress fields of anisotropic cylinders of any thickness. Their results are compared with FE analyses, and it is observed that according to a Tsai-Wu failure criterion, thick pipes fail because of tensile stress in the circumferential direction. Instead centered on the experimental level, Mertiny et al. [51] introduce a comparison of pressurized pipes of various stacking sequences. The convenience of placing hoop dominated plies in the outer layers is identified to resist internal pressures better. The stresses reported in this work are calculated based on thin wall approximations, although justified on the production of relatively thin testing specimens.

The mechanical response of cylindrical shells shows to be useful in assessing the structural behavior of the cylindrical section of CPVs while it can also reasonably predict the occurrence of burst if the residual strength of the domes is sufficient to avoid their failure. Notwithstanding, the analysis of pressure vessels as pipes disregards the complexity of the domes and the dome transition regions, and with them, the uncertainty that arises in their strength determination. This assumption implies that principal aspects of the design are ignored, hence only justifying the simplification of pipes for practical purposes for preliminary and fast analysis.

3.2. Fundamental Work in the Analysis of Pressure Vessels

The most fundamental works in the analysis of pressure vessels are based on the derivation of the governing equations of thin shells of revolution, as carried by Love, Reissner, Goldenveizer, and others, and reviewed by Vinson, J. R. [52]. These investigations are based on the isotropic materials assumption, although it is observed from the work of Hofeditz [29] that there has also been a lasting interest to account for the filament wound orthotropic characteristics.

Concerning the study of isotropic pressure vessels, Baličević et al. [35] present a stress analysis of cylindrical vessels with elliptical heads. In this work, the solutions to the differential equations of shells of revolution are approximated by the membrane and moment theories superposition. This approach enforces thin wall conditions and allows determining the distribution of internal forces and moments. The results show that a critical strength position of the vessel is nearby its knuckle, where successive positive and negative meridional moments appear and overlap with the dominating circumferential forces. A distribution of moments like the one presented in fig. 3.1 appears from the rigid connection between cylinder and dome. By impeding their relative rotations, the opposite deformation slopes that they would experience if connected by hinged joints are effectively counteracted.

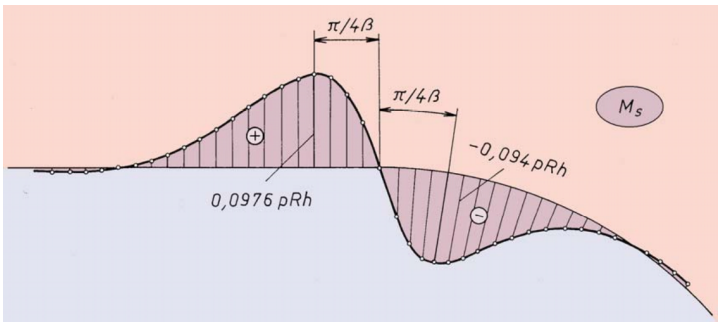


Figure 3.1: Meridional moment distribution due to internal pressure at the knuckle of an isotropic vessel with elliptical heads (taken from[35])

The initial form of analysis of composite materials is based on their unidirectional reinforcement characteristics, the so-called netting theory, [18]. According to the netting theory, the composite structure carries its load solely by fiber tension, which means that an optimum design is found from the fiber orientation, and correspondingly the surface shape, that results in an isotensoid solution, [53]. The in-plane force resultants in a shell of revolution according to the netting theory can be generally expressed as, [19],

$$\begin{aligned} N_s &= \sigma_L t_R \cos\alpha^2 \\ N_\theta &= \sigma_L t_R \sin\alpha^2 \\ N_{s\theta} &= 0, \end{aligned} \tag{3.1}$$

where the subscripts s and θ indicate respectively the meridian and circumferential directions of the shape. The stress in the fiber is defined by σ_L, while t_R and α refer to the thickness and the orientation of the layer along the meridian direction.

Besides, the internal forces in a general shell of revolution with double curvature can be written as, [19],

$$\begin{aligned} N_s &= P \cdot r_\theta/2 \\ N_\theta &= [2 - r_\theta/r_s]\, P r_\theta/2 \\ N_{s\theta} &= 0, \end{aligned} \tag{3.2}$$

where P is the internal pressure, and r_s and r_θ refer to the principal (meridional and circumferential) radii of curvature. Then, the isotensoid solution is obtained from the coupling of the internal force definition with the filament path orientations introduced in section 2.5.

The isotensoid solution is described in the work of Zu et al. [32] for the non-geodesic filament paths depicted in eq. (2.1). The derivation is based on the fact that at the infinitesimal level, internal forces generated by the hydrostatic pressure are in equilibrium with the reaction resultant f from the supporting surface in fig. 3.2,

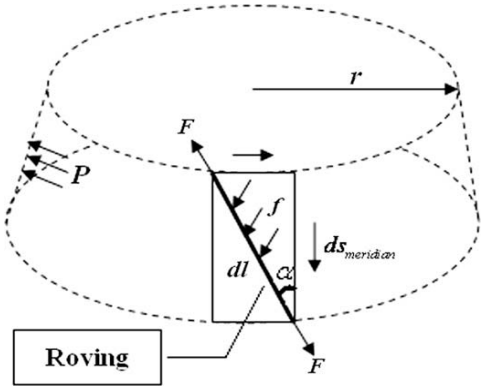


Figure 3.2: Infinitesimal ring element belonging to a shell of revolution and used to derive the isotensoid non-geodesic path solution (taken from [32])

$$N \cdot f \cdot dl = P \cdot 2\pi r ds_{meridian}, \tag{3.3}$$

with N being the number of roving bundles. dl is the infinitesimal length of the roving, P is the internal pressure, r is the local radius of curvature and $ds_{meridian}$ is the infinitesimal length of the meridian. The reaction force f is decomposed in its transverse (f_b) and normal (f_n) components, [32],

$$
\begin{aligned}
f_b &\approx F \cdot k_b \\
f_n &\approx F \cdot k_n \\
\lambda &= \frac{f_b}{f_n} \\
f = \sqrt{f_b^2 + f_n^2} &= F k_n \sqrt{1+\lambda^2},
\end{aligned}
\tag{3.4}
$$

where F refers to the roving force, and k_b and k_n indicate the transverse and normal filament curvatures. Then, the infinitesimal equilibrium equation is expressed as:

$$
\frac{NF}{\pi P} = \frac{2r\cos\alpha}{k_n\sqrt{1+\lambda^2}}. \tag{3.5}
$$

If, according to the Euler formula, [54], the normal filament curvature k_n is written in terms of the meridional and circumferential shell curvatures, it is obtained:

$$
k_n = \frac{r''}{(1+r'^2)^{3/2}}\cos\alpha^2 + \frac{1}{r\sqrt{1+r'^2}}\sin\alpha^2, \tag{3.6}
$$

defining r' and r'' as the first and second derivatives of the radius r with respect to the axial coordinate z. The second derivative of the meridian profile is then obtained by introducing the expression of the normal filament curvature k_n in the equilibrium equation, [32],

$$
Z'' = -\frac{\left(1+z'^2\right)\left(S\cdot z'\cdot\tan\alpha^2\cdot\sqrt{1+\lambda^2}+2r^2\cdot\sec\alpha\cdot\sqrt{1+z'^2}\right)}{S\cdot r\cdot\sqrt{1+\lambda^2}}, \tag{3.7}
$$

with $S = NF/\pi P$. This allows the non-geodesic filament path equation, eq. (2.1), to be simplified with the substitution of eq. (3.7), into

$$
\frac{d\alpha}{dr} = -\frac{\tan\alpha}{r} - \frac{2\lambda r\sqrt{1+z'^2}}{S\sqrt{1+\lambda^2}}. \tag{3.8}
$$

Correspondingly, the simultaneous solution to eqs. (3.7) and (3.8) results in the isotensoid meridian profile and its corresponding non-geodesic path. The netting theory stands for modeling the composite material response with the use of analytical expressions. This approach renders a fast solution to relatively complex surfaces described analytically or, correspondingly, that is discretized in simpler components. However, the validity of the results is limited because of the unidirectional reinforcement assumption and the thin wall hypotheses, essentially putting it in disuse against the almost as fast but more realistic CLT.

3.3. Applications of The Classical Lamination Theory to the Analysis of CPVs

The CLT frames the elastic constitutive formulation that considers the orthotropy of the layers of a composite material, with the corresponding kinematic, force resultant and equilibrium equations. It is based on the hypothesis that layers are perfectly bonded and that normal plane sections remain normal and plane after deformation. The force resultants can be related with their corresponding strains as:

$$
N_{s\theta} = [A]\cdot\epsilon_{s\theta}, \tag{3.9}
$$

where, if considering membrane behavior only, the force resultant tensor is $N_{s\theta} = [N_s, N_\theta, N_{s\theta}]^T$, the strain tensor is $\epsilon_{s\theta} = [\epsilon_s, \epsilon_\theta, \epsilon_{s\theta}]^T$ and the extensional stiffness matrix $[A]$ is defined as $[A] = \sum_{k=1}^{n}[\overline{Q}]^{(k)}\cdot(t_k) = t\cdot[\overline{Q}]^{(k)}$. The variable t_k refers to the thickness of the kth layer and the variable t refers to the total thickness of the stackup. Correspondingly, the stiffness of the kth layer of the stackup in the coordinate axes s and θ is defined by $[\overline{Q}]^{(k)}$, and is written in terms of the local stiffness of the layer as:

$$[\overline{Q}]^{(k)} = [T]^{-1} \cdot [Q] \cdot [T], \tag{3.10}$$

being $[T]$ the tranformation matrix of the second-order stiffness tensor from the local to the global configuration coordinate system. The components of both the transformation matrix and the lamina stiffness matrix $[Q]$ are detailed in Jones [45]. The stress-strain relation of the kth layer is expressed as

$$\sigma_{s\theta}^{(k)} = [\overline{Q}]^{(k)} \cdot \epsilon_{s\theta}^{(k)} = [\overline{Q}]^{(k)} \cdot \epsilon_{s\theta}, \tag{3.11}$$

meaning that the stress components at each individual layer expressed in terms of the membrane forces result in

$$\sigma_{local}^{(k)} = [T] \cdot [\overline{Q}]^{(k)} \cdot [A]^{-1} \cdot N_{s\theta}. \tag{3.12}$$

The use of CLT is broadly present in the extensions and refinements of the analytical design space methodologies of CPVs. Although the netting theory is convenient for preliminary designs of composite shells, works have shown that the matrix strength has an essential role in the internal force distribution, and as a result, in the optimum dome shape, [20, 21, 30]. The study presented by Hojjati et al. [20] uses the CLT to account for the orthotropy ratios of the composite material while filaments follow geodesic paths. The influence of the transverse stiffness is observed to shift the optimum dome shape, whenever an isotensoid state is sought, from a hemispherical solution (isotropic material) to an ellipsoidal netting analysis solution (no transverse strength).

In the investigation of Liang et al. [21], the optimum dome shape and the various stress fields in the dome, are compared with the netting theory methods proposed by Fukunaga and Uemura [19]. The CLT and geodesic filament paths are used together with an optimality condition based on the Tsai-Wu failure criterion, serving this also as the dome thickness definition rule. The work concludes that the optimum dome shape shows to be very similar to that of an ellipse, while the so-called shape factor $\overline{K}$, is improved over the netting analysis counterparts,

$$\overline{K} = \frac{PV}{W\,(\sigma/\gamma)}, \tag{3.13}$$

with P, V and W denoting internal pressure, internal volume, and dome weight. The ratio σ/γ refers strength-to-density relation, where the strength may be taken as the composite tensile strength X_T. In this investigation, failure is observed to be controlled by the pole opening and vessel knuckle transverse stress components.

Following, Madhavi et al. [55] use the netting analysis as a preliminary tool of a later more in-depth CLT investigation. These authors assume membrane loads only and geodesic filament paths, to ultimately implement a progressive damage prediction methodology. The procedure presented is further developed by Musthak et al. [56] by accounting for FSDT and third-order shear deformation theory (TSDT) as extended versions of the CLT.

In the case of Zu et al. [27], the CLT under plane stress assumptions is used to explore the structural efficiency of domes following non-geodesical winding patterns and a dome thickness distribution calculated from the Tsai-Wu criterion. The optimization problem presented is constrained to the isostrain condition in the dome region, whereas the objective is to minimize the strain energy density. This work compares shape factors, eq. (3.13), to show the improved performance of non-geodesics over geodesic path definitions. However, it also acknowledges the limitation in the thickness prediction because of its lack of connection with the real winding patterns followed during production. It is also discussed that the thick wall condition in the domed regions possibly introduces significant bending and out-of-plane stresses that may affect the results. Zhou et al. [34] obtains a similar conclusion regarding the improved structural performance of non-geodesics by the minimization of the shape factor inverse, eq. (3.13), for various winding patterns and a thickness prediction based on the Knoell's method, [57]. In this case, the structural solution is obtained from FE analysis, while the particle swarm optimization (PSO) is used to find an optimum based on a Tsai-Wu failure criterion constraint.

One of the strengths of the CLT is that its relatively low computational cost makes it a convenient tool to perform optimization, whereas furthermore, detailed FE analysis serves as a solution refinement. This approach is followed by Alcántar et al. [11] to optimize the number of layers, thicknesses, cylindrical section orientations, and sweep circumferential angles of CPVs. Calculations are assisted with FE

in vessels with geodesically wound tows, where both the genetic algorithm (GA) and the simulated annealing (SA) optimization techniques are used. The fiber direction stress in the cylindrical region is studied and presented to be more significant in the helical inner layers than in the outer ones. However, after the hoop layers drop, this tendency appears to reverse. As the dome approaches the pole opening, subsequent reversals take place, likely influenced by the load transfer scheme induced by the boss.

It is also reported by Roh et al. [9] that the fiber direction stress pattern along the vessel longitudinal path. In this investigation, a preliminary vessel sizing is obtained from the netting analysis, and the following detailed results are obtained with FEs software. Analyses are performed on various vessel sizes, length to diameter ratios, hoop winding angles, and reinforcement patches. It is noticed that by reducing the inner layers hoop stiffness in the cylindrical region, the fiber stress variation through-the-thickness tends to be more uniform. This tendency is depicted in fig. 3.3 where the inner layers show a higher stress values in the cylindrical region of the vessel. Besides, the helical stress reversals shown after the vessel circumferential ply drop location indicate part of the complex stiffness distribution in these regions. The work of Roh et al. [9] also concludes that the material increase follows a linear relation with the tank volume from the design results on various vessel sizes.

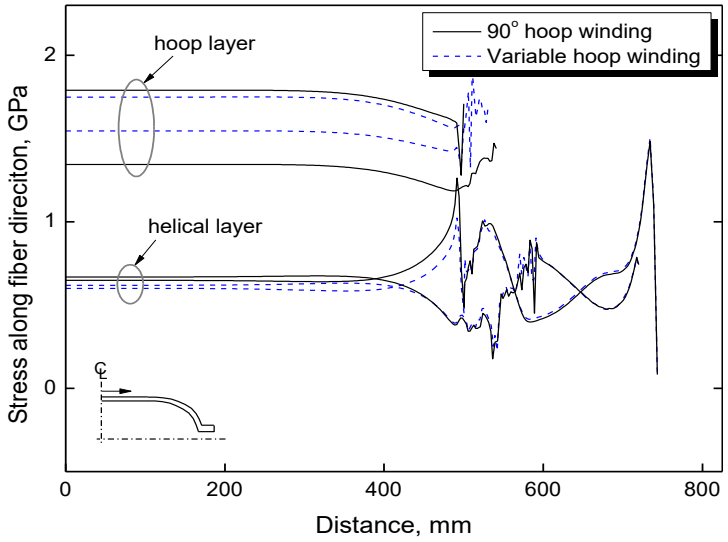


Figure 3.3: Fiber stress distribution along a vessel meridional path for a constant 90 degree hoop winding (black) and a multi-sequence hoop winding (blue) (taken from [9])

The analysis of CPVs employing the CLT appears as a versatile tool for the reduction of the computational cost of more detailed FE solutions. Some of these applications stand as its use for preliminary vessel sizing or vessel variable optimization. Notwithstanding, the CLT is limited, as the netting theory, in the reproducing the thick wall condition of commercial composite vessels.

3.4. Thick-wall FE Analysis Solutions and Failure Modeling of CPVs

The CPV specification of 700 bar NWP introduced in section 2.1 causes the design of pressure vessels to fall within a thick-wall definition rapidly. This boundary might be arbitrarily defined as the wall thickness that reaches 5 to 10 % of the inner diameter, and causes flat orthogonal sections to deform into non-flat, non-orthogonal. The thick pipe analytical solution methods presented in section 3.1 are not generally expansible to the analysis of CPVs, and only within simple geometries, like the spherical vessel solution of Roy and Massard [58], can a thick multilayer theory be readily developed.

The existing gap in the analysis level is bridged with the use of FEs by allowing the discretization of complex geometries. This approach permits to define a set of material constitutive equations on generated geometry sub-domains, while fundamental element equilibrium and corresponding kinematic constraints are imposed, [59]. Among the advantages of FEs analyses are the possibility of accounting for non-linearities at the material level, modeling large deformations, and reproducing contacts between components. Another relevant possibility is to predict failure based on a determined stress state and following, to reproduce damage progression by adequate material degradation laws until the final collapse happens.

The analysis of CPVs through FE analysis is here divided according to their scope. Therefore, solutions based on the generally applicable mesoscale analysis are presented in section 3.4.1, whereas more detailed investigations based on multiscale modeling are introduced in section 3.4.2. Finally, a separate section is designated in section 3.4.3 to the efforts of authors in modeling material variability and the influence of the manufacturing process in the structural response.

3.4.1. Mesoscale Solutions

The mesoscale modeling of composite materials assumes that the distinct mechanical properties of its constituents are represented by a homogeneous orthotropic continuum, where different theories are applied to treat their elastic and damaged stages. This one appears as the most generally applicable approach for the analysis of composite materials because of its modeling simplicity and its meaningfulness at the structural scale of engineering interest. The constitutive response before the triggering of damage is generally assumed purely elastic, whereas failure is predicted using various phenomenological criteria, and damage is modeled within the framework of CDM or cohesive zone models, [60]. The topics of failure criteria and damage modeling are further examined in chapter 8 and chapter 9, where their applicability to the current investigation is put into context.

The relevance of the full vessel thickness consideration in the determination of accurate stress fields is presented by Son and Chang [61] for a geodesically wound dome. It is shown that by using a thin wall approach, the stresses on the vessel knuckle are underestimated, while with a hybrid thick dome thin cylinder strategy, the knuckle gets overstressed because of the mesh mismatch numerical singularity. In this investigation, a metallic boss and liner are modeled by accounting for their elastoplastic response, while contact conditions are also defined with the composite reinforcement. The characterization of the material properties is achieved by producing specimens of similar fiber volume content to the filament wound material, and validation is based on the correlation with an experimentally determined burst pressure.

In the works presented by Leh et al. [8, 22, 62] a comprehensive methodology is developed to define non-geodesic filament windings at the dome regions, perform FE simulations with the prediction of damage and optimize the vessel stacking sequence. A calculated vessel thickness profile is used to construct FE models like the one depicted in fig. 3.4, where both axisymmetric and three-dimensional approaches are followed. The vessel material properties are defined from filament wound coupons that include interwoven filament tows, although these are presented to be ultimately fitted to approximate the experimentally measured displacement. No boss plasticity is considered, and the interface between liner and composite is treated as tied. The progressive damage laws used are developed ad-hoc based on the Hashin-Rottem failure criterion, [63], while the results of axial, radial displacement and burst pressure are correlated with physical experiments. The results of the simulations show that a general lower axial stiffness and burst pressure is obtained. Among the reasons for this mismatch, it is suggested the possibly inadequate identification of the strength properties of the wound material, the insufficiently accurate identification of the ply thicknesses after winding consolidation, the helical ply relaxation at the domes that lead to lower fiber volume contents in this regions, the inadequate damage variables modeling and the absence of plasticity in the metallic bosses, [62].

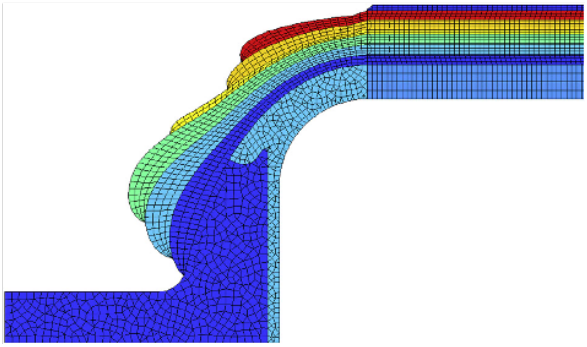


Figure 3.4: FE model of a CPV with metallic boss and plastic liner where different colors indicate different material definitions (taken from [22])

The progression of damage in thick CPVs is also accounted in the work of Berro Ramirez et al. [10] by carrying an axisymmetric simulation of a CPV geometry defined with the WCM of the Abaqus FE software. A progressive damage model developed by the author is used to account for layer delamination and diffuse matrix damage, [64, 65], whereas its parameters are adjusted to the results from tensile coupon testing, [66]. A polymeric liner is featured and modeled to be tied to the composite reinforcement, while the constitutive response of the metallic boss accounts for plasticity. A physical full-sized tank test on which failure occurs in the cylindrical region is carried to correlate its burst pressure with the results of the simulations. During this test, strain data from embedded optic fibers in the circumferential layers are additionally gathered and correlated with the numerical results. A mismatch in the early stages of the axial displacement is identified between experiment and simulation; it is suggested to be related to a gap between the liner and composite shell created during the manufacturing process. The magnitude of this gap is inspected through computerized tomography (CT) images like the one presented in fig. 3.5. As a result of accounting for this geometric mismatch, a considerably more accurate correlation is reported in the axial displacement.s

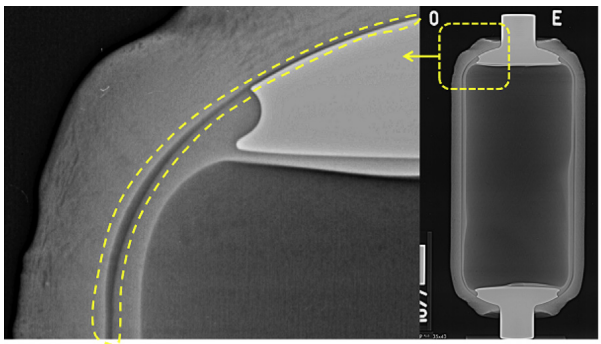


Figure 3.5: Gap between liner and composite reinforcement created during the manufacturing process of a CPV (taken from [10])

A comparatively more robust approach for the material characterization is introduced by Magneville et al. [67] to reciprocally validate the results of filament wound plates through FE analysis load-strain comparisons. The obtained material properties in this work are then used in the modeling of an axisymmetrical CPV where the multi-sequence layup definition of Leh et al. [8] is used, and a combined mechanical and thermal loading is applied. The depiction of ply thicknesses and fiber volume contents is obtained from CTs scans and microscope observations of tested specimens that permit the adjustment of the material parameters to the ones of the real vessel. The progression of failure is modeled from the CDM implementation of Ladeveze and Le Dantec [68] and features a viscous time delay effect that reproduces diffuse damage growth, although it disregards interface delaminations. Correlation is performed by comparing axial and radial displacement of a tested vessel with the results of the simulation, where an initial stiffness non-linearity is argued to be caused by a manufacturing gap between composite and liner. Correspondingly, The elasto-plastic behavior of the boss is modeled and observed to have a significant influence on the axial displacement response.

The combined loading state encountered during fast refueling of internal pressure and thermal loading is also accounted in the work of Gentilleau et al. [69]. An axisymmetric model is built from the dome filament path and thickness definition of the WCM of the Abaqus FE software, where a simple damage model that couples mechanical and thermal failure is implemented. Material properties are identified from coupons extracted from filament wound cylinders that are tested for tensile, transverse and shear loading, permitting to determine the stiffness characteristics of the interwoven helical plies homogenization of those of corresponding $\pm\alpha$ laminates. A metallic liner is modeled accounting for its elastoplastic constitutive behavior, whereas no experimental correlation is presented.

Another original progressive failure analysis methodology is proposed in the investigation of Wang et al. [70] from the Hashin failure criteria, [63], and the material degradation framework of CDM. Besides accounting for intralaminar damage, this strategy also models delamination by embedding cohesive elements at the interface between wound layers and between the composite and the metallic liner. The model is constructed on a solid geometry, where plasticity is considered for the metallic liner constitutive behavior. The material properties are obtained from tensile tests results and are iteratively fitted by

comparing the output of simulations and an experimentally measured tank burst.

3.4.2. Multiscale Solutions

An alternative method for modeling damage progression of composite materials is based on the multiscale analysis of the constituents. It represents the lowest scale of idealization that is usually achievable for engineering purposes and permits approximating the detail damage mechanisms of matrix plasticity, cracking, and fiber-matrix debonding, [71]. However, multiscale analysis strategies do not directly address the specific CPV construction in terms of filament winding paths, dome shapes, and ply drop locations. These possibly have a relevant impact on the burst pressure estimation and result from distinct micromechanical characteristics of the constituents because of their different fiber volume and porosity contents.

Based on the micromechanics of failure (MMF) and the micromechanics progressive damage modeling (MPDM), a methodology is applied in the work of Wang et al. [72] to a solid geometry model of a CPVs. The implementation is based on a macromechanical analysis of the component that serves as a loading condition for a micromechanical unit cell model. Failure and, if applicable, damage are calculated at this level and amplified back to the macro-level by the correlation of the current stress levels and the stress distribution under unit mechanical loads presented in fig. 3.6. With the feedback of the unit cell model the stresses at the component level can be recalculated and load increased until final collapse. The material properties at the micromechanical level are obtained from standard uniaxial laminate tests that are back-calculated according to the unit cell model presented in the investigation. The presented model shows a metallic liner of elastoplastic constitutive behavior that is simulated as tied to the composite reinforcement. Correlation with experimental results is presented by comparing the burst pressure estimation of a tank that fails in its cylindrical region.

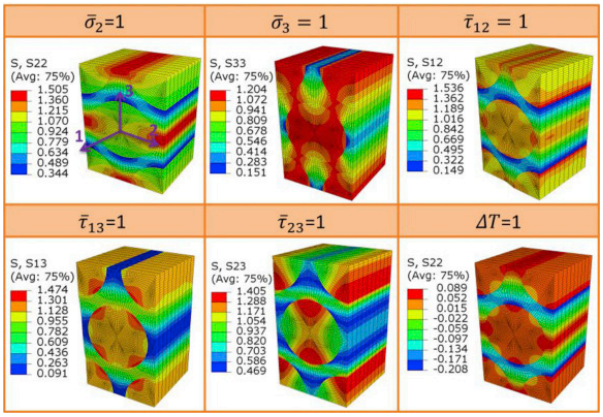


Figure 3.6: Stress distributions in a unit cell model under unit mechanical loads for linking with the macromechanical stress state (taken from [72])

Alternatively, CPV micromechanical failure is predicted in the work of Liu et al. [73] by accounting for the stochastic nature of fiber breakage. Matrix cracking is modeled at the cell level following a CDM approach, whereas the interface between fiber and matrix is considered to follow cohesive laws. It permits to link the stiffness degradation of the representative volume element (RVE) to the macroscopic stiffness of the vessel, where the burst pressure prediction is correlated with the result of a physical experiment. The multiscale linking is achieved by assuming that at the ply level, the stress in the fiber direction is approximately equal to the one at the micromechanical scale. Therefore, the longitudinal elastic modulus is degraded according to an empirically fitted expression that accounts for the number of failed matrix elements over the total. The material properties are determined by iteratively comparing the solid geometry simulations results and the experiments. Correspondingly, geodesic filament paths are defined, and a metallic liner is included with no consideration of the material yielding.

3.4.3. Material Variability

The filament winding manufacturing process of CPVs described in chapter 2 is shown to influence the resulting material characteristics of the component relevantly. This variation is connected with the vessel stacking sequence and winding pattern design and impacts the distribution of fiber volume content,

porosity, and void formation. Furthermore, the mechanical properties of the material are affected by the intrinsic variability of the composite material concerning fiber packing and strength and filament bandwidth and thickness. In this regard, authors show an increasing awareness of the influence of these parameters on the vessel burst strength, which translates into the consideration of material variability in the presented simulations. One of these examples is the investigation of Gentilleau et al. [74], that by further developing the damage model introduced in Gentilleau et al. [69], accounts for the statistical variability of the fiber bundle strength in the burst pressure prediction.

Correspondingly, the work of Harada et al. [75] accounts for the inhomogeneity of the fiber packing in burst pressure estimation. Simplified models accounting for the variable fiber volume contents are developed, where the amount of fibers is fitted to probability distributions. The analysis is performed on axisymmetric models with geodesically wound dome paths on which the elastic constants of each layer are calculated according to their measured fiber volume contents. The mechanical properties of the constituents are likewise derived from the data of the suppliers, whereas the existing metallic liner is modeled as elastoplastic and perfectly bonded with the composite reinforcement. Correlation with full tank experiments is performed by comparing surface strain measurements on various circumferential locations and by burst pressure comparison. Additionally, the determination of the different failure locations in the different fiber bundles is accomplished by measuring their fractured length, root location, and fracture morphology determination in a scanning electron microscope (SEM). As a result, a significant burst pressure variation is presented when good layer packaging is ensured, revealing the relevance of this subject.

The inherently stochastic material properties of the vessel component are modeled by Rafiee and Torabi [76] within the solid geometry CDM implementation of Wang et al. [70]. Variables like the fiber volume content, the final winding orientation, and the mechanical material properties are accounted as following arbitrarily chosen probabilistic functions, which lead to stochastic distributions of the vessel burst pressure like the one presented in fig. 3.7. Correlation of the results is performed with the comparison of the stress components of analytical CLT solutions and the comparison of an experimentally tested vessel burst pressure. The analyzed vessels include a metallic liner of elastoplastic constitutive behavior whose influence on the results is assessed by alternatively calculating the mechanical response of the linerless tank.

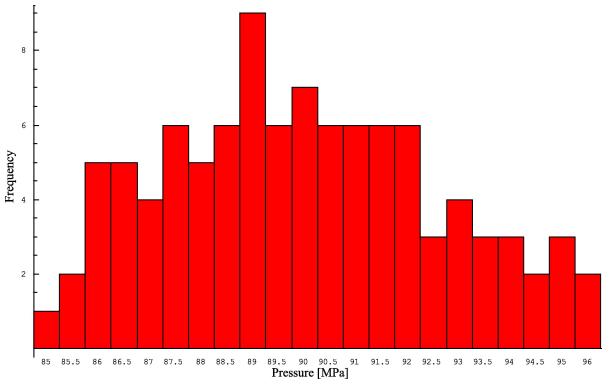


Figure 3.7: Statistical distribution of the burst pressure of a CPV resulting from the stochastic input variables definition (taken from [76])

In the case of Ellul and Camilleri [77], composite pipes are modeled when the porosity content of the material and the thickness of the chopped strand mat used as liner are randomly varied. The modeling approach is based on a shell element formulation, and a sudden stiffness drop after damage onset is predicted with the Tsai-Wu failure criteria. Likewise, the porosity content is accounted for by a reduced material thickness because of the existence of entrapped air. The results are correlated with experimental tests, where discrepancies are noted after FPF is reached.

3.5. Foresight in the Analysis of CPVs and Research Questions

The review of the most relevant aspects for the simulation of CPVs presents a series of factors that profoundly impact the results of their structural analysis. These factors appear to be the outcome of the vessel design (layer stacking sequence, circumferential ply taper, filament path orientation, and wind-

ing pattern), and its filament winding manufacturing process (variable layer thickness, ply compaction gradient and resin accumulation). Consequently, the internal load paths are defined, and with them, the elastic response of the tank. Degradation of the material is expected, which is anticipated to be initially triggered by the stress concentrations arising from the sudden stiffness changes. As a result, the development of damage in the material causes cracking in the direction transverse to the fiber that, whenever different ply orientations exist, connect through delaminations. This progressive degradation of the matrix constituent leads to an internal load redistribution to the fibers, eventually experiencing a considerably more catastrophic failure mode. Since this type of failure puts at risk the integrity of the vehicle and its occupants, the reliable estimation of the burst pressure stands as the central design aspect in the commercial development of pressure vessels.

Nevertheless, being the validation of simulation results an essential step in their reliable design usage, it is observed that this is performed to a limited extent in the available literature. These appear to be generally achieved by the correlation of vessel axial an radial displacement, [10, 62, 69, 75, 77], and their burst pressure estimation, either by comparison of failure criteria, [61], or the definition of progressive damage models, [10, 62, 70, 72]. However, cylindrical failure consistently appears to be the burst driver, which avoids the validation of the simulated mechanical response in the more complex dome regions that appear as the limiting factor in optimizing the tank design. Burst pressure in the cylindrical region can be predicted in a reasonably accurate form from the thick-wall analytical analysis of section 3.1.

In the prediction of CPV burst pressures, simulations stand as a tool to replicate vessel mechanical responses behind physical tests and analytical solutions, while reaching where experimental data acquisition systems are limited. To this purpose, simulations can lead the path towards reduced manufacturing material usage by modeling the impact of material property variability in, for instance, the premature failure of the dome and dome transition regions. A sufficient remaining dome strength causes then burst to happen in the cylindrical section that, because of its highly consistent material properties, can be reliably predicted. Hence, the focus of the simulation work needs to be set on the estimation and validation of the mechanical response outside the cylindrical section, which would permit the forecast of undesirable failure modes and design against them. In this sense, the accuracy of the simulation is relevantly rooted on aspects like the determination of the material strength properties from wound samples, the precise definition of the vessel wall thickness, the fiber angle, the variation of the fiber volume content towards the domes, the material degradation scheme, the yielding of the metallic parts, and the winding process simulation, [8].

As a result, there is an opportunity in studying the simulation of thick wall CPVs with a damage progression model implementation, whose results can be validated employing DIC, [78] and AE, [79]. This task defines the main research question to be answered with this project, expressed as to how well an adequate modeling strategy accounts for the manufacturing-induced characteristics of CPVs in computationally cost-effective FE simulations. Accordingly, the main research question is expanded with the definition of sub-questions, which are referred to as:

- What aspects of the manufacturing process influence the CPV mechanical material characteristics, and to which process and geometry variables are they linked?

- Can these mechanical properties be reliably identified in a final product, and is their distribution consistent with other manufactured components (different stacking sequences, dome geometries, dome transition regions)?

- Is it possible to account for the variability of mechanical properties in a sufficiently accurate model of the burst pressure of CPVs?

- Which modeling strategies (type of analysis, geometric setup, type of element, interface treatment, failure criterion, progression of damage) are the most reliable while computationally cost-effective?

- Can the results of modeling be correlated with the tank burst pressure, vessel displacement (axial and radial), and outer surface strains measured from experiments? Can these correlation results be extrapolated to CPVs of different scale, stacking sequence, and winding patterns?

In a like manner, the research objective is set to determine the methodologies that allow modeling the heterogeneity of mechanical material properties of CPVs. Therefore, allowing to improve the accuracy and reliability of the predicted failure compared with the current status. This task is achieved by quantifying the variability of the composite material characteristics over the vessel, including these in physically representative modeling, and the correlation with physical testing results. From the current knowledge, no sufficient attention is observed in the holistic between material properties, manufacturing processes, and structural conceptualization. Correspondingly, in the development of this project, the following sub-goals are defined:

- Identification of the mechanical properties of the composite material, which are influenced by the manufacturing parameters, and which set the boundaries to which the quantification and identification process is limited.
- Quantification of the variability of mechanical properties within the cylindrical, dome and dome transition regions of the vessel, presenting the sensitivity of these to the manufacturing process variables.
- Identification and implementation of modeling techniques that effectively account for the material properties characteristics previously studied to generalize the method to a variety of inputs.
- Correlation of the results obtained from the proposed methodologies with the existing testing campaigns as a matter of verifying the physical soundness of the approach and validating the outcome of it according to the requirements of the modeling.

4

Analysis Methdology Overview

Description of the Methodology

The primary aim of the current research is to develop a framework for the analysis of CPVs that is sufficiently general to be applied to a wide range of vessel designs. It is intended that the quality of the results obtained is proportional to the level of sophistication of the modeling while remaining computationally tractable. Hence, this chapter introduces a suitable succession of steps that, as combined, form a robust methodology capable of handling the design and manufacturing complexities of CPVs. This task motivates that correlation with experimental and analytical results is performed at various stages to ensure that the origin of discrepancies is properly traceable. For instance, the geometric configuration of the vessel is verified before FE models are built, while elastic mechanical responses are correlated before damage development is regarded.

It is derived from the discussion presented in chapter 2 and the current results of the analysis in chapter 3, that the path for achieving reliable burst pressure estimations goes through the consideration of some of the vessel manufacturing-induced features. These include the variable fiber orientations in the dome, the location, and taper of the circumferential ply drops, the spatial variation in fiber volume contents and porosity, the characteristic material properties of filament wound plies, and the relative thick vessel walls. To establish the intended framework, it is first necessary to model these features and then analyze them, which would ultimately allow optimizing the vessel design to meet the established application requirements.

The approach followed in this investigation can be streamlined mainly to the physical vessel design, the modeling of the relevant features of this vessel for a FE calculation, and the solution and correlation of the obtained results. This overview is schematically presented in fig. 4.1, where each of the presented blocks refers to one of the primary framework levels. Correspondingly, sub-blocks are depicted where the methodology requires a distinct output to be achieved, such as the ply contour smoothing needed to handle unrealistic thickness profile calculations that possibly result from the filament winding process simulation.

Vessel Design

The physical vessel design consists of the definition of the vessel stacking sequence, the dome filament paths, and the winding pattern. These steps characterize the shape of the composite reinforcement that is wound on a given mandrel shape and necessarily constitute the vessel structural design variables. They determine the directional distribution of stiffness and, subsequently, the preferred load paths when the vessel is subjected to internal pressure.

The vessel architecture description permits to compute the motions of the multi-axis robot that carries the winding, while this is also closely related to the specific selection of manufacturing parameters, like the winding type (wet vs. dry), the filament tension, the bandwidth and thickness, and the winding speed. Resulting from the vessel architecture definition and the manufacturing parameters configuration, the final filament orientations, and layer thickness are predicted. In the engineering practice, these result from the computation of the robot motions and the associated layer thickness increase by commercial software. One example of this software is the ComposiCAD™ tool used within the Hydrogen

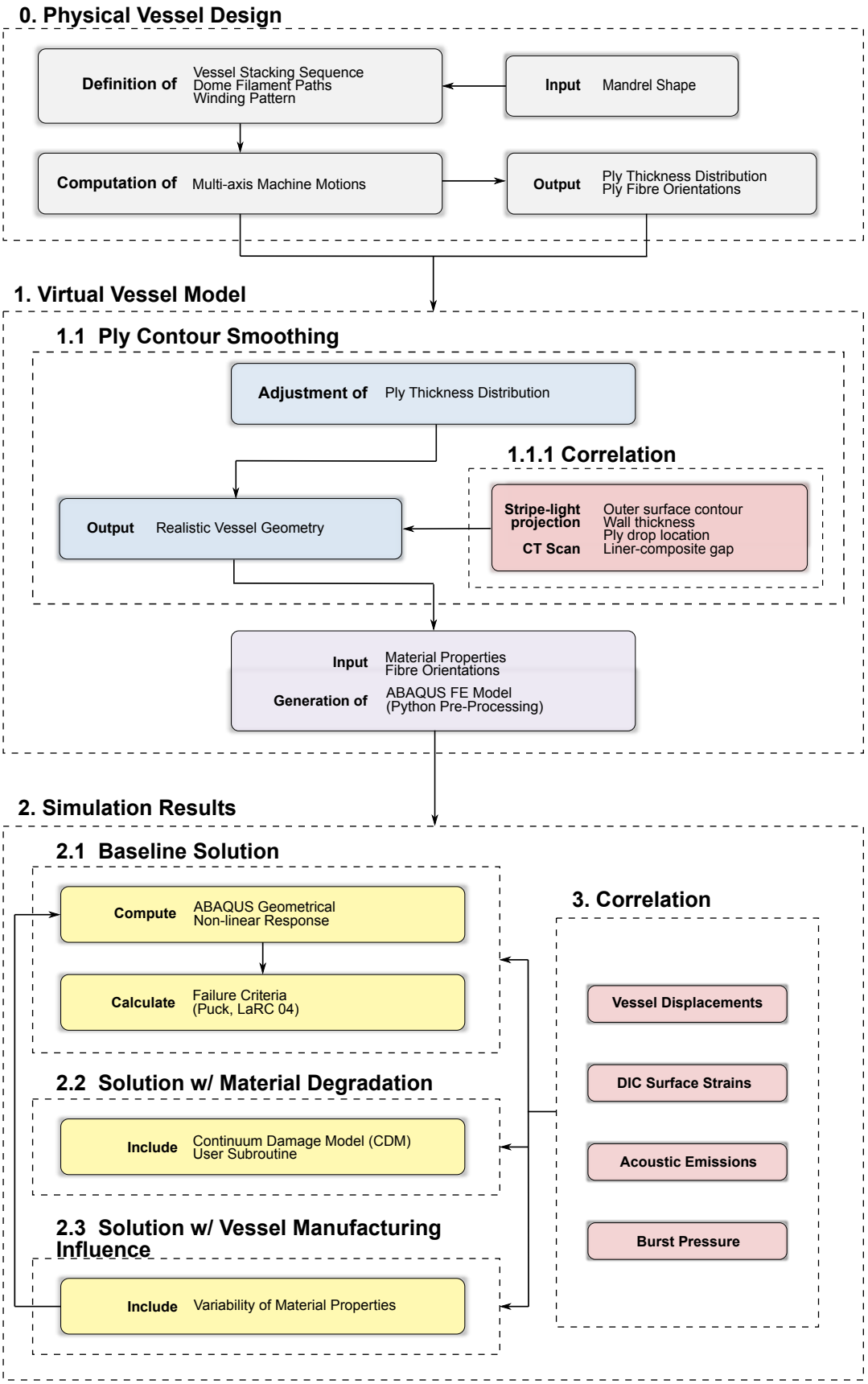


Figure 4.1: Overview of the steps taken to establish a robust methodology for the analysis of CPVs

Pressure Tank Project at Daimler AG, and whose coupled definition of filament path and ply thickness, is in the most general case, reduced to a methodology like the one presented in section 2.5.

Characterization of the Geometry

Besides a filament winding machine motion calculation being able to accurately estimate the tow positioning and its corresponding contribution to the thickness profile, it likely cannot accurately account for the repositioning of composite bands during manufacturing. This repositioning mostly consists of the layer filament readjustment because of successive tows wound over them. These generate friction forces on the existing surface, hence inducing relative displacements of the underlying filament bands. An additional source of inconsistency between the filament winding simulation and the real product arises, as introduced in section 2.3, from the viscous deformation of the vessel during the curing process. This deformation of the uncured composite reinforcement appears to be driven by the sustained internal pressure on the plastic liner and compressive radial pressure induced by the winding. As a result, tows are further readjusted, whereas a mandrel deformed shape is also induced, generating a manufacturing gap when the internal pressure inside the liner is eliminated.

Furthermore, thickness estimation discrepancies appear from the consolidation that tow winding generates on the underlying covered plies. This effect is the result of the applied tow tension component normal to the surface, which effectively reduces the thickness of the inner layers by promoting outward resin flow. The normal tow contact pressure varies with the relative filament orientation, making the consolidation level a variable that also changes through the vessel geometry. In this regard, circumferential ply winding in the cylindrical region generates considerably larger normal forces than the corresponding helical ply winding. Lastly, the combined influence of the tow adjustment and layer thickness variation locally changes the pre-tension state of the wound filaments, causing so-called relaxation. This effect consists of a loosening of the composite filaments that generate fluffing in the domes that influence the thickness profile shape and increases void formation.

In the context of the current project, a ply thickness distribution adjustment appears to be necessary for the satisfactory geometrical definition of the vessels analyzed through FE. The output of the commercial software ComposiCAD™ appears to be inadequate for a realistic mechanical response simulation as it renders a mismatching final vessel thickness prediction. Therefore, the sources of these discrepancies are qualified in section 5.2 to approach a vessel thickness profile smoothing methodologically and robustly.

The revised CPV geometry estimation is then correlated with stripe-light projections and CT images of manufactured reduced-scale components, which validate the sufficiently good representation of the real vessel. The profile adjustment is divided into three main steps; first, unrealistic ply thickness accumulations are smoothed in a volume-preserving form according to the subsequent ply winding directions. Second, a manufacturing gap is introduced between composite reinforcement and liner from the observed induced deformations during production; and third, layer groups thicknesses are adjusted empirically according to their expected consolidation. These steps are intended to lead to a close representation of the real vessel thickness profile that correspondingly couples with the filament orientation definition. It is assumed that, by adequately representing the thickness distribution, the local fiber orientations are also reasonably depicted, hence avoiding the need for probing the varying filament paths directions on the complex dome surface.

Construction of a FE model

The geometrical description is the first input of an FE model, which in the case of the present project, is approached for a solid vessel definition. This representation permits the reproducing of the non-linear thick-wall normal stress gradient through-the-thickness while also accounting for the non-linear stiffening effects of the geometrically non-linear deformations. The definition of such a detailed geometry requires adequate modeling of the features that influence the vessel response, and which can be referred to as the mesh construction presented in section 7.2. These characteristics include the circumferential ply drop arrangement, the boss end composite reinforcement geometry, and the resin pocket generation during winding.

Independent layer meshes are created from the individual ply geometry discretization, also permitting to define the interactions existing between the vessel features clearly. Correspondingly, helical fiber directions are locally defined for each element representation from an interpolated orientation profile resulting from the filament winding software calculation. The intertwined helical ply construction

is then respectively modeled as a set of balanced subplies to eliminate the shear-extension coupled response of conventional $[+\alpha, -\alpha]$ stackups.

The FE model construction is accomplished from a parameterized preprocessing of the ply contour adjustment outputs in the Abaqus 2017 FE software, [38]. Such an approach allows a timely definition of the meshing constraints, interactions, boundary conditions, and load applications while providing flexibility to build geometries of different vessel architectures. As far as the variability of the material mechanical properties is concerned, these are modeled by a vessel heterogeneous material definition derived from the characterization campaign introduced in chapter 6. The relevance of the helical ply construction in the elastic and strength characteristics of the composite material is accounted for by the coupon testing of filament wound flat shear specimens. Furthermore, testing of coupons with multiple porosity definitions allows conveniently identifying the influence of the void contents in the matrix and fiber dominated mechanical properties and eventually adjusting their definition to their vessel location.

Validation of Results

Results are obtained at different levels of sophistication depending on whether the vessel is regarded as constitutively non-linear elastic, if damage onset and progression is predicted, and in case material heterogeneity is coupled with the previous. To this purpose, simulation outputs consist of through-the-thickness stress, and strain along meridional paths, average dome and cylinder surface strain and through-the-thickness failure criteria and damage results. Hereof correlation is carried from the simulated elastic vessel response in chapter 7, which also permits the prediction of failure in chapter 8. Available experimental results of vessel displacements and surface strain obtained using DIC serve to ascertain the representativeness of the model.

Likewise, the onset of damage prediction is compared with the recorded AEs during tank pressurization and the corresponding burst modes and pressures, hence allowing the identification of the local stress states that trigger them. Further detail is obtained from the modeling of the progression of damage in chapter 9, which considers the effective stiffness reduction and the load redistribution during high loading. In light of a considerably more complex calculation process, a refined burst pressure estimation can be obtained while the localization of AEs serves as a validation tool for the damage growth prediction. Iteratively implemented with the previous steps, the variability of the material properties is accounted in chapter 10 by reproducing the more complex heterogeneous elastic and damage responses. Results are correspondingly correlated with the displacement, strain, damage progression, and burst data permitting to assess the relevance of the modeled variability.

The hereby proposed methodology intends to cover the most critical steps in the robust analysis of CPVs. This analysis contributes to understanding the vessel mechanical response, standing as an essential tool in the design and development of components of increased reliability and narrower safety factors. All in all, the approach followed in this work contributes to the predictable vessel burst characterization by accounting for various geometrical features resulting from their design and manufacturing (realistic thickness profile, material properties, and ply drop geometries), and by correlating simulation results with relevant experimental data.

5

Geometrical Definition of the CPV

Commercial filament winding software appears to be generally limited in accounting for the manufacturing induced tow readjustments and the uncured material deformation in their thickness profile calculations. They show to experience this despite adequately characterizing the multi-axis robot motions and the nominal composite band positioning, which requires an improvement of the thickness estimation for its use in the numerical modeling of CPVs. Among the effects experienced by filament wound components throughout their manufacturing are tow lateral displacements, viscous deformation before full resin cross-linking, local ply compaction, and filament relaxation. The existence of discrepancies between the real vessel and the contour profile estimated by the filament winding software substantiates the definition of a ply thickness adjustment sub-framework in this chapter.

An introduction to the characterization techniques of vessel thickness is first presented in section 5.1. Then, the methodology with which a ply profile is adjusted from the available geometrical output of the ComposicaD™ software is described in section 5.2, permitting to analyze the geometry of various stacking sequences in section 5.3. The chapter concludes with the results of the vessel thickness profile prediction in section 5.4, where the detailed description of the mentioned vessel definitions is referred to in appendix A.

5.1. Introduction to the Vessel Thickness Characterization Techniques

A coherent depiction of the vessel contour is founded on the realistic estimation of the thickness increase during successive tow winding. However, the theoretical approaches should be experimentally correlated with measured vessel contours to validate the proposed methodologies. The simplest form of thickness determination is based on the observation of cut specimens. It permits to take direct measurements of the profile and to model it from image correlation. However, the cutting process entails an alteration of observed sample, hence, for instance, hindering the determination of the manufacturing gap between composite reinforcement and liner when the latter is already debonded.

Non-destructive measurement of the vessel outer contours is achieved with the scan of structured-light projections. This technique consists of the projection of narrow straight light stripes on the vessel surface that get distorted because of the component three-dimensional surface shape. Consequently, they can be observed with a camera and reconstructed into the actual shape of the object. This method is reasonably simple to implement, although it might face inaccuracies due to limited depth of field of the projector method, the resolution of the fringe projections, the interference of beam paths reflected in nearby objects, and the reliability of the stripe detection method, [80]. Furthermore, as the shape measurement is only carried from one perspective, the construction of a three-dimensional object requires a multiple perspective measurement combination in an adequate spatial reference system.

Alternatively, ultrasonics is another non-destructive measuring technique that determines wall thickness by monitoring the wave reflection time through a component wall, [81]. These wave reflections also permit to identify the presence of delaminations, matrix cracks, and their location within the thickness, although it appears to be a relatively slow process for which expertise is required for a rightful interpretation. Visualization is achieved in either A, B, or C modes of corresponding beam paths,

cross-sectional images, or zenith images. The high-frequency wave reflection brightness along a path is monitored with B-scans, meaning that they are particularly well suited for the probing of dome meridional cross-sections. Nevertheless, the measurement postprocessing can be challenging because of the non-flat inner contour shapes and the signal weakening with the increased thickness and the intermediate material imperfections. In this regard, the array beamforming technique trades increased penetration with reduced resolution, hence facilitating high thickness determination. Array beamforming is based on various ultrasonic probes synchronized in terms of phase, whose frequency is then adjusted to set the focus on the desired location.

The more sophisticated, non-destructive measurement technique of CT is based on the processing of radiographic measurements from multiple angles. As presented by Scott et al. [82], CTs permits to build virtual sections of an object with sufficient resolution to identify material imperfections. The quality of the system depends on the power of the X-ray source, the resolution of the background panel detector, and the number and exposure of frames taken. Furthermore, CT scans can also provide information on fiber breakage, intralaminar crack growths, and delaminations even during loading, as indicated by [82].

The presented techniques appear as all adequate choices for the contour and thickness vessel measurement, increasing sophistication from the direct vessel cuts to the X-ray imaging. To this purpose, the equipment available within the facilities of Daimler AG in Stuttgart is used. This consists of stripe light projection cameras Manta G-201-30fps by Allied Vision™, and a NanotomM General Electric™ x-ray CT scanning suite. Results are respectively processed by the software GOM™ Correlate and VGSTUDIO™ MAX.

5.2. Methodology for the Ply Thickness Adjustment

An approach for overcoming the discrepancies between the predicted vessel thickness and those observed in real components is presented in fig. 5.1. It is accomplished by successively adjusting the circumferential ply drop thickness, introducing a gap between composite reinforcement and liner, correcting the layer group thickness according to their consolidation level, and extrapolating the ply boss ends where the winding software export boundary is reached.

5.2.1. Readjustment of the Circumferential Tow Drops

Full mandrel coverage at the ply turn back location is typically enforced with the definition of supplementary dwell angles. These ensure that regardless of the angular position of the mandrel when the layer boundary axial coordinate is reached, the ply is wound to its full extent. The mandrel gets a full rotation without axial displacement, meaning that a local thickness surplus of a composite bandwidth is generated. In the absence of tow readjustments, this results in a thickness increase at the end of each layer, followed by a sudden vessel thickness decrease after the ply drop. Nevertheless, vessel manufacturing experience shows that these nominal thickness increases do not appear in real vessels because of the subsequent winding of layers. For instance, this is reasoned on a helical ply wound over a circumferential, whose axial load component is transferred through friction as a result of the filament winding tension. Hence, the low transverse stiffness circumferential tows get drawn, making the thickness increase to flush.

The analysis of a commercial software vessel output permits the identification of the arbitrarily defined ply drop tapering, which can be postprocessed to a more realistic thickness distribution. Tow readjustment is hereby modeled by identifying the plies that show the effect of a supplementary dwell angle definition, calculating the material excess over the nominal thickness of the layer, and adding this amount of material in a new tapered ply drop end. The approach considers that the winding software reasonably predicts the total amount of material wound on the vessel. This assumption appears to be acceptable considering that the composite mass prediction results from the direct calculation of the winding robot motions. Following, the new tow drop taper is defined from the existing taper solution to the given filament bandwidth. The nominal layer thickness used as a reference for the excessive material calculation is directly obtained from the thickness of the ply in the cylindrical region of the vessel. Here, for the used tows and their overlap factor, the corresponding layer thickness is defined, which is assumed to be prolonged in the layer drop location before the consideration of consolidation.

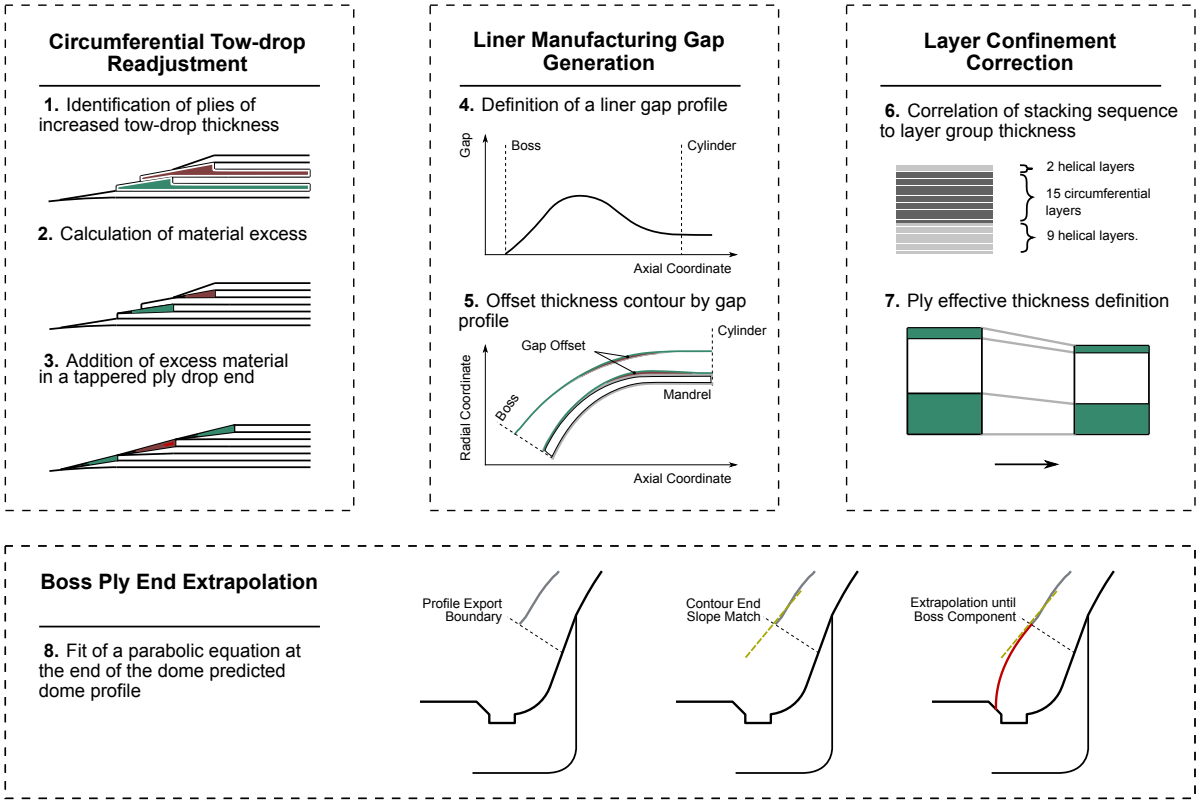


Figure 5.1: Overview of the steps followed to adjust the CPV geometry from the ComposicaD™ export

5.2.2. Generation of the Liner Manufacturing Gap

The smoothed vessel contour after tow drop readjustment might well not fully match a real vessel profile because of the existence of a gap between the composite reinforcement and liner. From the experience of authors introduced in section 2.3, the origin of this gap results from the sustained liner internal pressure viscously deforming the uncured composite material. However, the shape shown by this gap seems to be also related to the stacking sequence definition and the low rigidity of the liner, hence showing characteristically deformed liner shapes. For instance, the winding of successive helical plies of low angle in the cylinder generates relevant axial compressive loads at the dome poles that derive in swelling of the liner knuckles. At these locations, the dome has a tendency to deform with outward bending when the dome pole is subjected to axial loading, which, combined with the existing internal pressure, leads to a protrusion formation.

Following, circumferential ply winding can hardly counteract this effect because the circumferential ply tapering over the liner knuckle effectively reduces the total normal force generated. In opposition to the concentrated axial load introduced by helical ply winding, the initial winding of multiple circumferential plies generates a distributed radial load on the cylindrical region. This loading causes the unconstrained liner pole ends to displace axially, although in this case, the load induced by the subsequent helical winding is directly aligned with it. Liner knuckle swelling is already prevented by the restraint introduced by the circumferential plies hoop stiffness already in place, thus roughly maintaining the liner nominal geometry.

Quantitative estimation of the liner gap generated by the manufacturing process is necessary to adequately offset the thickness profile resulting from the tow drop readjustment. This offset leads to a virtual mandrel shape over which the composite ply thickness is added, hence forming an expanded vessel contour. Empirical estimations of the gap dispersion are derived by correlation with stripe light projection measurements and CT scans. These permit to quantify the discrepancy between the initial vessel contour estimation and the real component. The detailed prediction of the gap distribution from an analytical perspective is presented as a matter of further work because of the compound effect of vessel layup, filament tow filament tension, and resin viscosity. The liner deformation estimation is

founded on the equilibrium condition between the winding tension and the radial pressure applied on the underlying shape, [83]:

$$p = \frac{F \sin \alpha^2}{r\, w} \tag{5.1}$$

where p is the radial pressure per unit length, F is the filament tension introduced on the composite band, r is the radius of the underlying surface, α is the filament orientation angle, and w the tow width.

5.2.3. Correction for Layer Confinement

The applied radial pressure not only causes liner deformations but also generates the mentioned layer confinement. The uncured composite material behaves like a saturated porous material following Terzaghi's Principle. Hence, when subjected to an external load, the stress is initially carried by resin pore pressure. However, the viscosity of the resin permits an outward flow because of the gradient induced by the atmospheric pressure condition on the outer surface of the vessel. The outwards resin flow consequently transforms the generated pore pressure in effective through-the-thickness compression of the fibers leading to the so-called consolidation. This behavior implies that the applied pore pressure, and as a result, the radial stress gradient experienced by the resin, varies in time and decreases to zero as resin flow develops. Consequently, a decrease in the layer thickness and an increase of the fiber volume content are produced by the resin escape.

Resin flow on a porous media like the composite material can be modeled with Darcy's Law:

$$q = -\frac{k}{\mu} \nabla p \tag{5.2}$$

being q the instantaneous flow rate, k the fiber bundle permeability, μ the resin viscosity and ∇p the gradient of the current radial pressure. The thickness decreases magnitude because layer consolidation can be computed from the volume of resin that escapes through the layer stackup. It constitutes a coupled system of equations in time derived from the mass conservation principle that includes the fiber volume content, the radial pressure, the thickness reduction, and the corresponding stress and strains in the deformed configuration.

Solutions to this problem are presented by Cai et al. [83] and further developed by Banerjee et al. [84] with the inclusion of non-linear stiffness terms of the fiber bundle. These researchers establish a theoretical framework to determine the fiber bundle stiffness and its permeability from material constants, considering the current fiber volume fraction, the fiber volume fraction below which the fibers do not carry any load, and the fiber volume fraction above which any transverse flow stops. Subsequently, the coupled flow and material response is calculated during the winding time with the radial pressure load increase of every successive ply addition.

The resin flow additionally influences the solution to the consolidation problem during curing. Increased temperatures initially generate a viscosity drop in the resin before cross-linking fully develops, meaning that in light of the high initial viscosity values, the most relevant share of the resin flow occurs during this time. Estimation of the thickness decrease introduces additional non-linearities in the fiber bundle and resin constitutive relations by coupling the thermal elastic response of the fiber bundle, the curing kinetics of the resin, and the rheology response of the composite system. Besides the solution to the resin flow problem presenting a comprehensive depiction of the layer consolidation process, it requires the detailed characterization of the composite material properties before full curing. It introduces significant complexity in the eventual mechanical response definition of the vessel, hence justifying that within the limited time frame of the current project, layer consolidation levels are correlated with vessel through-the-thickness samples CT scans.

5.2.4. Extrapolation of the Boss Ply End

The final step of the ply thickness profile adjustment is the solution to the ply boss end contour. In a like manner to the circumferential ply drop readjustment, helical layers experience relative displacements to accommodate the boss turning shape. In addition to this, the shape of the mandrel contour generally changes from convex to concave, implying that the filament winding software cannot determine the layer contour by simply offsetting the accumulated ply thickness. This limitation is overcome by extrapolating parabolic ply ends from a sound vessel thickness prediction location in the form of:

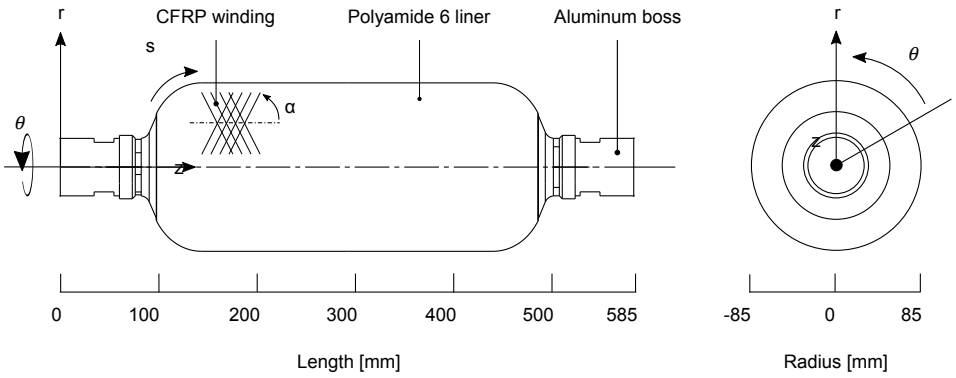


Figure 5.2: Diagram of a plastic liner and the subsequent CPV construction (taken from Nebe et al. [12])

$$r(y) = A_0 + A_1 \times y + A_2 \times y^2 \quad \text{for} \quad y_{turn} \leq y \leq y_{sound} \tag{5.3}$$

where r and y refer respectively to the radial and axial coordinates of the vessel. The axial vessel coordinate at which the ply turns around is indicated by y_{turn} and translates in the coordinate at which the extrapolated parabolic profile intersects the mandrel shape. Likewise, y_{sound} is the arbitrarily chosen axial coordinate that serves as a boundary condition for the contour definition. The parameters A_0, A_1 and A_2 are coefficients to be defined from the thickness and the slope continuity of the thickness profile. In the presented case, continuity in the curvature is not enforced, and a shape parameter is defined instead.

The steps introduced in this section aim at improving the geometrical depiction of the CPVs by correcting the geometry output of a filament winding software in terms of the as-manufactured features of the vessel. It is introduced that rheological modeling of the uncured composite can well depict the viscous deformations experienced by the composite material winding. Nevertheless, this modeling is complicated because of its coupled thermal and non-linear mechanical characteristics; besides, material rheological properties are correspondingly required. In a simplified version of this stage, gap and layer confinement levels are empirically correlated from measured geometries employing stripe light projections and CT images.

5.3. Experimental Analysis of the Vessel Geometry

5.3.1. Description of the Vessel Manufacturing and Stacking Sequence

The methodology here presented is derived from the existing manufacturing process at Daimler AG and, although it is subjected to its specific definition, the attempt is to introduce it with a comprehensive perspective. The vessel manufacturing process is generally introduced in section 2.3, which in the context of the current project, consists of a robot-assisted dry winding on a polyamide 6 liner. This liner and boss configuration is depicted in fig. 5.2, where the relevant geometrical variables show a boss-to-boss length of 585 mm and a liner radius of 85 mm. Filament tension varies from 20 N for the winding of circumferential layers to 50 N in the case of low angle helical ones. Correspondingly, the internal pressure is applied to the liner during winding and curing with values ranging from 0.2 to 0.6 MPa. This internal pressure prevents the liner from collapsing due to the radial pressure induced by the winding until full resin cross-linking occurs. To this purpose, an oven curing cycle of 8 h at a temperature of 110°C is defined.

The mechanical response characterization is particularized for three different stacking sequences, whose layer group definition is introduced in table 5.1 and which are respectively referred to as W1A, E+ and B*. All three consist of a total number of 41 layers, out of which 11 are helically wound while the remaining 30 are circumferential. The difference between the three is the positioning and grouping of these layer definitions, hence permitting to identify the limit stacking sequence description in the vessel mechanical response. The W1A layup shows the majority of the helical plies wound on the inner side of the vessel, followed by the full circumferential ply stack, and two outer helical layers that wrap the latter and constrain it axially. On the contrary, the B* layup places the full circumferential ply stack on the inside, followed by the full stack of helical layers on the outside. A helical ply is nevertheless

left on the inside to ensure a smooth continuous inner surface. The definition of E+ reproduces an intermediate sequence between W1A and B* by alternatively winding subgroups of two helical and six circumferential plies.

Table 5.1: Layer group definition of the W1A, E+ and B* stacking sequences

Stack.	Gr. Num.	Name	Type	Number	Ori. (deg)	W. Pattern	Diagram
W1A	–	H1	Helical	9	19.90	Non-geo.	
	–	C1	Circ.	30	88.80	–	
	–	H2	Helical	2	19.90	Non-geo.	
E+	5	H1	Helical	2	19.90	Non-geo.	
		C1	Circ.	6	88.80	–	
	1	H2	Helical	1	19.90	Non-geo.	
B*	–	H1	Helical	1	19.90	Non-geo.	
	–	C1	Circ.	30	88.80	–	
	–	H2	Helical	10	19.90	Non-geo.	

Stack. – stacking sequence; Gr. Num. – number of groups; Ori. – filament orientation in the cylindrical region; W. Pattern – winding pattern; Non-geo. – non-geodesic winding pattern; Circ. – circumferential

Opposite bending-extensional couplings are expected from the W1A and B* stackups resulting from their extreme antisymmetry, whereas this is roughly eliminated in the E+ definition. Helical plies are wound with low constant angles through-the-thickness to make a clear distinction of the different directional stiffness properties of each of the layers. Furthermore, helical plies follow non-geodesic filament paths of approximate slippage potential 0.2, wound with a classical balanced interwoven pattern $[+\alpha, -\alpha]$ that cancel both shear-extensional and twisting-bending couplings.

Table 5.2: Length and diameter data of the W1A, E+ and B* stacking sequences

Stack.	Vessel ID	L. Wind. [mm]	L. Tot. [mm]	Mea. Dia. W. [mm]	Mea. Dia. [mm]	SP Dia. [mm]	Weight [kg]
W1A	01 - 0126	–	-5.8	–	192.2 ± 0.2	–	3.638
	01 - 0128	–	-4.8	–	192.7 ± 0.3	–	3.619
	01 - 0183	–	–	–	–	190.98 ± 0.09	3.587
	01 - 0184	–	–	–	–	–	3.566
	01 - 0192	-3.5	0.4	191.1 ± 0.2	192.9 ± 0.4	–	3.585
E+	01 - 0197	–	-3.7	–	192.5 ± 0.3	190.67 ± 0.05	3.649
	01 - 0201	-3.3	-3.5	191.8 ± 0.5	192.5 ± 0.3	–	3.646
	01 - 0268	-3.5	-3.2	192.0 ± 0.5	192.9 ± 0.7	–	3.630
	01 - 0271	-2.8	-2.2	191.9 ± 0.3	192.8 ± 0.6	–	3.671
B*	01 - 0190	–	-2.9	–	192.2 ± 0.3	190.07 ± 0.11	3.615
	01 - 0204	-2.5	-2.2	191.2 ± 0.3	192.4 ± 0.5	–	3.631
	01 - 0282	-3.8	-2.9	191.6 ± 0.8	192.3 ± 0.2	–	3.633

Stack. – stacking sequence; L. Wind. – measured boss-to-boss length difference between before and after winding; L. Tot. – measured boss-to-boss length difference between before winding and after curing; Mea. Dia. W. – measured diameter after winding; Mea. Dia. – measured diameter after curing; SP Dia. – stripe-light projection diameter; CT Dia. – CT scan diameter
Note 1: The liner has a nominal diameter in the cylinder of 170 mm

5.3.2. Discussion on the Liner Deformation during Winding and Curing

Vessel geometrical data concerning component length and cylindrical region diameter is presented in table 5.2 for various produced vessels. This data intends to depict the expected tendencies regarding liner deformation during the winding process and its repercussions on the final component shape. The dispersion of these results is illustrated by calculating the standard deviations of each vessel measurement, whereas scatter for the same stacking sequence is presented by showing results for various manufactured vessels. Length and diameter data is recorded from direct caliper measurements, whereas diameter data is also recorded from vessel stripe-light projections extracted from six equidistant longitudinal cross-sections, and averaged to obtain the presented values.

Geometrical measurements are reported in table 5.2 concerning the vessel length shortenings and

Table 5.3: Thickness data of the W1A, E+ and B* stacking sequences

Stack.	Vessel ID	CT Thick. [mm]	CT Thick. H1 [mm]	CT Thick. C1 [mm]	CT Thick. H2 [mm]	CT Gap [mm]
W1A	01 - 0126	10.49 ± 0.09	3.85 ± 0.06	5.42 ± 0.14	1.22 ± 0.10	0.90
(layer num.)		52	18	30	4	–
(average p. ply)		0.20	0.21	0.18	0.30	–
Stack.	Vessel ID	CT Thick. [mm]	CT Thick. G1 [mm]	CT Thick. G3 [mm]	CT Thick. G5 [mm]	CT Gap [mm]
E+	01 - 0203	10.85 ± 0.10	1.79 ± 0.02	2.05 ± 0.07	2.12 ± 0.05	–
(layer num.)		52	10	10	10	–
(average p. ply)		0.21	0.18	0.21	0.21	–
Stack.	Vessel ID	CT Thick. [mm]	CT Thick. H1 + C1 [mm]	CT Thick. H2 [mm]		CT Gap [mm]
B*	01 - 0204	10.89 ± 0.23	5.95 ± 0.13	4.94 ± 0.16	–	–
(layer num.)		52	32	20	–	–
(average per ply)		0.21	0.19	0.25	–	–

Stack. – stacking sequence; CT Thick. – CT scan thickness; CT Thick. H1 – CT scan thickness first helical layer group; CT Thick. C1 – CT scan thickness first circumferential layer group; CT Thick. G1 – CT scan thickness first layer group of helicals and circumferentials; CT Gap – CT scan gap between liner and composite reinforcement

Note 1: The thickness and gap measurements refer to the cylindrical section of the vessel, where the nominal tow thickness is 0.2 mm

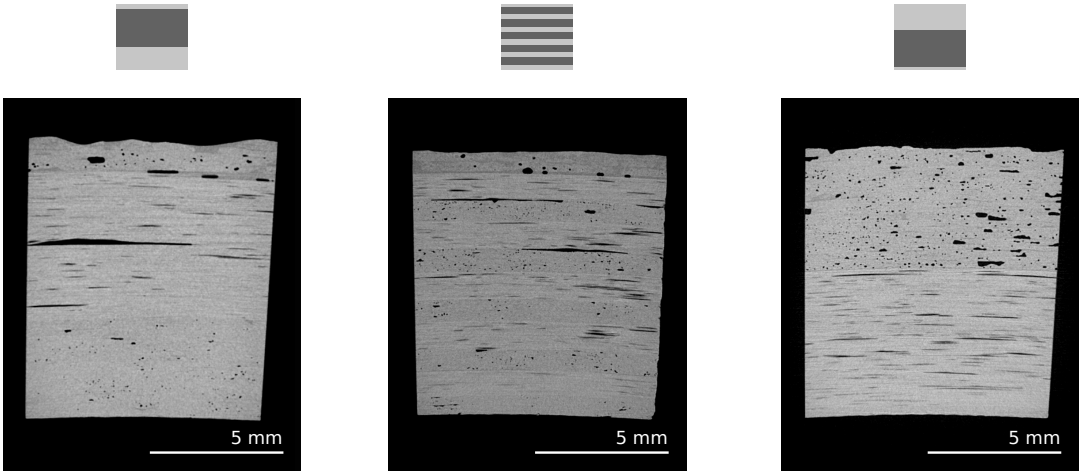
Note 2: The average per ply thickness is calculated assuming that helical plies are equivalent to the thickness of two circumferentials

the cylinder diameters. These are measured directly with a caliper, although stripe-light projections are additionally used to determine the cylinder diameter. Results indicate that the liner endures boss-to-boss length shortening after curing. This effect is maximum for the W1A layup, where multiple helical layers are wound directly on the liner. In the B* case, the first winding of circumferential plies correspondingly compensates the final shortening by producing an earlier slight axial expansion. In a like manner, the liner diameter reduces during winding of the first circumferential layers of the B* stacking sequence. A slight cylindrical expansion appears for W1A, which holds in the absence of liner wall buckling. The E+ vessel, constituting an intermediate solution between the former two, also shows in-between results. Withal, the apparent lengthening of the 01-0192 vessel stands as an anomaly, not being concluded whether this measurement results from any disturbances during the manufacturing. Correlating direct and stripe-light projection measurements still show a slight disparity, likely related to the unevenness of the outer surface of the manual tool and measurement inaccuracy. Concerning the vessel material mass, this shows to be consistent between stacking sequences because of the constant total number of layers definition.

Some direct measurements are also made between the winding and curing process, providing an insight into the rheological deformation experienced at this stage of the manufacturing. Concerning the measured diameters, it is apparent that the cylinder expands during the curing process for all three stacking sequences. Nevertheless, as far as the boss-to-boss length is regarded, it appears to either extend or contract. In this regard, it is possible to identify opposing effects concerning the vessel rheological deformation, as the expansion of the geometrically larger cylinder induces pole shortening whereas the internal liner pressure promotes its extension. Furthermore, helical ply relaxation is expected to cause increased compliance of the dome during this viscous deformation, although it is an aspect of difficult controllability that might relate with the scatter introduced in the vessel shortening.

5.3.3. Discussion on the Wall Thickness of the Composite Reinforcement

Wall thickness measurements and the corresponding confinement level are inferred from CT images of 10×10 mm^2 vessel samples. These are introduced in table 5.3, where a tendency towards increasing thickness from W1A to B* is shown. This tendency is coherent with the observations made in section 5.2 as the outer circumferential plies of W1A generate a larger compressive radial pressure than the analogous outer helical plies of B*, hence confining the inner layers. It is observed from the average ply thickness of the corresponding layer groups where helical layers are assumed to be equivalent to the thickness of two circumferential plies. Clear higher compaction is noted on the inner helical group



(a) W1A stacking sequence (b) E+ stacking sequence (c) B* stacking sequence

Figure 5.3: CT sample scans of the W1A, E+ and B* stacking sequences. The plane of scan presented is parallel to the circumferential direction of the vessel.

of W1A compared with the corresponding B*, even though the first still shows an average thickness larger than the nominal 0.2 mm tow used. The existence of this effect is coherent with the interweaving of the helically wound bands detrimentally impacting fiber packing, while also increasing voids and resin accumulations. This effect is further illustrated by the relatively large thickness of the outer helical group of W1A, that by corresponding to a two-ply stackup, indicates the existence of relevant layer defects.

Concerning the comparison of the circumferential group thickness, it would be beforehand expected that B* showed a lower thickness than the W1A case. Motivated by the higher number of layers wound over the circumferential group in B*, and the slightly higher radial pressure generated by the reduced winding radius. However, confinement and subsequent thickness reduction only occur if the resin is allowed to flow out, which is, in fact, significantly limited in B* by the low permeability helical layers. Its inner circumferential plies are restrained from compacting, which leads to a slightly larger presented thickness value than the W1A counterpart. The distinct extreme effects of W1A and B* are reproduced at a reduced scale in E+, where alternating groups of helical and circumferential layers indicate reduced consolidation level towards the outside.

The extent and quality of the layer defects is depicted in fig. 5.3 for an illustration of the sample CT images. The outer helical plies show large voids that arise from the helical bands waving, although good compaction virtually eliminates them, as in the case of W1A. Likewise, the circumferential stacks present gaps generally aligned with the vessel hoop direction, although the mild confinement induced by the outer helical ply winding of W1A and B* does not allow them to show as tight packing as they can potentially develop. It is not the case of E+, where the inner circumferential groups are significantly compacted because of the subsequent group winding.

5.3.4. Discussion on the Vessel Outer Contour

The distinct vessel knuckle shapes of the presented stacking sequences can be observed from their stripe-light projections. These are presented in fig. 5.4 to conform contour profiles along their meridional paths. Here, the W1A vessel seems to have expanded in this region compared with E+ and B*. Correspondingly, E+ appears to follow the W1A tendency nearby the cylindrical region while superposing the B* contour further towards the dome pole opening. Considering that the vessel architecture produces vessels of the virtually same mass, this appears to develop from the winding induced liner deformation and the subsequent layer consolidation.

The characteristic mandrel shape effectively generated from each stacking sequence winding builds into their expanded version during viscous regularization. Therefore, the induced vessel knuckle swelling anticipated from the W1A winding substantiates in its more prominent contour. This effect is considerably diminished in E+ while virtually eliminated for B*. The different vessel outer cylinder diameters are

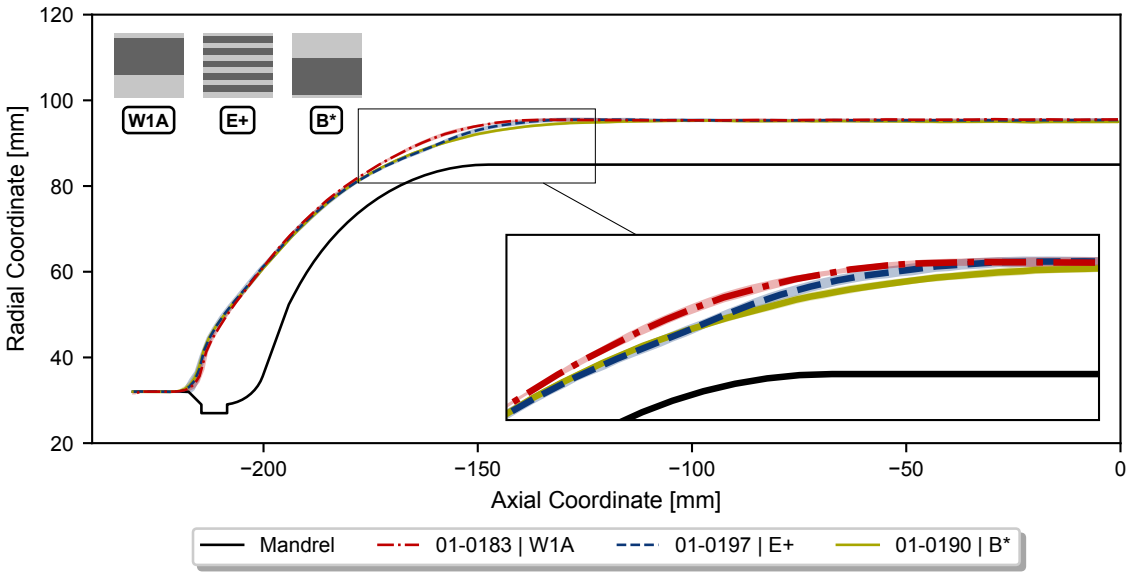


Figure 5.4: Comparison of measured stripe-light projection contours for the W1A, E+ and B* stacking sequences

also presented in a considerably more subtle form in fig. 5.4. Likewise, this difference can be argued to be caused by the initial mandrel deformation during winding. However, the outer diameter variation is considerably less prominent than the stacking sequence thickness contrasts presented in table 5.3, where this thickness difference appears as a more influential variable when a subsequent analysis is carried. An incorrect thickness prediction implies a definite change in the directional stiffness properties of the component to which the simulated stresses and strains are closely related.

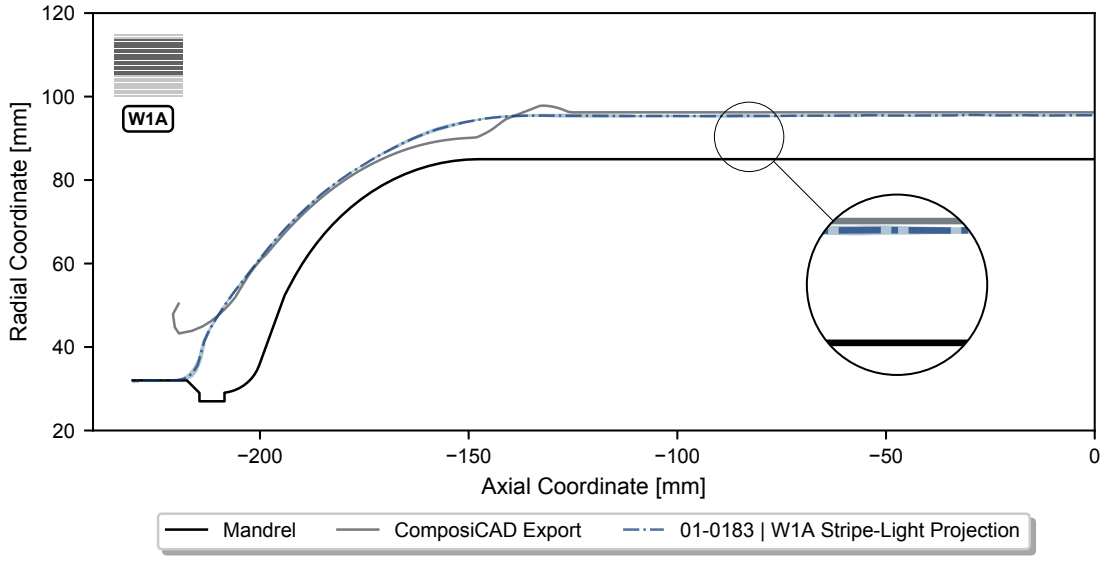


Figure 5.5: Comparison of measured stripe-light projection contour with the initial ComposicaD™ geometry prediction for the W1A stacking sequence

Some of the shortcomings concerning the geometry prediction made by the ComposicaD™ software

are reproduced in fig. 5.5 for a W1A layup. By comparing the thickness profile estimated by the filament winding software and the corresponding measured outer contour using stripe-light projections, a direct correlation is made on the magnitude of the existing discrepancies. These include the mismatch in the dome transition region and the dome end next to the boss, resulting in the filament winding software deriving its geometry prediction from the generated winding robot motions. Concerning the dome end next to the boss, the filament winding software depicts an additionally unrealistic outer profile because the thickness of the composite reinforcement is offset perpendicularly to the concave geometry of the boss fitting. A close look in the cylindrical region indicates that not considering layer consolidation, there is a mismatching wall thickness, even when only the outer surface results are regarded. The existence of a gap between composite reinforcement and liner leads to a real wall thickness smaller than what is predicted with a stripe-light projection contour, hence aggregating the discrepancy of the filament winding software output.

Lastly, the geometry analysis of various layups permits the correlation of the conceptual framework for the vessel ply adjustment with meaningful experimental data. This comparison allows identifying trends in the deformations experienced by the components during the manufacturing process, which concretize for the limit stacking sequences of W1A and B*. Understanding the manufacturing-induced geometrical characteristics of the vessel permits the evaluation of the quality of the thickness profile prediction. Moreover, as this directly impacts the subsequent mechanical response of the component, it allows associating further discrepancies with the specific geometrical characteristics defined.

5.4. Results and Discussion of the Geometry Prediction for Various Stacking Sequences

A realistic thickness profile of the W1A, E+, and B* stacking sequences are predicted within the framework introduced in section 5.2 and the description of the geometrical characteristics contained in section 5.3. In this regard, the initial geometry prediction of the filament winding software is first modified to a baseline geometry. The circumferential ply drop thickness is adjusted, the dome layer ends are defined, and the obtained contour is correlated with the vessel profile obtained through stripe-light projection. It permits the determination of the magnitude of a possibly existing gap between composite reinforcement and liner, although it disregards layer confinement. Second, the baseline geometry is adjusted with the ply consolidation levels identified from the CT sample scans depicted in fig. 5.3. In the case of the W1A stacking sequence, the profile is also correlated with the CT images of a half-vessel component. A refined geometry is obtained as a result, on which a more realistic gap and material thickness depictions are introduced.

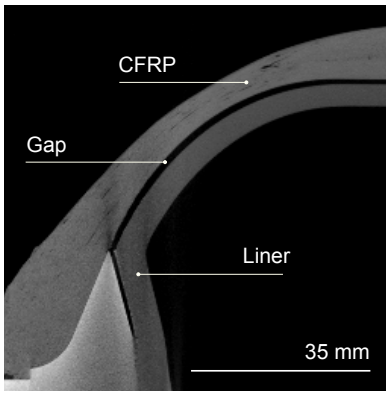
5.4.1. Prediction on the Liner Manufacturing Gap

The comparison of the baseline and CT adjusted geometries is illustrated in fig. 5.6 for the W1A stacking sequence. The predicted outer and inner contours of the vessel are depicted to show the difference in liner gap estimation and cylindrical region wall thickness, wherein the result is placed side-by-side with the corresponding dome region CT image of a vessel after the curing process, fig. 5.6a. Additionally, the predicted gap for either geometric configuration is presented along the axial coordinate of the vessel in fig. 5.6d. The magnitude of the gap is determined in the baseline configuration from the normal offset difference against the stripe-light projection contour and results in the presented sinusoidal shape.

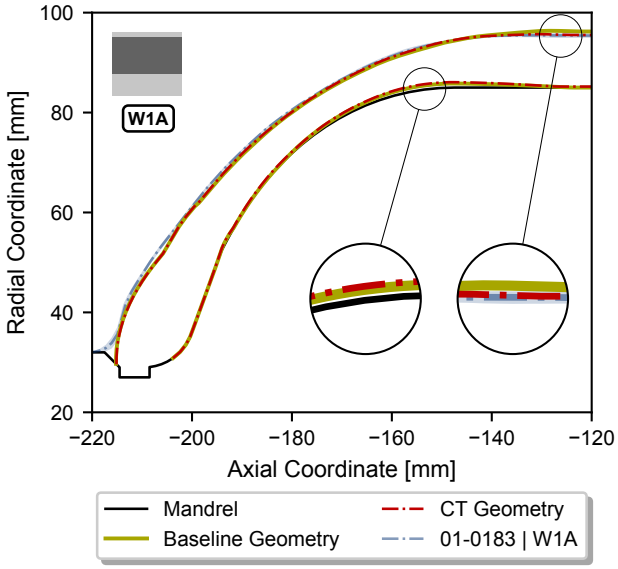
Following, the shape of this gap is scaled according to the CT image depiction, hence permitting to introduce the composite reinforcement offset in the cylindrical region. The subtle difference between the baseline and CT adjusted contours is highlighted within the spyglasses in fig. 5.6b. The combined thickness reduction because of layer consolidation and the associated liner gap increase is apparent for the CT adjusted geometry compared with the baseline configuration. Withal, among the limitations of the predicted contour methodology, no displacement of the boss is considered. It is perceived from the CT image in fig. 5.6a, that alongside the viscous deformation of the vessel a slight axial displacement of the boss exists. In the present approach, the boss is assumed to maintain its nominal position, generating a marginal disparity.

5.4.2. Prediction on the Layer Group and Vessel Boundaries

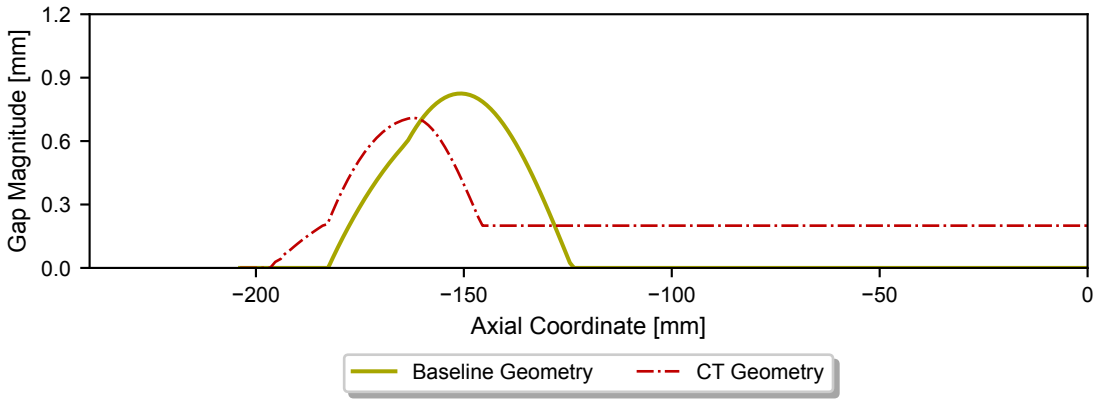
Resulting from the prediction of the circumferential group boundaries, an ensuing comparison of these is illustrated in fig. 5.7. Their reach within the dome is consequently presented for each of the considered



(a) CT scan



(b) Adjusted geometry



(d) Liner gap

Figure 5.6: Comparison of the stripe-light projection adjusted and CT adjusted contours of the W1A stacking sequence

layups, where the hoop ply stack through-the-thickness position directly influences this. The higher amount of low angle helical plies that are wound initially, the more significant is the boss-to-boss length reduction, hence relatively displacing the drop location of the overlying layers towards the dome pole. Resulting from this, the axial coordinate of the innermost circumferential respectively ply increases in the B*, E+, and W1A cases, also coinciding with the starting through-the-thickness position of the hoop layer group. The robot motion definition does not predict the liner shortening, therefore placing any subsequent layers at the axial coordinate of the undeformed mandrel shape. The liner deformation becomes less relevant with the higher number of layers wound, as the mandrel progressively increases its rigidity.

The adequacy evaluation of the ply thickness prediction is further presented for the W1A, E+ and B* stacking sequences in figs. 5.8 to 5.10. These, present the CT adjusted outer and inner contour results in comparison with the referenced ComposicaD™ geometry export, and the corresponding vessel stripe-light projection profile. A spyglass is added to point the thickness difference against the initial filament winding software geometry, the inner contour offset with respect to the mandrel, and the match

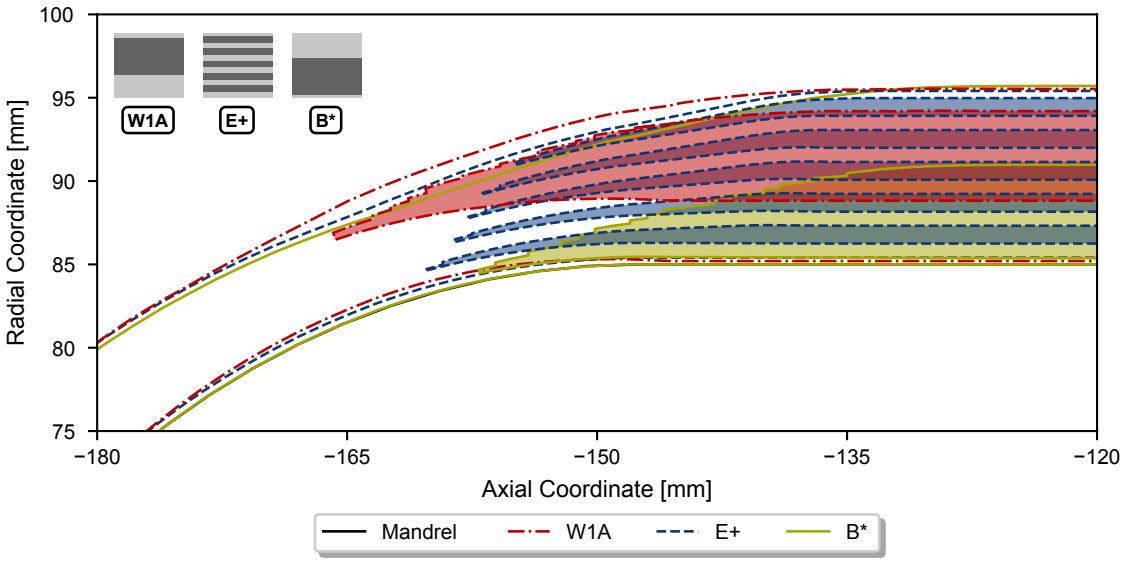


Figure 5.7: Comparison of defined circumferential group boundaries for the W1A, E+ and B* stacking sequences

with the experimentally measured profile.

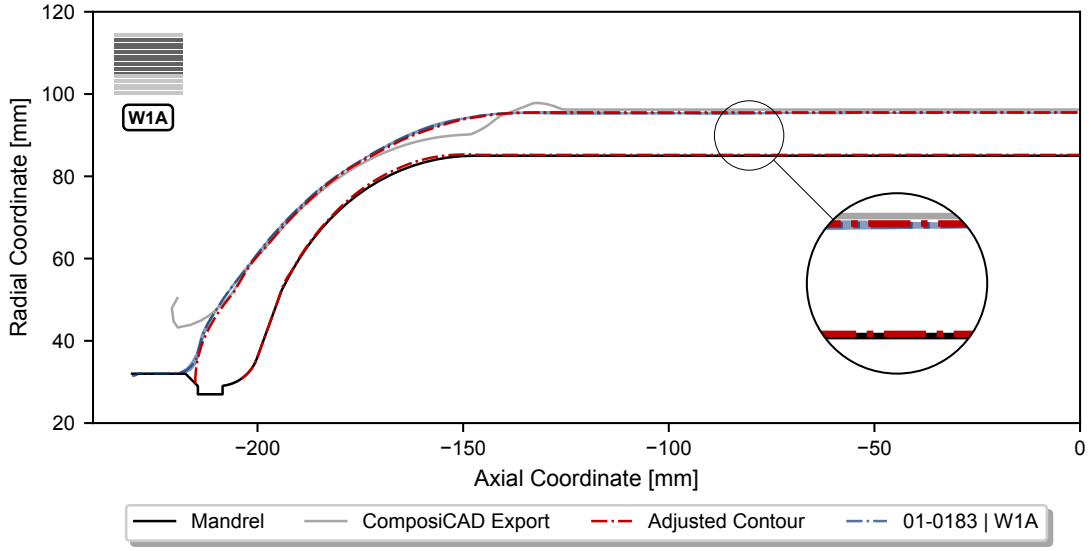
Additionally, the geometry of the layer group boundaries for each of the stacking sequences is presented in figs. 5.8 to 5.10 against the group contours observed in cut specimens. In all three cases, the general shape of the vessel group boundaries is adequately depicted, where the group tapering of the circumferential layers appears to be particularly well reproduced for E+ and B* stacking sequences. In the case of W1A, an apparent tapering length mismatch exists, underlined by a lightly exaggerated circumferential group boundary concavity at the circumferential ply end. This concavity arises from the offsetting of the initially predicted geometry to introduce the existing liner gap. If the subsequent layer confinement correction does not predict an adequate consolidation level for the inner plies along the dome transition region, an excessive inner group thickness is predicted, leading to the observed shape.

A source of inconsistencies in the correlation of the predicted geometric configurations relies on the usage of multiple experimental sources in the geometry adjustment. For instance, the gap distribution is, in the beginning, determined from the stripe-light projection measurement, which might later differentiate from the additional CT scan vessel inputs. Moreover, manufacturing variations exist inherently with the production process development, either in winding parameters changes or because of the condition of the materials. Particularly involving ply readjustments and viscous deformation before full curing, the age of the material used in the manufacturing appears as a relevant variable, limiting the viscosity of the resin and impacting the friction generated between tows. This effect is further influenced by the variability of fiber packing and resin contents between batches of the same material and withing spools of the same batch.

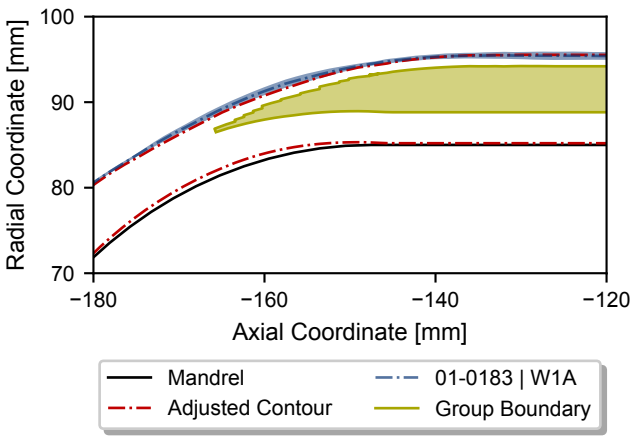
5.5. Concluding Remarks

The geometrical configuration of the vessel is presented to depend on its stacking sequence definition strictly. First, the ply drop location of subsequent plies is subjected to the shape of their underlying surface. This definition controls the angle difference in the dome shape and, ultimately, also the thickness increase. Second, the loading applied on the liner by the winding tension generates a characteristic deformed shape. Hence, its length and diameter are altered, while protruding knuckles may also rise. The ply drop location over the dome shape is altered by vessel shortening, thus relevantly influencing the defined vessel construction. Third, the sequence with which low angle and high angle layers are wound determines the amount of consolidation experienced by the inner layers.

Not only the wall thickness changes with the stacking sequence definition but also vary the material



(a) Comparison of the inner and outer adjusted vessel contours with the thickness profile export from ComposicaD™ and a vessel stripe-light projection contour

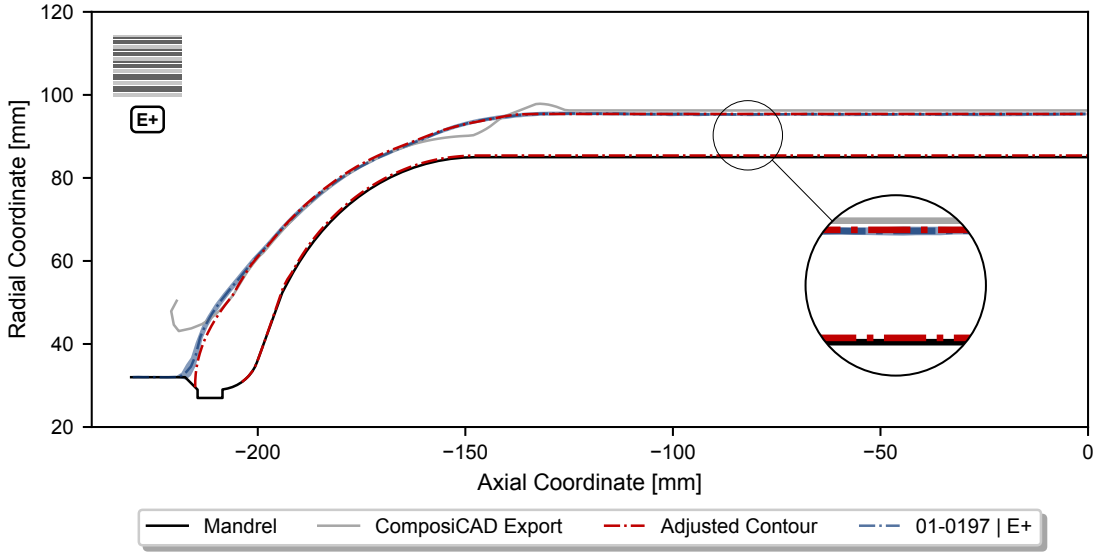


(b) Group boundary

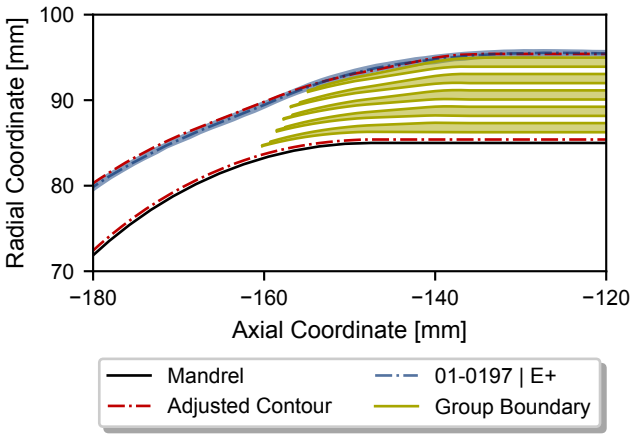


(c) Cut specimen

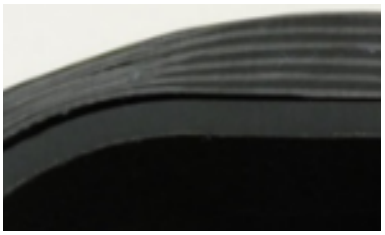
Figure 5.8: Comparison of the CT adjusted contour of the W1A stacking sequence with experimental data



(a) Comparison of the inner and outer adjusted vessel contours with the thickness profile export from ComposicaD™ and a vessel stripe-light projection contour

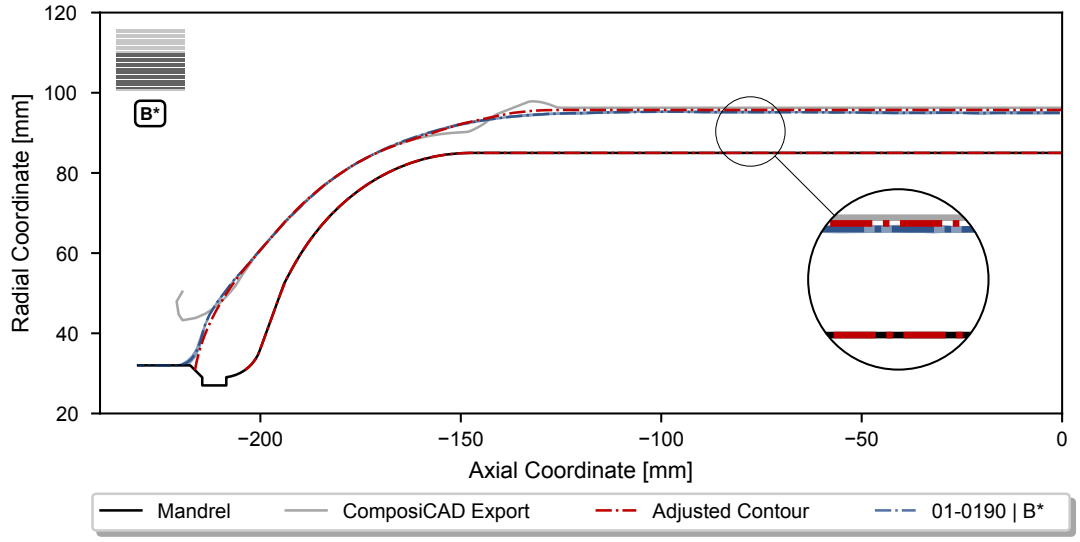


(b) Group boundary

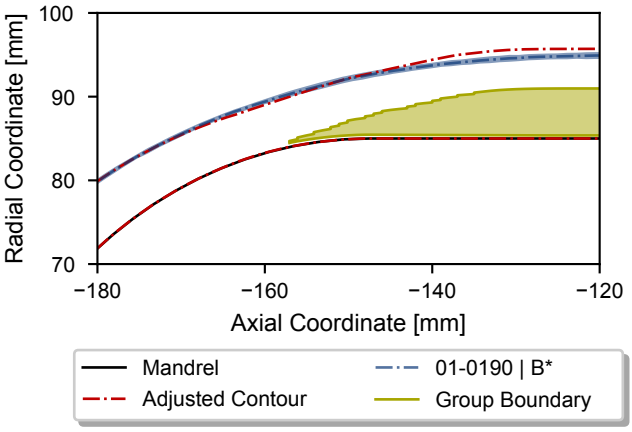


(c) Cut specimen

Figure 5.9: Comparison of the CT adjusted contour of the E+ stacking sequence with experimental data



(a) Comparison of the inner and outer adjusted vessel contours with the thickness profile export from ComposicaD™ and a vessel stripe-light projection contour



(b) Group boundary



(c) Cut specimen

Figure 5.10: Comparison of the CT adjusted contour of the B* stacking sequence with experimental data

characteristics (fiber volume and porosity contents). Lastly, plies are likely to readjust because of the residual tension in the composite bands after winding. Layers are prone to displace if transversal loading is applied to them, which is additionally eased during the low viscosity regime of the matrix curing process.

Following, it is argued that the correct calculation of the winding robot motions is not sufficient for adequately depicting the final vessel geometrical configuration. In the particular case of the ComposicaD™ software, discrepancies with experimental measurements are observed in the predicted thickness of the composite reinforcement, the ply drop tapering, and the geometry of the dome end next to the boss. Consequently, a framework for correcting some of these limitations is implemented to generate representative geometries for the subsequent numerical analysis. This framework accounts for a considerable amount of experimental input, which intends to mitigate the difficulty of predicting analytically the uncured deformation of the composite reinforcement. The primary sources of experimental data include cut specimens, outer contour stripe-light projections, and CT scans. These consist of through-the-thickness samples and, in the case of the W1A stacking sequence, to half-vessels.

Ultimately, the adjusted vessel contours appear to approximate the geometry of the real vessel closely. As a critical aspect of the adequate depiction of the stiffness distribution in the dome transition region, the boundary of the circumferential ply stacks also needs to be adequately correlated with the produced components. In the present work, this is carried only by qualitatively comparing the predicted geometries with cut specimens, which does not allow determining their real geometry unequivocally. A comparison with CT scans of the dome region stands as an alternative to determine the group start and end locations and their tapering length.

6

Experimental Characterization of Material Properties

This chapter presents a material properties characterization approach in its application to CPVs. The varying complexity in the deformational analysis and the damage progression modeling techniques of CPVs requires the definition of correspondingly specific material properties. These include the material elasticity characteristics, its strength, and the properties for the propagation of damage. They intrinsically couple with the produced fiber orientations and the final layer thickness. The definition of these variables appears to be closely related to the filament winding manufacturing process, where parameters like the winding type (wet vs. dry), the filament tension, the roving bandwidth, and the winding speed are presented to have an influence, Cohen et al. [26], Cohen [85]. In this regard, the correlation between these parameters and the geometrical configuration of the vessel is discussed in chapter 5 in light of the level of consolidation experienced by the uncured composite material. This consolidation level varies along the axial coordinate of the vessel because of the different radial load applied on the mandrel by the specific layup architecture and the filament tension. As a consequence, the fiber volume and porosity contents vary along the vessel meridional location, what relative to the composite material construction, also impacts its material mechanical characteristics.

The vessel material heterogeneity in the elastic response is accounted for by testing specimens of various fiber volume contents and porosities. In contrast, the fracture toughness of the filament wound material is also reported for the average quality of the material. The chapter introduces the various possibilities for testing material properties in CPVs in section 6.1, including mechanical characteristics, fiber volume, and void contents. Next, the design and manufacturing of the material characterization test specimens are outlined in section 6.2 by emphasizing the procedures through which representativeness of the CPV material is sought. Specimens are manufactured to test stiffness, strength, and fracture toughness properties on flat wound plates of the same material batch and spool. The corresponding specimen plates are produced in the facilities of Daimler AG and tested at the Institute of Aircraft Design, University of Stuttgart. Lastly, the results of specimen testing are discussed in section 6.3 and section 6.4.

6.1. Overview of the Material Properties Determination

The approach followed for the analysis of the CPV directly relates to the material properties needed to characterize it adequately. Therefore, this can be practically divided by whether modeling takes place at the micro or the mesoscale. Concerning the first, material properties need to be defined at the constituent level, what is, however, indicated by Hinton and Soden [86], to not be generally straightforward estimated. This results from the complex stress state in the constituents in rather simple test definitions, which can be illustrated by the alternative pure tension, biaxial loading, and shear, experienced by the matrix under a macroscopic longitudinal tensile conditions [87]. In the case of the second, the determination of mechanical properties at the ply level is instead more accessible because of the approachable specimen scale and the assumption of homogeneous orthotropic material responses. Nevertheless, this characterization can only be meaningful if the manufactured specimens

represent the macromechanical attributes of the filament wound CPV. These include aspects like the layer consolidation induced by the stacking sequence and the fiber tension, the curing cycle in the absence of external pressure, the layer architecture, and the shape of the part.

Regarding the material characterization at the ply level, the review presented by Perry et al. [88] introduces various of the relevant specimen configurations for this purpose. In consequence, the mechanical definition of the CPV may be represented by either flat panels (unidirectional, cross or angle plies), small diameter tubes with mostly hoop or high-angle helical layers, thin large-diameter cylinders in the form of rings or curved tensile coupons, and thick large diameter cylinders in the form of rings or out-of-plane coupons. The evolution in the complexity of these tests is illustrated in fig. 6.1, where also the coupon geometrical aspect is indicated.

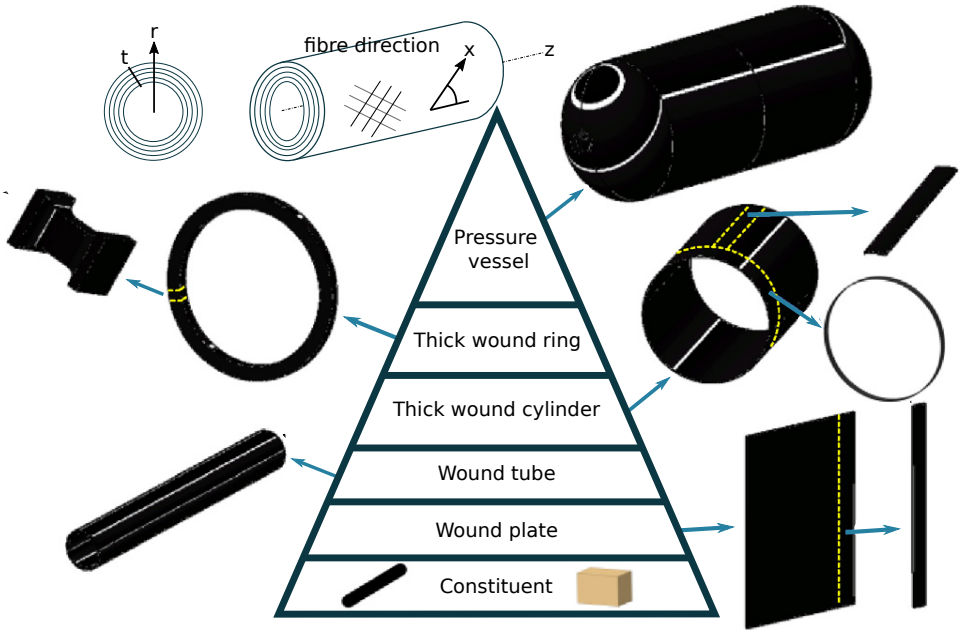


Figure 6.1: Pyramid of material tests in application to CPVs (adapted from [88])

The number of material properties needed for an analysis definition is determined from its constitutive behavior description. Therefore, the number of elastic constants required to define a material orthotropic response is nine (three normal moduli, three shear moduli, and three Poisson's coefficients), whereas they reduce to five if the transversely isotropic assumption holds. This assumption implies that the material has an axis of symmetry about which the properties definition does not vary, which consequently limits the required constants to a longitudinal and transverse normal modulus, Poisson's coefficients, and a shear modulus. For filament wound flat coupons, standard test methods are available to determine the in-plane mechanical properties under tensile loading, [89–91]. According to these, longitudinal and transverse modulus and strength are obtained from unidirectional 0 and 90 degrees coupons. In the case of shear, these are calculated from $\pm$ 45 degree angle-plies.

Extracting tensile specimens from a filament wound cylinder is presented as an alternative to flat coupon testing when their resulting fiber volume and void contents are too dissimilar from the produced vessels. However, it is not possible to wind fibers aligned with the axial direction in the cylinder, meaning that these coupons are only suitable for transverse and shear property extraction. However, as indicated by Perry et al. [88], a reverse calculation of the longitudinal properties is possible from the laminate plate theory and the transverse and shear properties. Investigations in which cylindrically wound components are used for the characterization of material mechanical properties of CPVs, are the works of Pilato [92], Gentilleau et al. [69] and Christ [93]. One of the main limitations of coupon extraction is that the cutting of the composite material can produce edge damage. Delaminations and additional stress concentrations might be created resulting from this circumstance, hence leading to premature failure of the specimens and diminishing the relevance of the results.

The use of tubes for transverse and shear properties estimation has the advantage of reproducing the no free-edge boundary condition of CPVs, although achieved at the expense of introducing a

strong geometrical bias because of the pronounced component curvature. Testing of filament wound composite cylinders is the method proposed by the MIL-HDBK-17-1F [94] to determine the transverse and in-plane shear properties, [95, 96]. The first is obtained by applying tensile loading on the hoop wound cylinder using a special fixture, whereas the second uses the same geometrical configuration to generate torsion in the cylinder, hence translating in in-plane shear of the layup. Similarly, a direct method for obtaining the strength of the composite material in the hoop direction is by testing filament wound rings. According to this method, the longitudinal modulus and strength are predicted from a uniform internal pressure application. However, both the conventional split-disk test, [97], and a quadrant-ring test modification, [98] seem to fail in applying a sufficiently uniform loading to correlate ring and flat specimen test results adequately. This limitation is overcome with the proposal of Bois et al. [99] to test rings by driving a conical fitting through their opening. This mechanical type of testing avoids the intrinsic difficulty of using hydraulic pressurizing devices in application to narrow cylindrical rings, [100], although it has to confront the stick-slip condition of pushing one metallic part through another.

Testing of out-of-plane mechanical properties is achieved by cutting through-the-thickness specimens from thick filament wound rings for longitudinal and out-of-plane shear testing. Concerning the longitudinal property testing, specimens are shaped in their waist to be more suitable for the determination of elastic properties, following the so-called RARDE configuration, or for the strength determination, by presenting a circular waist. The specimen load is transferred by bonding metallic bars to its ends, leading to a setup like the one depicted in fig. 6.2. The RARDE profile shows a waist similar to an ellipse on which the central part is left plain to reduce the stress concentration on this section, which generally causes its failure at the bar bonds instead. In the case a circular waist is defined, failure is considerably more likely to occur in the central section, which correspondingly facilitates the strength property calculation, [101]. About the out-of-plane shear, the MIL-HDBK-17-1F [94] recommends using the V-notched beam method on through-the-thickness specimens, [102]. This method applies a scissoring load on a flat material strip that includes opposite V-shaped notches to induce a rather uniform shear field. The existence of shear is coupled with the asymmetric bending induced by the loading application, which obstructs the elastic constant determination by introducing deleterious strain components.

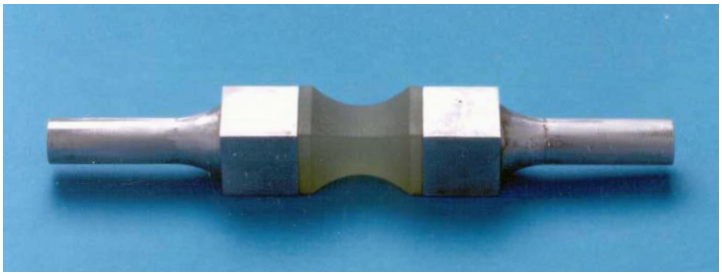


Figure 6.2: Specimen for the test of through-the-thickness mechanical properties with a circular waist and bonded loading rods (taken from [101])

As the fiber volume and void contents of the composite material vary along the vessel, it is comparatively relevant to identify these for their correlation with the elastic, strength, and fracture properties. They reflect on the robustness of the manufacturing process and the adequacy of a vessel architecture in rendering a coherent composite material construction. The standard method for constituent content calculation is based on ignition of composite samples to determine the amount of reinforcement. By comparison with the initial composite weight and volume and the known constituent densities, the matrix volume and void contents are ultimately computed, [103, 104]. This approach is robust, although time-consuming if a large number of samples have to be analyzed.

Consequently, a determination based on SEM observations can be used alternatively, as presented in its application to CPVs in the work of Harada et al. [75]. After sample extraction and polishing, the cross-section observations are converted into binary images and post-processed for the fiber volume content measurement. However, the microscopic observations do not allow to accurately identify the porosity value because the measurement lacks volume information. These void contents can, alternately, be estimated from three-dimensional CTs and their subsequent image post-processing. This approach provides information on the spectrum of porosity and its spatial distribution, although it requires a rather costly high-resolution image acquisition.

The CPVs virtual simulation is acknowledged to be founded on a reliable characterization of the material properties that result from manufacturing. However, as a close relation exists between the produced stacking sequences and the resulting material response, it can be concluded that a representative testing coupon choice is required to account for this intrinsic variability. In this regard, the influence of porosity in the strength determination appears as a relevant characteristic in the CPVs design because of the presence of matrix controlled failure modes. Gaps appear to have a role in the matrix failure modes as crack nucleators, hence impacting the material strength by the increased porosity and the helical layer architecture that results in lower compaction. Moreover, as porosity is closely related to the layer consolidation and, derived from it, with the fiber volume content, this is also related to the strength in the longitudinal direction.

6.2. Design and Manufacturing of Test Specimens

6.2.1. Design of Testing Plates

The testing of fundamental material properties is carried in the current project to define a representative input for the analysis of FE models. To this purpose, flat filament wound plates are produced with the corresponding manufacturing parameter configuration of the vessels, which includes the winding type, the filament tension, and the curing cycle. These specimens are conceived with a twofold purpose, on the one hand, tensile tests are carried to determine the elastic and strength characteristics in the fundamental longitudinal, transverse and shear components; while on the other hand, specimens are tested to determine their fracture toughness in the Modes I and II through double cantilever beam (DCB) and end notch flexure (ENF) fixtures.

The mechanical properties of the composite material are determined through flat wound plates because of the convenient simplicity of their test methods. However, this is done in exchange for the free-edge influence on triggering premature failure and the assumption that the coupon construction with outer unconstrained plies adequately reproduces the real CPV material. Concerning stiffness and strength testing, unidirectional filament wound specimens are produced according to ISO 527-4:1997 [90] for the determination of their longitudinal and transverse ply properties, whereas $\pm$ 45 plates are wound correspondingly according to ISO 14129:1997 [91] to determine shear characteristics. The influence of various void contents is considered during these properties determination in light of the varying material consolidation experienced by the produced CPVs. Therefore, specimens are manufactured with a qualitative control of their consolidation level that, following, serves to represent the sensitivity of the respective mechanical properties to it.

Regarding testing the material fracture toughness, unidirectional flat plates are wound as per standards ASTM D5528-13 [105], ASTM D7905 / D7905M-19e1 [106] with the inclusion of an insert at their midplane. In these cases, fracture toughness values are obtained from the progression of a delamination front, which hence requires unidirectional coupons to ensure a gradual crack growth. Despite the helically wound configuration being more representative of the vessel construction, the interaction between consecutive bands would likely arrest the crack growth and render the toughness results invalid.

Unidirectional specimens are directly representative of layers aligned with the hoop direction, albeit they disregard the strength detrimental effect of interweaving helical bands. A comparison of tensile testing of helically wound cross-ply plates and their laminated counterparts provides a means for quantifying this effect. Withal, this still requires the previous determination of the unidirectional properties and has been left as a matter of future work. The interwoven helical ply construction is used for the manufacturing of the $\pm$ 45 plates. It conveniently produces the angle-ply alignment with the filament winding method, while it also intrinsically represents the structure of the shear loaded helical plies of the CPV. The influence of the interweaving effect in the shear stiffness and strength characteristics can be quantified by comparing their results with laminated $\pm$ 45 plates. Nonetheless, this has also been left as a matter of future work, including the detailed assessment of the interwoven material properties representativeness in the helical laminated subply modeling presented in section 7.2.

6.2.2. Manufacturing of Specimens

The flat plates used for the extraction of the material characterization specimens are wound on the special tools depicted in fig. 6.3 to obtain components of approximate dimensions of 310 by 230 mm. The unidirectional coupons are manufactured in the tool shown in fig. 6.3a that, besides controlling the



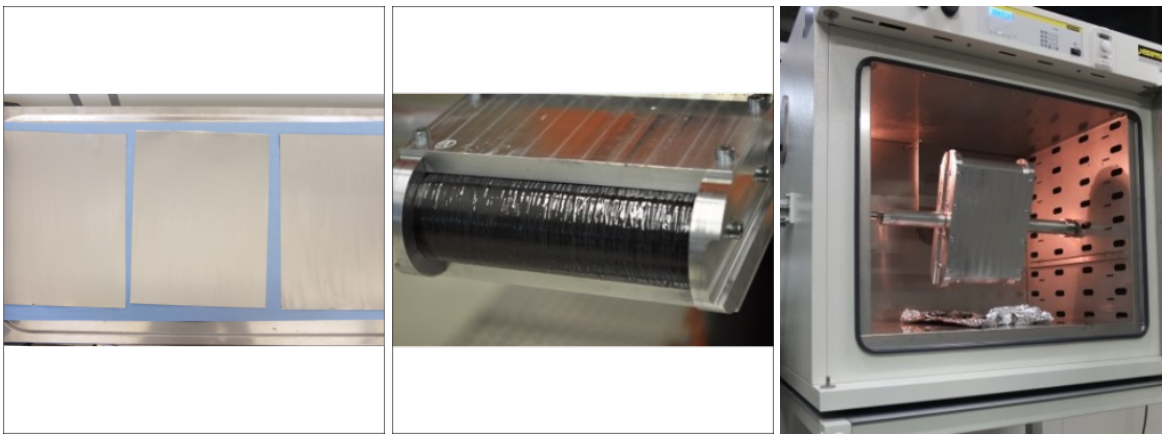
(a) Unidirectional specimen plate (b) Helical $\pm$ 45 specimen plate

Figure 6.3: Winding processes of the unidirectional and helical $\pm$ 45 specimen plates in their corresponding flat surface mandrels

geometrical dimensions of the produced plates, also permits the fitting of a molded case that enforces layer consolidation. The mold case used in the unidirectional specimen plates is designed to enforce a plate thickness of 2 mm on a 9 layer layup of 0.2 mm nominal thickness rovings. This shows comparable fiber volume and void contents to those of the CPV circumferential layers that respectively appear in the magnitudes of 58.5 % and 1.5 %.

Instead, winding of $\pm$ 45 plates requires the considerably larger apparatus presented in fig. 6.3b. It provides enough tool length for the angle change at the turnaround locations. While also ensuring the right orientation in the central section. It is convenient to fit the produced specimens plates in the tool used for the unidirectional counterparts. Therefore, porosity contents and curing cycles are ensured in close conditions to the ones defined for the unidirectional specimens. The central section of the wound fixture in fig. 6.3b, is thus cut and manually transferred to the unidirectional tool to enforce a consolidation level similar to the real vessel. The helically wound plates are formed by 5 layers of approximately twice depth of the unidirectional ones for bands of 0.2 mm nominal thickness and 14 mm nominal width. These plates, which slightly overpass the thickness of the unidirectional ones, are necessary to ensure a representative porosity content of the interwoven construction of composite bands.

The varying porosity contents sought in the material characterization investigation are accomplished by alternating metallic shims between the composite material and the mold case. This approach per-



(a) Shims for the control of the composite plate thickness (b) Consolidation with mold case (c) Jig setup for curing in oven

Figure 6.4: Tool preparation for the curing process, showing the consolidation of the test plates and the oven setup

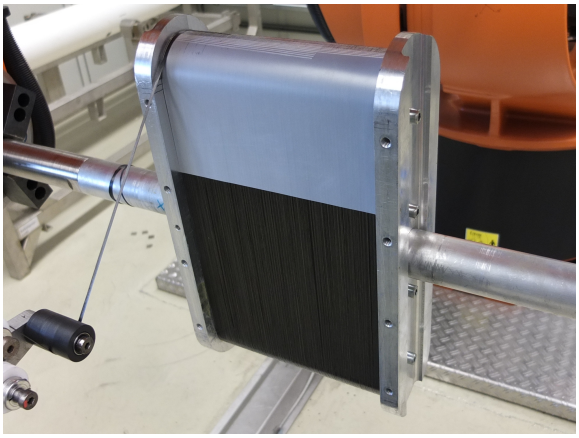
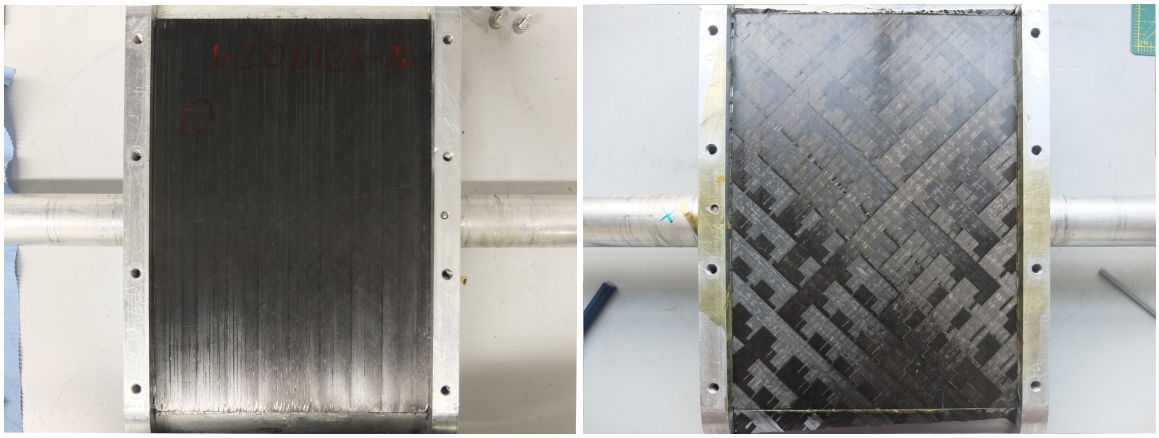


Figure 6.5: Winding process of the unidirectional specimens for fracture toughness testing. A PTFE insert is located on the specimen midplane to form an initial delamination length

mits to effectively reduce or increase the produced plate thickness and, consequently, define different consolidation levels for a fixed layup definition. The higher this level, the smaller the voids left between the wound rovings and the higher the fiber volume content resulting from the more pronounced resin outflow. A strong coupling results between the fiber volume and porosity contents tested, which is also expected during the produced CPV layer consolidation because void content reduces at the same time resin infuses out of the composite reinforcement.

The preparation of the filament wound plates for curing under the specified porosity values is illustrated in fig. 6.4. Metallic shims of 0.1 mm thickness like the ones presented in fig. 6.4a are used to modify the final thickness of the plate. A quantitative prediction of the final specimen porosity cannot be achieved with this method without a detailed analysis of the consolidation process. However, qualitatively it can be inferred that a higher consolidation level induces a higher resin outflow than a corresponding porosity reduction. This effect is expected from the fact that the resin in the uncured state principally supports the consolidation pressure and that the entrapped air needs to escape through the narrow side openings of the tool. A filament wound tool with the installed cases is shown in fig. 6.4b, where the rounded corners of the unidirectionally wound plate need to be trimmed to prevent the residual stress generated by the thermal expansion of the tool. This task is not necessary for the helically wound plates, as they are cropped to the right size before placement. Ultimately, the tool is placed in an oven with a rotating jig like the one illustrated in fig. 6.4c. A curing cycle of 8 h at a temperature of 110°C is applied, identical to the manufacturing process of the investigated CPVs.

Manufacturing of the specimen plates used for the fracture toughness determination is accom-



(a) Unidirectional specimen plate

(b) Helical $\pm$ 45 specimen plate

Figure 6.6: Specimens after curing of the unidirectional and helical $\pm$ 45 cases

plished in an analogous form to the winding of the unidirectional stiffness and strength counterparts. They characterize by the placement of a PTFE insert of 50 µm thick in the midplane of the 10 layer layup shown in fig. 6.5. The insert thickness choice above the standard reference of 13 µm is made upon the availability of the insert material and previous experiences on this type of testing. The insert is placed so the specimens are cut to the corresponding delamination length required by the DCB and ENF tests, [105, 106].

6.2.3. Discussion on the Manufacturing Results

The result of the specimen manufacturing for the unidirectional and $\pm$ 45 case is depicted for an average porosity content in fig. 6.6. It is noted that, even though the surface finishing is smooth for both cases, the helically wound plates show a higher concentration of resin on their surface. It appears from the non-uniform surface finishing generated by the interwoven filament winding that accumulates resin excess during layer consolidation. Following, 5 to 8 flat coupons are cut from every plate, together with 5 specimens for fiber volume and porosity content determination, as indicated by the template in fig. 6.7.

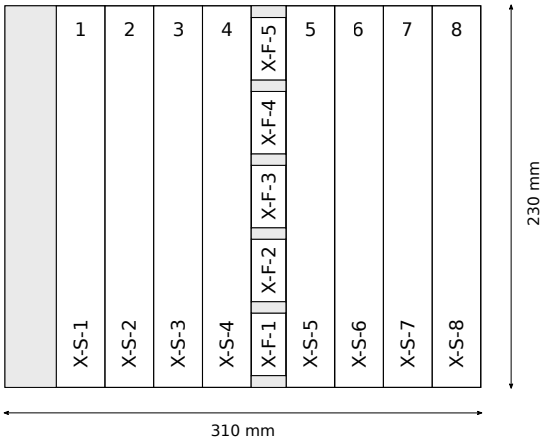


Figure 6.7: Template for the specimen extraction from the filament wound plate

The specimen dimensions required by the standard tests are reported in table 6.1, and complemented with the thickness results measured from the various porosity level configurations detailed in table 6.2. It is noted that even if the standard specimen widths are adequate for the testing of unidirectional layups, these fall short in the case of the helically wound plates. Composite bands of nominal width 14 mm are wound for these plates, appearing as excessively voluminous in the 25 mm wide standard specimens. Local imperfections existing in the band bondings may lead to premature failures

Table 6.1: Overview of the specimen dimensions produced for the material mechanical property characterization

Standard.	Type of Test	Stack.	Count	Test Len. [mm]	Tab Len. [mm]	Width [mm]	L. Rate [mm/min]
ISO 527	Tensile	$[0]_9$	5 to 8	150	70	15	2
ISO 527	Tensile	$[90]_9$	5 to 8	150	25	25	1
ISO 14129	Tensile	$[\pm 45]_5$	5 to 8	150	25	25	1
Standard.	Type of Test	Stack.	Count	Total Len. [mm]	Del. Len. [mm]	Width [mm]	L. Rate [mm/min]
ASTM D5528	DCB	$[0]_{10}$	5 to 8	250	50	25	1
ASTM D7905	ENF	$[0]_{10}$	5 to 8	200	50	25	0.5

Stack. – stacking sequence; Count – number of specimens extracted from each manufactured plate; Test Len. – length of the test specimen exculding the tab length; Total Len. – length of the test specimen including the delamination length; Del. Len. – length of the delamination insert at the specimen midplane; L. Rate – loading rate
Note 1: The initial delamination length of the DCB test does not include the width of the loading blocks

as these, are aggravated by the interlaminar stress generated at the free edges.

In the manufacturing of the specimens, the influence of the bandwidth in the result reliability was not timely identified, requiring the critical judgment of the result scatters concerning in-plane shear. Additionally, the relatively thin thickness of the manufactured specimens magnify this effect; outer ply failures let a correspondingly small amount of undamaged material to carry the applied load. These plies are anticipated to fail prematurely because of their unconstrained outer surfaces, thus inducing load redistribution and further damage in the inner layers, as reported in the investigation of Kellas [107].

Table 6.2: Overview of the specimen dimensions produced for the material mechanical property characterization (cont.)

Standard.	Stack.	Porosity	Mea. Thick. W. [mm]	Shim [mm]	Target [mm]	Mea. Thick. [mm]	Defects
ISO 527	$[0]_9$	Low	2.25 ± 0.02	−0.30	1.70	1.95 ± 0.02	Dints
		Medium	2.25 ± 0.02	0.00	2.00	2.10 ± 0.02	–
		High	2.25 ± 0.02	0.20	2.20	2.30 ± 0.02	Dry Surface
ISO 527	$[90]_9$	Low	2.25 ± 0.02	−0.30	1.70	2.00 ± 0.02	–
		Medium	2.25 ± 0.02	0.00	2.05	2.10 ± 0.02	–
		High	2.25 ± 0.02	0.20	2.20	2.30 ± 0.02	Pits
ISO 14129	$[\pm 45]_5$	Low	2.70 ± 0.10	−0.30	1.70	1.90 ± 0.02	–
		Medium	2.70 ± 0.10	0.00	2.00	2.00 ± 0.02	–
		High	2.70 ± 0.10	0.20	2.20	2.30 ± 0.02	–
ASTM D5528	$[0]_{10}$	Medium	–	0.00	2.20	2.25 ± 0.05	Pits
ASTM D7905	$[0]_{10}$	Medium	–	0.00	2.20	2.25 ± 0.05	Scratches

Stack. – stacking sequence; Mea. Thick. W. – measured specimen plate thickness after winding; Shim – accumulated shim thickness applied between the composite material and the tool case; Target – specimen plate thickness expected from the shim application on the 2 mm clearance of the tool; Mea. Thick. – measured specimen plate thickness after curing
Note 1: The values between brackets refer to the standard deviation of the samples

Concerning the produced specimen thickness, it is observed in table 6.2 that, besides applying shims to adjust this value to a defined target, some variability still exists compared with the final result. This effect shows a generally increased thickness in the cured plate against the target value, whose mismatch appears to increase with the higher level of consolidation. Nevertheless, such a non-linear response can be expected from the increased resistance to resin outflow with the higher consolidation induced. From the discussion in section 5.2, the resin roughly carries the surface pressure generated with the tightening of the tool case in the early stages. As resin viscosity increases during the early stage of the oven cycle, pressure is relieved from the resin by flowing out, increasing the rate for the higher load application. However, both viscosity and permeability appear as variables inversely proportional to the deformation rate, hence forecasting this opposition to consolidation.

Another aspect noticed is that, for the high porosity content configuration of the unidirectional plates, a final thickness slightly larger than the winding result is obtained, despite expecting a light consolidation. This effect is argued to originate in the thermal expansion of the component in the through-the-thickness direction in light of the mild surface pressure applied. Particularly to the unidirectional specimen plates, the through-the-thickness direction deformation is dominated by the resin properties, being these less stiff and more highly expansive than the fibers. An indicator of the likely borderline consolidation applied, in this case, is the slightly dry surface result reported in table 6.2, which furthermore shows that limited resin efflux occurred. Other surface defects reported include dints, pits, and scratches, which emanate from cured resin fragments detached from the reused winding tool and which, on occasions, they were shown to linger between the composite plate and the tool case.

All in all, the specimens used for the material property characterization are manufactured by following equivalent processes to the produced CPVs. These permit to account for the influence of the layer consolidation in the stiffness and strength determination and the helical winding pattern in the shear mechanical response. Still, there are various aspects because of which uncertainty of the results is expected, which involve the longitudinal and transverse characteristics of the helically wound plies, the alteration of the pure specimen stress fields because of the existence of free edges, and the meaningfulness of mean test results in the analysis by FE.

6.3. Results and Discussion of Material Stiffness and Strength

The manufactured specimens for tensile in-plane material properties are tested according to the standards ISO 527-4:1997 [90] and ISO 14129:1997 [91] for the longitudinal, transverse, and in-plane shear characteristics. Polymer tabs are adhesively bonded to the coupon edges for the load transmission from the machine to the specimen. Then, conventional strain gages are used to monitor longitudinal and transverse strain in the in-plane tensile tests, while a video extensometer is used in the in-plane shear.

Results for the fiber volume and porosity contents of each of the manufactured configurations are reported in table 6.3, whereas the results for the stiffness and strength determined from tensile testing are correspondingly detailed in table 6.4. Mean values are here presented together with their confidence intervals of 95 % to serve as an indicator of the statistical dispersion of the moderately small samples considered. The determined fiber volume contents and densities indicate that the various consolidation induced levels generated comparable resin outflow in the unidirectional and helically wound specimen plates, which is observed from their comparable results at each porosity level.

However, these porosity contents appear to differ significantly when the unidirectional cases are compared with the pm 45 plates. On the one hand, it appears that low porosities are challenging to achieve in the latter because of the complex interwoven band construction, preventing good overlaying of successive windings. On the other hand, very high porosities are also intrinsically prevented due to the tight entanglement of the composite material bands, which, consequently, auto-induces a light level of consolidation. Besides, some discrepancy also appears in the porosity between the manufactured unidirectional plates. It indicates the sensitivity of these results to small variations in the specimen production and the measurement method itself. Being the filament winding process, the material selection and the curing cycle identical for the cases presented, the noticed disparity is argued to result from the intrinsic material variability, the recycling of the shims used to control the consolidation level, and intractable deviations in the applied torque with which this consolidation is achieved.

Table 6.3: Results of the material characterization test for porosity and fiber volume content

Stack.	Porosity	n_f	Fibre-Volume [%]	Porosity [%]	Density [g/cm^3]
$[0]_9$	Low	5	62.24 ± 0.36	0.36 ± 0.04	1.57 ± 0.00
	Medium	5	59.17 ± 0.70	1.55 ± 0.66	1.54 ± 0.01
	High	5	56.55 ± 0.50	7.46 ± 0.82	1.45 ± 0.01
$[90]_9$	Low	5	62.94 ± 0.57	1.07 ± 0.53	1.56 ± 0.00
	Medium	5	60.02 ± 0.36	2.60 ± 0.43	1.53 ± 0.01
	High	5	56.77 ± 0.64	6.81 ± 0.31	1.46 ± 0.00
$[\pm 45]_5$	Low	5	62.90 ± 1.31	1.31 ± 0.72	1.56 ± 0.01
	Medium	5	60.17 ± 3.07	3.65 ± 1.26	1.52 ± 0.03
	High	5	55.01 ± 5.23	5.65 ± 1.93	1.46 ± 0.04

Stack. – stacking sequence; n_f – number of specimens tested for fibre-volume content and porosity

Concerning the test results introduced in table 6.4, a general trend towards reduced stiffness and strength is observed with the increased porosity. This tendency shows the impact of both the fiber and the matrix dominated properties, where a specific increase in result scatter is noticed for the in-plane shear response. In the case of the latter, the nucleation of matrix cracks is expected to couple with the existence of wide composite bands relative to the specimen dimension, which, because of their non-uniform bonding characteristics, reasonably lead to disperse damage onset loads. Additionally, minute variations are observed in the Poisson ratio results, whereas total carried loads also show to be comparable, as expected from the similar amounts of material comprised of all the specimens.

6.3.1. Longitudinal Tensile Tests

The influence of the porosity content in the longitudinal tensile properties of this filament wound composite material is illustrated in fig. 6.8. Firstly, fig. 6.8a depicts the stress-strain relations of the investigated configurations with the overlay of the sample mean curve and its confidence interval of 95 %. The sample average strength set is also calculated from the maximum stress born by each specimen and represented by the error bars in terms of stress σ and strain ε. Secondly, the elastic modulus E_{sec} and strength σ_{max} are shown in fig. 6.8b against the mean fiber volume content and porosity of

Table 6.4: Results of the material characterization test for stiffness and strength

Stack.	Porosity	n	A [mm^2]	E_{sec} [GPa]	ν [-]	F_{max} [kN]	σ_{max} [MPa]	ε_{max} [%]
$[0]_9$	Low	8	30.68 ± 0.42	136.84 ± 0.90	0.31 ± 0.01	82.38 ± 5.58	2675.13 ± 72.06	1.75 ± 0.04
	Medium	8	31.65 ± 0.21	131.09 ± 0.61	0.30 ± 0.01	72.38 ± 3.00	2286.64 ± 66.40	1.57 ± 0.04
	High	8	34.42 ± 0.05	120.00 ± 0.86	0.30 ± 0.01	77.63 ± 2.74	2254.31 ± 60.07	1.66 ± 0.04

Stack.	Porosity	n	A [mm^2]	E_{sec} [GPa]	F_{max} [kN]	σ_{max} [MPa]	ε_{max} [%]
$[90]_9$	Low	5	52.21 ± 0.09	8.91 ± 0.06	2.34 ± 0.18	44.72 ± 3.33	0.52 ± 0.04
	Medium	8	53.44 ± 0.06	7.90 ± 0.17	2.09 ± 0.18	39.07 ± 3.46	0.51 ± 0.04
	High	8	56.57 ± 0.08	6.85 ± 0.09	1.43 ± 0.19	25.35 ± 3.33	0.37 ± 0.05

Stack.	Porosity	n	A [mm^2]	G_{sec} [GPa]	F_{max} [kN]	τ_{max} [MPa]	$\tau_{5\%}$ [MPa]
$[\pm 45]_5$	Low	9	50.16 ± 0.17	4.06 ± 0.04	5.51 ± 0.41	54.98 ± 3.96	51.53 ± 0.84
	Medium	10	51.83 ± 0.23	3.85 ± 0.07	5.74 ± 0.59	55.34 ± 5.56	49.56 ± 2.02
	High	10	56.32 ± 0.14	3.41 ± 0.13	4.87 ± 0.66	43.27 ± 5.91	42.60 ± 3.70

Stack. – stacking sequence; n – number of specimens tested; A – specimen cross-section area; F_{max} – maximum load carried by the specimen; σ_{max} – maximum normal stress carried by the specimen; ε_{max} – normal strain carried by the specimen at the moment of maximum normal stress; E_{sec} – secant normal elastic modulus; ν – Poisson ratio; τ_{max} – maximum shear stress carried by the specimen; $\tau_{5\%}$ – maximum shear stress carried by the specimen truncated at 5 % shear strain; G_{sec} – secant shear elastic modulus

the set, where error bars are added to depict the dispersion of the measured porosities. Fiber volume measurements are presented through the average porosity values by forming a secondary non-linear horizontal axis, thence featuring with unequal separations the comparatively equidistant fiber volume measurements. The elastic modulus is calculated by linear regression of the stress-strain data points between 0.05 and 0.25 % strain values, where a purely elastic behavior is argued to exist. The stiffness and strength results are ultimately fitted to interpolation functions to permit the estimate of material properties for arbitrary porosity contents. This interpolation function is linear in the case of stiffness, whereas a quadratic spline fit is deemed more reasonable in the case of strength.

The trends observed for the longitudinal tensile loading indicate that even if stiffness reduces in an approximately linear form with the increased porosity, this deviates relevantly in the case of strength for the very low void content. Two significant factors are identified to impact this variability; the role of the porosity and fiber volume contents in defining the stiffness and the maximum load carried by the component; the reduced specimen cross-section that results from the higher consolidation level.

First, the increasing porosity can be related to more significant compliance of the resin, impacting the longitudinal load transfer between the fiber bundles. In order to carry the load collaboratively, fibers need to equate their longitudinal strain by generating shear loading through the resin; however, if there is a higher amount of pores, there is a reduced effective area in the matrix transferring this load, therefore reducing the specimen stiffness. Additionally, failure is expected to happen when fiber bundles start collapsing and cascading into a general failure. This response can be linked to the amount of resin and pores, as ineffective load transfer between fiber bundles leads to rapid specimen failure. In this matter, it is anticipated that low porosity and a sufficient amount of resin permit efficient load redistribution at damage onset, leading to a rather gradual collapse. However, with the limited amount of resin, it appears as the elastic energy released with single fiber breakages stays within the neighboring bundles, causing them to fail prematurely. This little gradation of the fiber failure process with increasing porosities and lower fiber volume contents stands as a possible reason because the relation between longitudinal strength and porosity should be non-linear.

Second, the specimen cross-sectional area reduces with the decreasing porosity level, resulting in higher material strength and stiffness values for the same applied load between the specimen configurations. This effect permits to show a clear increasing trend in the longitudinal strength and stiffness even though the amount of fibers for each specimen configuration is virtually the same. Withal, the maximum carried the material variability also impacts load within the material batch, which hinders the rightful interpretation when the statistical samples are insufficient.

6.3.2. Transverse Tensile Tests

Results for the transverse tensile properties are correspondingly presented in fig. 6.9. In a like manner to the longitudinal case, the stress-strain curves are illustrated in fig. 6.9a along their sample mean curve, confidence intervals of 95 % and error bars in terms of stress σ and strain ε. Moreover, elastic modulus E_{sec} and strength σ_{max} are shown in fig. 6.9b, where a purely elastic response is also assumed between 0.05 and 0.25 % strain values. The influence of porosity in the transverse mechanical characteristics is considerably more apparent than in the longitudinal case. When loaded with transverse tension, the less stiff matrix constituent experiences the largest strain component that, when reaching the material limit, develops in cracks spanning through the whole cross-section.

In terms of stiffness, cavities in the matrix constituent reduce the effective area that carries the load in the transverse direction. Hence, larger compliance of the matrix constituent is expected, directly relating to an increased local stress state. Concerning strength, cracks are anticipated to nucleate at material imperfections, where the micromechanical load path is forced to deviate. Regions of stress concentration are generated, ultimately surpassing the material strength and triggering failure.

Correspondingly, the relation of stiffness and strength with the increased porosity is depicted in fig. 6.9b to follow a nearly linear relation. Direct proportionality between the specimen cross-sectional area and the porosity content permit to anticipate this result, as the load transmission within the specimen appears to be primarily controlled by the quality of the matrix amid fibers.

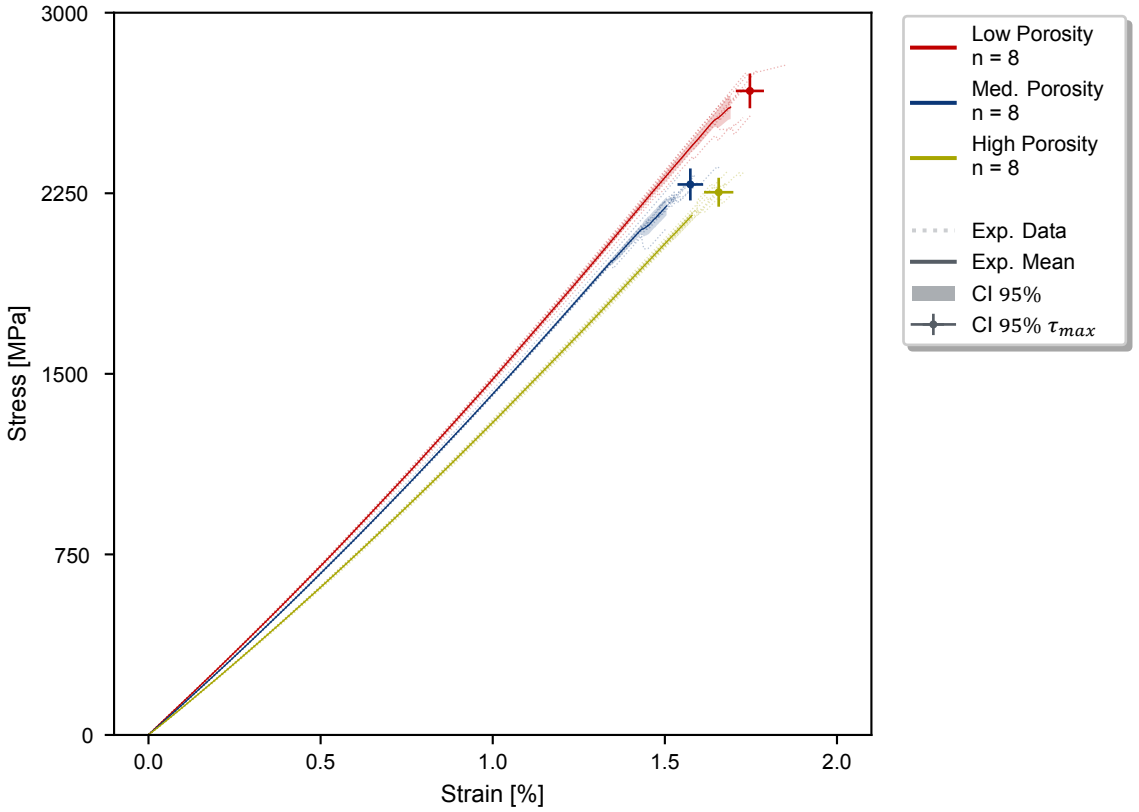
6.3.3. in-plane Shear Tensile Tests

In-plane shear behavior of the $\pm$ 45 helically wound plates is similarly depicted in fig. 6.10. Shear stress is obtained from the 45 degree rotation of the axial stress generated during the specimen tensile loading, whereas shear strain is calculated from the difference of the axial and transverse normal strain components. The shear stress-shear strain relations are presented in fig. 6.10a, showing a characteristic non-linear response at mildly high loads. This non-linearity is argued in the matrix ductility during degradation and the scissoring of fibers with the increased axial deformation. Such fiber rotation with increased loading is reported by Kellas [107] to be generally in the range of 1 ° per every 3.5 % shear strain, which hence sets a shear strain limit of approximately 5 % in the strength determination. This limit ensures that the nominal $\pm$ 45 orientation assumed in the shear stress and strain determination is not breached, while shear strains above this value are seldom encountered in structural applications.

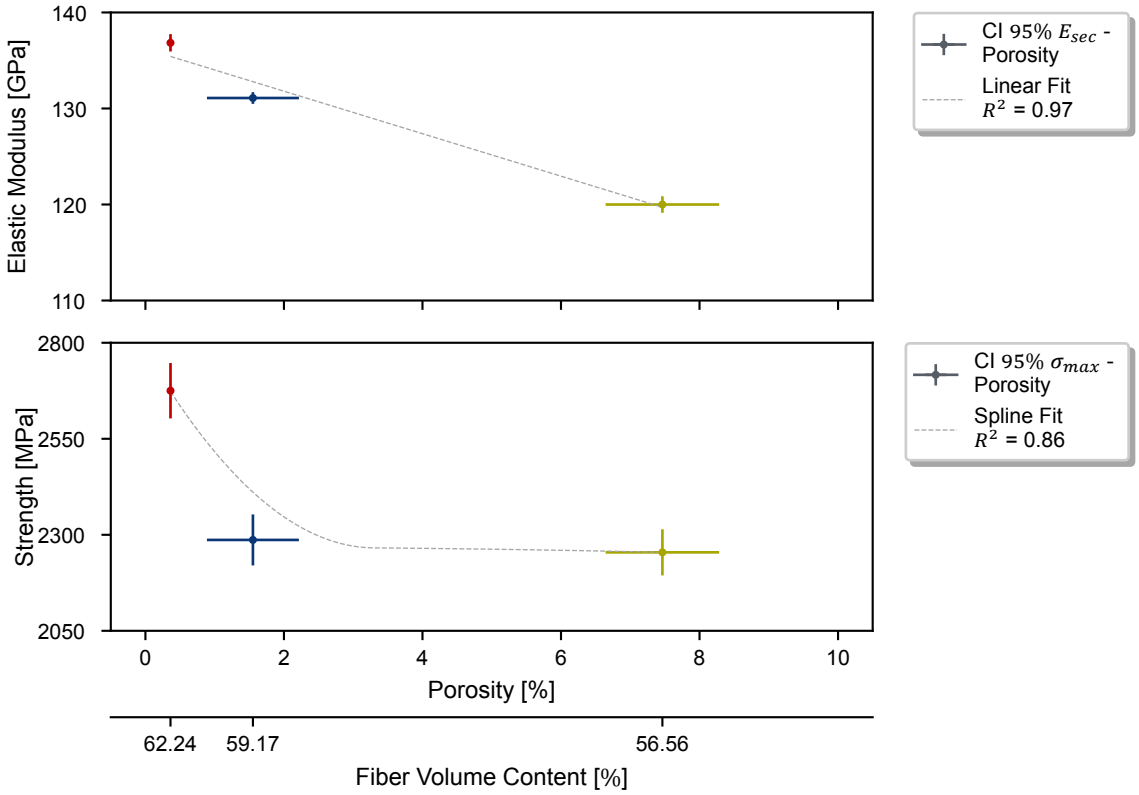
The reduction in shear modulus G_{sec} and strength τ_{max} with increasing porosity is presented as close to linear in fig. 6.10b, where the stiffness is calculated assuming an elastic response in the range 0.2 and 0.6 % shear strain. The porosity determination also shows significant scatter in these results because of the varying material confinement with the composite band interweaving. On the one hand, stiffness is impacted by the number of pores, as larger matrix compliance is inherently introduced with cavities. On the other hand, strength is influenced by the outer surface plies confinement that, upon their triggering of damage, also determine the overloading in the inner layers.

Overall, porosity shows to impact the failure sequence taking place in the in-plane shear tensile specimens, as also illustrated in fig. 6.11. Low porosity contributes to a uniform load distribution that, after degradation of the matrix, results in concurrent longitudinal failure of the $\pm$ 45 oriented fibers. This behavior is depicted for the extended fiber breakage in low porosity set in fig. 6.11 and the flat shear stress-shear shear strain relation after the non-linear deviation in fig. 6.10a. On the contrary, the slope in the non-linear regime is noticeably larger for the high void content set. Delamination of the outer plies seems to develop at relatively low load stages, hence causing load to be transferred to the undamaged inner plies. Besides matrix damage also generally progressing, load redistribution seems to be prompted before the outer layers fail. Hence, distinct inelastic deformation belts are created in the high porosity specimens of fig. 6.11. Ultimately, an intermediate response is observed for a medium porosity content concerning the shear stress-shear strain slope and the inelastic deformation remaining in the failed specimens.

It is also discussed by Kellas [107] that the outer surface plies are subjected to in-plane transverse stress instead of pure in-plane shear fields because of their local unconstrained position. They argue that this has a detrimental effect on the ultimately determined strength and that, therefore, shear strength values should be used with caution when obtained from tensile specimens. Additionally, the interlaminar free ply edge stress is generally not expected to impact the shear strength results, although, in light of the wide filament wound bands, a higher significance is anticipated. An aggregated outcome of these effects is pictured in the increasing result scatter in table 6.4 and the widening confidence

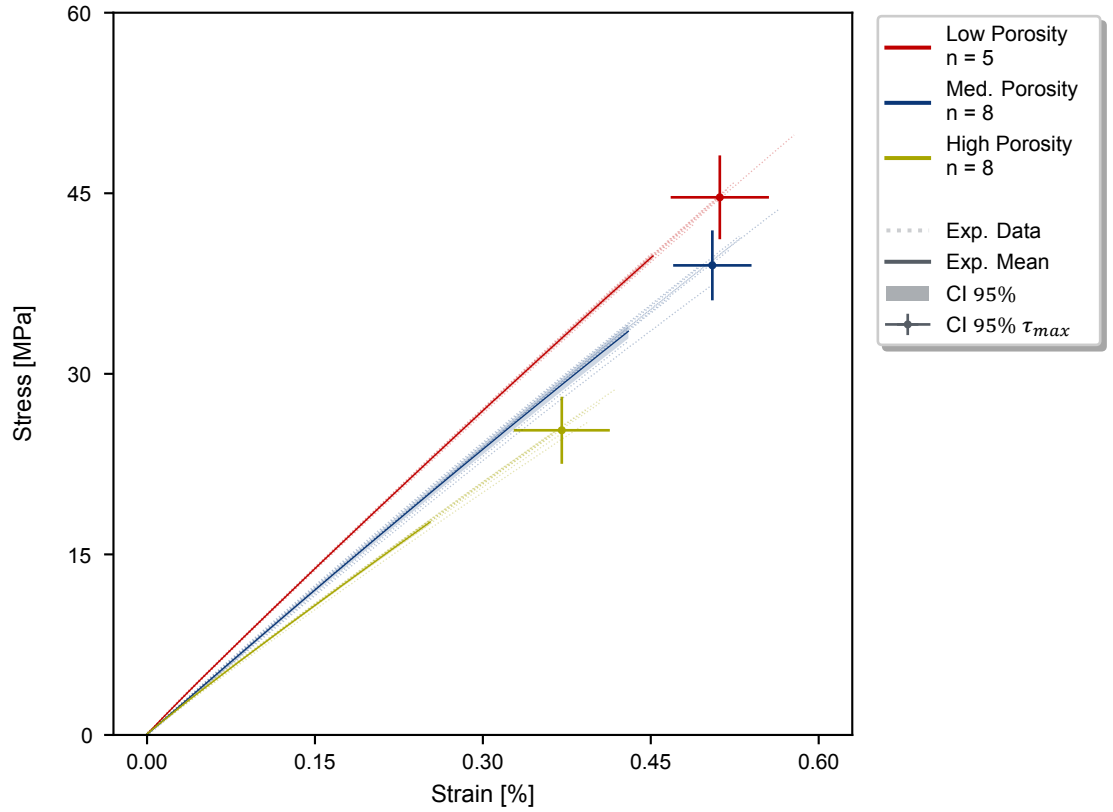


(a) Stress-strain curve

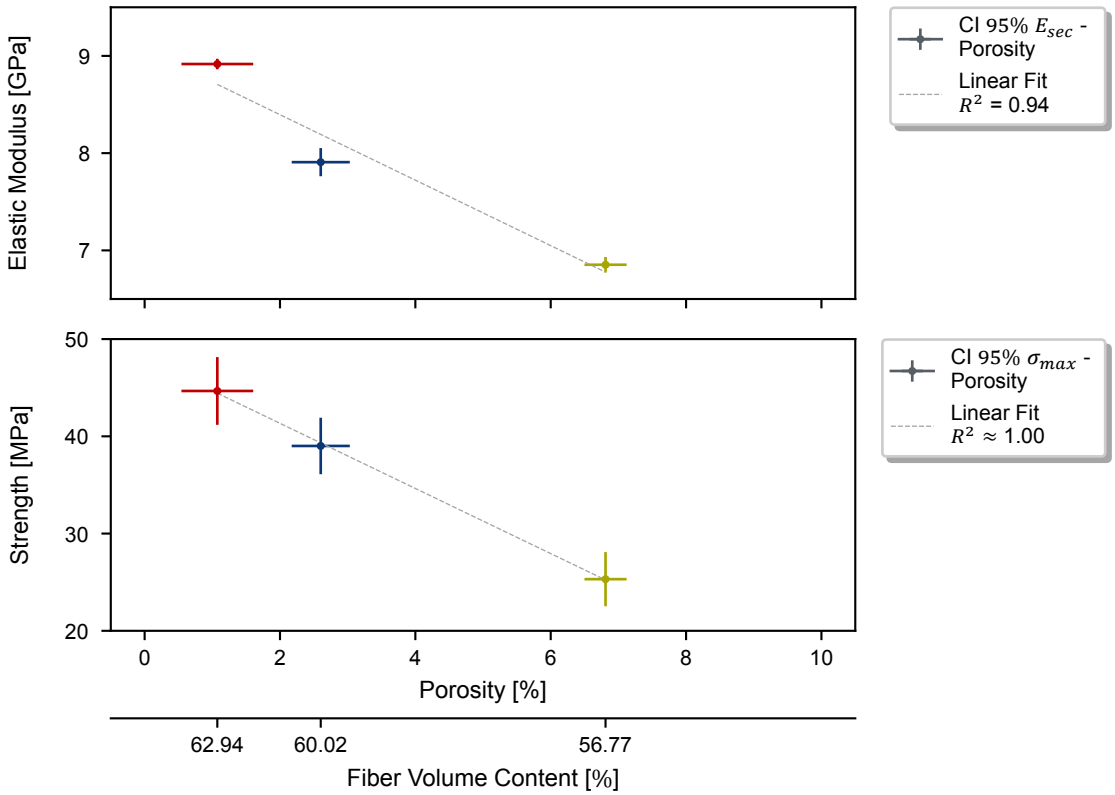


(b) Elastic modulus and strength against porosity and fiber volume content. The trend with increased porosity is adjusted to a fitting function to subsequently infer material properties from it

Figure 6.8: Results of the material characterization for the longitudinal tensile tests. Specimens are tested for low (red), medium (blue) and high (yellow) porosity contents

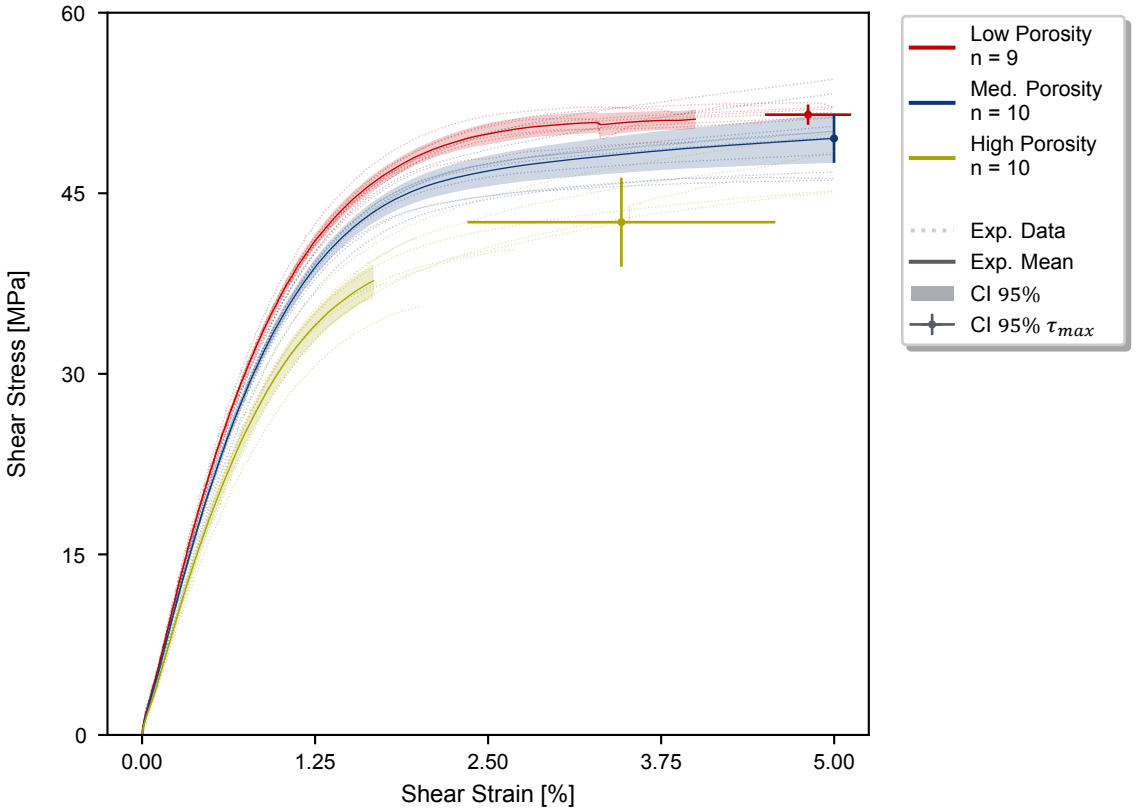


(a) Stress-strain curve

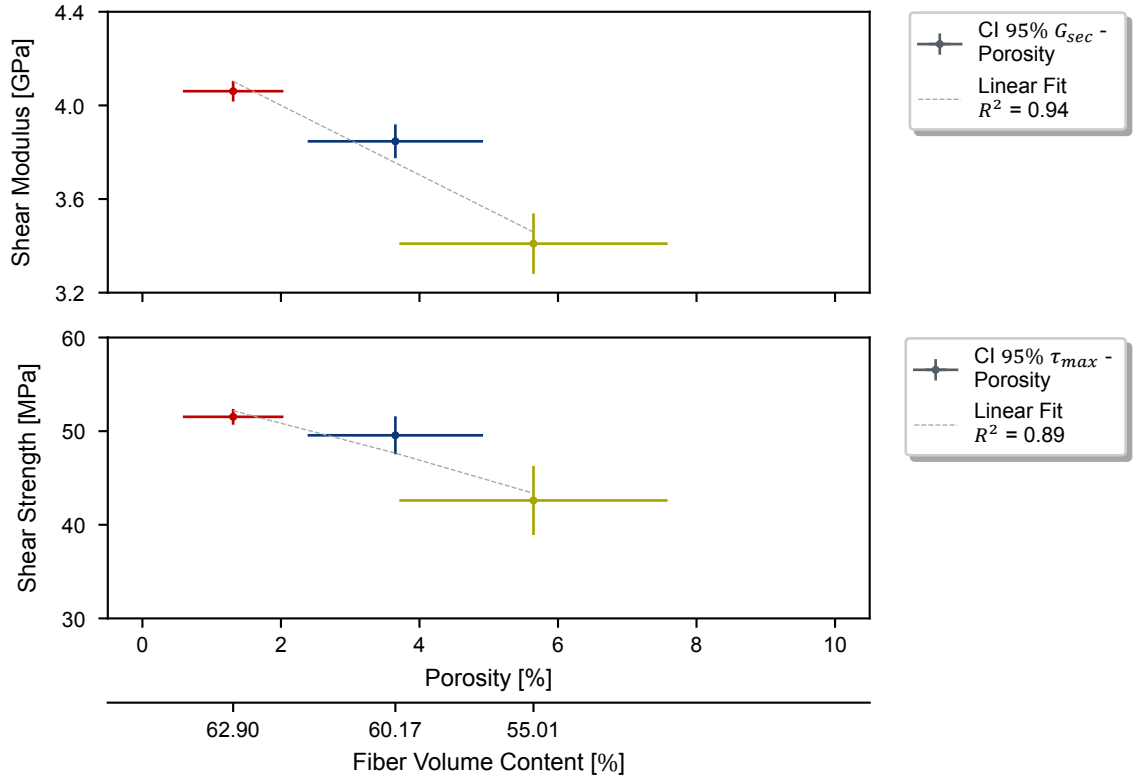


(b) Elastic modulus and strength against porosity and fiber volume content. The trend with increased porosity is adjusted to a fitting function to subsequently infer material properties from it

Figure 6.9: Results of the material characterization for the transverse tensile tests. Specimens are tested for low (red), medium (blue) and high (yellow) porosity contents



(a) Shear stress-shear strain curve

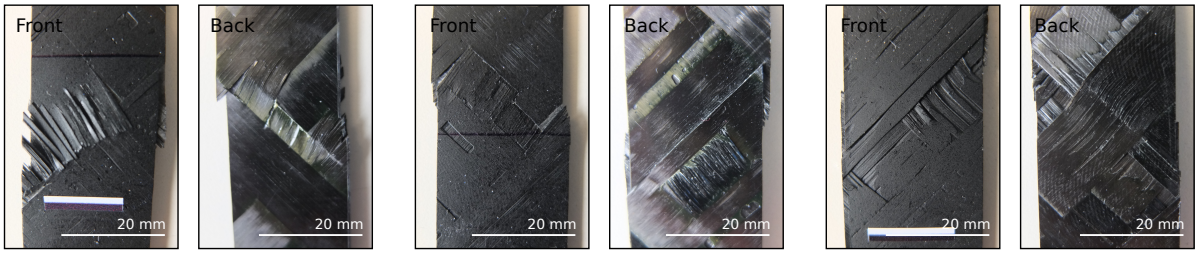


(b) Shear modulus and shear strength against porosity and fiber volume content. The trend with increased porosity is adjusted to a fitting function to subsequently infer material properties from it

Figure 6.10: Results of the material characterization for the in-plane shear tensile tests. Specimens are tested for low (red), medium (blue) and high (yellow) porosity contents

interval in fig. 6.10a. These appear to be exacerbated with the increasing porosity, likely due to the non-uniform distribution of the material imperfections.

Lastly, the 'in-situ' constriction is described by Camanho et al. [108] as the increased load-bearing capability of thin plies when embedded between layers of different orientations. The material fracture toughness increases in these conditions, making the layer strength vary with them being positioned on the inside or the outside. Nevertheless, this effect is presented to dilute when ply thickness becomes larger than 0.7 mm, [109]. Withal, being the defined stacking sequences in table 5.1 rapidly outside this category, no relevant influence of the "in-situ" effects is anticipated.



(a) Low porosity specimens (b) Medium porosity specimens (c) High porosity specimens

Figure 6.11: Failed specimens of various porosity contents after in-plane shear loading. The failed region varies from an energetic and destructive breakage for the low porosity specimens, to a ductile and compliant failure in the case of the high porosity specimens. Front (left) and back (right) sides of a failed specimen are presented for each porosity content

6.4. Results and Discussion of Material Fracture Toughness

Fracture toughness tests are performed in mode I and II according to tests ASTM ASTM D5528-13 [105] and ASTM ASTM D7905 / D7905M-19e1 [106]. Specimens are first used for DCB tests and, then, for the ENF experiments. Therefore, the initial delamination tip of the ENF specimens is not the blunt end of the manufactured insert, but the cracked end result from the DCB crack growth.

6.4.1. Mode I Fracture Toughness

Testing for DCB delaminations serves as an indicator of the damage tolerance of the composite material by measuring the opening forces that allow a crack front to advance. The fracture surface is created because of Mode I loading and is subjected to the specimen midplane insert as initiator. Load is applied in the current experiments through blocks of 20 × 25 × 20 mm, corresponding respectively with the variables $2L'$, b and $2t$. In this context, the fracture toughness $\mathcal{G}_I$ is defined as the loss of energy in the specimen because of an infinitesimal increment of the delamination length, which directly correlates with the applied load and opening displacement per cracked surface as

$$\mathcal{G}_I = \frac{3P\delta}{2ba} \tag{6.1}$$

being P the applied load, δ the opening displacement, b the specimen width and a the delamination length. However, deviations from the ideal elastic condition may exist because of the loading blocks adding a moment arm to the loading, the thin beam arms experiencing a large deformation, and the beam arms also slightly rotating at their fixed ends. This requires a correction on the previously assumed fracture toughness by considering the DCB result as contained on a slightly larger delamination $a + |\Delta|$,

$$\mathcal{G}_I = \frac{3P\delta}{2b(a + |\Delta|)}. \tag{6.2}$$

where the $|\Delta|$ distance is the horizontal axis interception of the cube root compliance C (ratio of opening displacement to applied load) with respect to the delamination length a. The calculated compliance and fracture toughness are then correspondingly adjusted by relating factors according to the measured opening displacement and delamination length as detailed in the standard, [105],

$$
\begin{aligned}
F &= 1 - \frac{3}{10}\left(\frac{\delta}{a}\right)^2 - \frac{3}{2}\left(\frac{\delta t}{a^2}\right) \\
N &= 1 - \left(\frac{L'}{a}\right)^3 - \frac{9}{8}\left[1 - \left(\frac{L'}{a}\right)^2\right]\left(\frac{\delta t}{a^2}\right) - \frac{9}{35}\left(\frac{\delta}{a}\right)^2 \\
C_{corr} &= C/N \\
\mathcal{G}_{I,corr} &= \mathcal{G}_I \frac{F}{N}.
\end{aligned}
\tag{6.3}
$$

Results for the delamination onset are reported in table 6.5 according to the detected non-linearity in the load-displacement curve and the visually observed delamination growth. Likewise, these are presented along with the confidence intervals 95 % to show the statistical significance of the measurements. In this regard, variables like the opening displacement, delamination length, and applied force at delamination onset show a noteworthy scatter. Such a scatter results from the intrinsic variability of the material at the crack tip, which is reported to not be uncommon in testing fracture toughness values, [105].

The values of the fracture toughness presented show that the delamination onset detection from non-linearity is more conservative than its visual observation. This effect agrees with the delamination front advancing faster on the central region of the specimen, hence deviating the load-displacement curve before any observation is made. Correspondingly, the correction for the non-linear specimen arm behavior shows to have a small impact on the fracture toughness results, also indicating that the magnitude of the non-linear effects is not severe.

Table 6.5: Results of the DCB characterization tests for mode I fracture toughness

Stack.	Type	n	b [mm]	h [mm]	a_0 [mm]	δ [mm]	P [N]	$\mathcal{G}_I$ [N mm^{-1}]	$\mathcal{G}_{I,corr}$ [N mm^{-1}]
$[0]_{10}$	NL	6	24.99 ± 0.02	2.29 ± 0.08	50.16 ± 0.43	6.67 ± 0.41	29.33 ± 4.28	0.23 ± 0.03	0.21 ± 0.04
	VIS	"	"	"	55.42 ± 0.93	9.84 ± 0.81	32.68 ± 4.22	0.35 ± 0.06	0.32 ± 0.06

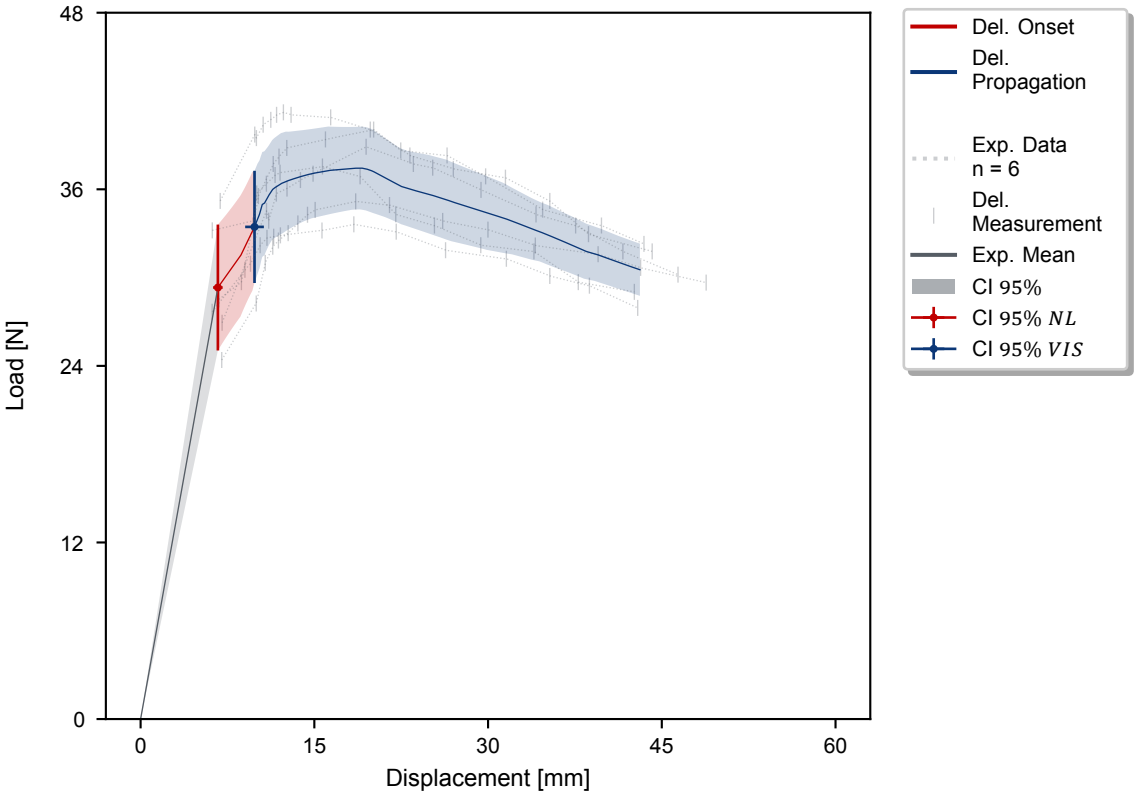
Stack. – stacking sequence; n – number of specimens tested; b – specimen width; h – specimen thickness; a_0 – delamination length at propagation onset; δ – opening displacement; P – applied load; $\mathcal{G}_I$ – mode I fracture toughness; $\mathcal{G}_{I,corr}$ – mode I fracture toughness corrected; NL – point at which load versus opening displacement becomes non-linear; VIS – point at which delamination is observed visually on specimen edge

Load-displacement curves and their related fracture resistance are depicted in fig. 6.12 for the ranges of delamination onset and delamination propagation. The first is indicated by the load and delamination ranges in which crack is first reported to grow from the non-linear load deviation and its visual observation. The second results from the subsequent delamination length measurements at multiple points of the cantilever beam opening. Visual monitoring of the delamination propagation is achieved through successive markings on the specimen side as indicated in fig. 6.13 and defined in intervals according to the ASTM standard, [105].

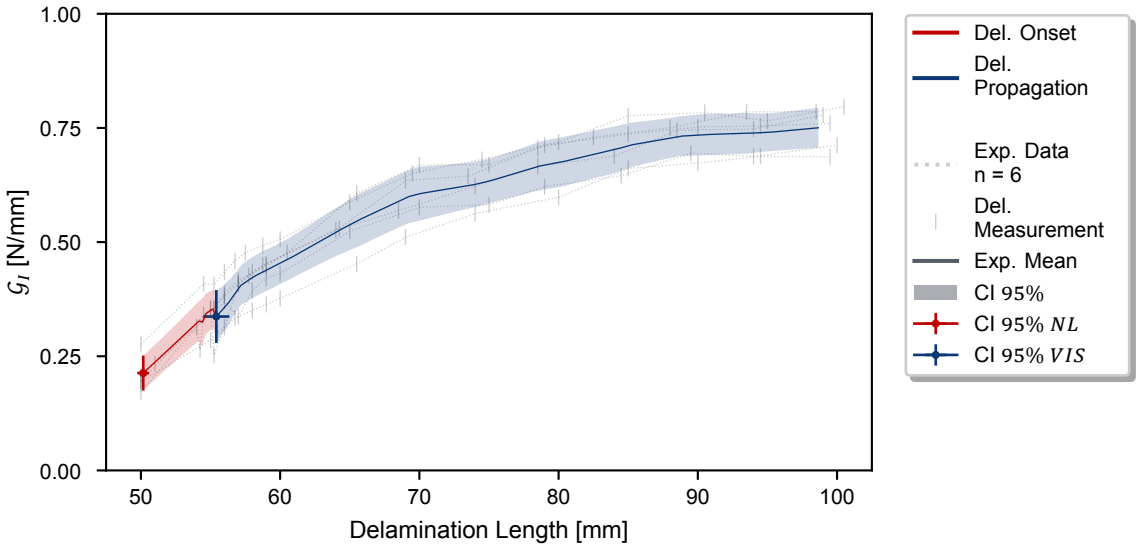
The load increase in load-displacement curves of fig. 6.12a indicates that the resistance towards delamination propagation is higher than the resistance towards delamination onset. Crack growth requires an increasing load, up to a maximum, after which it gradually decreases because of the larger moment arm of the applied force about the delamination front. The slope of the resistance curves depicts this effect in fig. 6.12b, where the early-stage high slope tends to flatten as the delamination propagates. Bridging of fibers because of the unidirectional filament construction justifies such an increase in the fracture toughness measurements, which, indicating a congenital effect to this stacking sequence definition, is not representative of general angle-ply construction. Fiber bridging is illustrated at the delamination front in fig. 6.13 by the trailing fibers that connect each cantilevered beam of the specimen.

6.4.2. Mode II Fracture Toughness

Crack growth tolerance under Mode II loading is measured through an ENF fixture on the specimens reported in section 6.4.1. This test consists of a three-point-bending test on which one of the sides



(a) Load-displacement curve



(b) Mode I fracture resistance curve

Figure 6.12: Results of material characterization for the mode I fracture toughness. Specimens are initially loaded until delamination onset. After unloading, specimens are tested again until full delamination growth takes place

of the specimen contains a crack, hence serving as a delamination initiator. Delamination growth is, overall, not stable in ENF tests, which makes it only feasible to determine the fracture toughness for delamination onset. The calculation is based on a compliance calibration (CC) method; first, the deformational response of the specimen is determined without fracture for various delamination lengths, while, second, the specimen is tested until crack growth.

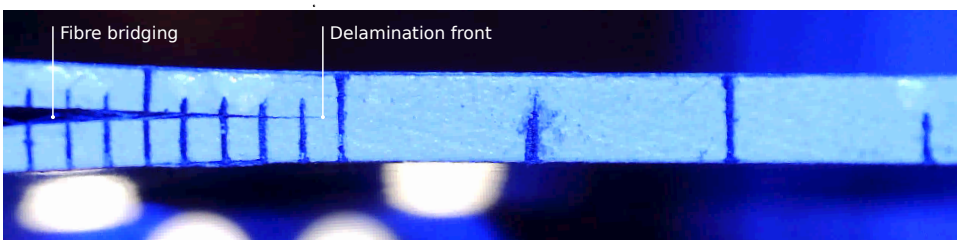


Figure 6.13: Visual determination of DCB test delamination growth

At each delamination length, the specimen is loaded and unloaded elastically to determine its compliance value. Following, a ratio m is obtained from the slope of the compliance points to the delamination length cubed, ultimately allowing to calculate a candidate fracture toughness $\mathcal{G}_Q$ from the maximum load carried by the specimen before fracture P_{max},

$$\mathcal{G}_Q = \frac{3mP_{max}^2 a_0^2}{2b} \tag{6.4}$$

being a_0 is the initial crack length for the fracture test and b is the specimen width. The delamination lengths of the CC method are respectively 20 and 40 mm, where a_0 equals 30 mm. Still, a candidate fracture toughness is accepted only if the portion that is applied during CC loading is between 15 and 35 % of the determined toughness value. This is calculated for each CC test as

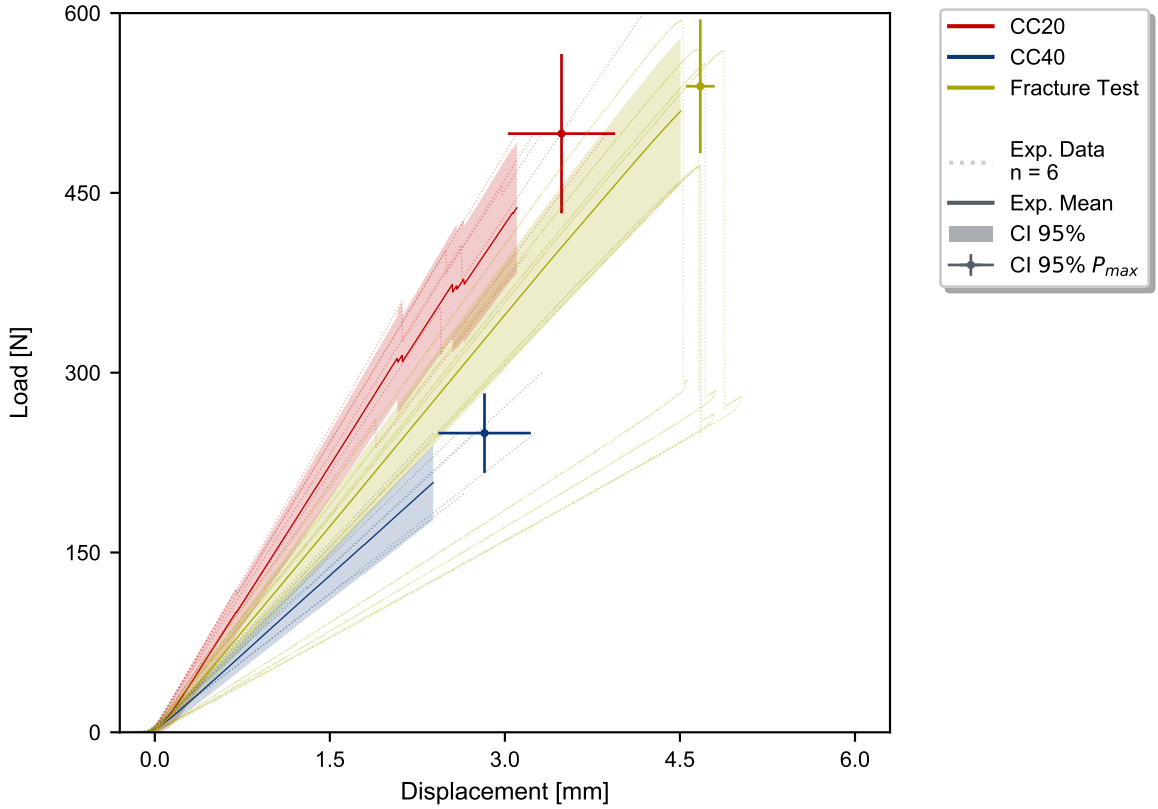
$$\%\mathcal{G}_{Q,j} = \left[\frac{100(P_j a_j)^2}{(P_{max} a_0)^2}\right]; \quad j = 20,\ 40\ mm \tag{6.5}$$

wherein $\%\mathcal{G}_{Q,j}$ are the values of $\mathcal{G}_Q$ associated with the compliance tests, P_j the peak value applied during CC and a_j their corresponding crack length. Testing for fracture toughness consequently requires to estimate the maximum load carried by the specimen upon fracture, so a fraction of it is applied during CC. This causes some of the results to be rendered non-acceptable depending on the initial guess made, and the intrinsic scatter of the material because of its developed bending stiffness.

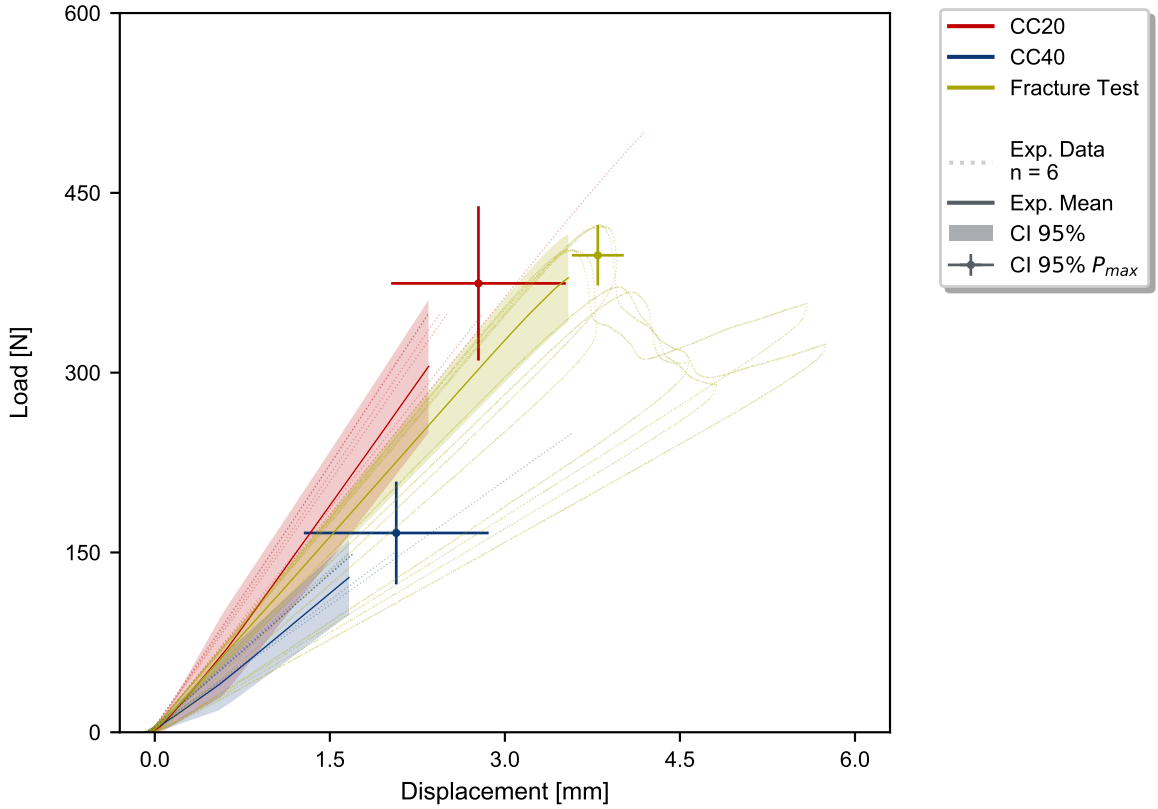
Mode II fracture toughness experiments are carried on the resulting specimens of the DCB testing and denoted as Non-precracked (NC). Then, new experiments are carried upon delamination and denoted as Precracked (PC). The outcome of these are reported in fig. 6.14 along their confidence intervals 95 %. Thus, indicating the load applied during CC and fracture testing, the slope of the compliance curve to the delamination length cubed, the candidate fracture toughness, and whether the test is accepted.

On the one side, the fracture toughness predicted for the NC configuration is higher than for PC, yet a sharp crack already exists in the NC case. This trend suggests that the crack front differs with the loading mode, generating distinct residual plastic strain fields in the matrix constituent ahead. When loaded in a new mode, it appears reasonable that the residual plastic deformation at the crack tip needs to change to a new critical state, It also shows a larger toughness than if a precrack already exists. On the other side, it is noted that the lower the bending stiffness, indicated by the specimen thickness, the larger its compliance, and the lower its maximum load upon fracture. Then, for the results reported, the specimens with the lowest bending stiffness show to lead to unacceptable fracture toughness guesses because of the excessive load applied during CC.

It is observed that the scatter in the NC tests is higher than for the PC cases, considering the variability of results. Consistent with the reasoned crack tip plasticity, switching between the residual form of the DCB experiments to the ENF test, a higher uncertainty exists than for an already existing precrack. Such a discrepancy is also visualized in the load-displacement curves presented in fig. 6.14 for each of the tested configurations. Here, the loading of the CC tests is depicted along with the fracture evaluation in each case, depicting the confidence interval 95 % and the corresponding error bar of the maximum load carried. In the case of the NC configuration in fig. 6.14a, ”jumps” in the load-displacement relation appear during the CC loading, which is then presented as big load drops when fracture is tested. Instead, the loading increase is smooth during calibration of the PC tests in fig. 6.14b, whereas upon delamination onset, a resistance curve comparable to that of gradual crack growth is illustrated.



(a) Non-precracked (NPC) delamination onset. Sudden load drops occur during testing, both during CC and at the onset of delamination



(b) Precracked (PC) delamination onset. A relatively progressive crack propagation occurs upon fracture testing

Figure 6.14: Load-displacement curves for the Mode II fracture toughness determination through the CC method. Specimens are successively loaded for delamination lengths of 20 mm (CC20) and 40 mm (CC40), before eventually tested for fracture.

Table 6.6: Results of the ENF characterization tests for mode II fracture toughness

Spec.	h [mm]	P_{20} [N]	P_{40} [N]	P_{max} [N]	m [N^{-1} mm^{-2}]	$\mathcal{G}_Q$ [N mm^{-1}]	$\%\mathcal{G}_{Q,20}$ [%]	$\%\mathcal{G}_{Q,40}$ [%]	Accepted?
Non-precracked (NC) tests									
1	2.15	400	200	471.62	$9.55 \cdot 10^{-8}$	1.15	32.0	31.9	Yes
2	2.33	600	300	568.64	$7.10 \cdot 10^{-8}$	1.24	49.5	49.4	No
3	2.36	500	250	594.32	$6.13 \cdot 10^{-8}$	1.17	31.4	31.4	Yes
4	2.35	500	250	569.86	$6.72 \cdot 10^{-8}$	1.18	34.2	34.2	Yes
5	2.31	500	250	558.14	$7.89 \cdot 10^{-8}$	1.33	35.6	35.6	No
6	2.21	500	250	472.72	$8.99 \cdot 10^{-8}$	1.08	49.7	49.7	No
Average accepted	2.29 ± 0.08	–	–	545.27 ± 46.58	$7.47 \pm 1.31 \cdot 10^{-8}$	1.16 ± 0.01	32.5 ± 1.0	32.5 ± 1.0	–
Precracked (PC) tests									
1	2.15	500	250	367.36	$1.08 \cdot 10^{-7}$	0.79	82.3	82.3	No
2	2.33	350	150	423.56	$8.01 \cdot 10^{-8}$	0.77	30.3	22.2	Yes
3	2.36	350	150	402.76	$8.67 \cdot 10^{-8}$	0.76	33.5	24.6	Yes
4	2.35	350	150	401.88	$8.24 \cdot 10^{-8}$	0.72	33.7	24.7	Yes
5	2.31	350	150	422.00	$8.23 \cdot 10^{-8}$	0.79	30.5	22.4	Yes
6	2.21	350	150	371.68	$1.05 \cdot 10^{-7}$	0.78	39.4	28.9	No
Average accepted	2.29 ± 0.08	–	–	404.38 ± 10.14	$8.72 \pm 4.85 \cdot 10^{-8}$	0.76 ± 0.01	33.5 ± 1.8	24.6 ± 1.3	–

Spec. – specimen number; h – specimen thickness; P_{20} – peak load during compliance calibration (CC) for a 20 mm delamination; P_{40} – peak load during compliance calibration (CC) for a 40 mm delamination; P_{max} – maximum applied load during fracture test; m – slope of the linear fit of compliance versus crack length cubed data; $\mathcal{G}_Q$ – candidate mode II fracture toughness; $\%\mathcal{G}_{Q,20}$ – percentage of the $\mathcal{G}_Q$ achieved during compliance calibration for a 20 mm delamination; $\%\mathcal{G}_{Q,40}$ – percentage of the $\mathcal{G}_Q$ achieved during compliance calibration for a 40 mm delamination

The sudden load drops during CC loading of the NC specimens can be correlated with marginal delamination increases, albeit not yet depicting fracture. This effect is possibly connected with changes in the plastic strain field of the crack tip, causing small failures in the NC specimens because of the combined mode II loading and the residual strain of the DCB experiments. In the PC tests, no sudden crack growth is reported, which can be argued in the more significant amount of plastic strain that the matrix constituent may develop when subjected to a single loading condition.

6.5. Concluding Remarks

Manufacturing specimens for material characterization is presented as a reasonable approach for describing the material properties of a real CPV based on their convenience for production and testing. In the context of this project, it is carried by winding flat plates that reproduce the manufacturing characteristics of the produced vessels. Unidirectional plates are used for the determination of longitudinal and transverse stiffness and strength, while $\pm$ 45 helically wound ones are deemed better representative of the shear characteristics. Additional unidirectional specimens are manufactured with an insert at their midplane to test fracture toughness in Modes I and II, hence describing the damage progression material characteristics. The specimens considered in the stiffness and strength testing account for various consolidation levels in the manufacturing, thus depicting the influence of porosity and fiber volume content in the characteristics of the material.

Increased porosity values show a general trend in the tested components towards reduced stiffness and strength. This effect appears to follow approximately linear progression in the matrix dominated transverse and shear properties, while this significantly deviates in the case of the longitudinal strength. Such an effect is argued on the fiber breakage clustering with the increased porosity, thus evolving in a non-linear pattern as the amount of cavities increases. Withal, the representativeness of the results is judged critically because of the limitations of coupon testing. The expected stress fields in the specimen are altered because of the existence of free edges, the material damage introduced while cutting, their intrinsic thin ply condition, and the load application through tabs, which deviate from the uninterrupted, thick-walled composite material in the manufactured CPVs. Furthermore, it is not clear

how well the unidirectional material properties characterize the longitudinal and transverse behavior of the interwoven bands in the helical layers. In this case, the material response is also influenced by the amount of resin between bands; it also introduces uncertainty in the robustness of the following numerical modeling.

Concerning the determination of the fracture toughness properties, crack growth is described from the energy they released during delamination onset and propagation. However, these characteristics appear to be only representative of the unidirectional stacking sequences, on which a clear damage propagation direction exists. Consequently, defining fracture toughness values for helically wound layers appears as a matter not adequately tackled. These layers experience transverse cracks in mixed-mode conditions that connect through delaminations, produce band detachment and, overall, arrest damage propagation because of the continuous fiber orientation change. The fracture toughness developed with this ply construction deviates from the unidirectional fiber assumption, also requiring rightful judgment when considered for modeling purposes.

7

Constitutively Elastic Analysis

The constitutively elastic response of CPVs stands as a first approximation to the complex mechanical behavior of these components, permitting to depict particularly well the stress-strain state of the structure at low internal pressure values. With the increased loading, damage is expected to develop, leading to an intrinsically non-elastic constitutive response, thus causing the vessel behavior to deviate from its elastic approximation. Nevertheless, the consideration of elastic material properties is still a meaningful approach at mildly high-pressure values because it permits to identify the sources of material non-linearity when correlated to experimental data. Besides, CPVs are subjected to relatively simple stress states based on the two-fold tensile loading in the meridional and tangential directions; indeed, it simplifies the complexity of the failure modes associated with the loading condition. Its stiffness distribution dominates the deformational attitude of a CPV and, therefore, also are the existing stress and strain fields resulting from the constitutively elastic material.

The objective of this chapter is to show the influence of the stacking sequence on the mechanical response of a CPVs by creating FE models of the adjusted vessel geometries in chapter 5. The mechanical response is analyzed with a focus on the deformational behavior of the dome transition region, the gradient of stress and strain through-the-thickness, and the vessel axial displacement component. Accordingly, results are correlated with experimental data whenever possible, considering the influence of the stacking sequence on the stress state used next in chapter 8 to estimate the burst pressure. To deal with the correlation of experimental and simulation results in a meaningful form, the chapter starts in section 7.1 by presenting the extent to which testing data can be used to validate simulation responses. Following, the construction of the FE model is presented in section 7.2, whereas results for various stacking sequences are depicted and discussed in sections 7.3, 7.4 and 7.6. Correspondingly, the influence of the circumferential ply-drop location on the B* stacking sequence is described in appendix B, whereas in appendix C, is depicted the sensitivity of the FE configuration deformational behavior.

7.1. Introduction to the Correlation of Results

The analysis of CPVs using virtual simulations can only be regarded as a representative description of the real structure behavior after an adequate validation of the assumptions made is presented. The results obtained from FE analyses need to be for that matter, compared with experiments where the fundamental physical characteristics are intrinsically depicted. Moreover, the correlation with analytical solutions can well illustrate the extent to which the analysis methodologies are relevant, while helping to benchmark their computational cost effectiveness.

The correlation of a simulated structural response with physical experiments can be regarded at the different levels of sophistication represented in fig. 7.1, where the most direct comparison can be arguably attributed to the vessel burst pressure. The loading stage at which the tank loses all its load carrying capability is easily identified from pressure tests, whereas it also has a clear significance from a product development perspective. Yet, as burst is the result of a relatively complex damage evolution process, it cannot be straightforwardly identified from a simulation standpoint. In the most fundamental approach, burst is determined by the pressure at which FPF takes place in the fiber direction, justified

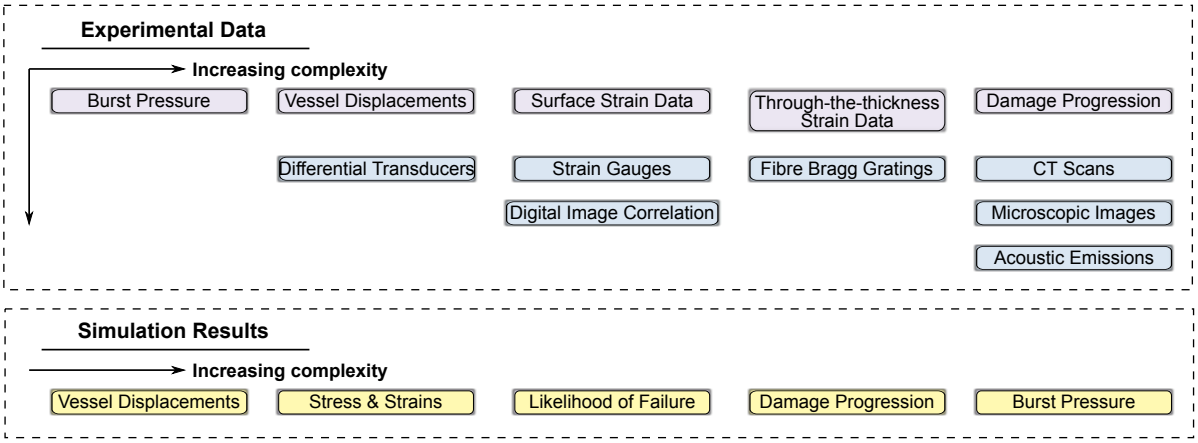


Figure 7.1: Overview of the increased levels of complexity in obtaining experimental data and extracting simulation results

on the sudden collapse failure that composite materials experience in this mode. In a more refined approximation, the increased loading causes gradual degradation of the matrix constituent, hence leading to fiber load redistribution and ultimately, a reduced burst pressure prediction. Correspondingly, the sophistication of the progressive degradation approach can be enhanced by considering the gradual fiber pack breakage that models initial material imperfections, like individual lower fiber strength, dry fibers and initial damages.

Instead, the elastic response of the component is what is most easily identified from a FE analysis results standpoint. This includes the computed elastic stress, strain and displacement under the defined loading conditions, where in the general practice, direct stress measurements cannot be made. Discrete displacement of a tested CPV can be, for instance, retrieved with the use of linear variable differential transducers (LVDTs). These, convert a rectilinear motion into an electrical signal, hence allowing to monitor the axial and radial displacement of the boss and cylinder. Nevertheless, the measured displacement are subjected to the non-linearities of the testing fixture, which can include geometric non-linearities, damage evolution or non-linear contacts. One example of its use is presented in the work of Berro Ramirez et al. [10], who find an initial axial displacement non-linearity because an existing manufacturing gap between the vessel composite reinforcement and the metallic boss.

The validation of the stress-strain fields obtained through simulations can be accomplished by the discrete probing of vessel strain measurements. To this purpose, a well established approach is based on the attachment of strain gauges (SG) on the component surface that, deforming during loading a calibrated resistance, permit to track deformations. The use of these devices is cheap and simple, although the measurements are limited to surface results and their validity diminishes if their installation does not ensure adequate alignment. A rather more sophisticated method is based on fiber bragg gratings (FBGs), that embed glass fibers within the composite material to retrieve discrete through-the-thickness strain values. These fibers determine the location and magnitude of strain components by the modification of an optical fiber light spectrum during local deformation. The use of FBG provides direct strain measurements from the vessel interior, although the controllability of their exact position is limited because of the sensitivity to the vessel manufacturing process. Moreover, the use of FBGs in CPVs can be restricted if the generally existing high fiber stress leads to sensor breakage, as experienced in the work of Kang et al. [110].

Correspondingly, surface strain mappings can be obtained using DIC. This technique requires taking successive images of a tested component, where the tracking of points of a multiscale speckle pattern allows monitoring their relative displacement. The use of DIC allows depicting the deformational response of pressure vessels in a much more comprehensive form than the discrete probing of SG and FBG. Moreover, it can be used to monitor defects of the component like notches or growing delaminations, as it is introduced in the work of Gasior et al. [78] in its application to CPVs. Surface strain mapping permits to detect this type of failures at relatively early load stages, while at the same time recognizing critically stressed areas. In the application of DIC to CPVs, the benchmark speckle pattern used to map the surface strain needs to be additionally triangulated to define the measured field surface projection. This arises from the intrinsically non flat vessel surface and requires a cali-

brated multiple camera setup to determine the geometrical shape on which the correlation is carried. An extension of DIC to bulk volume deformation mappings can be alternatively achieved with the use of so-called digital volume correlation (DVC) techniques, [111]. These, measure deformations of entire component volumes by self-correlating successive CT acquisitions. However, besides showing a high applicability to CPVs because of the monitoring of full strain fields, no implementations have been yet observed at this scale because of the elevated cost and complexity in the setup.

The depiction of damage progression in the vessel can be alternatively accomplished through customary CT scans and microscope images. For instance, the convenient CT image acquisition at different component loading stages permits to identify cracks growth at the micromechanical scale. This growth can be correlated with the results of damage progression analyses to determine the accuracy of the followed material degradation laws. Likewise, as also carried in the work of Harada et al. [75], microscopic observations are a useful complementary tool insofar they are able to illustrate the damage processes involving fiber breakage and fiber-matrix debonding. In terms of full-field mapping damage quantification, AEs analysis are presented by Dahmene et al. [79] to be a viable option based on the sound wave recording of different failure events. In the work of Torres [112], this is applied to causally link the recorded emissions during CPV pressurization to interfiber failure at mild loading stages, while the registered acoustic emission patterns are shown to be additionally correlated before burst with their stacking sequences. Nonetheless, the use of AE in the damage progression prediction of CPVs requires the placement of sound recording devices in a three dimensional array to capture the random localization of the emissions in the circumferential direction. In the case of Daimler AG, this is accomplished by the construction of the dedicated testing chamber depicted in fig. 1.2. This piece of equipment additionally hosts high-resolution cameras that allow the mapping of full vessel surface strain fields, thus achieving a comprehensive experimental characterization of the CPV mechanical response.

Analytical solutions do not fully represent the produced component, but they serve the verification of the physical soundness of simulation results. However, in their application to CPVs, these solutions can only be applied to simplified parts of the structure, like the cylindrical section, thin wall vessel approximations or idealized geometries resulting from the manufacturing process. An example of analytical solution correlation is introduced in the work of Torres [112], where FE analysis results of thin and thick cylinders are validated against three-dimensional elasticity solutions. Correspondingly, the vessel shape induced load distribution can be also be correlated with the internal forces and moments obtained for isotropic, [35] and orthotropic surfaces of revolution, [113]. Concerning the use of composite materials, the use of the CLT also stands as an intermediate step between a fully analytical solution and a FE simulation counterpart.

Ultimately, the correlation between experimental, analytical and numerical results, establish the framework within which the mechanical response of a vessel can be asserted to comply with its requirements. Particularly concerning experimental data, the level of sophistication of the characterization techniques implemented should respond to a robust engineering approach. This entails that tests results compare in complexity with the obtained simulation behavior, therefore, establishing adequate proportionality.

7.2. Definition of the FE Model

The realistic description of the pressure vessel geometry achieved in chapter 5 permits the development of a three-dimensional FE model within the explicit integration tool of Abaqus 2017, [38]. The solution through FE hence allows approximating the deformational and stress state of the component, ranging from its constitutively elastic behavior to the modeling of the damage progression, and the metallic boss component yielding.

The three-dimensional modeling of the vessel is motivated by the thick wall effect in the through-the-thickness distribution of in-plane normal stress. In the dome transition regions and boss ply ends, this is predicted to influence the generation of stress concentrations and, subsequently, the triggering of failure. In this regard, solid geometries are not limited to the Mindlin-Reissner flexural theory enforced in conventional shell elements, limiting initial flat sections to remain flat after deformation. Moreover, the three-dimensional geometry generation permits the reproduction of the interface between subsequently, wound layers and potentially predicts their damage onset. This approach appears to be of interest on the influence of the circumferential ply drop length and taper, where the mechanical response

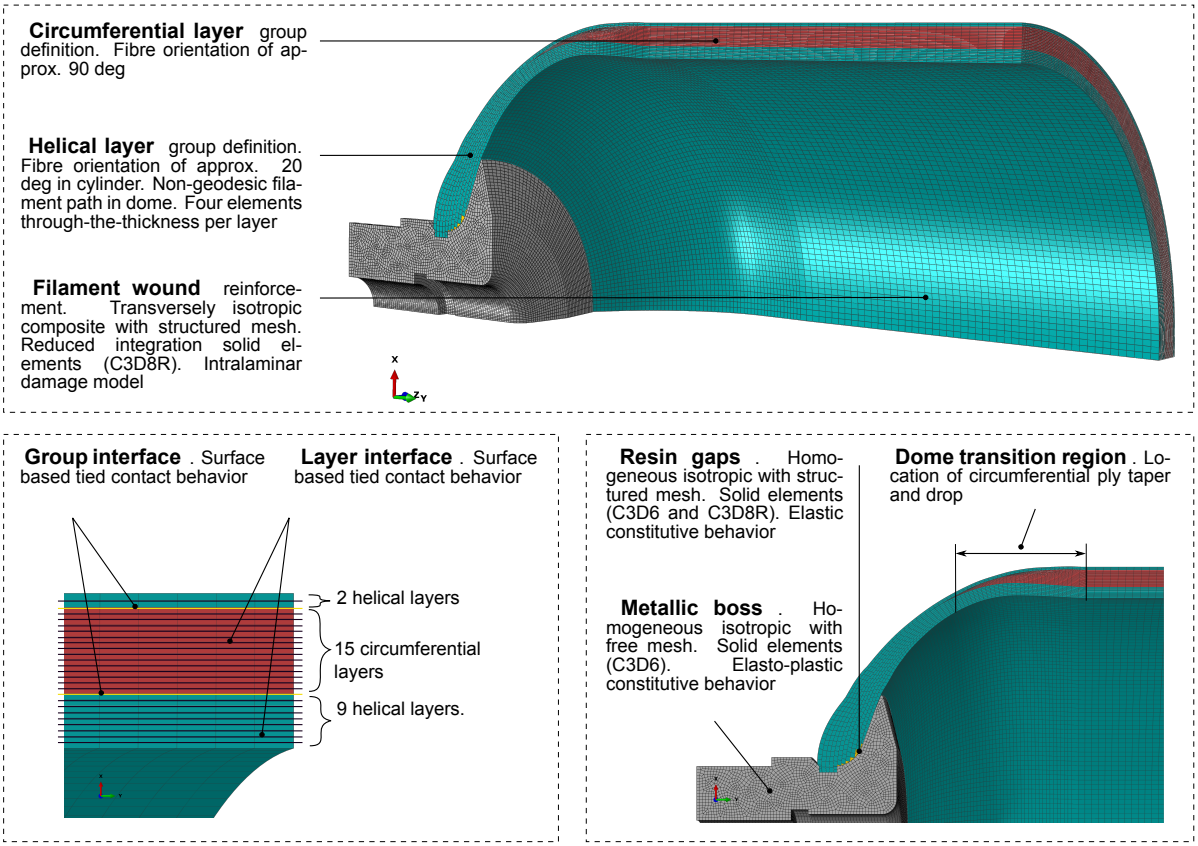


Figure 7.2: Structured FE mesh of the W1A stacking sequence with indication of the material property definitions and the layer types

of a vessel shows a tendency to strip the outer helical plies from their underlying circumferential ones, [12]. A solid geometry definition is also preferred here over axisymmetrical simplifications because of the stiffening effect of the geometrically non-linear deformation in the vessel hoop direction. Its expansion in the tangential direction causes a curvature reduction and a thinning wall thickness, translating into a more relevant membrane response because of the more uniform through-the-thickness hoop stress gradient.

In the course of the analysis of CPVs, an explicit solver choice resides in the convenience of expressing the element kinematics in a corotational system. This approach is favored in light of various non-linear responses, including geometrically non-linear deformations, contact interactions, and, ultimately, damage modeling. A corotational system implies that the state variable tensors rotate with each element local coordinate system, hence avoiding base configuration referencing computations and providing speed advantages. Nevertheless, the conditional stability of the explicit central-difference time integration limits the acceptable analysis time increments to be significantly smaller than their counterparts in implicit tools.

Symmetry conditions are applied to the defined vessel geometry in the three principal planes to limit the size of the model to one eight of the original tank. The configuration of the vessel is then formed by the composite filament-wound reinforcement and the metallic boss, where the plastic liner is not modeled because of its minimal structural strength. Likewise, the composite reinforcement geometry is generated by revolving a vessel cross-section based on the individual ply description retrieved through the geometry adjustment of chapter 5.

The composite reinforcement region, where damage potentially develops, is modeled as in fig. 7.2 with structured meshes within each individual ply. The material used in the filament winding process is a preimpregnated TCR T700/UF3369, whose average material properties are summarized in table 7.1 from the experimental characterization reported in chapter 6. Properties not defined from a characterization campaign are assumed from literature and indicated accordingly. These, are generally derived from unidirectional filament wound plates, where the subscript $\cdot_{fw}$ refers to a characterization based

on specimens with a helical architecture.

The material characteristics presented in table 7.1 compile the elastic, strength, and damage progression characteristics of the material. Therefore, they serve the following discussion concerning the constitutively elastic behavior of the vessels investigated, their failure predictions reported in chapter 8, and the modeling of damage introduced in chapter 9.

Table 7.1: Composite material properties

T700 - UF3369 Composite Reinforcement
Elastic Properties
E_{11} = 135.65 GPa ; E_{22} = 8.03 GPa ; $G_{12,\text{fw}}$ = 4.00 GPa
ν_{12} = 0.34 ; ν_{23} = 0.52[†]
Ply Strengths
X^T = 2524.20 MPa ; Y^T = 31.47 MPa
Y^C = 50.00 / 225.80 MPa[‡]; S^L_{fw} = 49.56 MPa
m = 0.375[*] ; n = 0.75[*]
Fracture Toughness Circumferential Plies
$\mathcal{G}_{1+}$ = 133.3 N/mm[†] ; $\mathcal{G}_{Ic}$ = 0.21 N/mm ; $\mathcal{G}_{IIc}$ = 0.76 N/mm; η = 1.634[†]
Fracture Toughness Helical Plies
$\mathcal{G}_{1+}$ = 133.3 N/mm[†] ; $\mathcal{G}_{Ic}$ = 80.00 N/mm[§]; $\mathcal{G}_{IIc}$ = 160.00 N/mm[§]; η = 1.634[†]
Misc.
ρ = 15.70 KN/m^3 ; μ = 0.3

[†] Assumed from Camanho et al. [114]
[*] Assumed from Dávila et al. [115]
[‡] The value of 50.00 MPa is assumed for the determination of failure in chapter 8 in the absence of further material characterization. The value of 225.80 MPa is obtained from the product supplier and considered in the modeling of damage in chapter 9
[§] Assumed for numerical stability

Values of fracture toughness are defined differently for the circumferential and the helical plies because of their distinct layer architecture. In the case of circumferential winding, the material characterization in unidirectional plates carried in chapter 6 is directly applicable, whereas, in the helical layers, comparatively larger fracture toughness is expected. As a result, arbitrarily high values are defined in the latter to represent the anticipated crack arrest of the interwoven band construction. Furthermore, these high values are expected to limit the numerical instability deriving from the progression of damage in the model by limiting the kinetic energy released during fracture.

Concerning the numerical formulation, solid three-dimensional reduced integration (C3D8R) is selected. The choice of reduced-integration solid elements resides in their computational tractability against fully integrated counterparts. At the same time, they still retrieve complete stress tensors that reproduce the coupled interaction in all principal element directions. Considering single integration point elements also facilitates the following implementation of damage progression models, where the stiffness degradation is specified unequivocally per element integration point.

Nevertheless, reduced-integration solid elements are limited in reproducing bending responses because of their lack of stiffness in these modes. Considering this effect demands a sufficient refinement of the mesh, both in-plane and through-the-thickness, that allows the normal stress gradient and the corresponding section warp during deformation. Stacking a high number of solid elements through-the-thickness also makes them prone to develop zero energy hourglass deformation modes, further encouraged by the stiffness change between circumferential and helical plies. Hence, controlling this spurious effect requires the provision of arbitrary artificial stiffness factors in the modes in which hourglass deform, while also considering a mild value of viscous damping during loading.

Another limitation of the solid element usage is that moderately high aspect ratio in the thickness direction is needed to lessen computational cost, which also locally challenge the numerical regularity of the solution. Mass scaling factors need to be prescribed to counteract the unmanageable low, stable increments resulting from relatively thin ply definitions. In the current case, these are assigned according to a variable description until stable increments in the order of $1 \cdot 10^{-7}$ s are reached.

The representation of the helical layers interwoven $[+\alpha/-\alpha]$ structure is achieved with the stacking, within each ply, of $[+\alpha/-\alpha/-\alpha/+\alpha]$ subplies. This inverted orientation configuration effectively elim-

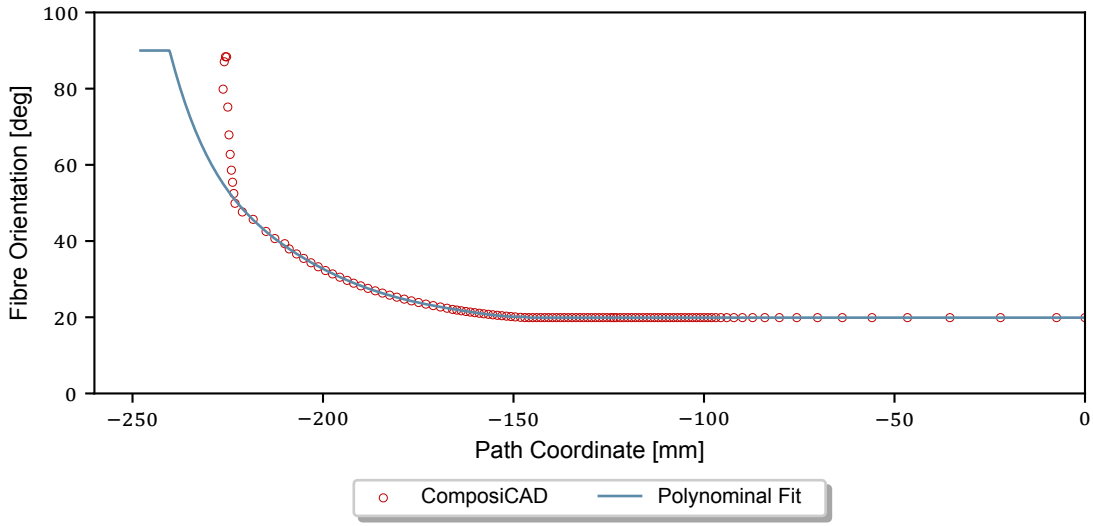


Figure 7.3: Comparison of the interpolated fiber orientation distribution with the ComposiCAD™ prediction for the outermost helical ply of the W1A stacking sequence

inates the shear-extensional coupling of ply mechanical response, while keeping the bending-twisting interaction about two orders of magnitude below the bending response. As indicated in fig. 7.2, the mesh is divided for every helical layer in four elements through-the-thickness that allow the assignment of the ply orientations and the modeling of a realistic mechanical response. Correspondingly, the different filament orientation described by the non-geodesic dome path generation of ComposiCAD™, is reproduced by the definition of custom local orientations at every element. The fiber orientation at each ply calculated by the filament winding software is interpolated to the element coordinates to generate a variable orientation profile like the one shown in fig. 7.3. At the ply boss ends, where the thickness definition of the filament winding software is inaccurate, the fiber orientations are extrapolated following a least-squares polynomial fit of sixth grade:

$$p(x) = p_0 + p_1 \times x + \cdots + p_k \times x^k \tag{7.1}$$

being $p(x)$ the fiber orientation angle approximation of k^{th} order for the vessel contour coordinate x and p_k the parameters of the fit. This coordinate is calculated by the arc length of the ply meridional cross-section path to establish a direct correlation between each axial and radial coordinate pair with their matching fiber angle. The result of the variable layer orientation definition is illustrated in the ply dome filament paths of fig. 7.4, where the mirrored patterns of each helical subply are presented.

Table 7.2: Resin constituent and metallic boss material properties

UF3369 Resin
Elastic Properties E = 2.83 GPa ; G = 1.05 GPa ; ν = 0.35
Misc. ρ = 11.80 KN/m^3 ; μ = 0.3
Al-6061-T6 Aluminum
Elastic Properties E = 68.90 GPa ; G = 25.94 GPa ; ν = 0.33
Plasticity Properties σ_y = 241.30 MPa ; σ_u = 290.00 MPa ; $\epsilon_{p,u}$ = 0.12
Misc. ρ = 27.00 KN/m^3 ; μ = 0.3

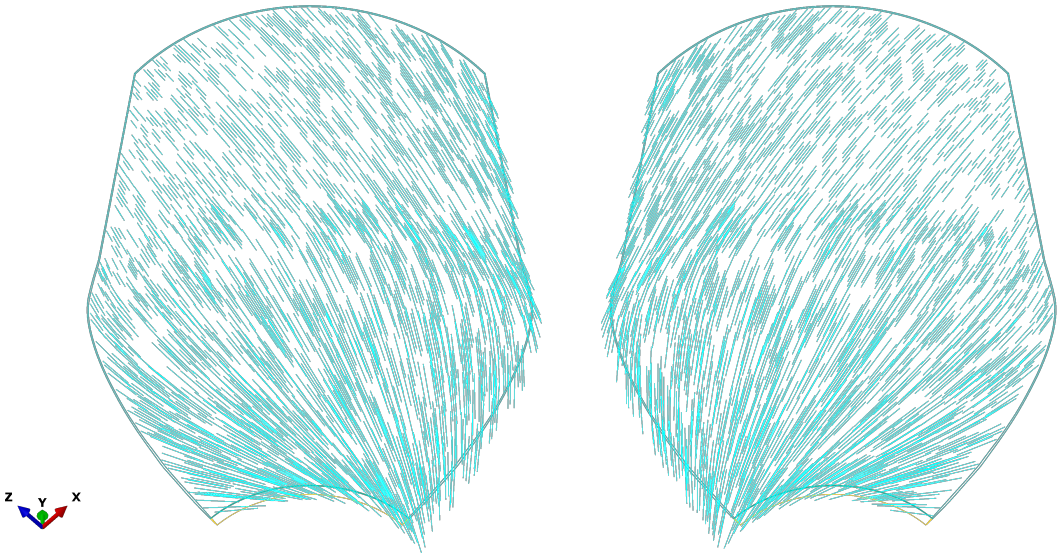


Figure 7.4: Positive and negative variable fiber orientation descriptions in the dome region of the W1A stacking sequence

Resin-rich gaps indicated in fig. 7.2 are detailed in the boss dome end, where the blunt composite layer drop fails to meet the matching geometry. Solid elements with reduced integration (C3D6R and C3D8R) are used in these regions, where the properties presented in table 7.2 are assumed from the product supplier to be purely elastic, isotropic and homogeneous. In a like manner, the metallic boss is allowed a free solid element mesh (C3D8R) with a typical elastoplastic constitutive behavior of an Al-6061-T6. The corresponding non-linear stress-strain curve is defined from the Military Handbook, [116], and the relevant material properties summarized in table 7.2.

A smooth amplitude curve definition achieves the load application on the exposed internal faces in the boss and the laminate up to an internal pressure state of 160 MPa. However, the hydrostatic pressure is reduced to 50 % in the inner boss conduit influenced by the liner fitting. Then, the outer boss conduit section is loaded as in fig. 7.5 with an outwards surface traction of 15 % magnitude of the applied pressure to represent the shear thread loading of the boss lock.

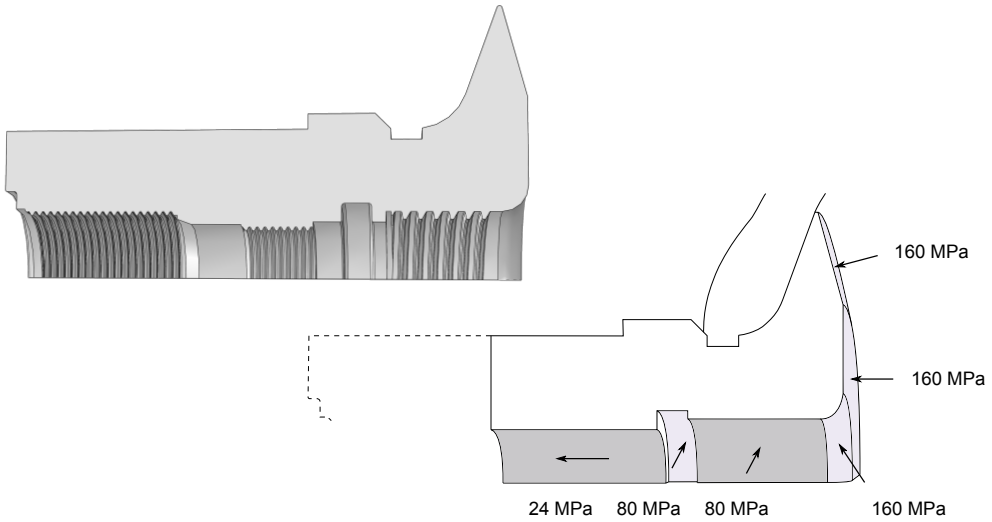


Figure 7.5: Original boss geometry and the simplified diagram with indication of the load application magnitude

Overall the model holds 900 450 C3D8R and 540 C3D6R elements, with a total number of variables of 3 659 214. The average composite reinforcement element has a length of 1.28 mm, and a

thicknesses of 0.12 mm and 0.83 mm for helical and circumferential layers, Simulations take approximately 1.5 h in an Intel Xeon CPU E5-2667 v3 28-core computing nodes under constitutively elastic assumptions, which increases to 40 h considering the damage progression modeling in chapter 9.

7.3. Results and Discussion of the Dome Transition Region Behavior

The directional distribution of stiffness in a vessel effectively influences the stress generated under the applied load, therefore controlling the deformational response of the structure and its likelihood of failure. Composite stacking sequences permit the tailoring of the meridional and tangential stiffness components, through-the-thickness, and along the axial direction of the vessel. This stiffness distribution stimulates the definition of advantageous load distribution schemes on top of their corresponding homogeneous material response, hence potentially improving the general vessel performance. Thus, the load pattern is influenced first by the geometrical configuration and, subsequently, by the stiffness changes introduced by the vessel architecture. The impact of these in the mechanical response is twofold: on the one hand, meridional and tangential strain gradients appear in the dome and dome transition regions because of the curvature and internal pressure component change; while on the other hand, the stress in the tangential and radial directions vary due to the thick wall condition of the vessel shape.

The balance between meridional and tangential stiffness is characterized by the relative tangential expansion in the cylinder and dome regions and the global vessel axial displacement. This stiffness transition is carried from the cylinder to the dome pole as, accordingly, the pressure loading switches from tangential to meridional dominated. Overall, stiffness variability is introduced by the drop of plies, which resulting from the sudden difference in material properties, also lead to stress concentrations that impact the eventual damage onset prediction. Concerning the uncluttered stacking sequence definition of the W1A, E+, and B* vessels, this effect is related to the tapering length in the transition between cylinder and dome. These vessels feature full stacks of low angle helical and circumferential layers, hence endorsing a foreseeable composite behavior and permitting to assess the extent to which an equivalent homogeneous orthotropic solution can be altered.

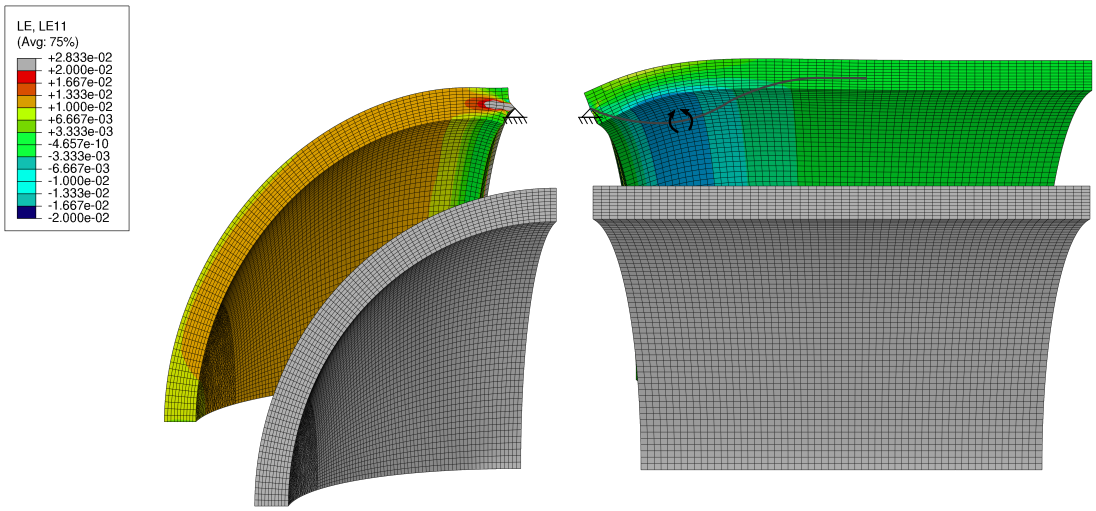
7.3.1. Prediction on the Behavior of a Homogeneous Orthotropic Vessel

In the first place, assimilating the mechanical response of a CPV to that of an orthotropic vessel illustrates the influence of comparable meridional and tangential stiffness definitions on the dome transition region. The meridional bending distribution conveniently depicts this response because it represents both the relative component tangential expansion and the generated through-the-thickness stress gradients. In fig. 7.6, the meridional strain field of a homogeneous orthotropic vessel is depicted at an internal load pressure of 160 MPa, where its equivalent engineering constants are derived from the material properties in table 7.1 and the stacking sequence definitions of table 5.1.

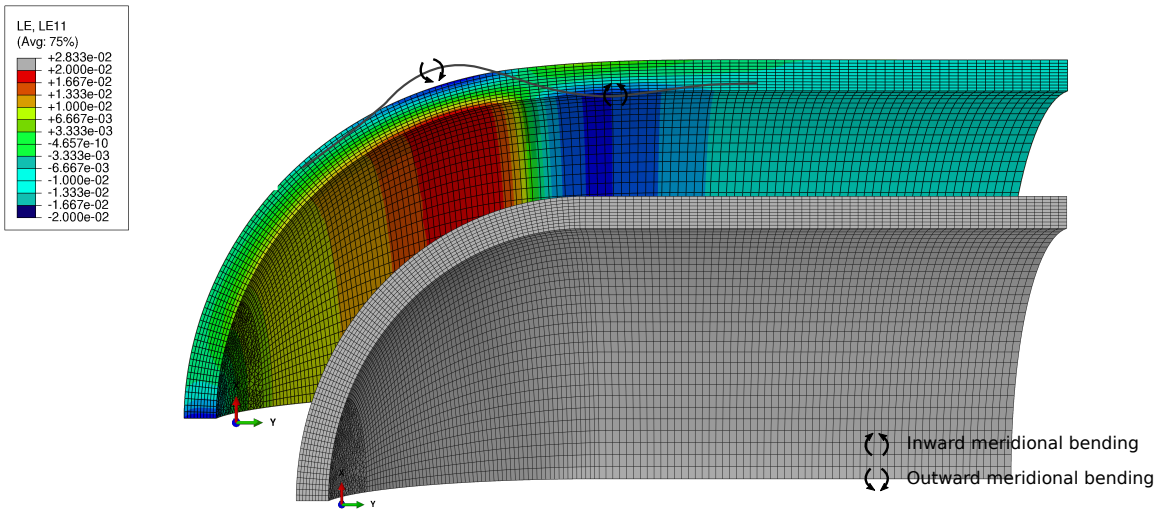
The mechanical response of an orthotropic vessel is comparatively presented for a detached dome and cylinder in fig. 7.6a and the full component in fig. 7.6b, being the detached interaction face assumed as simply supported. It is observed in fig. 7.6a that a simply supported ellipsoidal dome subjected to internal pressure expands as a membrane and rotates at its support with a negative slope, without generating any relevant meridional bending. On the contrary, the cylinder expands and rotates with a positive slope because of its edge radial displacement restraint, spawning inward meridional bending to match the unconstrained tangential expansion at a distance from the boundary condition. This tendency of the cylinder deformation is reproduced in the full orthotropic vessel of fig. 7.6b, where the axial expansion of the component induces a radial displacement restraint in the dome transition; as a result, also developing inward bending in the cylinder thereby. However, the opposite meridional deformation slopes of dome and cylinder still need to be assimilated into a matching shape that evolves in the outward bending of the dome transition region.

7.3.2. Prediction on the Deformed Shapes of the W1A, E+ and B* Stacking Sequences

Hereafter, the homogeneous orthotropic deformational behavior is altered by the stacking sequence definition of the W1A, E+, and B* vessels, whose corresponding deformed shapes are presented in



(a) Detached dome and cylinder with a simple support at the face of their connection



(b) Full homogeneous orthotropic vessel

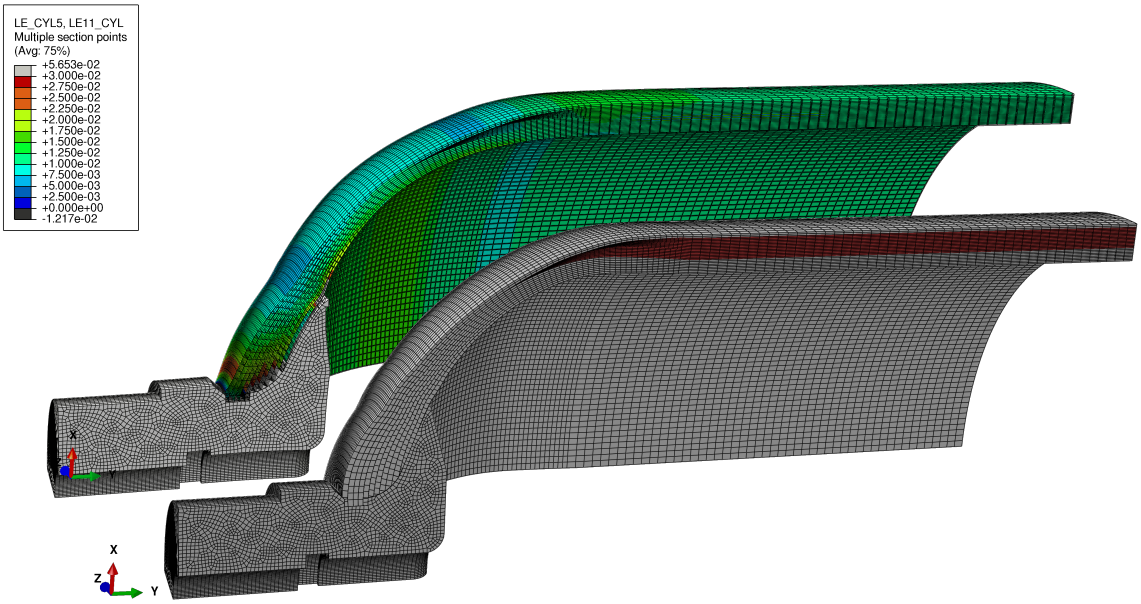
Figure 7.6: Deformed shape and meridional strain field of a homogeneous orthotropic vessel at a load pressure of 160 MPa. The deformed shape (colored) is presented against its undeformed configuration (gray). The successive inward and outward meridional bending in the dome transition region is indicated by the corresponding moment arrows

fig. 7.7. These depict their meridional strain field at a load pressure of 160 MPa and compare their original and deformed configurations. In these cases, the axial position where the circumferential ply stack is dropped appears as a function of the through-the-thickness location and directly correlates with the stacking sequence definition. It appears like the change of stiffness through the dome transition region is not only influenced by the group tapering slope, but also by how far into the dome do the stacks of hoop plies get. As already presented in fig. 5.7, the stack length of circumferential layers is dependent on their thickness position. The initial winding of low angle helical layers causes a liner shortening, shifting the relative position of the circumferential ply drop toward the dome. Additionally, the circumferential group is less constrained as it is placed toward the outside, which also permits the ply readjustment during curing. As a result, the W1A layup shows a group length 5 to 10 mm larger on each dome than the B* case.

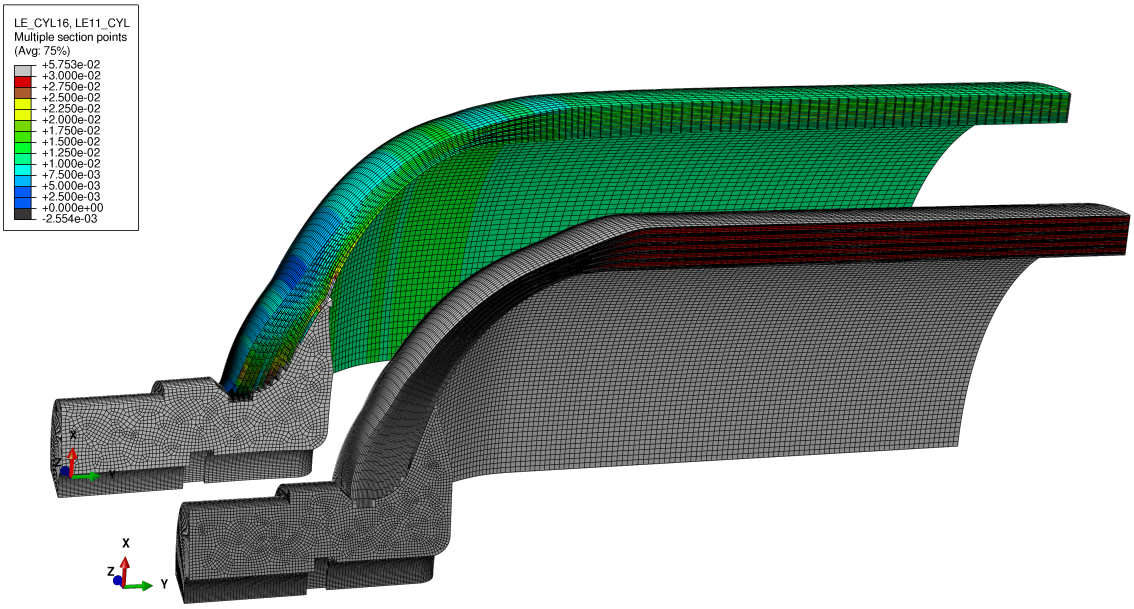
The extensive circumferential stack length of the W1A stacking sequence ensures a balanced meridional and tangential stiffness distribution in the dome transition region. This pattern generally constrains tangential expansion in the dome transition region and ultimately makes its deformed shape

in fig. 7.7a comparable to that of the orthotropic vessel in fig. 7.6. In this regard, the cylindrical region experiences inward meridional bending nearby the dome transition, resulting from the radial constraint imposed by the dome deformation in the cylinder end. Accordingly, outward meridional bending appears further into the dome, along with the circumferential stack tapering. This meridional bending takes place in sight of the considerable tangential stiffness of the remaining circumferential layers, and the necessity of matching the naturally opposing meridional deformation slopes of dome and cylinder.

With the circumferential ply drop end, the tangential stiffness in the dome plunges, allowing a swelling shape to develop in the lower quarter until the dome meets the aluminum boss. Here, the

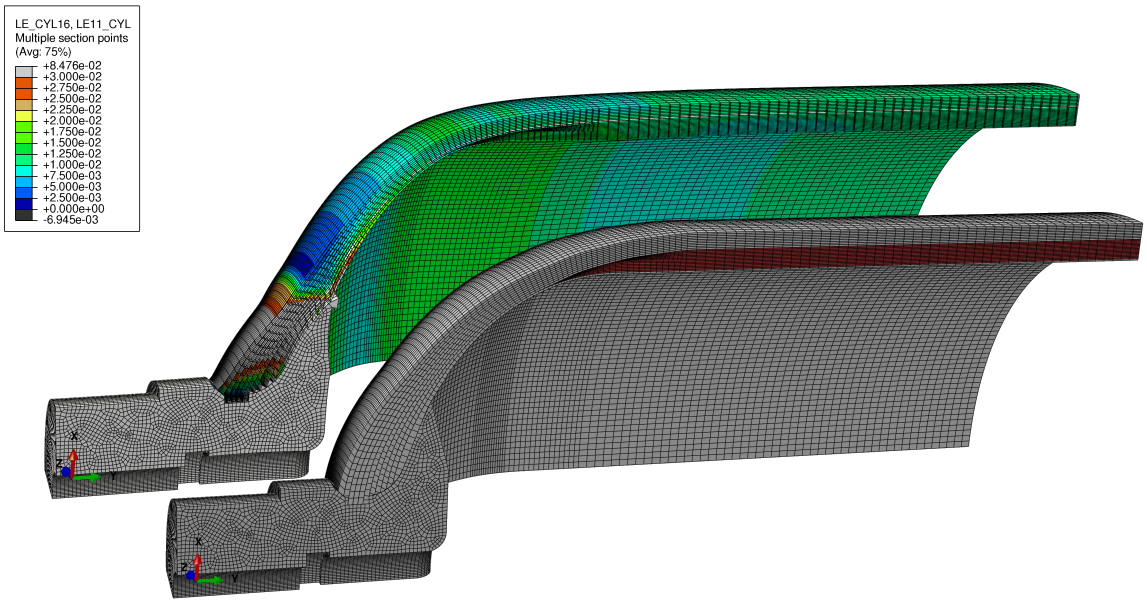


(a) W1A stacking sequence



(b) E+ stacking sequence

Figure 7.7: Deformed shape and meridional strain field of the W1A, E+ and B* stacking sequences at a load pressure of 160 MPa. The deformed shape (colored) is presented against its undeformed configuration (gray), where the circumferential ply stack is also indicated (red)



(c) B* stacking sequence

Figure 7.7: Deformed shape and meridional strain field of the W1A, E+ and B* stacking sequences at a load pressure of 160 MPa. The deformed shape (colored) is presented against its undeformed configuration (gray), where the circumferential ply stack is also indicated (red) (cont.)

bonded interaction between composite reinforcement and boss fundamentally alters the loading condition, ultimately turning it into the through-the-thickness shear. Withal, the meridional bending behavior of the W1A layup appears to be strengthened by the resulting extensional-bending coupling of the bottom helical layer stack. The axial load carried to maintain equilibrium between the two domes generates outward bending in the composite that adds to the outward meridional bending existing in the dome transition region. This deformation tendency further restrains the tangential expansion through the circumferential ply drop and supplement the radial constraint experienced by the end of the cylindrical region. Therefore, besides the layup also inducing outward meridional bending in the cylinder, its effect appears to be counteracted by the geometrically hampered tangential expansion.

On the contrary, the relatively early circumferential ply drop of the E+ and B* stacking sequences are presented in figs. 7.7b and 7.7c to a allow a relatively seizable tangential expansion of their dome transition regions. This effect is more significant for the B* layup than for the E+ vessel, considering a bulge appears to form ahead of the circumferential ply drop, where the helical layers depict a low angle orientation. Such a localized tangential expansion deviates from the orthotropic vessel response in fig. 7.6 and shows to rule the corresponding deformational behavior in the cylinder and the lower dome quarter regions. About the first, the bulge growth generates an expansive radial loading in the cylinder, which is inherently stiffer in the hoop direction. This cylinder edge loading creates outward meridional bending in the cylinder region next to the dome transition and, ultimately, turns into inward meridional bending within the bulge. Concerning the second, the tangential expansion experienced by the bulge generates a tensioning effect in the lower region of the dome, which, as a result, also effectively prevents swelling from developing in this region.

In the case of the B* layup, the extensional-bending coupling of the top helical layer stack appears to uphold the meridional bending behavior in a like manner to the W1A vessel. The axial load carried by these plies generates inward meridional bending that bolsters the formation of the bulge, therefore also promoting additional outer radial displacement of the cylinder edge. The stacking sequence also induces inward meridional bending in the cylinder, although this effect shows to be overridden due to the opposite cylinder edge expansion. Contrarily, the E+ configuration portrays an almost balanced stacking sequence definition that prevents the generation of extensional-bending effects. This behavior promotes the bulge growth to be less substantial than in the B* definition, consequently making the E+ configuration behavior dominated by the tangential expansion in the cylindrical region.

7.3.3. Prediction on the Outer Surface Strain of the W1A, E+ and B* Stacking Sequences

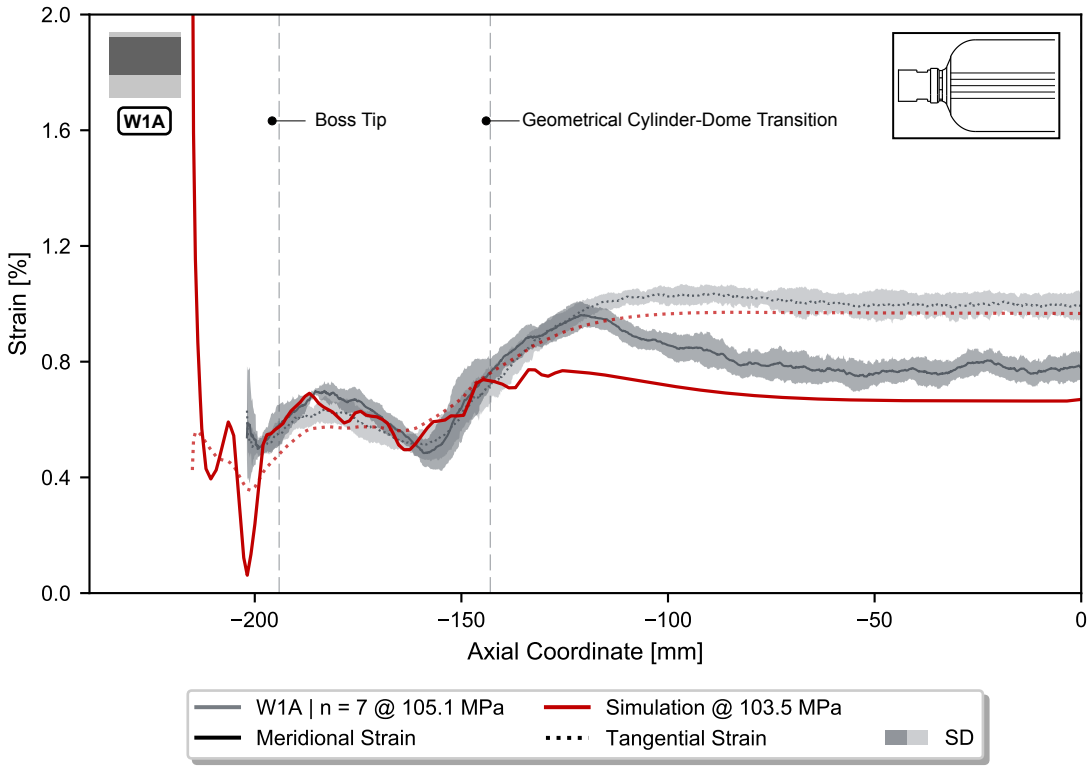
The dome transition region responses of the W1A, E+, and B* layups are also visualized through the outer surface variation along a vessel meridional path in fig. 7.8. In order to quantitatively assess the validity of the simulation results, the computed meridional and tangential strain components are comparatively reported against strain fields recorded during vessel pressurization using DIC. The mean response and the standard deviation illustrates the experimental data for the available stacking sequence sets, hence providing a measure of their corresponding scatter. Strain results are depicted at a pressure stage of 103.5 MPa for the W1A and E+ stacking sequences, that approximately corresponds with 125 % NWP. Likewise, this pressure stage is slightly lower in the case of B* because of its lower strength and limited to their average burst pressure. These constitute load states sufficiently elevated to illustrate the mechanical response of the vessel throughout its working conditions. At the same time, the likely existence of intralaminar damage also permits the evaluation of the magnitude of the disparity introduced relative to the constitutively elastic solution.

The outer surface strain variation of the W1A stacking sequence is depicted in fig. 7.8a, where the meridional bending response identified from its deformed shape is observed accordingly. Its behavior is represented by a local maximum of the meridional strain component at the end of the cylindrical region, followed by a local minimum right after the dome transition. The swelling shape in the dome is depicted next by a local maximum of less entity, which ultimately leads to a significant peak of the meridional strain at the boss location. This spike results from the tendency of the composite reinforcement to debond from the metallic boss and is unrealistic in the sense that cracks would develop locally to match the relative displacement difference. The gradual change of tangential stiffness existing in the dome transition region is described by the progressive reduction of tangential strain throughout. Nevertheless, this tangential strain reduction is halted after the circumferential ply drop because of the expansion in the swelled region of the lower quarter of the dome.

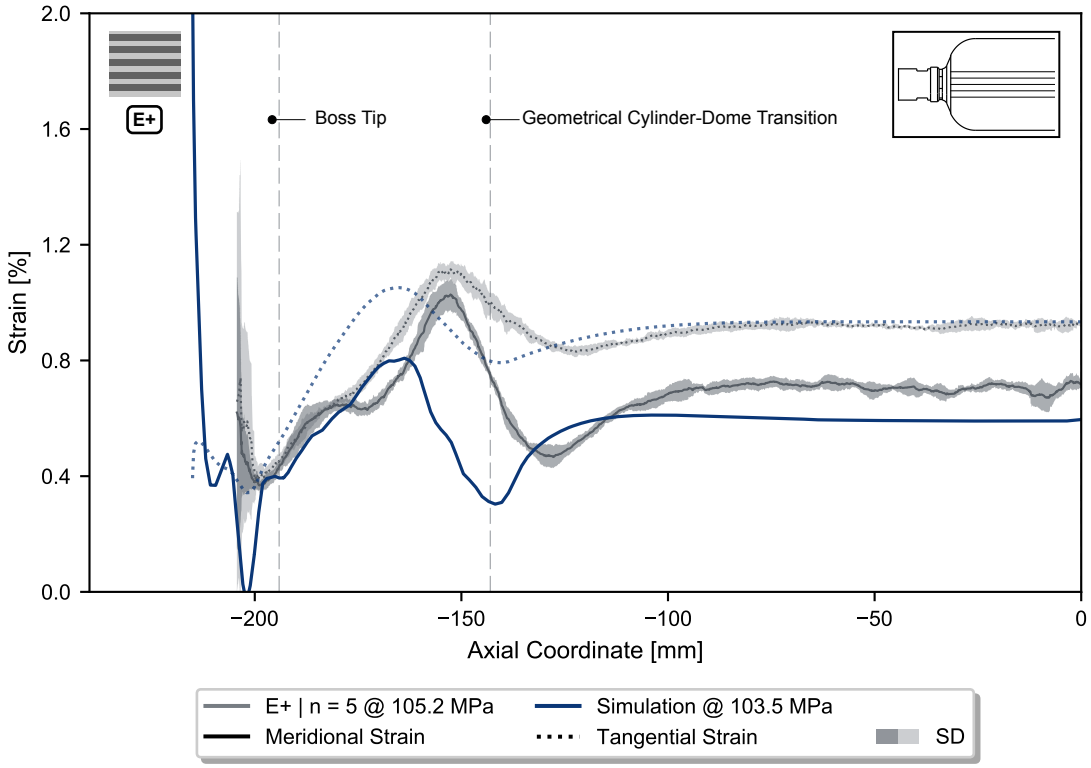
Overall, the presented results agree with the experimental data in their general trend and the magnitude of the tangential strain, whereas the meridional strain result appears to be underestimated in the cylindrical and dome transition regions. This effect is deemed reasonable due to the expected matrix damage, increasing the material compliance because of meridional loading while the fiber controlled tangential expansion maintains an elastic response until collapse. The discrepancy between experimental and simulation results is reported at various loading stages in table 7.3, where the meridional strain mismatch shows to be comparatively higher than the tangential strain result. A general trend towards an increasing relative mismatch with the higher loading is not observed from the maximum strain results, likely influenced by the load redistribution induced with the development of damage.

In the case of the E+ and B* layups, the formation of a bulge in the dome transition region is depicted in the outer surface strain components of figs. 7.8b and 7.8c where, in terms of meridional strain, the pattern identified in their deformed shapes is represented by the successive local minimum and local maximum in the cylinder and dome transition regions. These local meridional strain maximums coincide with the high curvature of the existing bulge that, likewise, is characterized by a significant local increase in the tangential strain. An unrealistic peak in the meridional strain component ultimately appears in the dome end next to the boss, which is assimilated to the tendency of the composite reinforcement to debond from the boss. The correlation with experimental data of the E+ and B* layup simulation results show good agreement in depicting the general deformational behavior. However, both results underestimate the meridional strain component in the cylinder and dome transition region. Likewise, the peak expansion of their bulge formation appears to be shifted towards the dome pole.

The trend in the meridional strain of the E+ and B* stacking sequences agrees with the observations in the W1A case. The lack of matrix damage in the simulation restrains the material transverse deformation, correspondingly influencing the matrix dominated meridional strain result. Its behavior is detailed in table 7.3, by showing that the meridional strain discrepancy outnumbers the mismatch of the tangential component results. Concerning the discrepancy in the location of the bulge apex, a strong relationship is anticipated with the circumferential stack end location and the group tapering slope. Minor differences in the geometry of this region imply relevant changes to the rapidly changing tangential stiffness, thus determining the magnitude of the observed swelling. Detailed identification of any discrepancies in this region requires experimentally portraying the extent of these layer groups, which was not yet possible at the moment of this work.

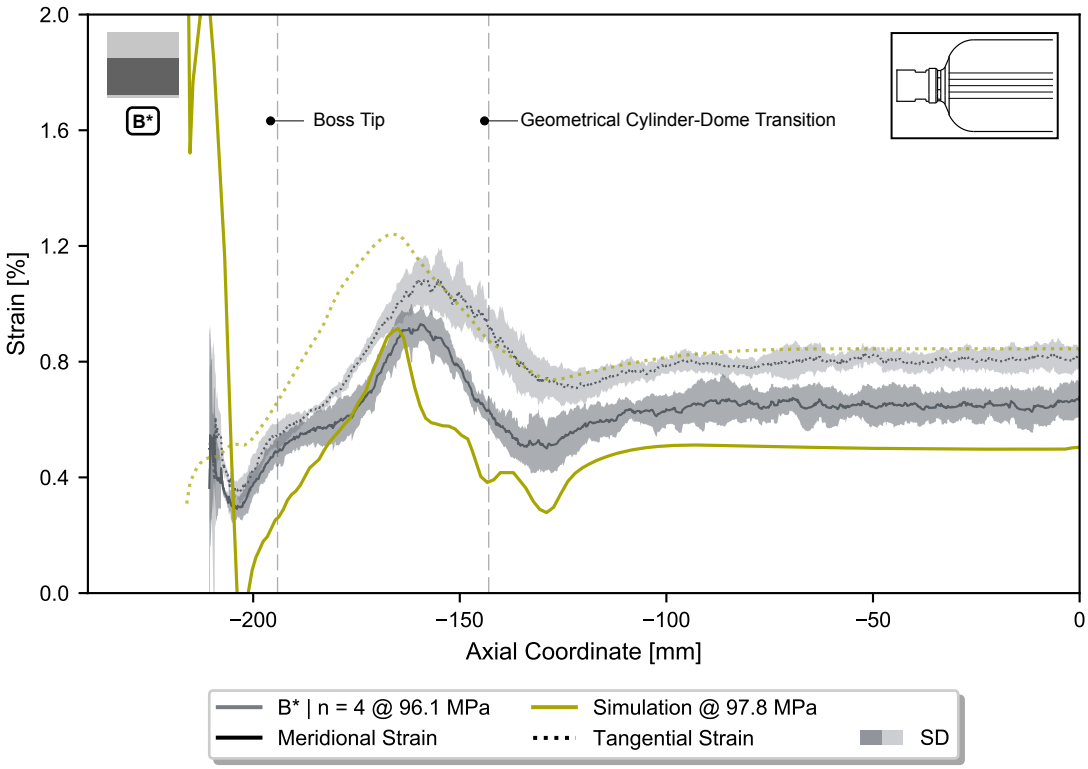


(a) W1A stacking sequence



(b) E+ stacking sequence

Figure 7.8: Comparison of the outer surface meridional and tangential strain of the W1A, E+ and B* stacking sequences at an approximate load pressure of 103.5 MPa. Numerical predictions are presented against average experimental results for a number of samples n, where their scatter is indicated by their standard deviation (SD)



(c) B* stacking sequence

Figure 7.8: Comparison of the outer surface meridional and tangential strain of the W1A, E+ and B* stacking sequences at an approximate load pressure of 103.5 MPa. Numerical predictions are presented against average experimental results for a number of samples n, where their scatter is indicated by their standard deviation (SD) (cont.)

7.4. Results and Discussion of the Through-the-Thickness Response along a Meridional Path

Analyzing the in-plane strain fields of the W1A, E+, and B* stacking sequences through-the-thickness further illustrates the stiffness induced load distribution in these configurations. It permits to identify the loading conditions in each of the distinct layer groups and, following, support the discussion on failure prediction in chapter 8. Through-the-thickness strain results mainly depict the meridional bending experienced in the vessel dome transition region, whereas they also illustrate the impact of a bulge formation in the circumferential layer stack.

The through-the-thickness meridional and tangential strain components along meridional paths are alternatively presented for the W1A, E+ and B* layups in figs. 7.9 to 7.11, where results are depicted at approximate load pressures of 103.5 MPa to complement the discussion of fig. 7.8. Simulation results are presented additionally against the experimental average outer surface strain obtained using DIC, thus also permitting to frame the extent to which these correlate with real vessel behavior.

7.4.1. Prediction on the W1A Stacking Sequence

The meridional strain of the W1A stacking sequence is depicted in fig. 7.9a, where, as previously discussed in section 7.3, there is a change in the meridional bending component. It varies toward the dome in the form of inward bending in the cylinder and outward bending in the dome transition. Furthermore, there are at least two additional aspects that can be derived from the through-the-thickness strain response. First, the meridional strain is substantially constant in the cylinder away from the dome transition, as it results from the axial load equilibrium between the two domes.

Then, despite the layup experiencing extensional-bending coupling, no through-the-thickness meridional strain gradient develops because of the material and loading axial symmetry of the cylinder. Sec-

Table 7.3: Results of the maximum meridional and tangential strain

Stack.	Pressure [MPa]		Max. Mer. Strain [%]				Max. Tan. Strain [%]			
	Exper.	Simul.	Exper.	Simul.	Diff.	Diff. (%)	Exper.	Simul.	Diff.	Diff. (%)
	34.6	35.1	0.37 ± 0.02	0.27	−0.10	−27.34	0.36 ± 0.02	0.33	−0.04	−11.02
	69.9	71.0	0.68 ± 0.02	0.53	−0.14	−21.15	0.70 ± 0.02	0.67	−0.03	−5.00
W1A	105.1	103.5	0.96 ± 0.05	0.77	−0.19	−19.66	1.04 ± 0.03	0.98	−0.06	−6.25
	140.0	140.0	1.22 ± 0.05	1.03	−0.19	−15.43	1.36 ± 0.04	1.32	−0.04	−2.79
	155.6	160.0	1.28 ± 0.05	1.17	−0.10	−8.02	1.47 ± 0.08	1.52	0.05	3.20
	35.2	35.1	0.35 ± 0.02	0.28	−0.06	−18.29	0.39 ± 0.04	0.37	−0.02	−6.15
	70.4	71.0	0.71 ± 0.03	0.57	−0.14	−20.07	0.71 ± 0.03	0.73	0.02	2.31
E+	105.1	103.5	1.03 ± 0.05	0.81	−0.22	−21.42	1.12 ± 0.03	1.05	−0.06	−5.69
	140.3	140.0	1.33 ± 0.05	1.06	−0.27	−20.26	1.48 ± 0.04	1.42	−0.06	−4.37
	154.1	160.0	1.39 ± 0.03	1.20	−0.19	−13.72	1.56 ± 0.04	1.63	0.06	3.95
	34.6	35.1	0.33 ± 0.01	0.35	0.03	7.78	0.35 ± 0.01	0.46	0.10	31.14
B*	69.8	71.0	0.67 ± 0.03	0.68	−0.01	−1.45	0.76 ± 0.06	0.91	0.14	18.62
	96.1	97.8	0.93 ± 0.06	0.91	−0.01	−1.69	1.08 ± 0.08	1.24	0.16	14.70

Stack. – stacking sequence; Max. Mer. Strain – maximum meridional strain; Max. Tan. Strain – maximum tangential strain; Exper. – Experimental data; Simul. – Simulation results; Diff. – absolute difference between Experimental data and Simulation results Diff. (%) – percentual difference between Experimental and Simulation results

Note 1: The pressure stages at which Experimental and Simulation results are presented slightly differs because of the unequal frequencies of the recording of results

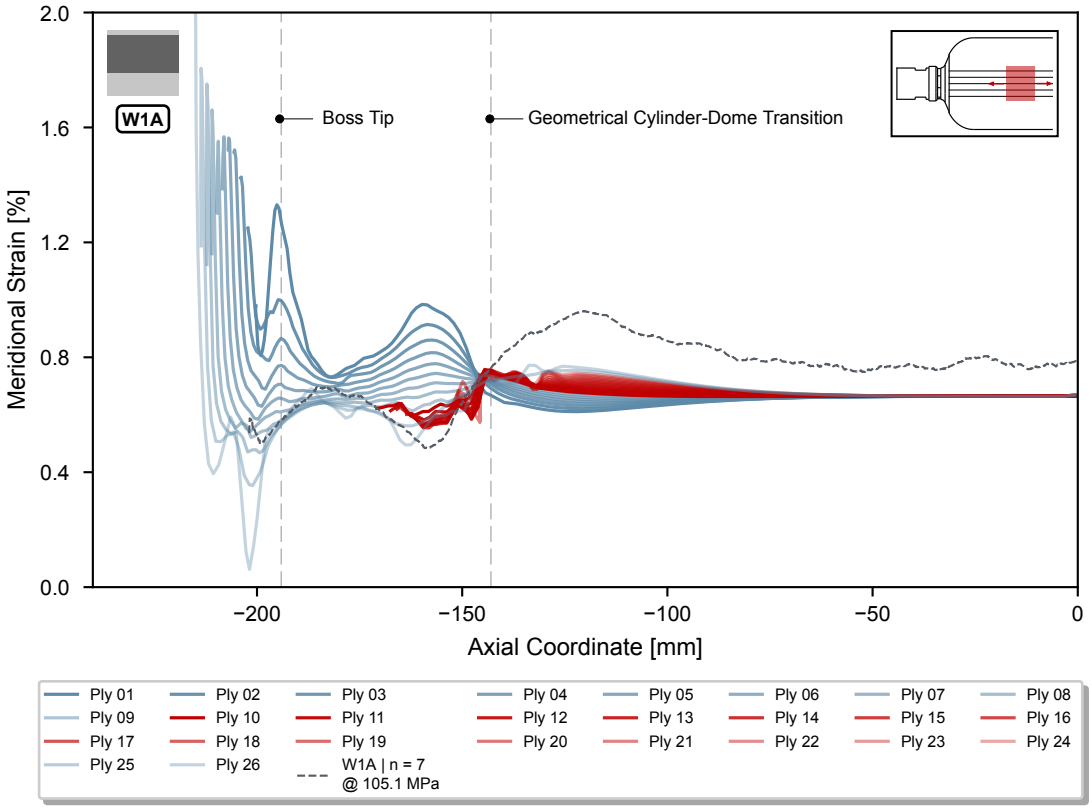
ond, the interaction between dome and boss generates a relevant through-the-thickness shear deformation in the composite reinforcement, emerging as high meridional strain in the lower dome quarter. This effect is also depicted in fig. 7.7 and visible by the comparison of the deformed and undeformed shapes in the dome pole end, where the boss contact condition forces the dome end to displace axially without expanding tangentially. However, this can only be accomplished by deforming the composite reinforcement in the meridional direction and generating a severe through-the-thickness strain gradient.

Contrarily to the meridional strain, a relevant gradient through-the-thickness is presented in fig. 7.9b for the tangential strain variation in the cylindrical region. This variation arises from the thick wall condition of the vessel and causes tangential stress to increase in the inner layers compared with the outer ones. The origin of this deviation lies in the coupled definition of radial and tangential stress, where the first reduces from the pressure condition on the inner surface to the free outer one. This radial stress is coupled with the tangential component through the radial stress gradient, which also determines the latter by maintaining the equilibrium of the differential cylindrical element, [117].

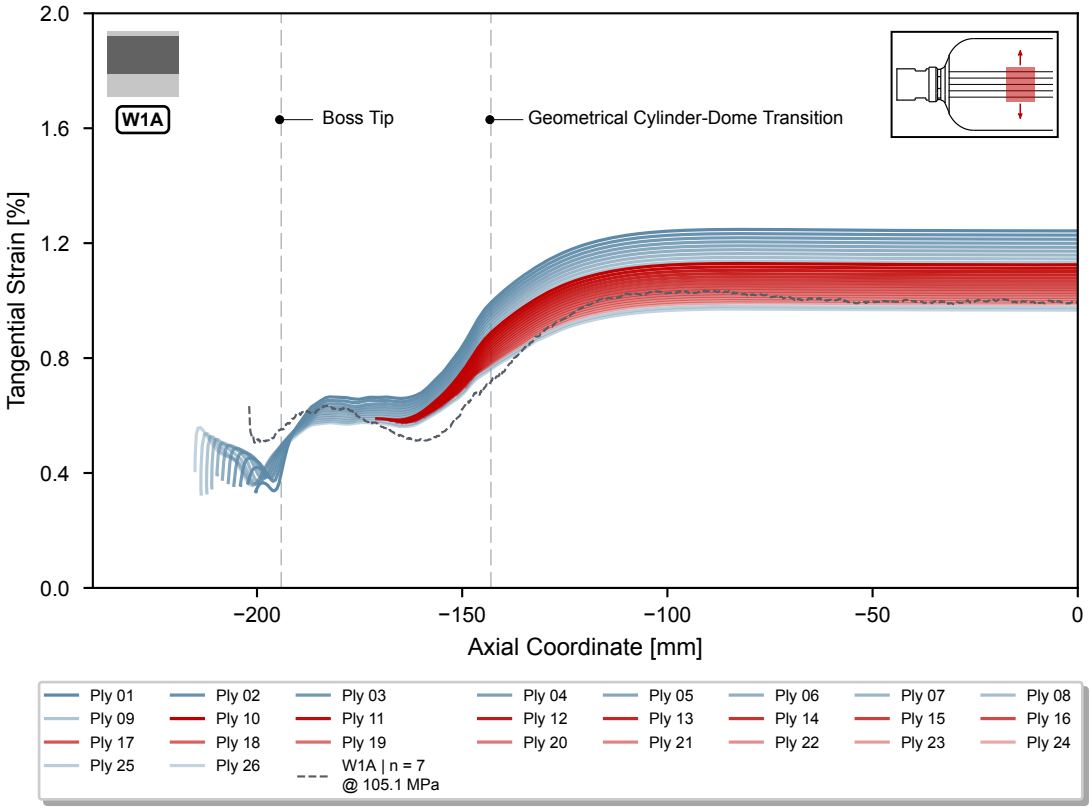
When the thickness of the vessel is thin, the gradient of the radial stress is approximately constant and generates uniform tangential stress. However, the radial stress reduces non-linearly with the radius when the wall is thick and accordingly develops a tangential stress gradient. This distribution is still directly proportional to the applied internal pressure, as illustrated in fig. 7.9b, where the tangential strain difference from inner to outer surface reduces towards the dome pole. About the dome end next to the boss, the strain pattern of the composite reinforcement appears to be influenced by the boss contact condition. In light of the high meridional strain existing in this region, it is anticipated to be led by the development of matrix damage.

7.4.2. Prediction on the E+ and B* Stacking Sequences

The deformational responses of the E+ and B* stacking sequences are already presented in section 7.3 to be comparable, which in the case of the meridional strain results in figs. 7.10a and 7.11a, characterize by showing a change in the meridional bending sign, from cylinder towards the dome pole. Outward meridional bending appears in the cylinder region, next to the dome transition, that swiftly changes to inward bending at the bulge location, eventually changing again towards the highly deformed dome end next to the boss. A tendency is predicted to develop higher meridional strain on the inner plies than in the outer ones considering the deformation of the lower quarter of the dome. This effect is related to the tensioning experienced by the lower dome quarter because of the formation of a bulge in the dome transition region. Throughout the loading of the E+ and B* layups, the axial pressure component

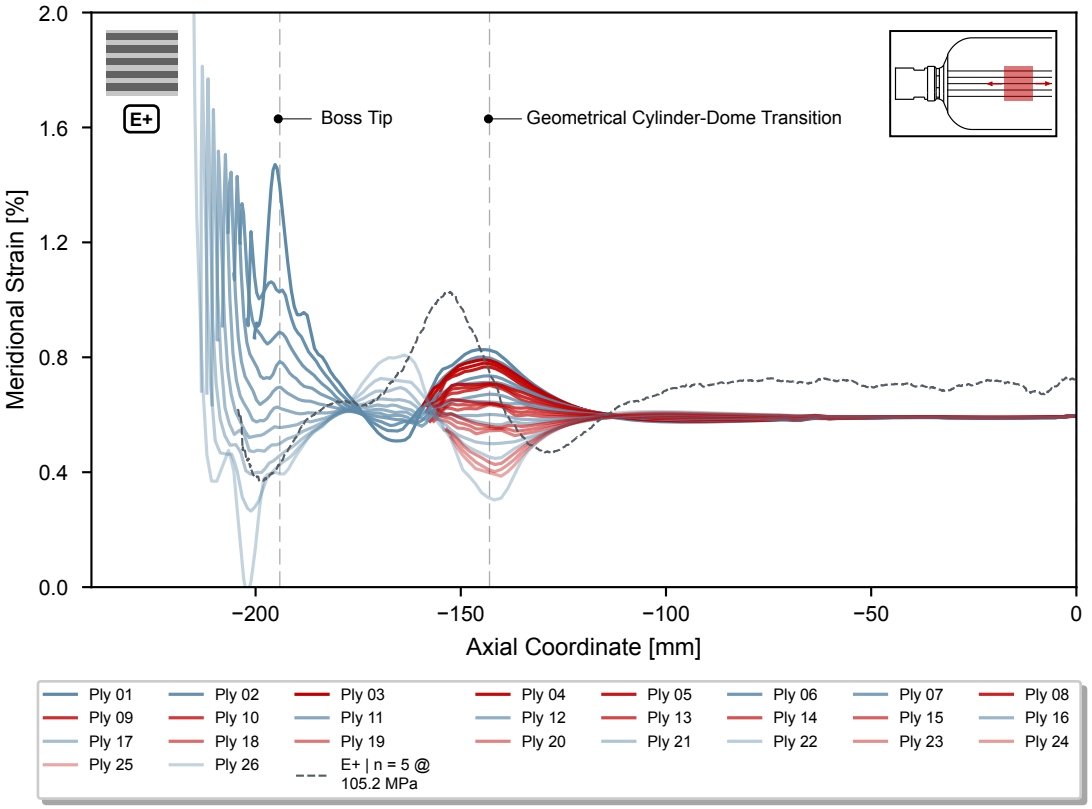


(a) Meridional strain

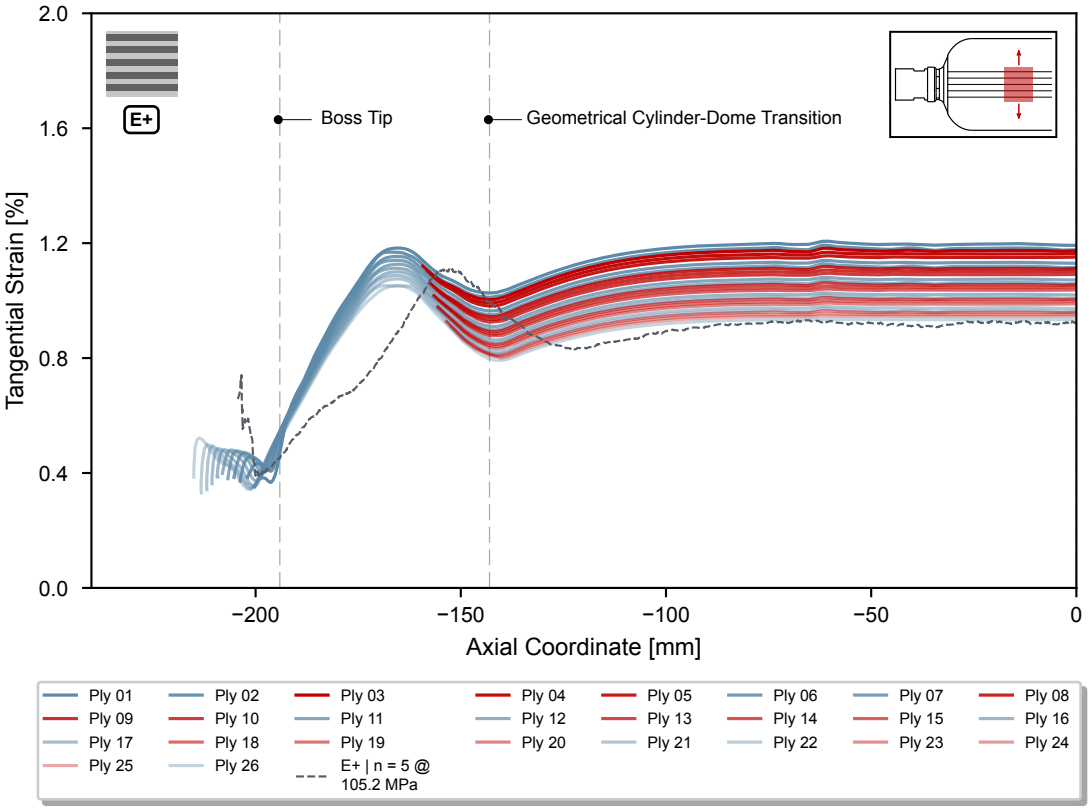


(b) Tangential strain

Figure 7.9: Through-the-thickness meridional and tangential strain of the W1A stacking sequence at a load pressure of 103.5 MPa. The layer count increases from inner to outer surface. Numerical predictions are presented against average experimental results for a number of samples n

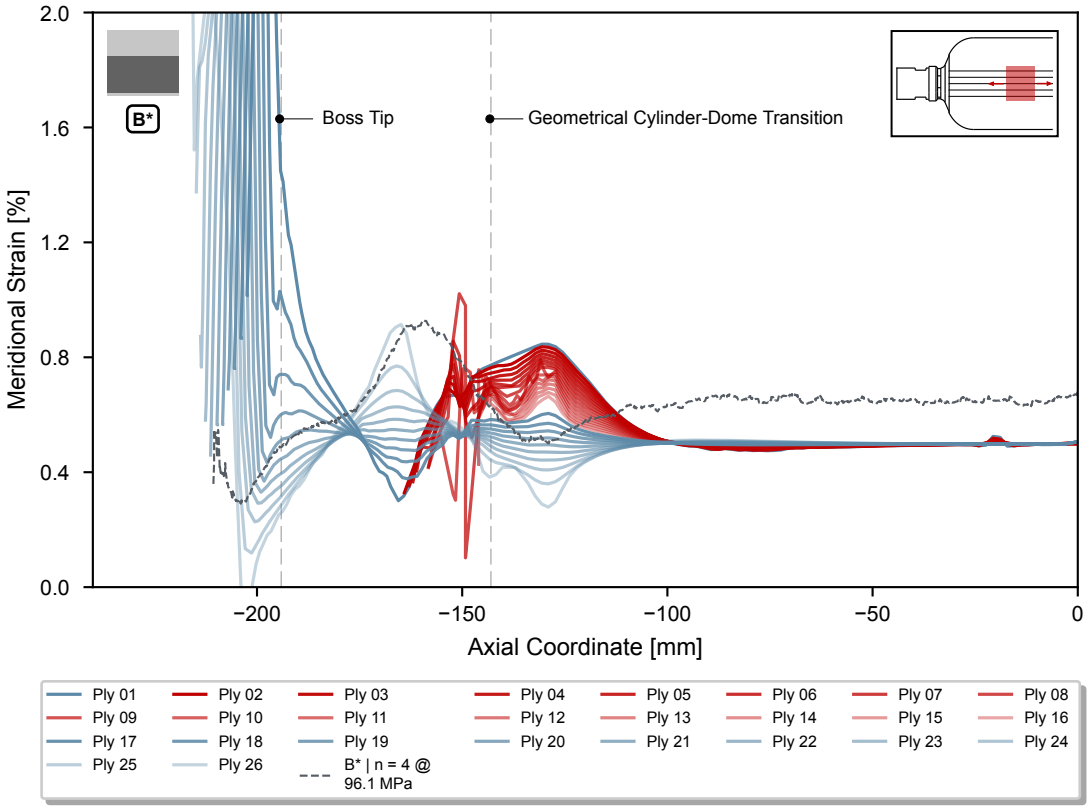


(a) Meridional strain

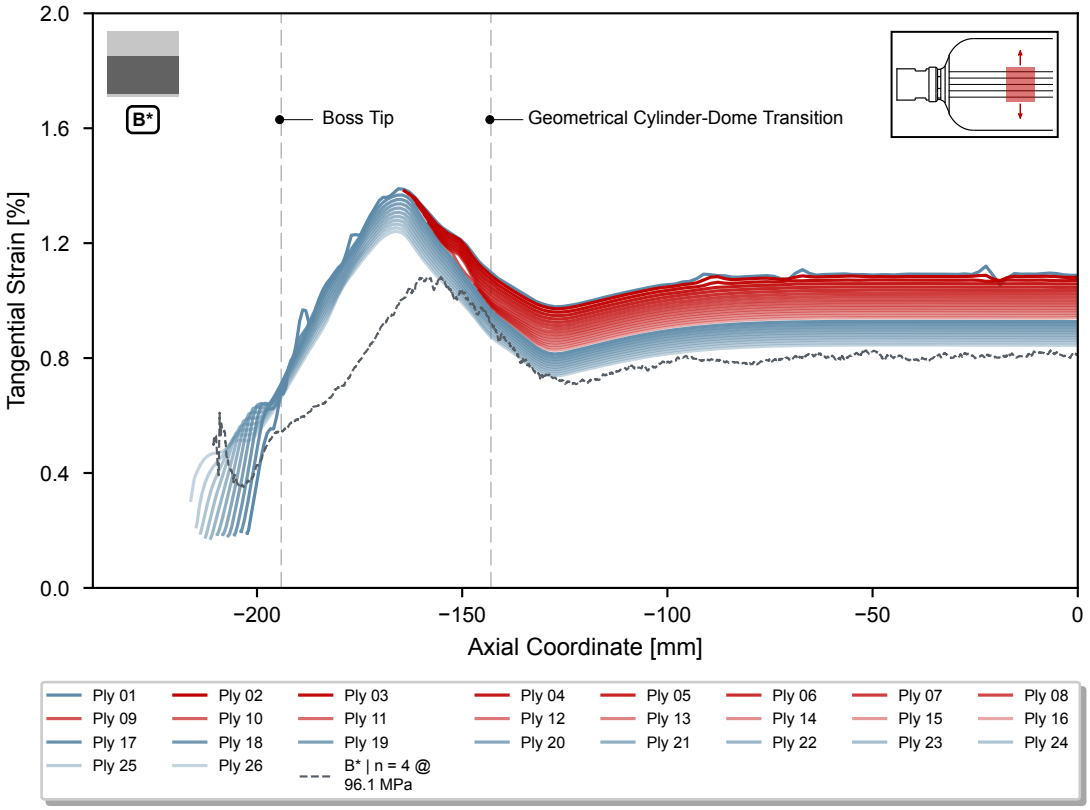


(b) Tangential strain

Figure 7.10: Through-the-thickness meridional and tangential strain of the E+ stacking sequence at a load pressure of 103.5 MPa. The layer count increases from inner to outer surface. Numerical predictions are presented against average experimental results for a number of samples n



(a) Meridional strain



(b) Tangential strain

Figure 7.11: Through-the-thickness meridional and tangential strain of the B* stacking sequence at a load pressure of 98.0 MPa. The layer count increases from inner to outer surface. Numerical predictions are presented against average experimental results for a number of samples n

forces the boss to displace axially while the bulge is deforming significantly in the radial direction. As a result, the lower dome quarter tends to straighten to meet these two opposing shifts, which ultimately generates higher meridional strain on the inner side.

Following, as the magnitude of the bulge formation is larger for B* than for the E+ configuration, the meridional strain experienced in the dome end next to the boss shows to be proportionally scaled. About the meridional strain component in the cylindrical region, a constant value is predicted where no influence from the dome transition region exists, although a mild through-the-thickness gradient builds towards the dome in the B* configuration, abaft the outward meridional bending region, and depicted in fig. 7.11a. The extensional-bending coupling induced by the stack of helical plies on top appears to promote this effect by inducing the component to bend inwards. Contrarily to the W1A layup, the dome transition region of the B* stacking sequence is loosely constrained in the tangential direction, which hence allows the stacking sequence induced deformation to develop nearby the cylinder edge.

The tangential strain response through-the-thickness depicted in figs. 7.10b and 7.11b also shows a variation along the meridional path according to the formation of a bulge in the dome transition region. This peak of the tangential strain component experienced at the bulge location coincides with the circumferential ply drop coordinate, which, indeed, indicates that the circumferential ply group tip is loaded relevantly in its tangential direction. The high hoop stiffness of the circumferential stacks restrains the dome transition bulge from developing, although this is achieved necessarily by generating correspondingly high fiber stress. In a similar manner to the W1A case, the tangential strain gradient shows to diminish towards the dome pole for the E+ and B* layups because of the changing pressure component.

7.5. Results and Discussion of the Cylinder Expansion

For the limit layups investigated, it is observed that the meridional and tangential strain components differ in magnitude in the cylindrical region, which is discussed additionally against their deformational behavior for the increasing pressure values. This discussion not only permits the depiction of their mechanical response but also illustrates how the induced load path in each of the limit layups determines the cylinder strength.

7.5.1. Prediction on the Tangential Stress and Strain

Differences in the magnitude of the predicted tangential strain appear to directly relate with the directional stiffness defined with the vessel stacking sequence design. The effect of this load path definition is presented in fig. 7.12 for the stress gradient through-the-thickness in the cylindrical region, and following, concerning strain in fig. 7.13. Results are presented along the thickness coordinate for various load stages and benchmarked against the equivalent homogeneous orthotropic behavior in fig. 7.6.

A homogeneous vessel shows a gradual decrease of tangential stress component because of its thick wall effect, whereas the magnitude of this variation is portrayed in fig. 7.12 to relevantly change in the composite cases because of the layer orthotropy. Thus, the B* stacking sequence concentrates its elastic energy on the inner layers, where the maximum tangential stress overpasses the homogeneous solution. The circumferential ply stress gradient similarly increases because of the lesser material thickness carrying the load in this direction. However, displacing the stack of circumferential layers towards the outside, as in W1A layup, the naturally occurring maximum stress on the inner side of the cylinder is displaced to the thickness coordinate of the first circumferential. As a result of this load deviation, the tangential stress of this layer becomes comparatively larger than the tangential stress at the same thickness position of the B* layup, although the magnitude of the maximum slightly decreases for the W1A configuration. This shift is caused by the tangential stress on the innermost helical of the W1A stacking sequence also increasing, thus marginally reducing the total elastic energy developed by the circumferential stack.

The E+ layup appears to be in an intermediate position between the W1A and B* definitions, where the staggering of circumferential groups shows a consistent stress attenuation along the thickness direction. Nonetheless, the maximum tangential stress surpasses the B* case, as derives from the innermost group of circumferential layers in the E+ configuration, concentrating a relevant amount of the tangential loading. This distribution results from their high directional stiffness, hence limiting the load transfer to the outer groups because of the otherwise required load path deviation. Withal, as part of the load is still carried by the outer circumferential groups, the tangential stress increases in these

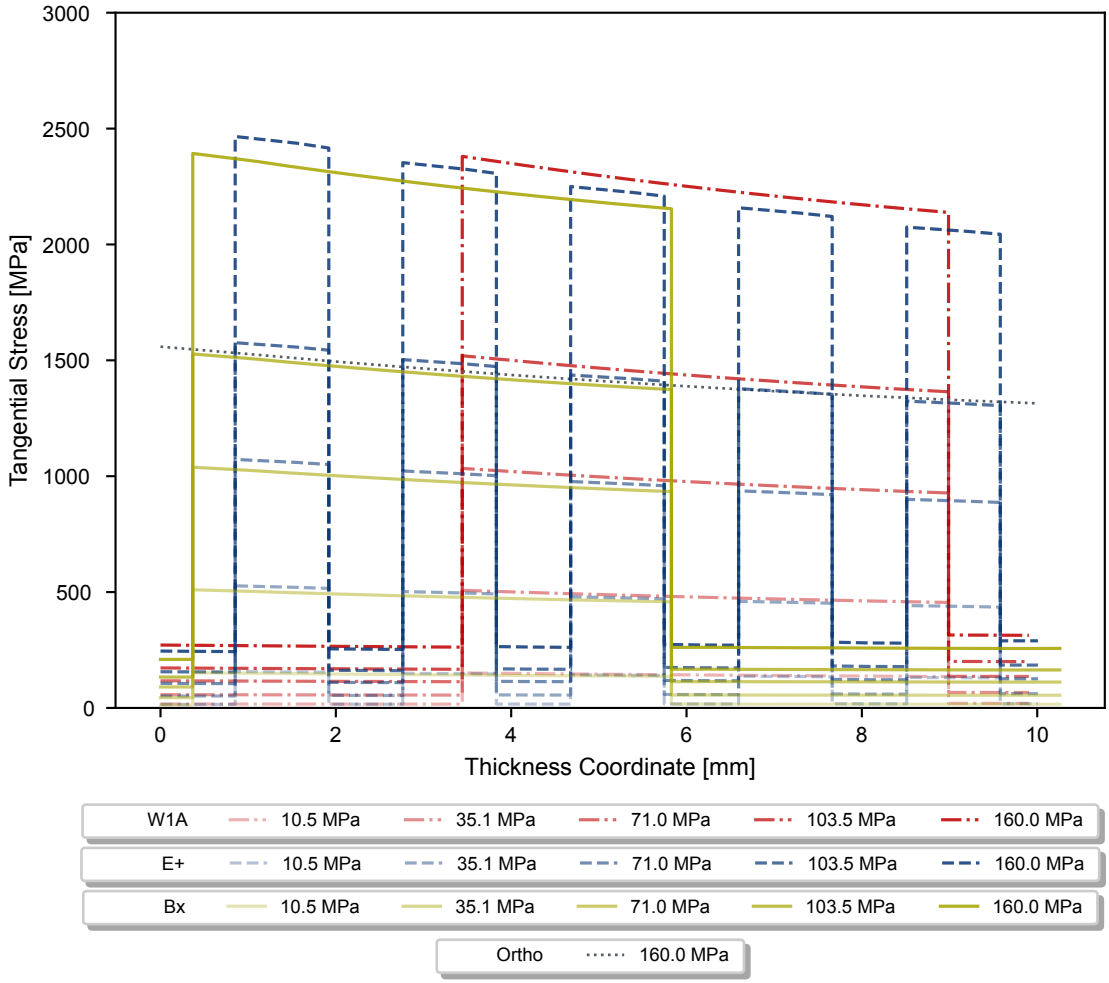


Figure 7.12: Comparison of the through-the-thickness tangential stress gradient of the W1A, E+ and B* stacking sequences in the center of the vessel. Results are presented against the response of an equivalent homogeneous orthotropic vessel (Ortho)

compared with the B* layup. The increment results in a tangential stress gradient of a comparable slope to the W1A and B* vessels that, in sight of the higher maximum stress, derives in an overall higher elastic energy developed by this configuration.

The through-the-thickness stress variation of a thick-walled cylinder implies that, as depicted in fig. 7.13, a more substantial tangential strain occurs on the inner surface than on the outside. Particularly to the B* layup, the high tangential stiffness of the inner layers limits the vessel expansion, making its tangential strain generally lower than the homogeneous vessel solution. On the contrary, loading the outer circumferential ply stack in the W1A stacking sequence is only possible when the corresponding inner helical layers deform tangentially and shift the load path toward the outside. Throughout the loading process, the inner helical plies start carrying the high load on the inner side of the vessel, but in sight of their low tangential stiffness, they deform and push the circumferential stack radially. This effect is presented in fig. 7.13 as a larger tangential strain magnitude of the W1A layup than the B* case, albeit still lower than the homogeneous vessel because of the high stiffness fibers. Correspondingly, the E+ stacking sequence appears as an intermediate case because of the almost symmetric tangential stiffness distribution of the staggered hoop layer groups. Concerning the strain gradients through-the-thickness, these appear to be comparable in all cases, considered the similar total component thickness and the analogous in-plane stiffness description.

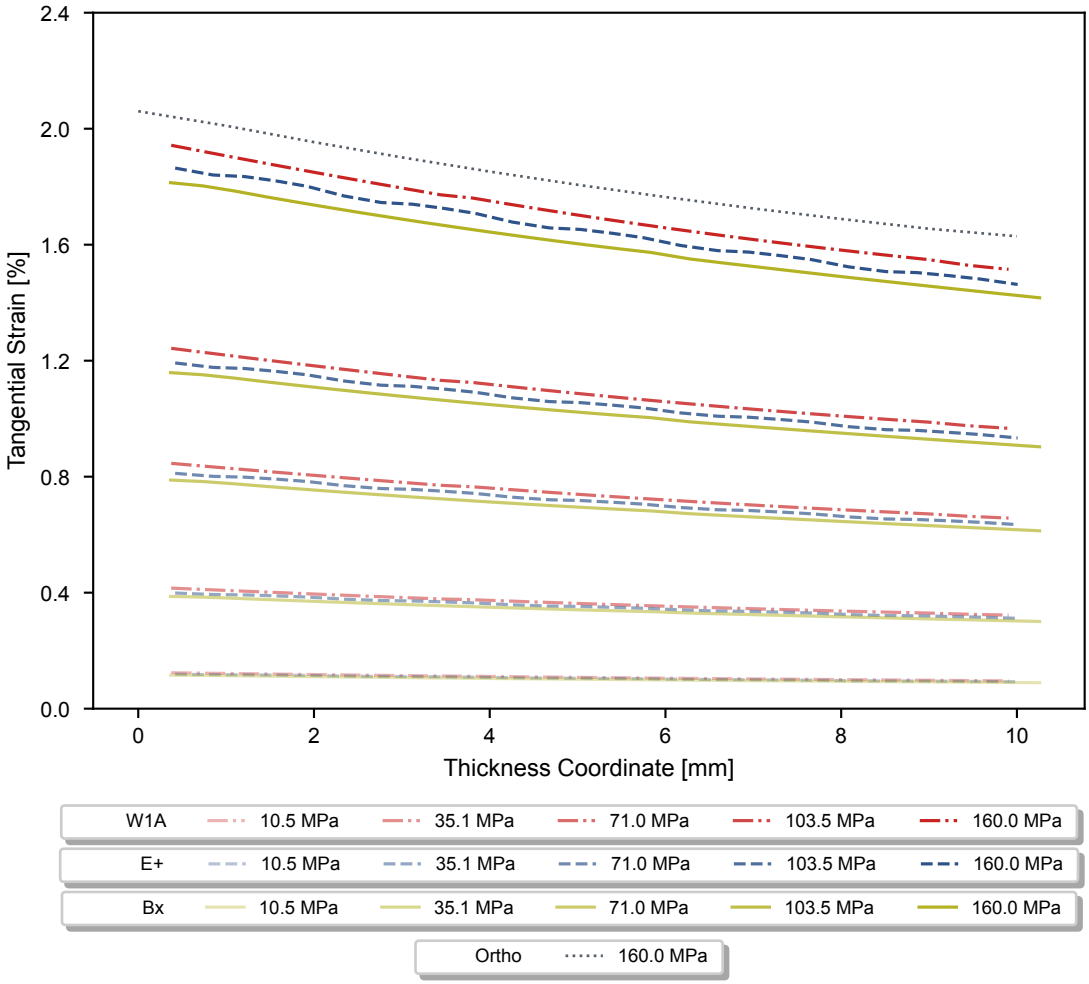


Figure 7.13: Comparison of the through-the-thickness tangential strain gradient of the W1A, E+ and B* stacking sequences in the center of the vessel. Results are presented against the response of an equivalent homogeneous orthotropic vessel (Ortho)

7.5.2. Prediction on the Meridional and Tangential Strain with Increasing Pressure

A complementary perspective on the stiffness gradient influence on the cylindrical region deformational behavior is presented by the evolution of the meridional and tangential strain components with the increasing internal pressure. This response is illustrated in fig. 7.14 by comparing the simulation prediction on the outer component surface with the average experimental results obtained using DIC. The displayed results are the average of three surface sectors of 200 mm length and 40° width that, because of their size, inherently account for part of the strain variation towards the dome transition. Direct proportionality is anticipated between the tangential and meridional strain components because of applied hydrostatic pressure loading. Therefore, the dome regions are equally loaded regardless of the cylinder tangential expansion, although the larger the latter, the more relevant the Poisson induced deformation in the cylinder walls. As the load transferred from pole to pole is independent of the tangential loading in the cylinder, as it is comparatively expanding, the effective meridional stress increases and the matching strain.

Concerning the meridional strain depicted in fig. 7.14a, both the experimental E+ and B* results are very similar in light of their comparable deformational behavior, while they also show to be smaller than the W1A layup in either case. This trend agrees with the one presented in the through-the-thickness tangential strain gradient in fig. 7.13, where the strain component is successively smaller for W1A, E+ and B*. Still, the surface average result of the E+ and B* is instead nearly coincident. This effect is argued to result from outer surface strain change from cylinder to the dome, ultimately balancing the

different responses at the vessel center illustrated in fig. 7.13.

In the W1A and E+ cases, prediction and experimental results agree at low-pressure stages but deviate after the 30 MPa stage is reached approximately. This behavior is expected because of the moderate pressure levels at which matrix cracks start to develop in the circumferential layer stacks, hence increasing the measured strain components compared with the constitutively elastic result. A more considerable discrepancy appears in the B* layup, where a mismatch with the experimental data is reported already at the early stages. This likely indicates an incorrect meridional stiffness definition in the cylinder. The average material properties in table 7.1 do not adequately represent the anticipated high porosity of the outer helical plies, hence requiring a more accurate material definition based on measured fiber volume and porosity contents.

In a like manner, the tangential strain data with the increasing pressure of fig. 7.14b shows an excellent agreement because of the more predictable fiber dominated response. The magnitudes of the E+ and B* layups show again to coincide in the experimental and predicted results while, according to the meridional strain trend in fig. 7.14a, the W1A is still larger. The magnitude of the result deviation is reported in table 7.4 where, with the higher loading, the predicted meridional strain increasingly deviates from the experimental measurements. Instead, the tangential strain results show a consistent discrepancy throughout increased pressure stages, as the development of matrix damage has a marginal effect on it.

Table 7.4: Results of the average meridional and tangential strain in the cylinder

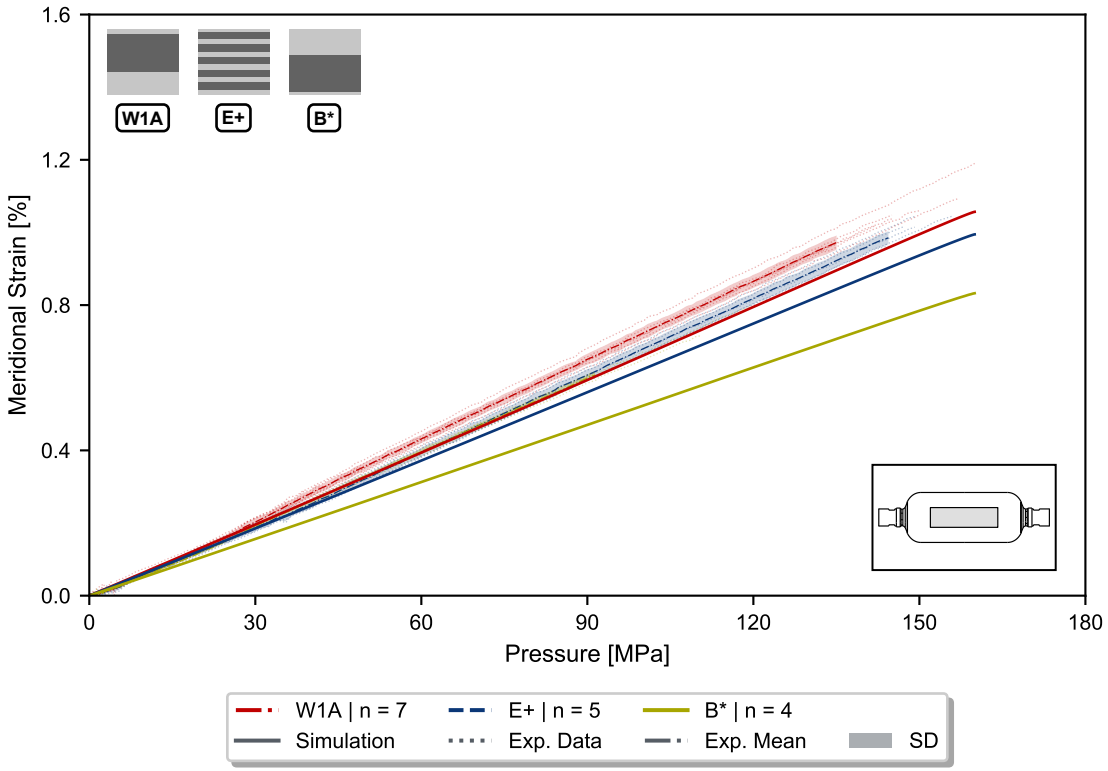
Stack.	Pressure [MPa]		Max. Mer. Strain [%]				Max. Tan. Strain [%]			
	Exper.	Simul.	Exper.	Simul.	Diff.	Diff. (%)	Exper.	Simul.	Diff.	Diff. (%)
W1A	35.4	35.1	0.24 ± 0.01	0.24	0.00	−0.68	0.33 ± 0.01	0.35	0.01	2.07
	70.1	71.0	0.50 ± 0.01	0.48	−0.03	−5.29	0.68 ± 0.01	0.69	0.01	1.10
	105.1	103.5	0.76 ± 0.02	0.71	−0.04	−6.06	1.01 ± 0.01	1.02	0.01	0.85
	139.0	140.0	0.97 ± 0.02	0.92	−0.05	−5.49	1.30 ± 0.01	1.32	0.02	1.87
	155.6	160.0	1.09 ± 0.02	1.06	−0.03	−2.71	1.46 ± 0.01	1.52	0.05	3.67
E+	34.6	35.1	0.22 ± 0.01	0.23	0.01	4.16	0.30 ± 0.01	0.32	0.02	4.98
	70.1	71.0	0.47 ± 0.01	0.45	−0.01	−3.27	0.61 ± 0.01	0.63	0.02	3.23
	105.2	103.5	0.71 ± 0.01	0.67	−0.04	−6.19	0.92 ± 0.02	0.94	0.02	2.71
	140.7	140.0	0.95 ± 0.02	0.87	−0.09	−9.51	1.21 ± 0.02	1.22	0.00	0.15
	154.1	160.0	1.04 ± 0.02	0.99	−0.04	−4.01	1.31 ± 0.02	1.40	0.09	6.43
B*	34.8	35.1	0.23 ± 0.01	0.19	−0.04	−15.41	0.30 ± 0.01	0.24	0.02	6.70
	69.5	71.0	0.46 ± 0.01	0.38	−0.09	−18.51	0.61 ± 0.01	0.51	0.03	4.36
	96.1	97.8	0.61 ± 0.01	0.50	−0.10	−17.12	0.85 ± 0.01	0.84	0.05	6.33

Stack. – stacking sequence; Max. Mer. Strain – maximum meridional strain; Max. Tan. Strain – maximum tangential strain; Exper. – Experimental data; Simul. – Simulation results; Diff. – absolute difference between Experimental data and Simulation results Diff. (%) – percentual difference between Experimental and Simulation results

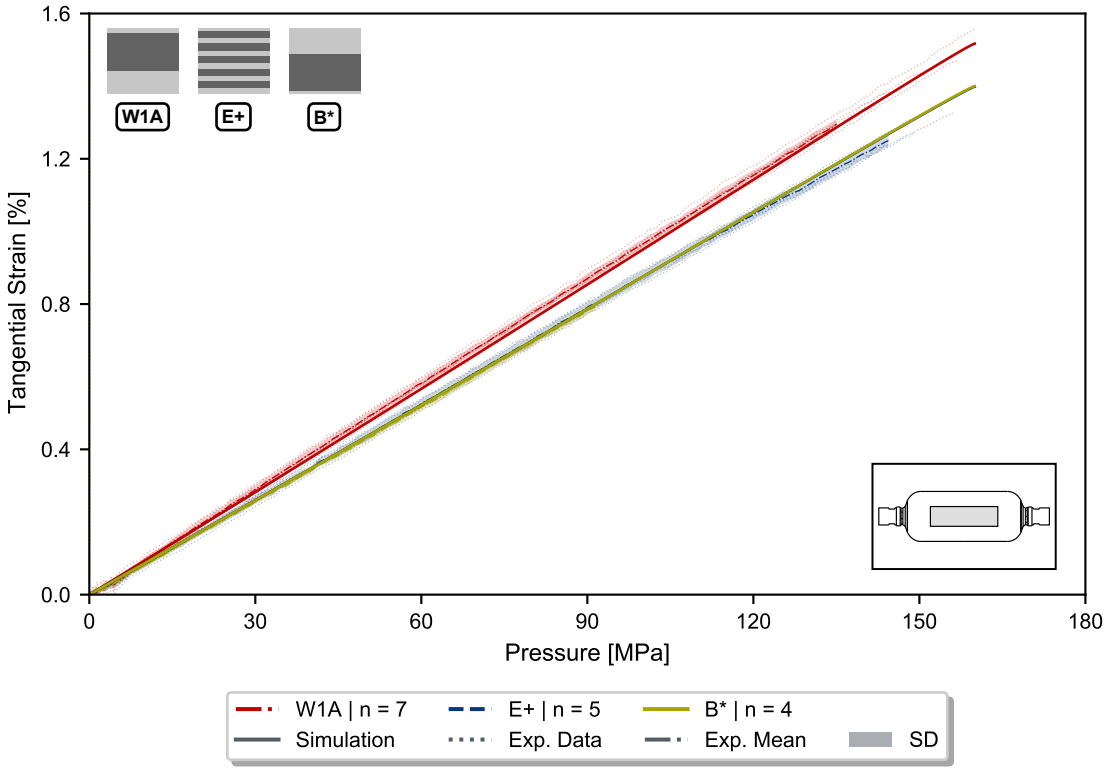
Note 1: The pressure stages at which Experimental and Simulation results are presented slightly differs because of the unequal frequencies of the recording of results

7.6. Results and Discussion of the Boss Axial Displacement

The deformational behavior of the cylinder and dome transition regions appear to be connected closely with the stacking sequence definition of the CPV. The description of the vessel architecture permits trading maximum cylinder tangential stress in exchange of component compliance, whereas this description also relevantly influences the tangential expansion on the dome transition and the likelihood of developing a protruding deformed shape. Therefore, the lower dome quarter response and the boss axial displacement are impacted by the vessel behavior upstream, which, besides the dome construction being equivalent for the W1A, E+, and B* layups, leads to distinct trends for each of the configurations. Therein, the boss axial displacement is a pertinent variable for the correlation of experimental and numerical results because it is measured straightforwardly during pressure tests. However, axial displacement follows from the aggregation of various mechanical effects that ultimately hinder its proper interpretation, including material deformation, geometry shape change during loading, boss yielding, and damage progression.



(a) Meridional strain



(b) Tangential strain

Figure 7.14: Comparison of the outer surface meridional and tangential strain of the W1A, E+ and B* stacking sequences. Numerical predictions are presented against average experimental results for a number of samples n, where their scatter is indicated by their standard deviation (SD)

A comparison of the predicted boss axial displacement of the W1A, E+, and B* stacking sequences is presented in fig. 7.15, where their pressure test measurements are obtained by DIC point tracking of the boss head. The influence of the stacking sequence on the boss axial displacement displays a similar trend to the meridional and tangential strain components in the cylinder in section 7.5. The E+ and B* configurations depict similar axial displacement, while the W1A layup respectively shows larger compliance. This tendency is sustained on the deformational behavior of the dome transition region and is illustrated in fig. 7.16 for the scaled deformed shapes of the W1A and B* layups, being the E+ vessel ultimately comparable to the latter.

On the one hand, the extensional-bending coupling of the W1A stacking sequence prompts the dome transition region to deform meridionally outward while this happens to be inward for the B* layup. On the other hand, the gradual directional stiffness change of the W1A layup hinders the upper dome tangential expansion, whereas the sudden drop in the B* case let a bump to sprout instead. The twofold influence of these effects restrains the W1A layup upper dome region from expanding tangentially, causing the lower dome quarter to spray and reveal a comparatively large boss axial displacement. In the case of the B* stacking sequence, the growth of a bulge stretches the dome region, causing it to cringe and limit the movement of the boss. Likewise, the E+ layup neither sufficiently restrains the tangential expansion in the dome region nor experiences a substantial bulge formation as the B* vessel, thus showing a halfway hampering of the boss displacement.

Nevertheless, the simulation and experimental result correlation presented in fig. 7.15 depicts relevant discrepancies in terms of the displacement magnitude. There is a displacement non-linearity in the early pressurization stages that are not reproduced in the numerical work. The existence of a non-linearity coincides with the work of Berro Ramirez et al. [66]; here, a gap between metallic boss and composite reinforcement is reported to be the origin of this behavior. Withal, this gap is not observed in the CT vessel scans of the current vessel definition presented in fig. 5.6a. The observation of the dome end next to the boss in section 7.6 , nevertheless, permits to identify resin-rich regions at the ply

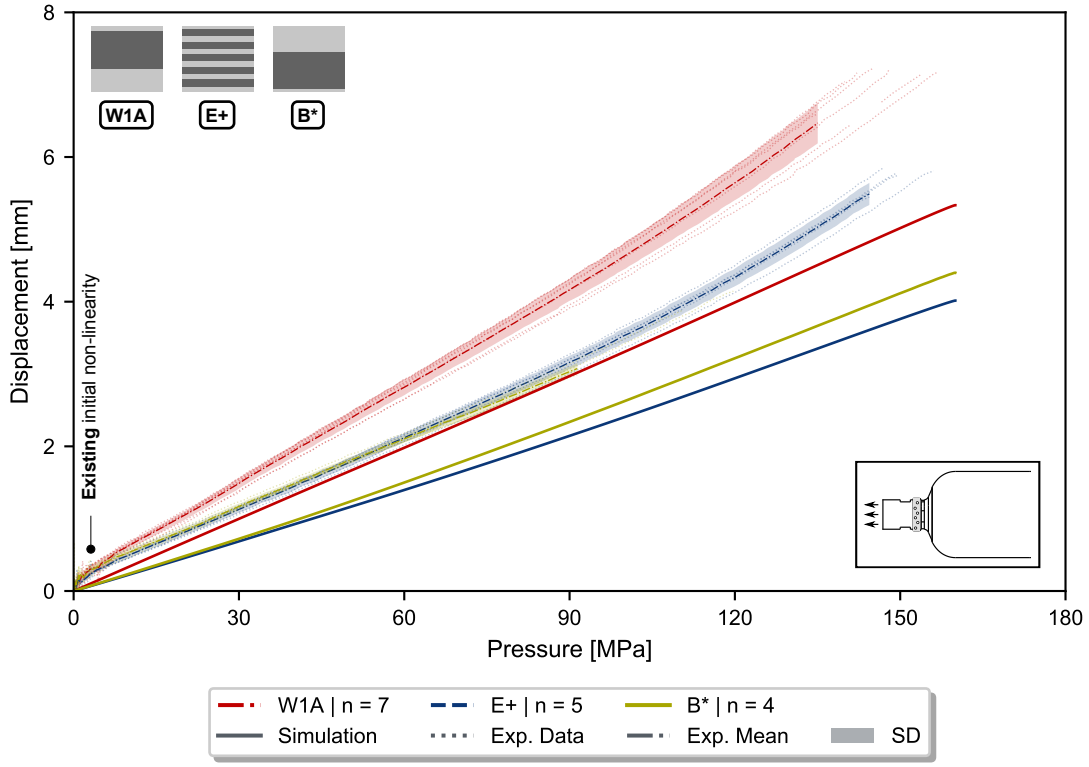


Figure 7.15: Comparison of the axial boss displacement of the W1A, E+ and B* stacking sequences. Numerical predictions are presented against average experimental results for a number of samples n, where their scatter is indicated by their standard deviation (SD)

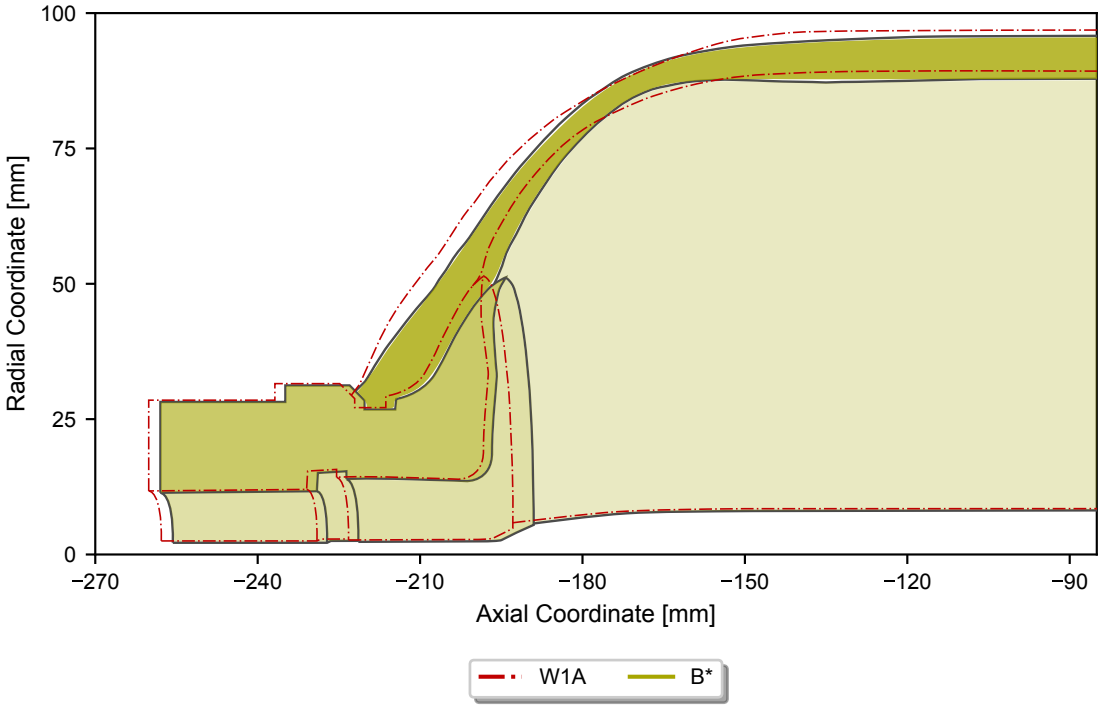


Figure 7.16: Comparison of the scaled deformed shapes in the dome of the W1A, and B* stacking sequences

tips, which become more pronounced in the torque safety groove of the boss shape. These pockets originate with the outflow of resin during the curing process that readily tends to fill the limited packing of the boss shape during winding.

Consequently, they comprise low strength material regions and are anticipated to fail during the early pressurization stages, allowing the boss to displace axially until it fully engages with the composite reinforcement. This early matrix crushing is captured during AE monitoring and presented in fig. 7.17b for the sound amplitude recording of the W1A stacking sequence against its applied pressure. The initial emissions presented are furthermore localized at the position of the boss in fig. 7.17c, while the more numerous and more intense emissions after the 30 MPa threshold are related to the intralaminar matrix damage growth.

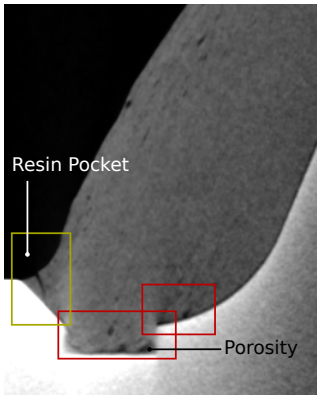
Following the initial displacement non-linearity, the slope of the simulation prediction appears to be underestimated slightly after the pressure stage of 30 MPa also shows to aggravate. Above this loading stage, the existence of damage in the matrix increases the vessel compliance, which from the AE recording of fig. 7.17, agrees with the significant increase in the reported acoustic events. The magnitudes of the axial displacement mismatch are reported in table 7.5 where, to present a more meaningful comparison, results are offset with respect to their linear fit in the 10 to 25 MPa pressure range. Hence, the influence of the initial non-linearity is disregarded, and the actual composite behavior is correlated with the simulation results. This comparison is alternatively illustrated in fig. 7.18, where it is shown that the mismatch between prediction and measurement comparatively increases with the higher loading.

The discrepancy of the boss axial displacement since the early pressurization stages shows that the mechanical response in the model is excessively stiff. In the absence of material damage, this can be related to a not sufficiently accurate thickness profile definition in the dome transition region. If the dome shape is not permitted to change sufficiently during deformation, the resulting axial displacement can be expected to be limited against the experimental results. Notwithstanding, the definition of a relatively coarse mesh of reduced integration solid elements may aggregate to this effect because of the relatively rough approximation they entail to the existing meridional bending response. Being the dome transition region an area of critical influence for the adequate correlation of the boss axial displacement, a more detailed investigation of its adequate modeling approach needs to be regarded.

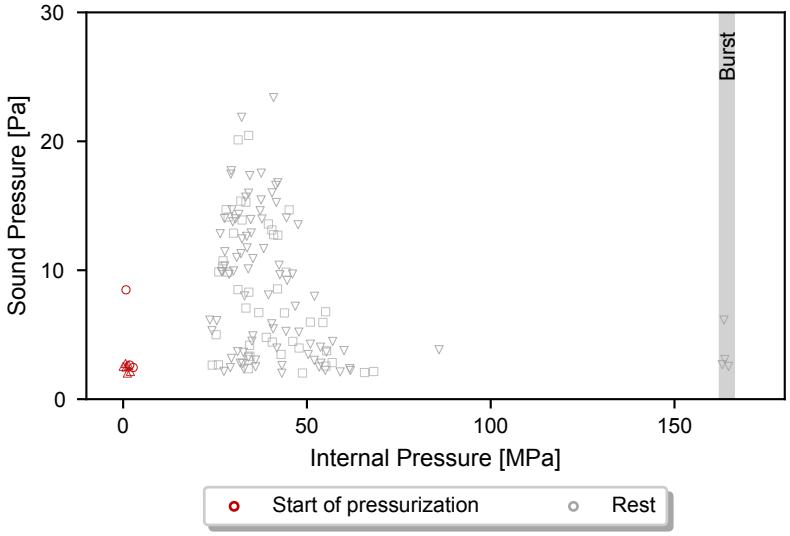
The results in fig. 7.15 indicate a slightly larger prediction of the B* axial displacement than the E+

layup. However, the relative cylinder expansion and the magnitude of the dome transition bulge in each of the configurations anticipated an opposite trend. This discrepancy is referred to as the maximum tangential strain predicted in the bulge of the B* stacking sequence shown in fig. 7.8, which appears to be moderately larger than the experimental result. Experiencing a larger tangential expansion in the dome, the B* vessel is also allowed to displace further axially because of the direct proportionality of these two.

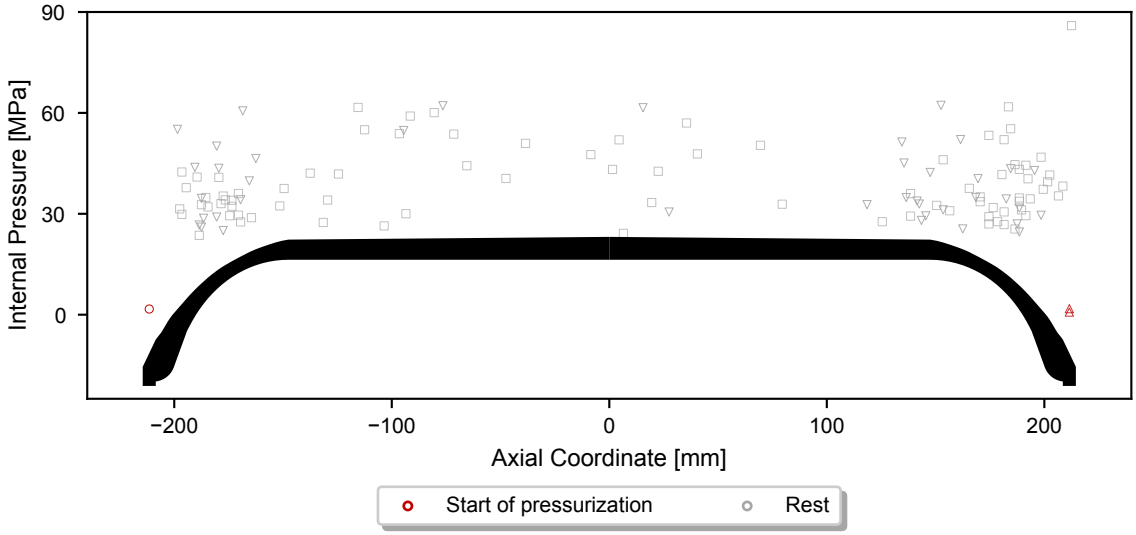
The yielding of the metallic boss part is also predicted to develop with the increasing loading. This is qualitatively presented in fig. 7.19 for the W1A stacking sequence at pressure stages of 103.5 and 160 MPa, where plastic strain is observed to develop through the relevant element cross-section. It develops first in the boss brim and its duct, resulting from the brim bending with the composite reinforcement load transfer. Still, the boss plastic strain does not surpass the general 6 % ultimate strain



(a) CT scan of the dome end



(b) Peak sound pressure of the AEs at low pressure stages in comparison with the following



(c) Localization of the peak AEs at low pressure stages in comparison with the following

Figure 7.17: Correlation of the resin accumulation at the boss end next to the boss with the recording of AE at low pressure stages of 01-0127 | W1A, 01-0183 | W1A, 01-0184 | W1A, and 01-0186 | W1A

Table 7.5: Results of the boss axial displacement

Stack.	Pressure [MPa]		Boss Displ. [mm]				Boss Displ. Trunc. [mm]			
	Exper.	Simul.	Exper.	Simul.	Diff.	Diff. (%)	Exper.	Simul.	Diff.	Diff. (%)
	35.5	35.1	1.72 ± 0.07	1.22	−0.50	−28.92	1.55 ± 0.07	1.22	−0.33	−21.42
W1A	69.1	71.0	3.26 ± 0.12	2.39	−0.87	−26.61	3.10 ± 0.12	2.39	−0.70	−22.72
	104.1	103.5	4.87 ± 0.19	3.56	−1.31	−26.93	4.71 ± 0.19	3.56	−1.15	−24.39
	139.0	140.0	6.46 ± 0.28	4.63	−1.84	−28.50	6.30 ± 0.28	4.63	−1.68	−26.64
	155.6	160.0	7.13 ± 0.28	5.33	−1.80	−25.15	6.93 ± 0.28	5.33	−1.60	−23.06
	34.1	35.1	1.28 ± 0.05	0.84	−0.44	−34.63	1.12 ± 0.05	0.84	−0.27	−24.77
E+	69.2	71.0	2.45 ± 0.07	1.70	−0.75	−30.04	2.29 ± 0.07	1.70	−0.59	−25.68
	104.2	103.5	3.72 ± 0.11	2.60	−1.12	−30.04	3.56 ± 0.11	2.60	−0.95	−26.82
	140.7	140.0	5.27 ± 0.14	3.45	−1.83	−34.63	5.11 ± 0.14	3.45	−1.66	−32.53
	154.1	160.0	5.75 ± 0.15	4.01	−1.74	−30.18	5.62 ± 0.15	4.01	−1.60	−28.52
	33.7	36.7	1.32 ± 0.04	0.88	−0.43	−32.96	1.16 ± 0.04	0.88	−0.27	−23.52
B*	70.8	72.6	2.41 ± 0.06	1.84	−0.56	−23.37	2.24 ± 0.06	1.84	−0.39	−17.77
	96.1	96.1	3.07 ± 0.08	2.51	−0.56	−18.19	2.52 ± 0.08	3.07	−0.39	−13.60

Stack. – stacking sequence; Boss Displ. – boss displacement; Boss Displ. Trunc. – boss displacement truncated at a pressure of 10 MPa; Exper. – Experimental data; Simul. – Simulation results; Diff. – absolute difference between Experimental data and Simulation results Diff. (%) – percentual difference between Experimental and Simulation results
Note 1: The pressure stages at which Experimental and Simulation results are presented slightly differs because of the unequal frequencies of the recording of results

value of tempered aluminum, also indicating sufficient strength against failure of the component. This behavior further coalesces with the lower dome region degradation predicted from the elastic deformational state in figs. 7.9 to 7.11, and ultimately aggregates to the stacking sequence influenced vessel deformed shapes discussed along fig. 7.16. Furthermore, these successive effects that collectively determine the boss axial displacement also cause the disparity between experimental and numerical results to increase compared with measurements of less uncertainty, like the cylinder meridional strain reported in table 7.4.

7.7. Concluding Remarks

Defining a constitutive elastic model permits the identification of the general mechanical response of the CPV when loaded with internal pressure. Furthermore, it permits to correlate its deformational behavior with experimental data, identifying the likely sources of discrepancy with the increased pressure loading. In this regard, the response of the W1A, E+, and B* stacking sequences are presented, where their distinct behavior is discussed concerning their outer surface strain components, the in-plane strain components through-the-thickness, the average cylinder surface response, and the boss axial displacement.

The deformational behavior of the W1A layup indicates that, by showing a circumferential ply stack that extends relatively far into the dome, a comparable response to a homogeneous orthotropic vessel is generated in the dome transition region. Instead, the E+ and B* stacking sequences show a characteristic response driven by the sudden tangential stiffness change after the drop of circumferential plies. This stiffness change leads to the formation of a bulge in their dome transition regions and, consequently, deviates from a homogeneous orthotropic behavior. Additionally, the severity of this bulge formation is related to the meridional extensional-bending coupling of the stacking sequence definition. As derived from the behavior of the W1A and B* layups, the stacking sequence alternatively endorses the constraint or the expansion of the upper dome, hence limiting or promoting the upper dome to protrude besides the directional stiffness change along the axial coordinate. In the balanced E+ configuration, this coupling is neutral and, therefore, neither favorably nor detrimentally impacts the geometrical behavior.

Analyzing the through-the-thickness deformational response of the E+ and B* layups shows that the formation of a bulge has a relevant impact in the mechanical state of the circumferential plies. The lack of tangential stiffness ahead of the circumferential ply drop location endorses a relevant local vessel expansion, which is principally restrained by the tangential stiffness of the hoop layers. Material conti-

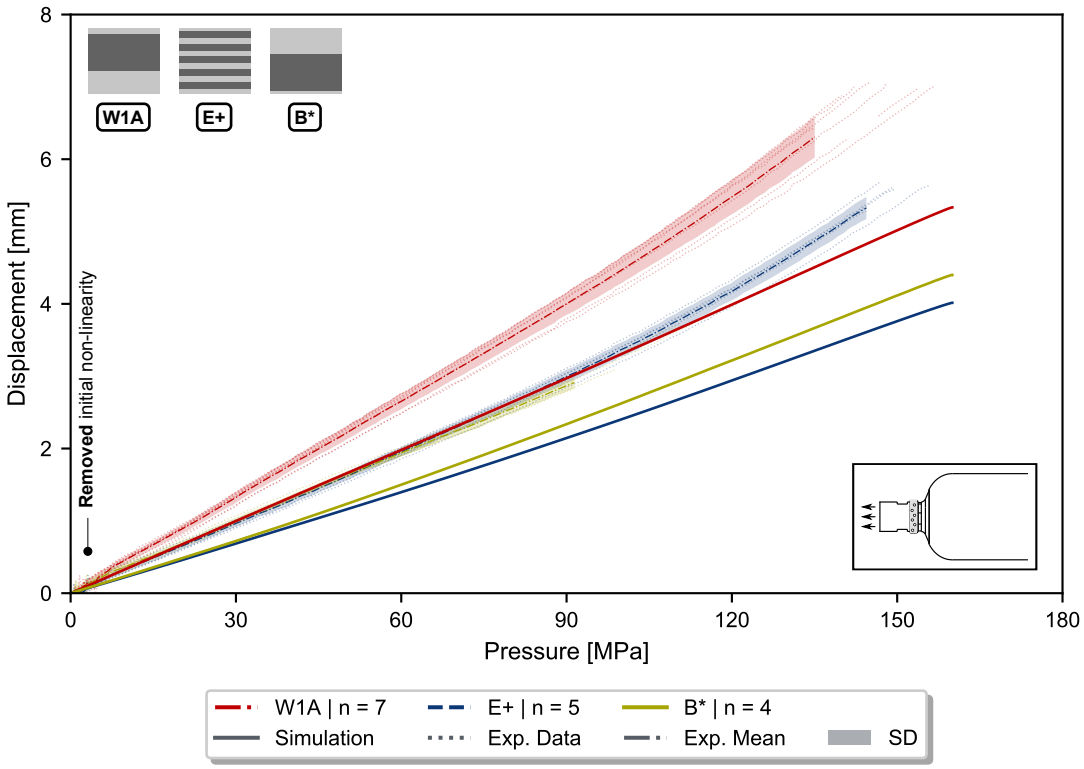


Figure 7.18: Comparison of the axial boss displacement of the W1A, E+ and B* stacking sequences after the elimination of the initial non-linearity

nuity requires the load applied within the bulged region to be transferred to the adjacent circumferential ply ends that experience relatively high fiber stress. If this stress increase of the circumferential plies in the dome transition region outnumbers the fiber stress state in the cylindrical region, premature failure of the vessel may also hamper its practical application.

The reported response in the cylinder ultimately indicates that a distribution of stiffness that locates the circumferential and high angle helical layers towards the outside benefits the strength. A higher tangential stiffness on the outer side of the vessel entails the maximum tangential stress to also shift towards this location. Nevertheless, as the inner layers comparatively expand to redistribute the load to

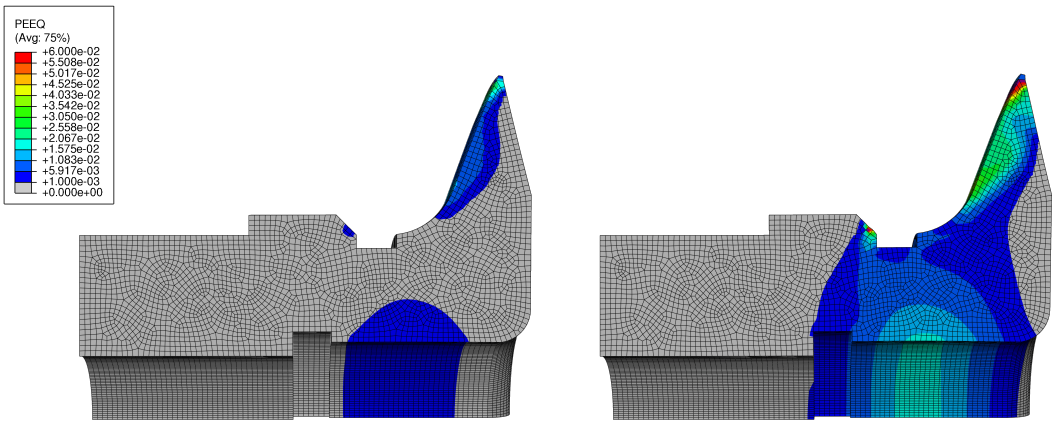


Figure 7.19: Plastic strain in the boss of the W1A stacking sequence at loading pressures of 103.5 (left) and 160 MPa (right)

the outer plies, the gradient of the tangential stress component becomes increasingly flatter. This effect implies that the difference in the fiber stress between the most and the least critically loaded plies is less severe. Therefore, the layup strength increases through a more uniform distribution through-the-thickness of the bestowed elastic energy, yet also increasing the compliance of the system. Accordingly, a more substantial tangential strain is permitted to develop in the innermost low angle helical plies, anticipating the following generation of deeper and denser matrix cracks.

Altogether, the correlation between simulation and experimental results shows good agreement in the general trends of the deformational response. Concerning the magnitude correlation, this is satisfactory for the tangential strain, but it is lightly underestimated regarding the meridional component. This mismatch appears to result from the material degradation with the increased loading in the real vessel, which is not considered in the constitutively elastic analysis, marginally influencing the former, but more severely impacting the latter. Additionally, the prediction of the peak bulge expansion location in the E+ and B* shows a slight deviation against the experimental measurement. Insufficiently accurate descriptions of the geometry and relatively coarse mesh definitions are anticipated to induce an excessively stiff response that hinders the general vessel compliance in the meridional direction.

Lastly, the boss axial displacement appears as a variable that comprehensively illustrates the complex deformational response of the CPV, dilating the influence of the stacking sequence definition in the cylinder and the dome transition regions. The magnitude of the meridional strain component in the cylinder and the change of dome shape during deformation are presented to relate directly with the measured displacement of the boss. At the same time, the progression of damage in these regions foretells increased vessel compliance, leading to load redistribution and a further change of the dome shape. As it is also relevantly influenced by the progression of damage, the boss axial displacement appears as a valuable indicator of whether a simulation is depicting a realistic deformational response of the vessel. In this regard, the trend of the predictions at low-pressure stages appears to consistently underestimate the experimental results, hence also illustrating an excessively stiff response and hindering its adequate validation.

8

Prediction of First-Ply-Failure

The constitutively elastic response of a CPV inherently disregards the non-linearities related to the onset and progression of damage; nonetheless, it still permits to estimate the triggering of failure from the prevailing stress and strain states. This prediction is based on the mechanics of failure of composite materials and, ultimately, correlates these with the mechanical response of the homogeneous orthotropic FE elements. Failure criteria are based on the distinct matrix and fiber degradation modes of composite structures, where the first characterizes by gradually diminishing stiffness as the bearing capability increases, and the second releases high amounts of energy while it abruptly collapses. Consequently, the evaluation of failure criteria allows predicting the burst of the CPV by the load stage at which fibers are expected to break.

The objective of this chapter is to weigh the applicability of FPF criteria in estimating the burst pressure of CPVs. This prediction is evaluated against the constitutively elastic results of chapter 7, where the predicted burst pressures and their corresponding collapse modes are correlated with experimental data. To this purpose, the chapter introduces the mechanisms of failure in composite materials in section 8.1 as a foundation for the predicted failure pattern discussion. Following, failure criteria relevant for their use in CPVs is revised in section 8.2 regarding the assumptions they make and the level of analysis complexity they require. Ultimately, results for the W1A, E+, and B* stacking sequences are presented and discussed relative to their damage patterns in section 8.3.

8.1. Introduction to Failure in Composite Materials

The appearance of failure in a composite structure can be regarded as the material degradation triggered after reaching some of its strength limits. The composite characteristics of the material entail that multiple degradation processes may coexist, allowing to redistribute the loading while still increasing the bearing capacity internally. Various authors have reported this progressive degradation process during the testing of CPVs, [10, 70, 73], and stands out as a relevant feature in the determination of the burst location (cylindrical vs. dome region) and the robustness of that estimation.

As it is known, composite materials are formed by fibers that are embedded in a polymeric matrix, where the fibers themselves have much higher stiffness and strength than the surrounding resin. However, the resin has an essential role as a binder permitting the fibers to carry load collaboratively, bridging the load paths between yarns of broken fibers and introducing transverse strength. Whenever a composite structure gets increasingly loaded in tension, the resin ensures there is a shear load transfer between the fiber bundles. If fibers are defective from the production process, fiber and resin debond, or the resin reaches its shear strength, the load is increasingly concentrated on the pristine fibers left. As this concentration process develops, more and more fiber yarns fail, leading to a rapidly unstable collapse process. It is observed that the tensile failure process is, after all, fiber orientation dominated, which permits to establish a good correlation with the specific test-determined material strength properties.

If transverse or shear dominated loading exist, the resin is instead the element that maintains the integrity of the part. It ensures that the applied load is transferred to the fibers, although, in opposition to the tensile loading case, these lose their bearing capacity when degradation in the matrix happens.

Thus, the limited strength of the resin results in a somewhat restricted structural performance of the component under these types of loading. A similar situation arises when compression is applied, as the fibers show low lateral stability. This loading case requires the resin to bear the load in the fiber yarns seeking to deform out-of-plane that, with the initiation of matrix degradation, leads to instabilities of the type of kink bands. These elements appear as localized shear deformation belts and involve a complex combination of failure modes, including further matrix cracking, compressive fiber breaking, and fiber-matrix debonding. Therefore, the more complex and erratic matrix dominated failure modes make the involved resin strength properties not as consistently determined as the fiber dominated ones.

Coherently with the internal pressure loading of CPVs, the composite material fundamentally experiences tensile stress in the axial and tangential directions, whereas radial compression exists through-the-thickness. The type of failure in the fibers is, as a result, predominantly tensile, being the helical and circumferential plies correspondingly aligned with the prevailing loading directions. However, dome to dome axial load transmission results in transverse tensile stress in the circumferential ply stack, whereas tangential expansion in the dome transition region has an equivalent effect in the helical layers. Therefore, tensile matrix failure is expected in these cases, although, concerning the inner plies, the pure tensile transverse loading turns into a biaxial condition. This effect is caused by the combined radial compressive and transverse tensile stress components, hence possibly shifting the critical failure mode as the radial stress increases towards the inside. In this case, the critical fracture plane may deviate from the pure through-the-thickness direction, also impacted by the longitudinal shear generated by the particular helical layers fiber orientation.

The influence of the transverse and shear stress sign on the matrix constituent crack growth is illustrated in fig. 8.1. In the case of tensile loading, and even if subjected to longitudinal shear loading, the fracture planes follow orientations perpendicular to the loading direction. Notwithstanding, if compressive loading and shear coexist, the fracture surface shows an angle φ with the loading direction that varies from 0 to 53 degrees. This angle variation has a direct impact on how cracks develop through the thickness and connect with existing delaminations, thus impacting the damage tolerance of the component [118, 119]. The angle limit of 53 degrees can be experimentally determined in pure loading conditions and responds to the critical shear plane in the presence of surface friction (increased angle over the 45 degree maximum shear plane).

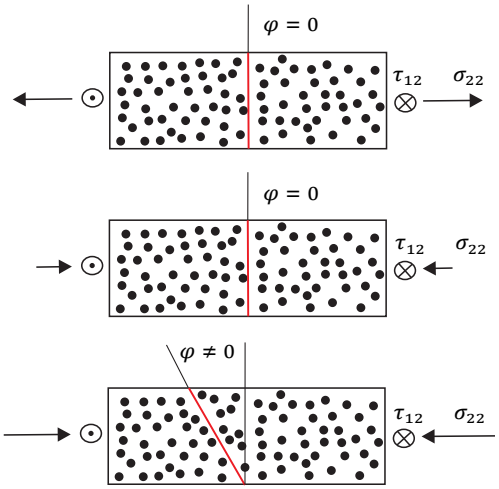


Figure 8.1: Representation of matrix cracks depending on the sign of the transverse stress (adapted from [119])

Correspondingly, delaminations consist of the degradation of the interface between the plies that constitute the CPV stack. The existence of interlaminar stress triggers failure, arising to maintain mechanical equilibrium in the presence of through-the-thickness in-plane stress gradients, [120]. These stress components are more relevant in thick stackups of plies with the same layer orientation because the load that ensures strain compatibility has to be transferred through a lower number of interfaces. Concerning CPVs, helical and circumferential plies tend to be grouped to minimize transition winding circuits that, as a consequence, increase the likelihood of delamination failures by leading to relatively thick layer stacks. Additionally, interlaminar stress also arises from the stiffness mismatch between helical and circumferential plies at their drop location. This mismatch generates different load patterns

for each of the layers and ultimately requires interlaminar stress to ensure displacement continuity. Mainly, helical plies carry most of the load in the axial direction meaning that the composite mechanical response is ensured by generating shear meridional stress in the circumferential ply interface. Then, depending on whether the helical ply is situated above or underneath the circumferential counterpart, an additional tensile or compressive normal stress component is created, potentially leading to a delamination onset.

8.2. Criteria for Failure Prediction

8.2.1. Fundamental Failure Criteria

Failure criteria define the strength limits of the composite material and, as a consequence of the intricate damage process, generally refer to the various failure modes arising from loading. They are represented at the ply level by assuming homogeneous orthotropic material properties at each discretized element, where the main complexity resides in the interaction of the various stress components that trigger the damage process. The onset of material degradation is regarded as the FPF, whereas its subsequent evolution is subjected to various modeling approaches of increased elaboration. Alternatively to the ply level failure determination, the micromechanical modeling of damage initiation predicts failure from the individual constituent response, [72, 73]. Thus, the averaged element responses of the fibers and matrix are extrapolated to the ply level, where they define an equivalent macromechanical behavior that reproduces the damaged state of the component.

Withal, the most fundamental criterion for the FPF is defined by the Maximum Stress. This prediction does not account for the interaction of the various stress components in the creation of damage, although it still allows identifying distinct failures modes. It can be expressed as

$$\frac{\sigma_{11}}{X_T} = 1, \quad \frac{\sigma_{22}}{Y_T} = 1, \quad \frac{\sigma_{11}}{Y_C} = 1, \quad \frac{\sigma_{22}}{Y_C} = 1, \quad \frac{|\tau_{12}|}{S} = 1, \tag{8.1}$$

where the subscripts σ_{11}, σ_{22} and τ_{12} refer to the in-plane longitudinal (fiber direction), transverse and shear components of the stress tensor. Correspondingly, the parameters X_T and X_C indicate the longitudinal strength properties of the material in tension and compression. Likewise, Y_T, Y_C and S specify the in-plane tensile and compressive transverse strengths and the in-plane shear strength.

Among the most generally used interactive failure criteria is the so-called Tsai-Wu, [121]. In opposition the Maximum Stress, the Tsai-Wu defines a quadratic interaction criterion that does not differentiate between failure modes

$$F_1\sigma_{11} + F_2\sigma_{22} + F_3\tau_{12} + F_4\sigma_{11}^2 + F_5\sigma_{22}^2 + F_6\tau_{12}^2 + 2F_7\sigma_{11}\sigma_{22} = 1, \tag{8.2}$$

with

$$\begin{aligned} F_1 &= \frac{1}{X_T} + \frac{1}{X_C}, \quad F_2 = \frac{1}{Y_T} + \frac{1}{Y_C}, \quad F_3 = 0, \\ F_4 &= -\frac{1}{X_T X_C}, \quad F_5 = -\frac{1}{Y_T Y_C}, \quad F_6 = \frac{1}{S^2}, \\ F_7 &= \frac{1}{2Y_T}\left[1 - (F_1 + F_2)\,Y_T - (F_4 + F_5)\,(Y_T)^2\right] \end{aligned} \tag{8.3}$$

allowing to include the contributions of distinctive tensile and compressive strengths in an all-inclusive damage variable. In the presented definition, the factor F_7 is regarded to this end as the interaction parameter.

8.2.2. Puck's Failure Criteria

Further developments are presented by the Puck criterion, [87], where a clear differentiation of modes is made. Not only longitudinal to transverse directions are separated, but failure in the resin is categorized according to the modes depicted in fig. 8.1. This classification allows accounting for the interaction of the stress components that cause different orientations of the matrix failure plane and, in extension, allowing to consider combined loading states. Their longitudinal failure criterion is presented to be fiber dominated, although with the consideration that under combined loading, the Poisson effect of the

transverse stress is not negligible. It is argued that the material fails whenever the stress ”in the fibers” reaches the state where the composite fails at uniaxial loading. Therefore the criteria are expressed as:

$$\frac{1}{\pm X_{T,C}}\left[\sigma_{11}+\left(\nu_{21}-\nu_{21,f}m_{\sigma f}\frac{E_{11}}{E_{11,f}}\right)(\sigma_{22}+\sigma_{33})\right]=1, \tag{8.4}$$

with ν_{21} indicating the Poisson effect in the longitudinal direction because of transverse loading. The longitudinal and transverse stiffness are presented as E_{11} and E_{22}, which, correspondingly, allow to define the orthotropic relation $\nu_{12}/E_{22} = \nu_{21}/E_{11}$. The subscripts $\cdot_f$ refer to variables applicable to the fibers alone, while σ_{22} and σ_{33} show the transverse stress components in the in-plane and out-of-plane directions. It is assumed that the strain at the fiber and matrix varies at the micromechanical level because of the modulus difference. Nevertheless, a biaxial strain state seems to exist in reality in the matrix close to the interface with the fibers, [87]. This effect is arbitrarily accounted in the failure criterion by the factor $m_{\sigma f}$, that is proposed to be 1.1 for CFRPs. Furthermore, the tensile (positive) or compressive (negative) strengths are applied whenever the result of the expression in brackets refers to the corresponding stress state, indicated by a likewise positive or negative value.

Although the criterion presented by Puck is considerably more sophisticated than the Maximum Stress or the Tsai-Wu criteria, it lacks to account for the influence of shear stress on the compressive failure case. This aspect leads to the fiber kinking flaw and its subsequent matrix failure, resulting in relevantly lower strengths than the predicted by pure compressive fiber damage, [87]. Moreover, Puck’s criterion does not account for the constraining effect that thin plies experience when they are embedded within the laminate, and that affects the transverse and shear strengths [108].

The development of the matrix damage criteria results from the experimentally observed interaction between transverse and shear stress, and their fracture surface orientations. On the one hand, the combined effect of these two components is observed to lead to a lower strength than the pure transverse and pure shear values. On the other hand, a moderate compressive transverse stress allows to sustain a higher shear stress than the pure mode strength. To this is added that there is a critical ratio of compressive transverse and shear stress at which the resin fracture angle deviates from 0 to 53 degrees. If these effects are illustrated in a failure envelope, a diagram like the one in fig. 8.2 is obtained. Here, Y_C^A refers to the compressive transverse strength at which the fracture plane starts to deviate, while p_{22}^c indicates the slope of the corresponding failure envelope for transverse compression, approximated to 0.25 for CFRP. The different matrix failure modes are classified as

- *Mode A*. Defined by transverse tensile and longitudinal shear stress. Fractures run in the thickness direction and are separated from each other because during the tensile loading cracks nucleate wherever voids or stress concentrations exist. From a macroscopic perspective, there is a gradual degradation of the transverse and shear stifness;

$$\sqrt{\left(\frac{\tau_{21}}{S}\right)^2+\left(1-p_{21}^t\frac{Y_T}{S}\right)^2\left(\frac{\sigma_{22}}{Y_T}\right)^2}+p_{21}^t\frac{\sigma_{22}}{S}=1 \quad \text{for} \quad \sigma_{22}\geq 0, \tag{8.5}$$

  with p_{21}^t equal to 0.3.

- *Mode B*. This mode is controlled by the longitudinal shear stress, where the fracture plane occurs in the perpendicular direction to the tensile stress associated with the shear loading. As a simultaneous compressive transverse stress also exist, the cracks do not tend to open and the stiffness degradation is less significant than in *Mode A*;

$$\begin{gathered}\frac{1}{S}\left(\sqrt{\tau_{12}^2+(p_{12}^c\sigma_{22})^2}+p_{12}^c\sigma_{22}\right)=1 \quad \text{for} \quad \sigma_{22}<0 \quad \text{and} \quad 0\leq\left|\frac{\sigma_{22}}{\tau_{12}}\right|\leq\frac{\tau_{23}^A}{|\tau_{12}^c|}\\ \tau_{23}^A=\frac{S}{2p_{12}^c}\left(\sqrt{1+2p_{12}^c\frac{Y_C}{S}}-1\right); \quad \tau_{12}^c=S\sqrt{1+2p_{23}^c}; \quad p_{23}^c=p_{12}^c\frac{\tau_{23}^A}{S},\end{gathered} \tag{8.6}$$

  with p_{21}^c equal to 0.2.

- *Mode C*. In this case the compressive transverse strength dominates and the fracture surface angle gradually increases up to 53 degrees. Moreover, the generated matrix cracks can be easily connected with each other through bridging delaminations;

$$\left[\left(\frac{\tau_{12}}{2(1+p_{23}^{c}S)}\right)^{2}+\frac{\sigma 22}{Y^{C}}^{2}\right]\frac{Y^{C}}{(-\sigma_{22})}=1 \quad \text{for} \quad \sigma_{22}<0 \quad \text{and} \quad 0\leq\left|\frac{\tau_{12}}{\sigma_{22}}\right|\leq\frac{|\tau_{12}^{c}|}{\tau_{23}^{A}}, \tag{8.7}$$

where $p_{12}^{t,c}$ and $p_{23}^{t,c}$ are defined as the slopes of the corresponding failure envelopes for in-plane shear and out-of-plane shear, [87].

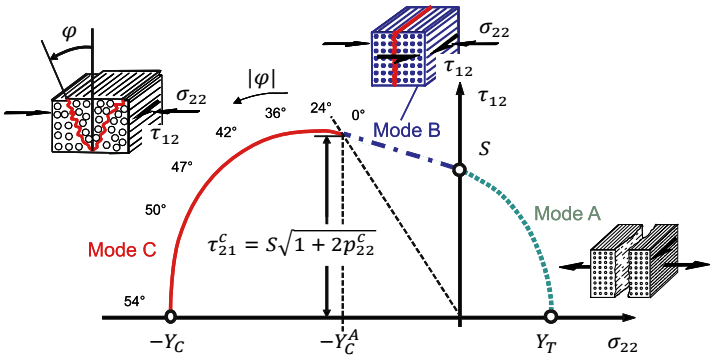


Figure 8.2: Failure envelope for the interaction of the transverse and shear in-plane stress with the identification of the various intralaminar matrix failure modes (adapted from [87])

8.2.3. LaRC04 Failure Criteria

Because of the limitations of Puck's criterion, and in the context of an industry that seeks advancements in the numerical modelling capabilities regarding composites application, a 'World Wide Failure Exercise' was proposed to trigger experts in further detailing theories for the prediction of failure, [86] . In due time this led, among others, to the development of the Langley Research Center (LaRC) theory family, [108, 109, 122, 123]. This family of criteria is based on the physics of failure and aims at providing a comprehensive solution to a generally combined loading condition. In the case of the LaRC04 criteria presented by Pinho et al. [109], this is achieved by proposing six different criteria modes that depend on empirical variables. These include the three-dimensional stress state of a representative element and allow one to identify the fracture planes with further generality than with the combined transverse and shear stress. Among its most relevant characteristics, a non-linear shear behavior is accounted. As far as fiber kinking is concerned, it is assumed that matrix degradation is the trigger of failure, taken to be sensitive to the fiber misalignment angle because of manufacturing limitations and loading deformation.

As follows, the six identified modes are divided between the three transverse and the three longitudinal failure mechanisms. The three LaRC04 transverse failure modes correlate with the ones presented by Puck, [87], and are defined for the tensile and compressive cases, wherein the latter, a distinction is made to whether biaxial or shear loading dominates. In the case of the longitudinal failure modes, a maximum stress tensile fiber failure criterion is defined, in contrast to the formation of fiber kinks under compressive loading. When longitudinal compression controls, failure is predicted by evaluating the transverse failure criteria, either tensile or compressive, in the plane where kinking takes place. In this case, a preliminary check in the fiber kinking prediction is made to determine if instability is prompted instead. This situation arises when the linear shear loading slope does not intersect the non-linear material response, as defined by the limit state in the rightmost case of fig. 8.3. The different failure modes are classified as:

- *Matrix tensile failure*. Defined as a polynomial mixed-mode criterion expressed in terms of the stress intensity factors. These are represented by the quotient of transverse ply stress to ply strength, where g is the ratio of mode I to mode II fracture toughness. An additional element is

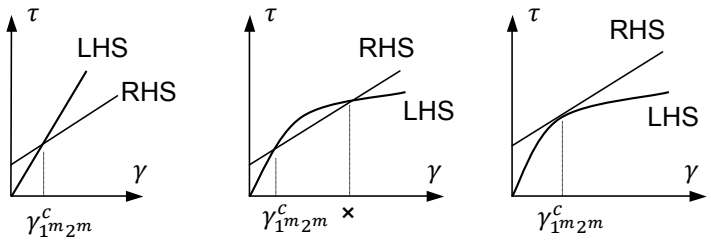


Figure 8.3: Representation of the combination of a linear shear loading law (LHS) and a shear material response law (RHS) when this is linear (left), non-linear with two intersecting points (center) and non-linear and tangential (right) (taken from [109])

added to include the influence of in-plane and through-the-thickness shear;

$$(1-g)\frac{\sigma_{22}}{Y^T}+g\left(\frac{\sigma_{22}}{Y^T}\right)^2+\frac{\Lambda_{23}^o\tau_{23}^2+\chi(\gamma_{12})}{\chi(\gamma_{12}^u)}=1 \quad \text{for} \quad \sigma_{22}\geq 0, \tag{8.8}$$

where $\chi(\gamma_{12})$ indicates the elastic energy accumulated by shear deformation γ_{12}, the superscript in γ_{12}^u refers to the shear strain at failure, and Λ_{23}^o is an elastic constant derived from the material in-plane properties, [109].

- *Matrix compressive failure*. This mode is developed from the criteria of Puck, [87], by accounting for the combined effect of tangential stress in the transverse and longitudinal directions. As matrix compression is shear dominated the criteria is alternatively evaluated for the fracture plane switching crack surface φ.
  - Uniaxial compression

$$\left(\frac{\tau^T}{S^T-\eta^T\sigma_n}\right)^2+\left(\frac{\tau^L}{S^L-\eta^L\sigma_n}\right)^2=1 \quad \text{for} \quad \sigma_{22}<0 \quad \text{and} \quad \sigma_{11}\geq -Y^C, \tag{8.9}$$

    where η^T and η^L are the friction coefficients in the transverse and longitudinal directions that impact the effective material strength. The transverse shear strength is determined from the pure uniaxial compression as indicated by Dávila et al. [122], while the transverse and longitudinal properties are assumed to follow the relation $\eta^L/S^L=\eta^T/S^T$. The stress components in the fracture plane are obtained from the rotation of the stress tensor in the range $[-\pi/2,\pi/2]$,

$$\begin{aligned}\sigma_n&=\frac{\sigma_{22}+\sigma_{33}}{2}+\frac{\sigma_{22}-\sigma_{33}}{2}\cos 2\alpha+\tau_{23}\sin 2\alpha\\ \tau^T&=\frac{\sigma_{22}+\sigma_{33}}{2}-\frac{\sigma_{22}-\sigma_{33}}{2}\sin 2\alpha+\tau_{23}\cos 2\alpha\\ \tau^L&=\tau_{12}\cos\alpha+\tau_{31}\sin\alpha\end{aligned} \tag{8.10}$$

  - *Biaxial compression*

$$\left(\frac{\tau^{Tm}}{S^T-\eta^T\sigma_n^m}\right)^2+\left(\frac{\tau^{Lm}}{S^L-\eta^L\sigma_n^m}\right)^2=1 \quad \text{for} \quad \sigma_{22}<0 \quad \text{and} \quad \sigma_{11}<-Y^C, \tag{8.11}$$

    being n, T and L the directions normal, transverse to the fibers and parallel to the fibers within the matrix compression fracture plane φ, [109].

- *Fiber tensile failure*. Based on a maximum stress criterion;

$$\frac{\sigma_{11}}{X^T}=1 \quad \text{for} \quad \sigma_{11}\geq 0, \tag{8.12}$$

- *Fiber compressive failure*. Failure in this mode is predicted by evaluating the corresponding matrix failure criteria in the plane where kinking takes place ψ. This is defined by the combination

of transverse and through-the-thickness stress that favors crack growth the most, which is expressed as $\tan 2\phi = 2\tau_{23}/(\sigma_{22} - \sigma 33)$, [109]. Local stress components are calculated within this plane that are, furthermore, subjected to the fiber misalignment because of the existing shear loading in the kinking plane. This misalignment determines the local matrix stress state and is obtained from iteratively solving the generally non-linear shear constitutive response that is, for instance, represented by the law of Ramberg and Osgood [124]. Following, depending on whether tensile of compressive matrix stress exist in the misalignment frame, two criteria arise;

– *Matrix tensile stress in the fiber misalignment frame*

$$(1-g)\frac{\sigma_{2^m2^m}}{Y^T} + g\left(\frac{\sigma_{2^m2^m}}{Y^T}\right)^2 + \frac{\Lambda_{23}^o \tau_{2^m3^m}^2 + \chi(\gamma_{1^m2^m})}{\chi(\gamma_{12}^u)} = 1 \quad \text{for} \quad \sigma_{11} < 0 \quad \text{and} \quad \sigma_{2^m2^m} \geq 0, \tag{8.13}$$

wherein the superscripts $\cdot^m$ refer to the stress components in the misalignment frame.

– *Matrix compressive stress in the fiber misalignment frame*

$$\left(\frac{\tau_{1^m2^m}}{S^L - \eta^L \sigma_{2^m2^m}}\right)^2 = 1 \quad \text{for} \quad \sigma_{11} < 0 \quad \text{and} \quad \sigma_{2^m2^m} < 0, \tag{8.14}$$

Despite the more sophisticated failure criteria predicting damage onset under complex loading conditions, they do so at the expense of a considerably complex calculation process. The amount of required material properties increases with the level of sophistication, while their description also becomes more burdensome and costly. Consequently, the choice of a specific failure criterion needs to be based on whether the increased level of elaboration justifies the required by the purpose of the simulation.

8.3. Results and Discussion on Failure Prediction

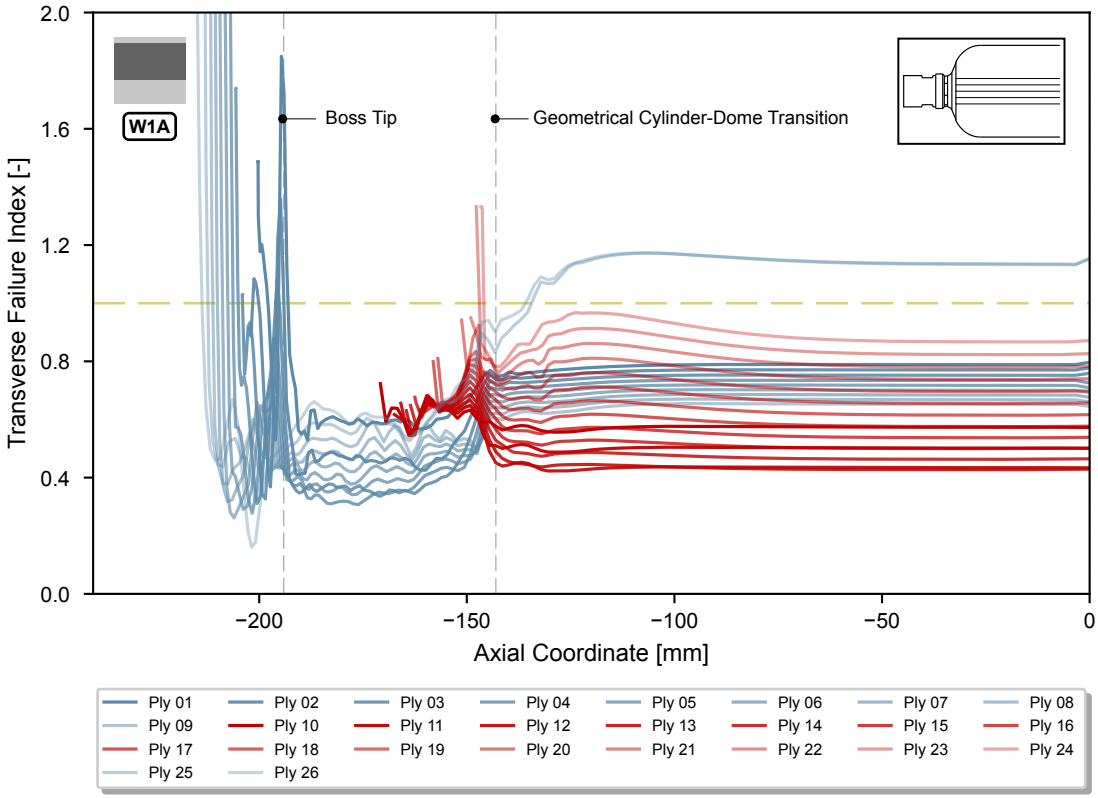
The evaluation of the failure likelihood directly results from the representation of the non-uniform stress of the CPV in its local material coordinates. It permits to express the relevant stress components in the fiber, transverse, and through-the-thickness directions while, furthermore, establishing the reference system on which the critical plane of fracture and its failure index is calculated.

Subsequently, the likelihood of damage onset is linked to the combination of stress that generates a critical constituent load condition. This material state is represented through the FPF estimations in section 8.2, where their good experimental correlation is ultimately subjected to the existence of material imperfections in the form of intralaminar porosity, fiber misalignment, faulty fiber-matrix bonding, and interlaminar voids. The origin of these discrepancies is not intrinsically modeled in a constitutively elastic response, albeit their existence permits to correlate the critical load paths in the component and to depict the influence of the spatial variation of material properties.

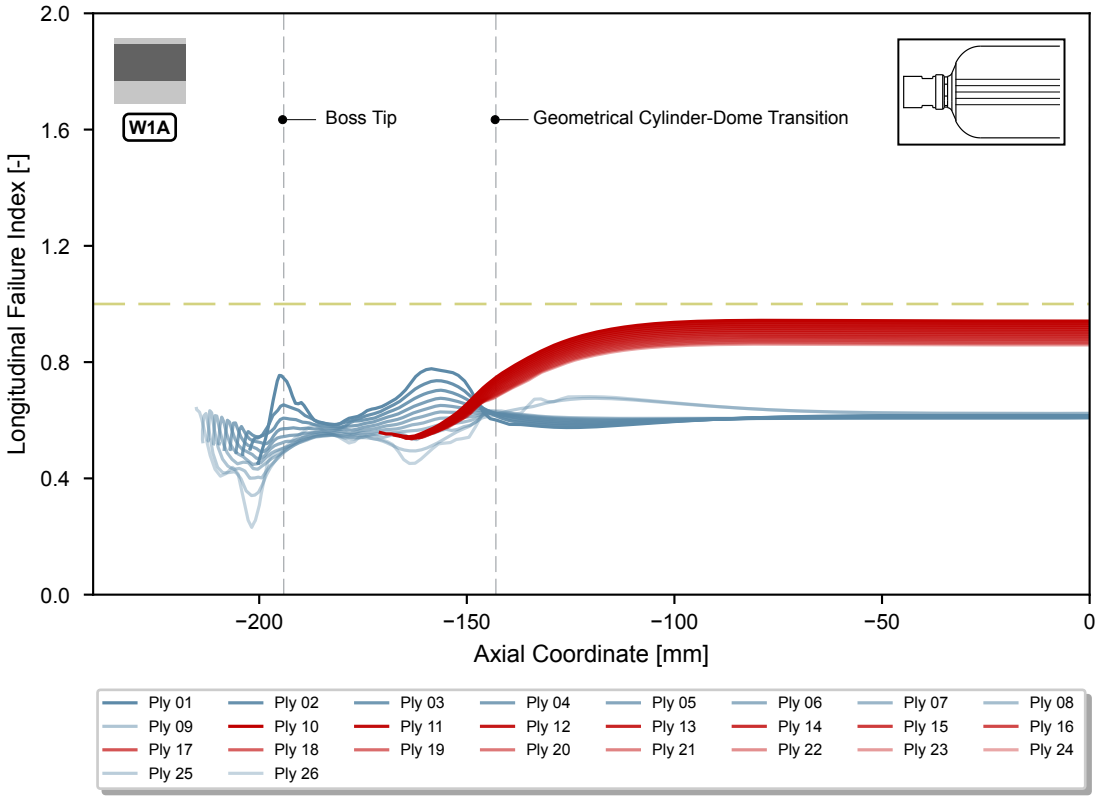
Results of failure criteria are presented in figs. 8.4, 8.6 and 8.8 along a meridional vessel path for the W1A, E+ and B* stacking sequences. These are comparatively shown for the matrix and fiber constituents, referring to the pressure stages representative of the degradation onset in the circumferential ply stack. Additionally, the matrix failure index field is illustrated along to the vessel geometry in figs. 8.5, 8.7 and 8.9, also indicating the alternative, tensile or compressive, forecast failure modes.

The pressure stages for failure triggering in the dome and cylindrical regions are reported in table 8.1 according to the material strength properties of table 7.1. Withal, a relatively lower material compressive strength $Y^C = 50.0$ MPa is considered, showing the potential change of failure mode with the through-the-thickness position. The definition of this material strength results from a late identification of the actual compressive properties of the material and an initially too cautious strength assumption. It limits the experimental correlation of results through-the-thickness but, complementarily, shows the sensitivity of the failure mode to this variable.

Both the criteria of Puck and LaRC04 are weighed in the matrix damage onset prediction, while Puck's criterion is solely regarded concerning fiber breakage. The former is considered because of the convoluted combination of biaxial transverse and shear stress components that influence matrix degradation, therefore justifying the assessment of the presented criteria applicability. The latter is lastly preferred by cause of the LaRC04 maximum longitudinal tensile stress criterion, disregarding the Poisson effect contribution to the fiber constituent loading.



(a) Matrix tensile failure criteria according to LaRC04, [109], at a load pressure of 35.1 MPa



(b) fiber tensile failure criteria according to Puck, [87] at a load pressure of 160 MPa

Figure 8.4: Through-the-thickness matrix and fiber failure criteria of the of the W1A stacking sequence

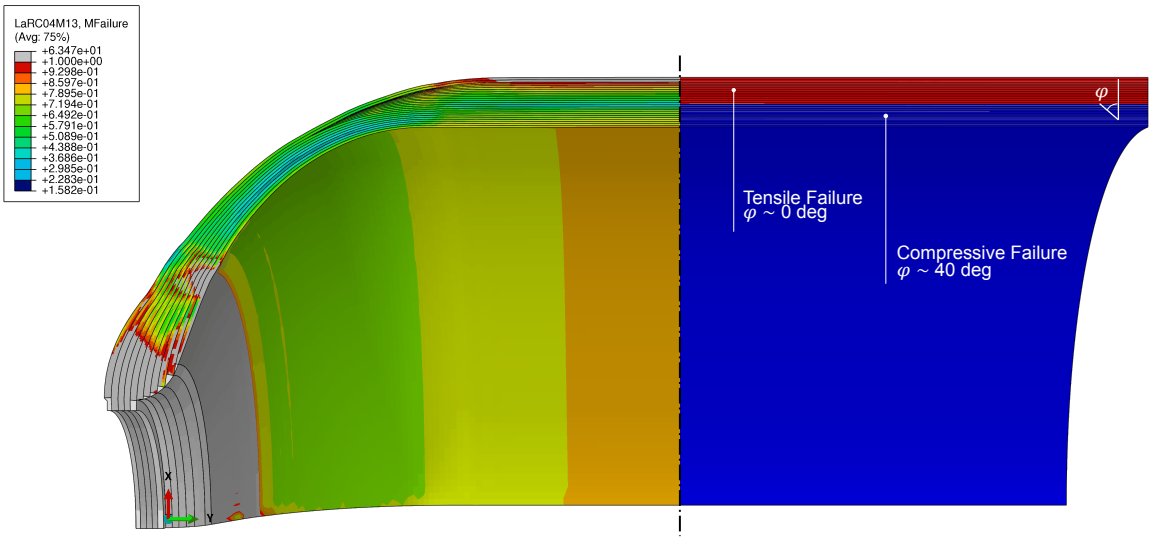


Figure 8.5: LaRC04 matrix tensile failure field of the W1A stacking sequence at a load pressure of 35.1 MPa

8.3.1. Prediction on the W1A Stacking Sequence

Matrix failure criteria evaluated in the W1A stacking sequence is referred in figs. 8.4a and 8.5. These indicate that outer plies are likely to fail first, starting with the exterior helical layers and following with the circumferential ply stack. The likelihood of transverse failure in the hoop layers reduces towards the inside because of an analogous trend in the axial stress component. This stress component is linked to the meridional load transferred from dome to dome and the through-the-thickness distribution induced by stacking sequence unbalance. Moreover, it is also linked to the tensile tangential loading and the radial compressive stress experienced due to the thick wall effect. The first two promote tensile meridional stress components in the inner layers, while the last one induces a compressive reaction through the Poisson effect. As a result, the axial stress component is of tensile type and larger on the outer layers, where the influence of the radial stress is minimum.

The matrix failure index is presented to relatively increase again in the inner circumferential plies. The combined meridional tensile and radial compressive stress components create a biaxial stress state in the material, hence shifting the material degradation mode towards a compressive type. As illustrated in fig. 8.5, this happens in planes at an angle with the through-the-thickness direction and further extends in the stack of inner helical plies. These also experience in-plane shear stress, therefore, causing their matrix failure index to increase over the inner circumferential plies. The shear loading condition is a direct consequence of the misalignment of the helical ply fibers relative to the principal loading direction. In this regard, the shear stress allows for deviating the loading, meridional and tangential, to the more stiff fibers constituents, while nonetheless, detrimentally impacting the transverse loading condition of the ply.

In the dome region, helical plies progressively change directional stiffness; at the same time, the pressure loading component also shifts from radial to axial. The fiber orientation of the helical layers develops into better aligned with the internal pressure resultant; thus, trading matrix loading to fiber stress and decreasing the likelihood of transverse failure. Still, this tendency gets truncated by the subsequent load path change with the boss interaction. At this location, helical layers feature orientations orthogonal to the meridional direction, making the transverse stress components drastically increase. This effect is exacerbated by the through-the-thickness shear deformation of the composite reinforcement next to the boss, causing matrix damage to be predicted since early loading stages.

Results reported in table 8.1 indicate that Puck's predictions are marginally more conservative than the outcome of LaRC04. In the dome region, failure is predicted at a significantly early stage, where this is justly impacted by the concentration of stress in the contact between composite reinforcement and boss brim tip. Following, this is detailed for the outer helical layers, and the circumferential stack, being the corresponding trends towards failure coherent with the discussed higher likelihood on the outer side. Withal, the presented failure index in the circumferential ply stack disregards the unreasonable

distortion of results because of numerical singularities. These, are observed in the dome transition region of fig. 8.4a, where drastic increases in the failure index are predicted at the circumferential ply drop location. These appear to develop from the lousy element aspect ratios of the circumferential layer ends, which, besides decreasing accuracy, are deemed acceptable in light of the more tractable computational cost.

Fiber failure in the W1A layup is ultimately predicted in the cylindrical region, thus relating to a burst event on which this collapse mode prevails. This is depicted in fig. 8.4b as a result of the high tangential stress occurring in the circumferential ply group. In this case, the innermost circumferential layers are critical, logically deriving from the increased stress state of the inner surface that results from the thick cylinder wall condition. Correspondingly, helical layers are not that severely loaded in the fiber direction. The axial loading they experience in the cylinder is low relative to the group thickness, whereas, instead, the matrix constituent carries the loading in the tangential direction. This predisposition tends to invert in the dome transition region, where the gradual drop of circumferential plies and the matching change of the helical layers fiber orientation, achieve a smooth switch in the directional stiffness.

In the dome transition region of the W1A stacking sequence, the gradual directional stiffness change shows a longitudinal failure index reduction in the circumferential ply stack in exchange for an analogous increase of the helical one. The continuous orientation shift of the latter leads to a more advantageous distribution of stiffness in the lower dome quarter, where meridional bending transforms into meridional membrane loading. This shift causes the longitudinal failure index gradient between the inner and the outer plies to reduce before the influence of the boss becomes apparent and alters the load path. On the one side, the contact between the composite reinforcement and the boss brim shows a relatively high likelihood of developing a narrow fiber breakage on the innermost layer. On the other side, the fiber failure criterion in the dome end next to the boss stagnates, resulting from the tangential expansion restrain of the metallic boss connection.

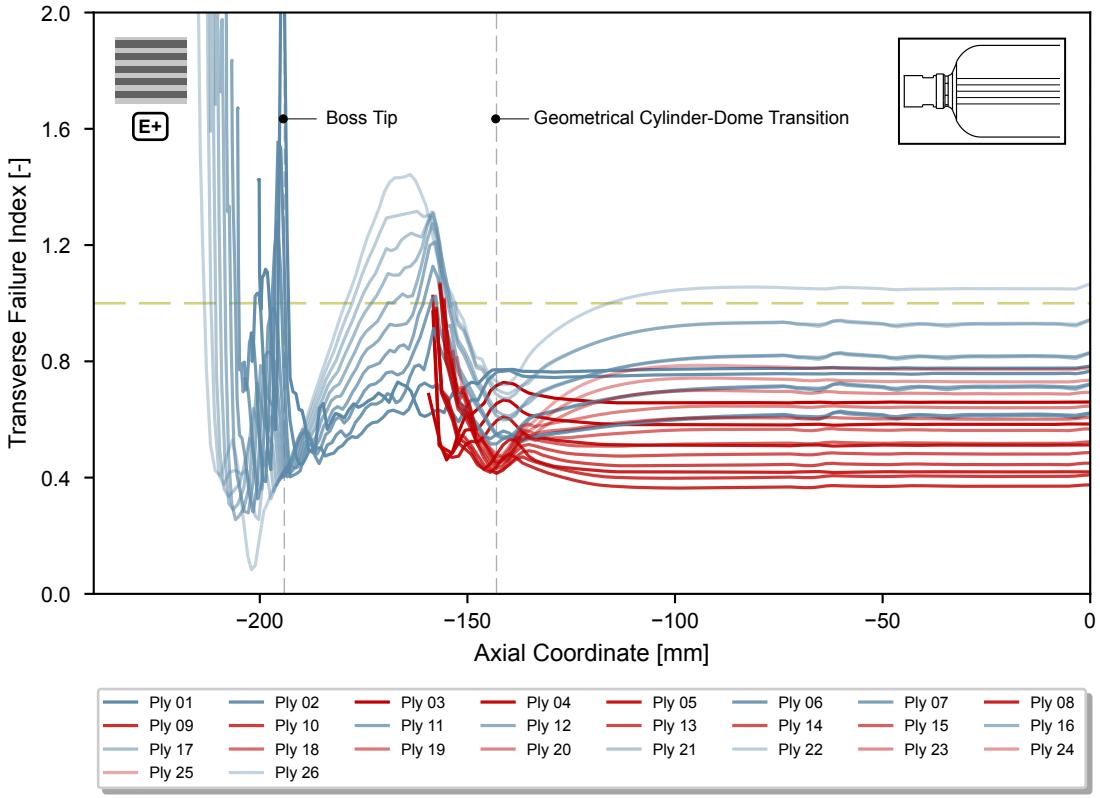
8.3.2. Prediction on the E+ and B* Stacking Sequences

Concerning the cylindrical regions of the E+ and B* stacking sequences, comparable trends to the W1A configuration are presented in figs. 8.6a and 8.8a. Degradation is predicted first on the outer layers, with a decreasing transverse failure index towards the inside, until radial compression overrules and matrix damage is predicted to initiate because of the latter. Particularly to the E+ case, the influence of the load distribution on the helical plies is depicted with a comparatively larger transverse failure index than their neighboring circumferential layers, hence dictated by the actual in-plane shear. Concerning the B* configuration, this distinction between helical and circumferential plies is alternatively depicted by the unpaired failure index estimation in the inner helical.

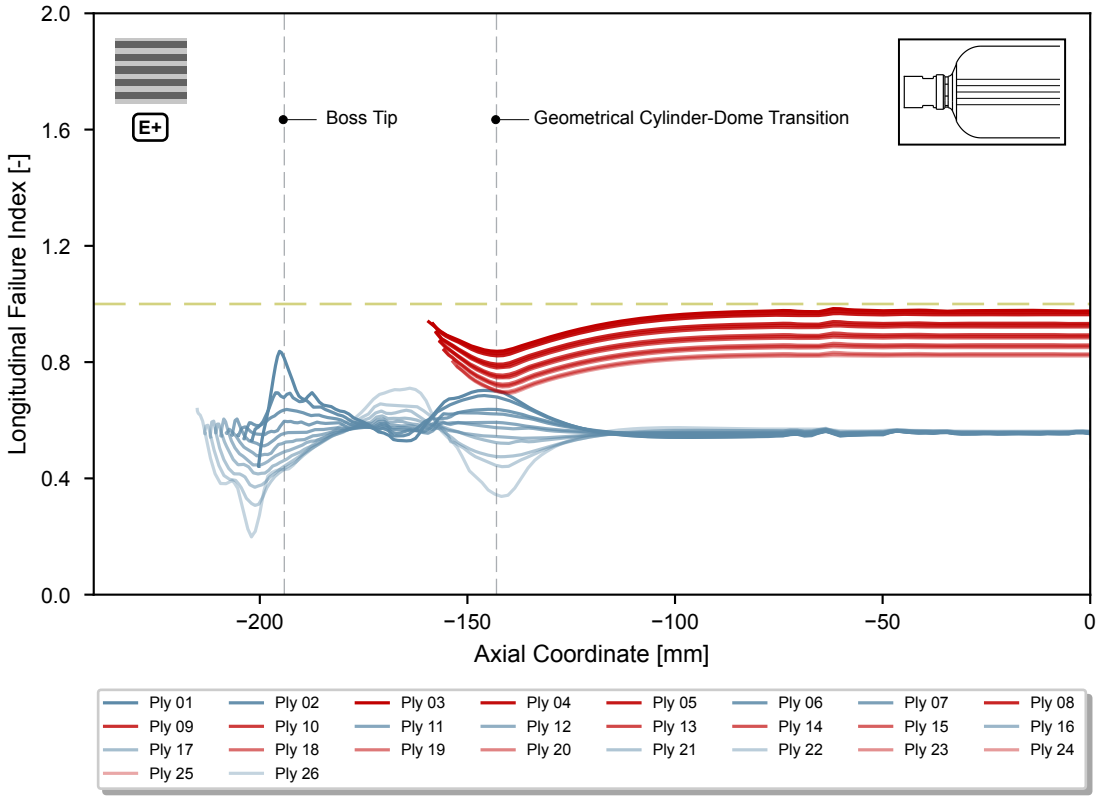
Triggering of matrix failure appears to happen later in the E+ and B* cases than in the W1A configuration, as detailed in table 8.1, also following a comparable tendency to the tangential stress and strain discussed in section 7.4. The respective more substantial tangential expansion experienced by a vessel that locates its high tangential stiffness plies towards the outside also generates more significant meridional stress components. Therefore, failure in the outer plies in the cylinder is predicted earlier in these cases, as the magnitude of the meridional stress also influences damage onset. This trend is predicted by both the Puck and LaRC04 failure criteria, where the first stands as lightly more conservative.

The sudden tangential stiffness drop of the E+ and B* vessel configurations characterize by generating a protruded expansion in the dome transition region. The lack of high tangential stiffness circumferential or high angle helical plies requires the low hoop stiffness helical layers to carry the applied loading in the corpus of the protrusion. The relatively seizable tangential expansion generates relevant shear and transverse stress components in these layers that, as shown in the depiction of figs. 8.6a and 8.8a, derives in a significant increase of the matrix failure index prediction. The likeliness of failure reduces in the lower dome quarter because the filament path orientation of the helical plies changes, although, along with the load path modification of the boss and composite reinforcement contact, it escalates again. Related to the bulge expansion, the lower dome quarter experiences considerable loading due to the opposing boss axial displacement and dome transition tangential expansion. This response generates high meridional stress and through-the-thickness shear, thus exhibiting a comparatively severe stress concentration at the contact between the composite reinforcement and the boss brim tip.

Likewise, the presence of a protrusion in the dome transition region of the E+ and B* configurations



(a) Matrix tensile failure criteria according to LaRC04, [109], at a load pressure of 35.1 MPa



(b) fiber tensile failure criteria according to Puck, [87] at a load pressure of 160 MPa

Figure 8.6: Through-the-thickness matrix and fiber failure criteria of the of the E+ stacking sequence

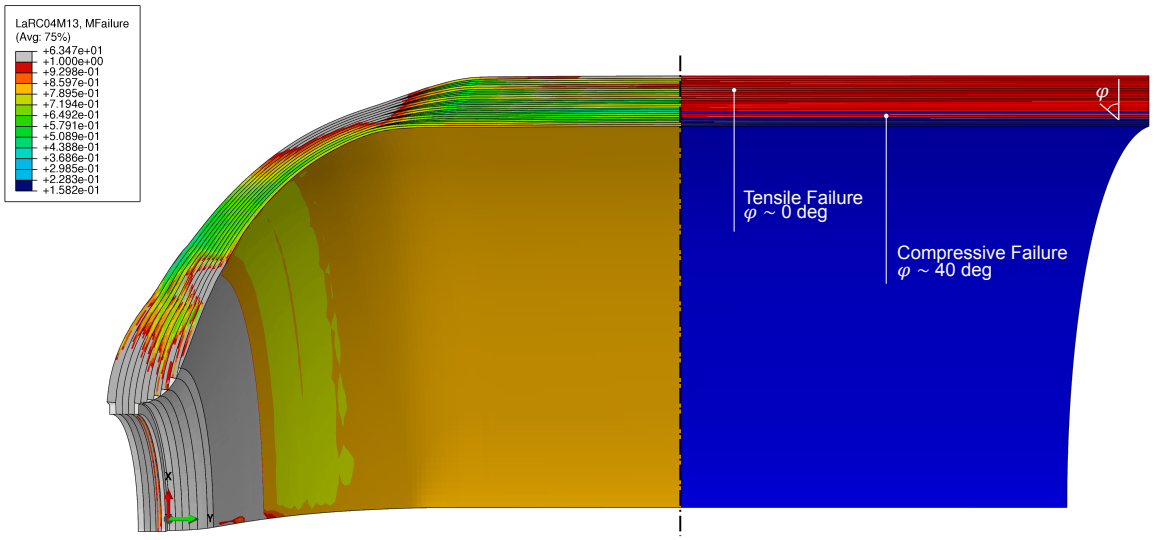


Figure 8.7: LaRC04 matrix tensile failure field of the E+ stacking sequence at a load pressure of 35.1 MPa

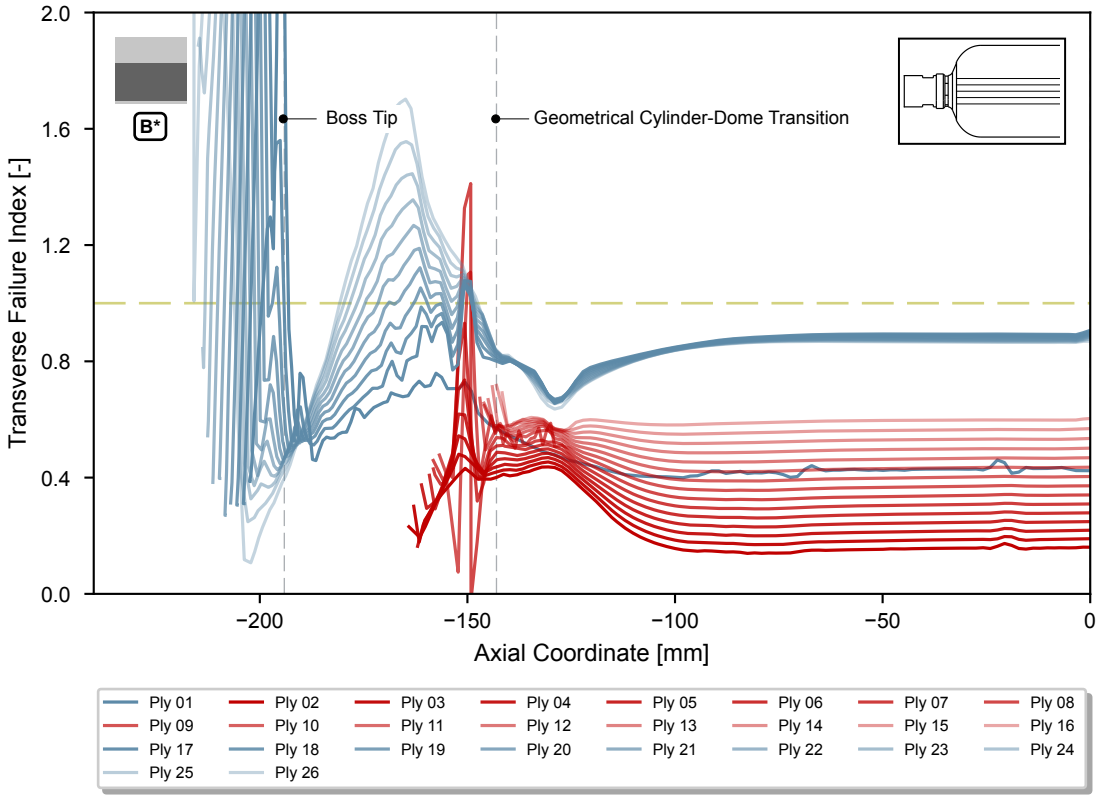
appears to relevantly influence the prediction of fiber failure in fig. 8.8b. Helical plies are subjected to the succession of outward and inward meridional bending, respectively experienced in the cylinder end and the dome transition region. Simultaneously, the tangential stress at the drop location of the circumferential stack plies increases similarly to the magnitude of the tangential expansion ahead. The first causes alternating longitudinal stress increases in the inner and outer helical plies, whereas the critical increase of the second possibly derives in an early component collapse. The magnitude of the bulge expansion appears to determine the extent to which this tangential stress increases, overruling the loading in the cylindrical region or falling short against it. This is the case of the B* architecture, where failure of the dome transition region is reported from experimental tests before the stress reserve in the cylinder is depleted. Such a tendency is anticipated to be further aggravated in the case progressive damage exists. The higher compliance of the helical layers within the existing bulge has a direct impact on the subsequent load redistribution and, thus, in the load carried by the remaining circumferential layers.

The trends towards the triggering of failure detailed in table 8.1 show, in a similar manner to the constitutively elastic response in section 7.4, that the E+ layup depicts an intermediate mechanical response between the W1A and the B* cases. It develops from the helical and circumferential ply groups staggering, which leads to the prediction of a lower likelihood of matrix failure in the cylinder than the W1A layup but more substantial than the B* case. Likewise, the formation of a mild protrusion in the dome transition region results, at this location, in a higher matrix damage likelihood than W1A, but lower than the B* stacking sequence. The E+ layup also shows a slightly higher tendency to collapse because of fiber failure in the cylinder than the W1A vessel, which is consistent with the higher tangential stress experienced by the former, already illustrated in fig. 7.12. Still, its sufficient hoop stiffness in the dome transition region prevents a premature fiber breakage at this location and renders comparatively larger reliability than the B* description.

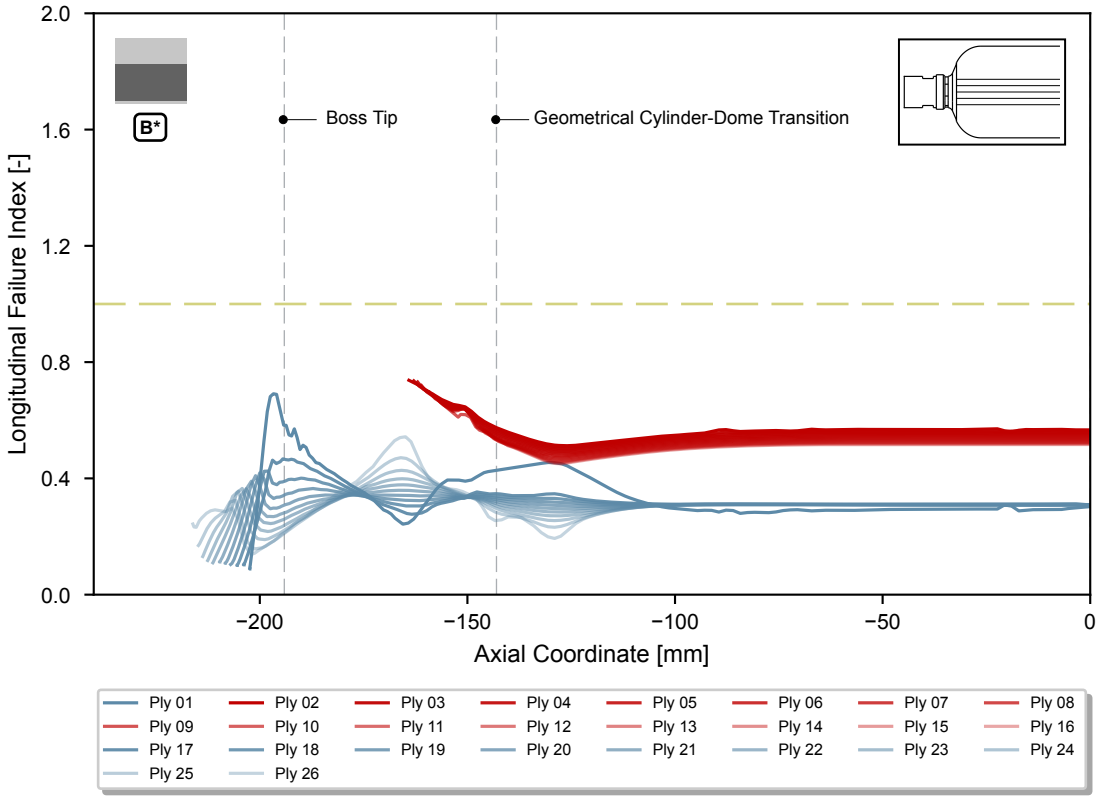
8.3.3. Correlation with Experimental Results

The failure triggering predictions are ultimately correlated with experimental results in table 8.2, reporting the mismatch relative to matrix crack onset in the cylindrical region and the final burst pressure. These are determined from AEs recording during pressurization tests, hence permitting to recognize the pressure of the circumferential stack damage onset through their high fracture energy released. Alternatively, matrix cracking in the helical layers cannot be unequivocally identified because the fiber orientation changes induce crack growth arrests, consequently corresponding with a diffuse damage progression type and non-easily tractable AEs.

Transverse damage onset in the circumferential stack is identified from the first AE that surpasses the threshold of 0.3 Pa amplitude in the range of 5 to 75 MPa internal pressure. Still, this is subjected



(a) Matrix tensile failure criteria according to LaRC04, [109], at a load pressure of 35.1 MPa



(b) fiber tensile failure criteria according to Puck, [87] at a load pressure of 98 MPa

Figure 8.8: Through-the-thickness matrix and fiber failure criteria of the of the B* stacking sequence

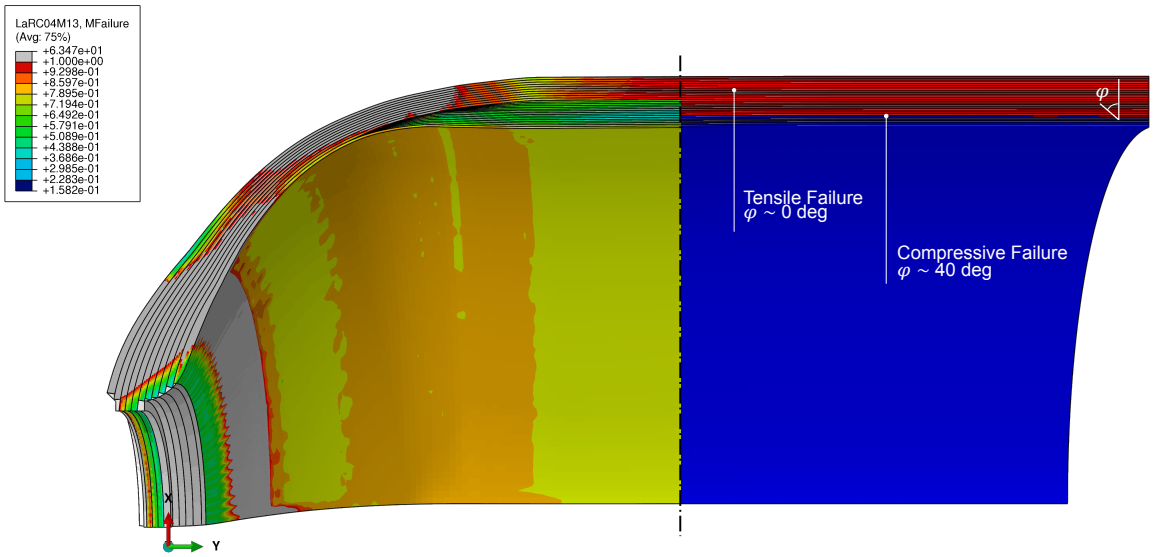


Figure 8.9: LaRC04 matrix tensile failure field of the B* stacking sequence at a load pressure of 35.1 MPa

to material imperfections forming at the interface between ply groups, including voids and resin-rich areas. Such features are anticipated to have a noteworthy influence on the local material strength, as accordingly observed during the material property characterization in chapter 6. In this regard, it is prevailing that both in the W1A and B* configurations, the first recorded AE is significantly lower than the predicted failure in the hoop layer group, whereas concerning E+, what is perceived is a substantial experimental data scatter.

Triggering and subsequent growth of cracks through areas of low strength is illustrated by the observation of CT samples after pressurization up to 105 MPa. This material degradation is represented in fig. 8.10 for the cylindrical region of the W1A layup, where a successive connection of pores is recognized along the interfiber crack surface. Additionally, the interface between the circumferential ply stack and the outer helical plies in this stacking sequence appears to be comprised of resin and cavities. The depiction of cracks in the circumferential ply stack is complemented with the analogous in the helical layers. Cracks in the circumferential ply stack grow rapidly through-the-thickness and along the circumference, whereas the continuous fiber orientation changes hamper these in the helical layers.

Withal, the crack pattern in the circumferential ply stack illustrated in fig. 8.10 responds to a failure mode dominated by tensile stress components through the whole through-the-thickness coordinate. The fracture plane develops parallel to the direction of compressive loading, thus indicating that this mode is not driving the material degradation. Such crack growth indicates that considering a matrix compressive strength $Y^C = 50.0$ MPa is overly conservative; moreover, that the matrix compressive

Table 8.1: Results of the damage onset pressure stage at different vessel locations

Stack.	Criteria	Helicals				Circumferentials	
		MF Dome	FF Dome	MF Cyl.	FF Cyl.	MF	FF
W1A	Puck	10.7	205.9	31.5	234.8	35.1	169.5
	LaRC04	10.7	–	32.6	–	36.1	–
E+	Puck	13.3	191.1	33.2	228.6	41.6	162.6
	LaRC04	13.5	–	34.1	–	43.3	–
B*	Puck	12.4	141.5	37.7	215.1	45.4	132.6
	LaRC04	12.3	–	38.1	–	46.2	–

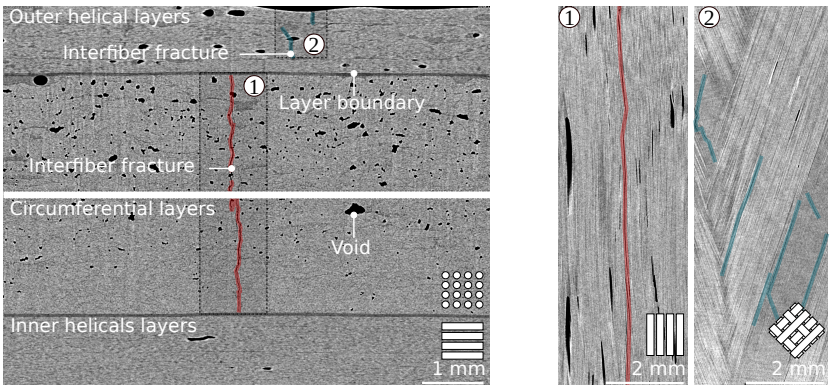
Stack. – stacking sequence; MF – matrix failure pressure stage; FF. – fibre failure pressure stage; Dome – failure prediction in the dome and dome transition region; Cyl. – failure prediction in the cylindrial region

Table 8.2: Comparison of the damage onset prediction with experimental data

Stack.	Vessel	Experimental		Simulation					
		MF Cyl.	Burst	MF Puck	Diff. (%)	MF LaRC04	Diff. (%)	FF. Puck	Diff. (%)
W1A	01 - 0128	25.2	165.3	35.1	39.3	36.1	43.3	169.5	2.5
	01 - 0183	24.2	162.4	"	45.0	"	49.2	"	4.3
	01 - 0184	24.5	162.4	"	43.3	"	47.3	"	3.2
	01 - 0192	23.2	156.9	"	51.3	"	55.6	"	8.2
E+	01 - 0175	49.1	156.1	41.6	−15.3	43.3	−11.8	162.6	4.2
	01 - 0201	50.1	149.4	"	−16.9	"	−13.6	"	8.8
	01 - 0268	21.0	147.5	"	98.1	"	106.2	"	10.2
	01 - 0271	24.0	144.4	"	73.3	"	80.4	"	12.6
B*	01 - 0190	23.3	101.2	45.4	98.5	46.2	98.3	132.6	31.0
	01 - 0243	22.3	110.5	"	103.6	"	107.2	"	20.0
	01 - 0257	24.8	91.4	"	83.1	"	86.3	"	44.9
	01 - 0281	21.7	119.7	"	109.2	"	112.9	"	10.7
	01 - 0282	20.4	98.9	"	122.5	"	126.5	"	34.1

Stack. – stacking sequence; MF Cyl.– matrix failure pressure stage identified in the cylinder by means of AE; MF Puck – matrix failure pressure stage in the circumferential group of plies according to Puck; MF LaRC04 – matrix failure pressure stage in the circumferential group of plies according to LaRC04; FF Puck. – fibre failure pressure stage according to Puck; Diff. (%) – percentual difference between experimental and simulation results

material characteristics are ultimately relevant for the following modeling of damage progression in chapter 9. A matrix compressive strength $Y^C = 225.8$ MPa obtained from the material supplier indicates that compressive damage is improbable for maximum internal pressure values in the vicinity of 160 MPa.



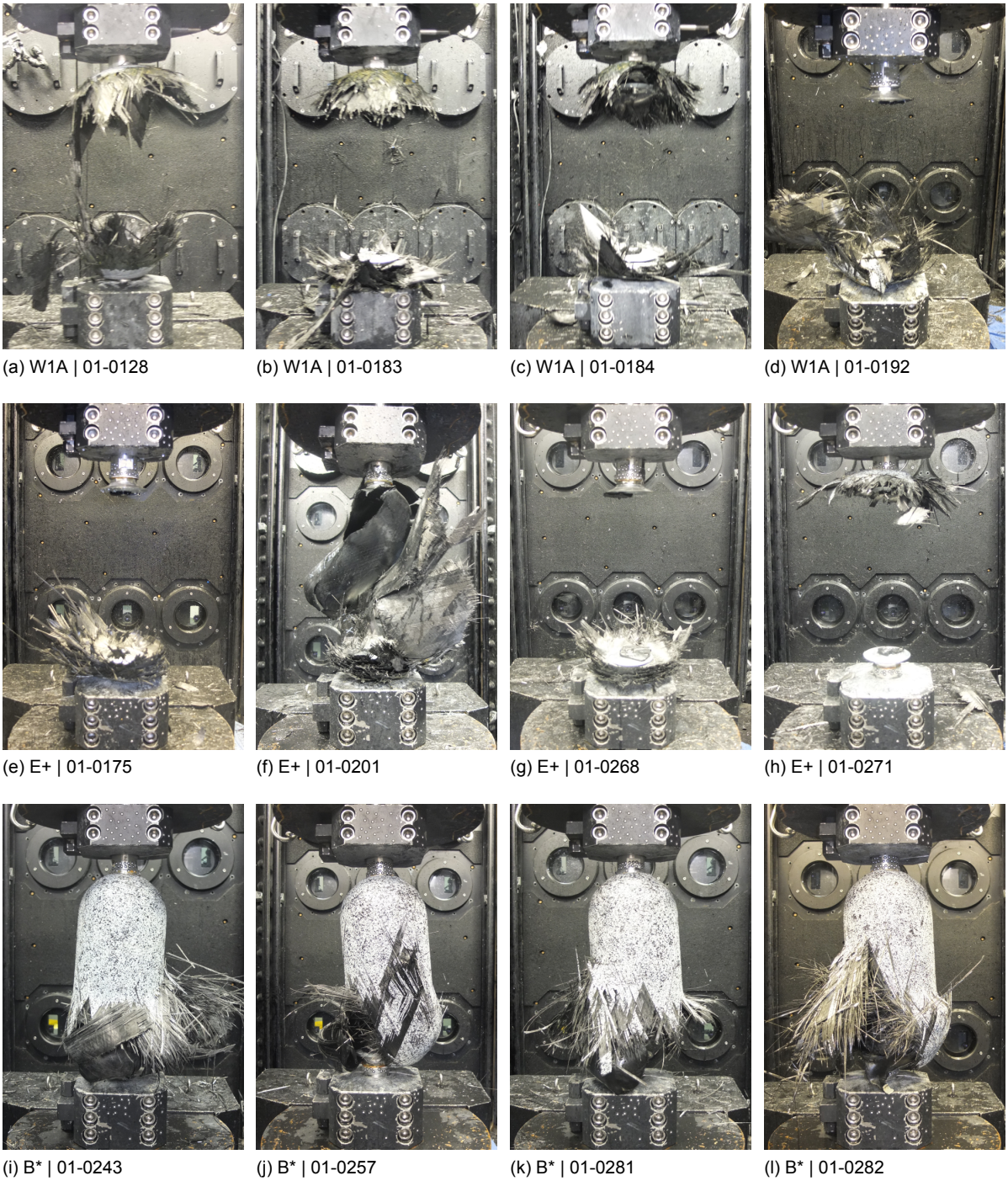
(a) Circumferential view. Crack propagation through-the-thickness

(b) Top view. Crack propagation in-plane

Figure 8.10: Interfiber fracture in circumferential and outer helical layers of the W1A stacking sequence after pressurization up to 105 MPa

As follows, the burst pressure estimations presented in table 8.2 show to be reasonable for the W1A and E+ layups, where their respective fiber failure predictions indicate burst in the cylindrical region. Withal, these estimations are imprecise when burst takes place away from the cylinder, being damage progression and subsequent load redistribution intrinsically connected with them. This discrepancy in the burst pressure is portrayed in the B* stacking sequence, which despite showing a tendency to burst in the dome transition in fig. 8.8, does not yet accurately estimate the experimental result.

The predicted burst modes are related to the result of experiments through the vessel remainder after the burst in fig. 8.11. These experiments show that burst destroys the entirety of the cylindrical region in the W1A configuration, while it relatively preserves the dome ends. A similar pattern is noticed for E+, although one of the domes appears to be consistently annihilated. Concerning B*, an apparent failure exists in one of the domes that, correspondingly, permits the rest of the vessel to maintain its



(a) W1A | 01-0128 (b) W1A | 01-0183 (c) W1A | 01-0184 (d) W1A | 01-0192

(e) E+ | 01-0175 (f) E+ | 01-0201 (g) E+ | 01-0268 (h) E+ | 01-0271

(i) B* | 01-0243 (j) B* | 01-0257 (k) B* | 01-0281 (l) B* | 01-0282

Figure 8.11: Vessel remainder after burst testing

integrity roughly.

These modes of final collapse are coherent with the predictions in figs. 8.4, 8.6 and 8.8. Particularly in the E+ configuration, the dome transition and cylinder regions are predicted to be similarly loaded, thus likely relating to a final collapse that prompts failure of one of the domes along with the cylinder. In the case of B*, the prediction of a localized breakage correlates with the observed dome blowout taking place at relatively low-pressure stages. The released energy is ostensibly lower, whereas total breakage appears to be constrained to a limited region around the circumference.

8.4. Concluding Remarks

Evaluating failure criteria on the constitutively elastic results of a CPV has a twofold outcome, determining the onset of material degradation and approximating the pressure stage at which burst is taking place. The first happens because of the matrix reaching its maximum stress state, prompting subsequent load redistribution upon the existence of damage and, overall, increasing the component compliance. Correspondingly, the burst event is estimated when fibers lose their load-bearing capability. As a primary limitation to the vessel burst approximation by FPF, no influence of the material degradation is regarded, therefore, not accounting for the increased stress component in the fibers because of load redistribution.

Matrix damage onset is estimated according to two failure criteria, Puck and LaRC04. They permit to compare their adequacy consequent to the combined loading condition in the filament wound plies, yet marginal differences are reported between the two. Nevertheless, the correlation of failure onset with experimental results shows that, particularly to the circumferential ply stack, the damage prediction is overestimated. Transverse damage is determined from the average property definition in table 7.1, which hence disregards the decreased material strength of regions where porosity and fiber volume contents are respectively higher and lower than the average. These regions appear in the outer circumferential plies because of resin outflow during winding and curing. They coincide with the location where the transverse stress components are expected to be maximum, ultimately reasoning the observed discrepancy.

Results for the W1A, E+, and B* stacking sequences show a likelihood of transverse damage in the cylindrical region directly related to their tangential expansion. Therefore, the W1A case, which presents the most substantial cylinder compliance in section 7.5, also reports the earliest triggering of failure in this region. The response in the cylinder response in the E+ and B* layups comparatively reproduces a later damage onset in the matrix, related to a higher amount of load carried by the fibers in the circumferential plies. Nevertheless, both stacking sequences depict a relevant local tangential expansion in the dome transition region, allowing an earlier matrix degradation to lead there instead.

Concerning the prediction of burst, the constitutively elastic response permits to identify the type of collapse experienced by the vessel. It is possible to predict a cylinder failure in the circumferential plies or, otherwise, if the stiffness distribution drives an alternative burst in the dome transition region. In the latter case, it is observed that the high vessel compliance ahead of the circumferential ply drop is compensated by a tangential stress increase in the hoop layers, adjacent to the formation of the bulge. The reported stress increase predicts a premature vessel collapse when the stress state in the circumferential ply end surpasses that in the cylinder, as in the case of B*, while failure is still dominated by the cylinder strength otherwise, as in the case of E+.

Predicting a burst event in the cylindrical region shows a small mismatch with the experimental results (< 10 %), for both the W1A and E+ cases. However, the use of FPF flounder in depicting an accurate burst pressure if damage progression dominates outside the cylindrical region. This is the case of B*, for which a considerable discrepancy with test results still exists (20 - 30 %). In conclusion, failure criteria appear as a useful tool in determining the strength of the CPV. Withal, it requires a subsequent, more detailed damage progression modeling when load redistribution to the fibers may prompt a premature burst. Such a failure is the case of the B* vessel, where higher compliance in the bulged region directly correlates with increased loading in the circumferential plies beside it.

9

Modeling of Damage Progression

Damage stands as a broad concept involving the degradation of the material, at scales that range from the constituent to the structural component. Therefore, its modeling alternatively develops from the formulations that achieve a representation of material at each involved level, [71]. First, micromechanics deals with the mechanisms with which the matrix and fiber constituents fail, correlating them with the ply material degradation and representing the general structural behavior. Second, mesomodeling is based on the representation of plies as a homogeneous orthotropic material, where the damage initiation and progression is defined within the continuum and represented by constitutive laws. While third, damage is represented at the structural level by hard discontinuities whose propagation is defined by case-dependent softening and critical energy release laws. Herein, mesoscale-based CDMs is possibly the most widespread damage modeling approach because they couple naturally with the continuum definition of FE analysis. In their basic form, they introduce damage in a material by degrading its stiffness, while cohesive zone models are also compatible with them if fracture at the finite element interfaces is a relevant characteristic.

This chapter extends the burst pressure prediction capability of FPF calculations by accounting for the degradation of the matrix and fiber constituents in the constitutively elastic analysis of chapter 7. Material degradation in the composite vessel reinforcement is considered as implemented by Soriano and Díaz [125] within the framework of the CDM CompDam developed by Leone et al. [1]. A perfectly elastic orthotropic behavior is assumed before the triggering of damage, which is then evaluated from independent transverse and longitudinal direction failure depictions. To this purpose, an overview of the CompDam model implementation is firstly presented in section 9.1, where its main characteristics are discussed concerning their representation of the CPV mechanical response. Following, results of the damage progression evaluation are reported in section 9.2 and discussed against the FPF burst pressure estimations referred in chapter 8.

9.1. Implementation of the CDM Model

The use of CDM models appear as a convenient tool in the representation of material degradation of CPVs because their implementation is performed at the ply scale, where robust analysis methodologies already exist, and their level of development is sufficiently high to reproduce the material mechanics of failure. CDMs assume that the composite layers behave as a homogeneous material with orthotropic properties, wherein predefined failure criteria are employed to predict the onset of damage. Subsequently, the advancement of damage is represented by penalizing appropriate stiffness components until no more load carrying capability is left. This process is ruled by softening laws that need to deem the successive failure events occurring, such as fiber-matrix debonding and fiber fracture. As CDM implementations only deal with failure within the composite layer, the general consideration of damage in the ply interface needs to be achieved through alternative cohesive models. However, results may lack accuracy in this case, when there is a strong coupling between transverse matrix cracking and delamination, [126].

Modeling damage from a continuum representation entails various limitations that arise from the homogenization of a complex material construction to that of a single element. Firstly, this generally

leads to mesh dependency effects in the matrix crack growth, which can, nonetheless, be partially overcome by the introduction of viscosity, [64, 126]. Likewise, the progression of damage within an element is controlled by experimentally measured fracture toughness. Its determination permits to regard its failure from a crack that completely goes through it, although as it is also related to the element elastic energy, it has to be normalized concerning its size. Furthermore, as no physical matrix and fibers exist within the continuum, no clear difference can be made for resin cracks running parallel to the fibers or perpendicular (and through) them, which indeed experience distinct growth resistances.

The model CompDam implemented in this work considers transverse damage by embedding matrix cracks within the continuum element that are then evaluated according to cohesive failure criteria to determine the triggering of failure, Leone et al. [1]. This approach was initially proposed by Camanho et al. [119], and further developed by Leone [127] to consistently account for material degradation from the bulk material and inelastic deformations at each load state. In addition to this, material damage in the longitudinal direction is accounted for by penalizing the appropriate stiffness tensor components according to a non-interacting maximum strain criterion. The use of a smeared crack approach is advantageous for the current filament wound vessel modeling because fracture planes are not restrained to follow material orientations. In the context of interwoven helical plies idealized as successive stratified subplies, matrix cracks can grow in any direction solely based on the local stress state. On the one hand, this permits cracks to develop in a diffuse form, as is expected from the complex band structure of helical plies, while mesh dependency is limited. On the other hand, this might predict cracks growing perpendicular to the fiber orientation while the corresponding fracture toughness is derived for interfiber crack growth.

9.1.1. Modeling of Transverse Damage

Transverse damage is produced by failure of the matrix, hence regarded by the smeared crack surface representation, where a single scalar damage variable is calculated from the cohesive damage model of Turon et al. [128, 129]. The corresponding fracture plane displacement jumps are calculated from a deformation gradient tensor decomposition $\mathbf{F}$, in elastic, $\mathbf{F_B}$, and cracked components, $\mathbf{D}$, [127]. To this end, the magnitude of each of these components is determined from the configuration that minimizes the residual difference between the cohesive surface stress vector and the bulk material stress projection in that plane,

$$\boldsymbol{\sigma}_{Res} = \boldsymbol{\tau} - \mathbf{t} \cdot \mathbf{R}_{cr}^{T}, \tag{9.1}$$

where $\boldsymbol{\sigma}_{Res}$ is the residual stress vector, $\boldsymbol{\tau}$ is the stress vector in the cohesive interface, and $\mathbf{t} \cdot \mathbf{R}_{cr}^{T}$ is the bulk material stress tensor projection in the crack surface basis coordinate system $\mathbf{R}_{cr} = [\hat{\mathbf{e}}_F \quad \hat{\mathbf{e}}_N \quad \hat{\mathbf{e}}_T]$. The basis coordinate system $\mathbf{R}_{cr}$ is illustrated in fig. 9.1, where it is accordingly formed in the cohesive surface by the orthogonal vectors in the fiber, $\hat{\mathbf{e}}_F$, crack-normal, $\hat{\mathbf{e}}_N$, and transverse directions, $\hat{\mathbf{e}}_T$.

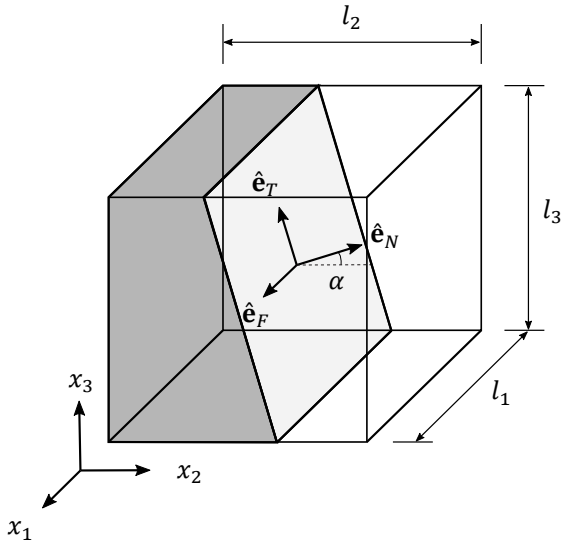


Figure 9.1: Crack orientation of the continuum in the reference configuration (adapted from [127])

Accordingly, the stress vector $\boldsymbol{\tau}$ acting in the cohesive interface is formed by an elastic $\boldsymbol{\tau}^{\mathbf{coh}}$ and a friction component $\boldsymbol{\tau}^{\mathbf{f}}$ as $\boldsymbol{\tau} = \boldsymbol{\tau}^{coh} + \boldsymbol{\tau}^{f}$, with

$$\boldsymbol{\tau}^{coh} = \begin{bmatrix} k_F(1-d_2)\delta_F \\ k_N(1-d_2)\delta_N - k_N d_2\langle -\delta_N \rangle \\ k_T(1-d_2)\delta_T \end{bmatrix} \tag{9.2}$$

being k_i and δ_i the cohesive penalty stiffness and the displacement-jump vector components in the i directions, and d_2 the scalar matrix damage variable. The Macauley operator $\langle x \rangle$ represents the fact that the existence of damage does not alter the normal compressive stress in the fracture plane.

The cohesive stress vector $\boldsymbol{\tau}^{\mathbf{coh}}$ is hence evaluated from the calculated crack opening vector and the arbitrarily chosen cohesive penalty stiffness, that are large enough to ensure elastic displacement continuity while preventing numerical difficulties because of ill-conditioned matrices, [127]. Correspondingly, the friction stress component $\boldsymbol{\tau}^{\mathbf{f}}$ is considered by introducing a Coulomb law within the cracked surface of the continuum as described by Turon et al. [129]. Friction is relevant in fractured but contacting surfaces, as it permits to account for the induced tangential stress due to applied normal load. The effect of friction increases the effective stress at the cohesive interface during crack propagation and results in a purely Coulombian friction model when damage fully develops. Therefore, it also increases the cohesive surface shear strength as a function of the surface normal loads, [129]. The friction stress is expressed as

$$\boldsymbol{\tau}^{f} = \begin{bmatrix} -\bar{d}_2 \mu \tau_N^{coh} \dfrac{\tau_{sh}^{coh}}{|\tau_{sh}^{coh}|} \\ \tau_N^{coh} \\ -\bar{d}_2 \mu \tau_N^{coh} \dfrac{\tau_{sh}^{coh}}{|\tau_{sh}^{coh}|} \end{bmatrix} \tag{9.3}$$

with τ_{sh}^{coh} calculated as $\tau_{sh}^{coh} = \sqrt{(\tau_F^{coh})^2 + (\tau_T^{coh})^2}$, and $\bar{d}_2$ being a normalized damage variable representing the area of the damaged area A_d over the area of the integration point A_c, [129],

$$\bar{d}_2 = \frac{A_d}{A_e} = \frac{d_2}{\dfrac{2k_F \mathcal{G}_{IIc}}{S_L^2}(1-d_2) + d_2}. \tag{9.4}$$

The basis of crack surface is determined at the onset of damage from the angle that maximizes the result of the Benzeggagh and Kenane [130] cohesive failure criterion. The transverse damage activation function $\mathcal{F}$ is then defined from the crack displacement magnitude δ, the loading function $\mathcal{L}(\delta)$, and the linear softening relation d_2, as presented in the work of Turon et al. [128]

$$\mathcal{F}(\delta, d_2) = \mathcal{L}(\delta) - d_2 \leq 0, \tag{9.5}$$

with

$$\mathcal{L}(\delta) = min\left\{\frac{\Delta^f(\delta - \Delta^o)}{\delta(\Delta^f - \Delta^0)}, 1\right\} \tag{9.6}$$

that defines a linear softening relation as constitutive law, depicted in fig. 9.2.

The displacement jumps at damage onset (Δ^o) and damage propagation (Δ^f) are accordingly represented from the mode I and shear

$$\begin{aligned} \Delta^o &= \left\{(\Delta_3^o)^2 + \left[(\Delta_{sh}^o)^2 - (\Delta_3^o)^2\right] B^\eta\right\}^{1/2}, \\ \Delta^f &= \frac{1}{\Delta^o}\left[\Delta_3^o \Delta_3^f + \left(\Delta_{sh}^o \Delta_{sh}^f - \Delta_3^o \Delta_3^f\right) B^\eta\right] \end{aligned} \tag{9.7}$$

where η is the Benzeggagh and Kenane [130] mixed-mode interaction parameter and B the local mixed-mode ratio $B = \Delta_{sh}^2/\delta^2$. The term Δ_{sh} represents the displacement jump in the plane of the crack as

$$\Delta_{sh} = \sqrt{(\delta_F)^2 + (\delta_T)^2}. \tag{9.8}$$

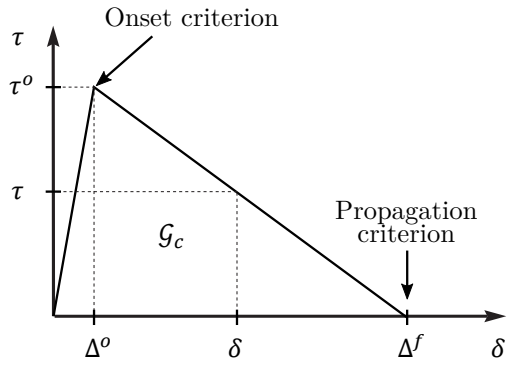


Figure 9.2: Cohesive model constituve relation (adapted form [131])

The displacement jumps at damage onset are expressed fromt the pure mode I and shear strengths Y^T and Y^{sh} and the pure mode penalty stiffness k_I and k_{sh},

$$\Delta_3^o = \frac{Y^T}{k_I}; \qquad \Delta_{sh}^o = \frac{Y^{sh}}{k_{sh}}, \tag{9.9}$$

while the pure mode I and shear fracture toughness define the displacement jumps at damage propagation,

$$\Delta_3^f = \frac{2\mathcal{G}_{Ic}}{Y^T}; \qquad \Delta_{sh}^f = \frac{2\mathcal{G}_{IIc}}{Y^{sh}}. \tag{9.10}$$

Regarding the bulk stress tensor projection $\mathbf{t}$, this is calculated from the Cauchy stress tensor as $\mathbf{t} = \boldsymbol{\sigma}_B \cdot \hat{\mathbf{e}}_N$. Accordingly, the bulk material tensor is calculated from the bulk deformation gradient $\mathbf{F_B}$ and the second Piola - Kirchhoff stress tensor $\mathbf{S}$,

$$\mathbf{S} = \mathbf{C} : \mathbf{E} \tag{9.11}$$

$$\mathbf{E} = (\mathbf{F}_B^T \mathbf{F}_B - \mathbf{I})/2 \tag{9.12}$$

$$\boldsymbol{\sigma}_B = \mathbf{F}_B \mathbf{S} \mathbf{F}_B^T \mid \mathbf{F} \mid^{-1} \tag{9.13}$$

wherein $\mathbf{E}$ is the Green-Lagrange strain tensor, $\mathbf{I}$ is the identity tensor and $\mathbf{C}$ is the material stiffness tensor. The use of the second Piola - Kirchhoff stress tensor and the Green-Lagrange strain tensor is justified by Rose et al. [71] to represent more adequately the large deformations involved in a material locally experiencing damage due to failure in a roughly undamaged region.

9.1.2. Modeling of Longitudinal Damage

Concerning the evolution of longitudinal damage, only degradation because of tensile loading is considered by reason of the applied internal pressure loading. In this regard, longitudinal tensile damage development implies the presence of fiber-matrix debonding and pullout. The fracture toughnesses for these modes are not easily calculated from standard procedures, [119], what derives in the CompDam implementation to consider longitudinal damage as the non-interactive constitutive model of Maimí et al. [132, 133]. Damage is hence accounted by the penalty of the lamina compliance tensor by the longitudinal damage variable d_1,

$$\mathbf{H} = \begin{bmatrix} \frac{1}{(1-d_1)E_1} & -\frac{\nu_{12}}{E_1} & 0 \\ -\frac{\nu_{12}}{E_1} & \frac{1}{E_2} & 0 \\ 0 & 0 & \frac{1}{G_{12}} \end{bmatrix}. \tag{9.14}$$

In this case, damage onset is predicted by a non-interactive maximum strain criterion. Likewise, damage evolution is represented by a bilinear relation depicted in fig. 9.3, which is generated by the superposition of the fiber-matrix debonding and fiber pullout failure mechanisms.

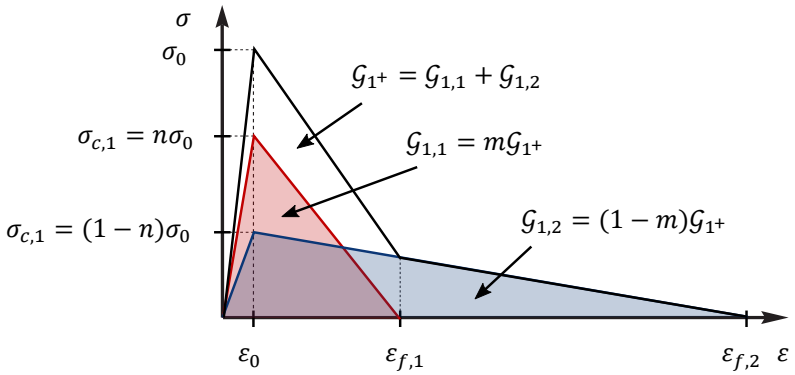


Figure 9.3: Bilinear softening law (adapted from [115])

As presented by Dávila et al. [115], these values of fracture toughness can be derived from the resistance curve analysis of crack growth perpendicular to the fiber direction. This permits to define the softening law proportions m and n that, correspondingly, characterize the damage progression, [115]. The damage variable is then expressed in a similar manner to the linear softening relation of the cohesive law in eq. (9.6) as,

$$\varepsilon_{f1} = \frac{2\mathcal{G}_{1^+} m}{l^* X^T n}, \quad \varepsilon_{f2} = \frac{2\mathcal{G}_{1^+}(1-m)}{l^* X^T (1-n)} \tag{9.15}$$

$$d_{1,1} = \frac{\varepsilon_{f,1}(\varepsilon_{11} - \varepsilon_0)}{\varepsilon_{11}(\varepsilon_{f,1} - \varepsilon_0)}, \quad d_{1,2} = \frac{\varepsilon_{f,2}(\varepsilon_{11} - \varepsilon_0)}{\varepsilon_{11}(\varepsilon_{f2} - \varepsilon_0)} \tag{9.16}$$

$$\mathcal{F}(d_1) = min\{n(d_{1,1} - d_{1,2}) + d_{1,2}, 1\} - d_1 \leq 0 \tag{9.17}$$

where the characteristic element length l^* is regarded as square root of the area that represents an integration point, $\mathcal{G}_{1^+}$ is the fracture toughness in the fiber tensile direction, and X^T is the longitudinal tensile strength of the material.

A consequence of modeling damage progression by penalizing the stiffness tensor introduces the possibility of experiencing local snap-backs in the stress-strain relations, [134]. Therefore, a requirement on the mesh definition is that the element size has to be smaller than the experimentally measured fracture toughness to prevent elemental energy unbalance,

$$l^* \leq \frac{2E_{11}\mathcal{G}_{1+}}{{X^T}^2} \tag{9.18}$$

with E_{11} indicating the longitudinal material modulus.

All in all, the material architecture and the applied loading show to profoundly influence material degradation, also inherently constrained to the mesh discretization. In order to achieve a robust simulation of this type phenomena, sufficient validation with experimental data is necessary to prove the adequacy of the various approaches, although the acquisition of these data may pose a challenge in itself. Moreover, the limitations and opportunities of a proposed damage progression in their application to CPVs seems to be only possible from a thorough understanding of the mechanic and numerical simulation requirements associated with it.

9.2. Results and Discussion of Damage Progression

9.2.1. Prediction on the Damage Progression of the W1A Stacking Sequence

The progression of damage in composite materials is inherently connected with the development of matrix cracks, diminishing the stiffness of the component and distributing the load to the more resilient fibers. In the context of the CompDam model implementation described in section 9.1, this is depicted

by the transverse damage variable at pressure stages from 35 to 103.5 MPa presented in fig. 9.4. Within this load range, failure in the matrix spans from triggering to almost extending in the entirety of the vessel, hence permitting to identify the predicted damage sequence and correlate it with the available experimental data concerning AEs and vessel observations. The ensuing applied load is carried by the fibers, ultimately cascading into their breakage and the burst event.

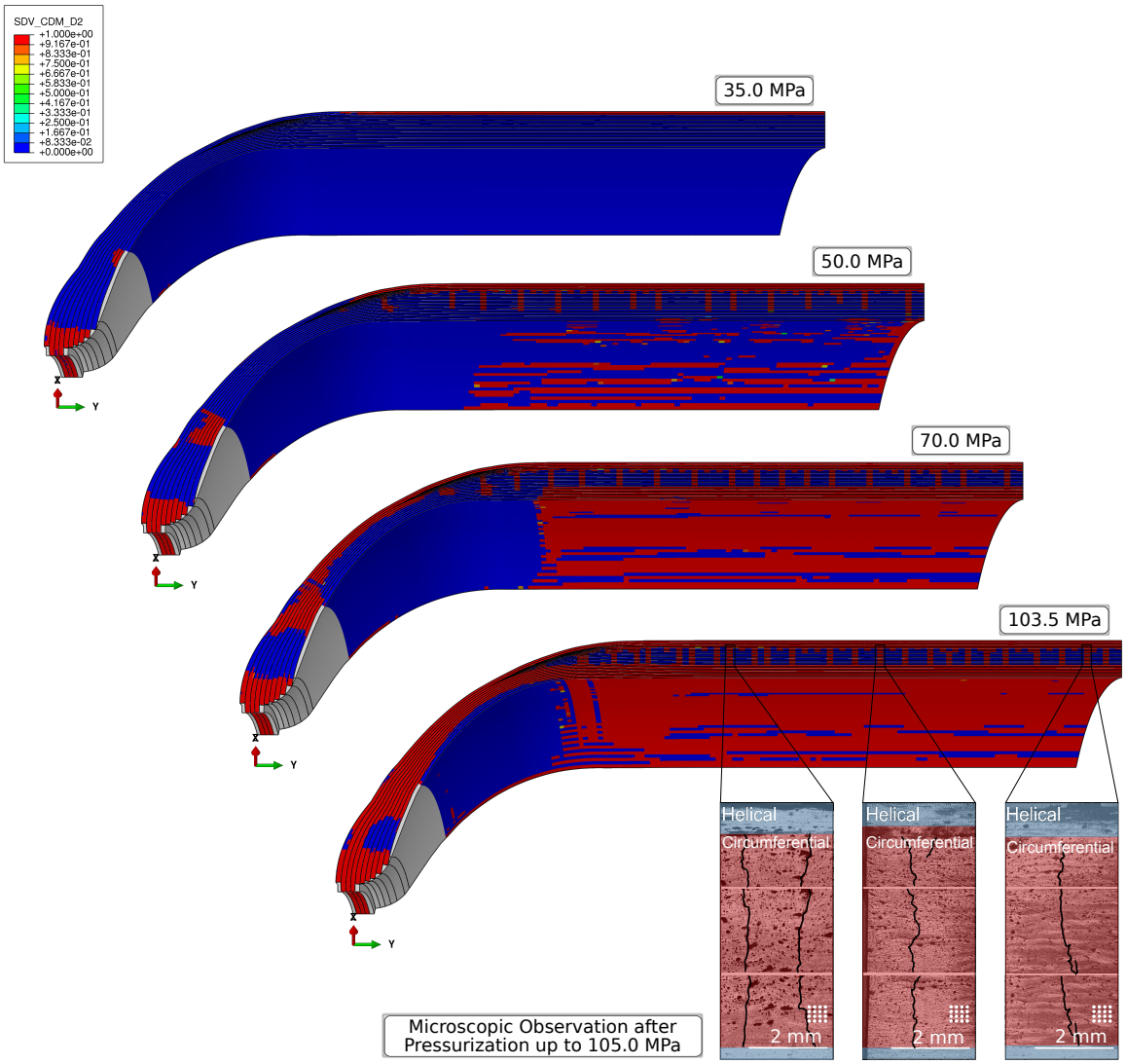


Figure 9.4: Predicted transverse damage of the W1A stacking sequence at load pressures of 35, 50, 70 and 103.5 MPa. The predicted cracks through-the-thickness in the circumferential ply stack are additionally compared with microscopic observations of samples after pressurization up to 105 MPa

Material degradation is predicted first (20 to 25 MPa) in the lower dome quarter resulting from the rigid interplay between boss and composite reinforcement. The dome end next to the boss is also the location where significant meridional and through-the-thickness shear stress components are identified in the constitutively elastic analysis of section 7.4, thus leading to the highest failure criteria predictions in section 8.3. Besides, the concentration of stress in the lower dome quarter further substantiates at the tip of the boss brim, where the composite reinforcement experiences a drastic stiffness change and also an early damage onset. Damage progression is followed by the degradation of the outer helical plies (30 to 35 MPa) where, as argued in section 8.3, meridional stress is expected to be maximum. Consequently, this derives in a critical combination of transverse and shear stress components that triggers failure earlier than the underlying circumferential stack.

Failure in the hoop plies is subsequently predicted in the cylinder-dome transition region (35 MPa). The aggregated vessel expansion and meridional bending appear to motivate a critical load state at

this location, agreeing with the estimation concerning failure criteria shown in section 8.3. However, damage is not extensively visible until lightly higher pressure loads, when rapidly growing through-the-thickness cracks are depicted. This crack growth is motivated by the relatively low fracture toughness defined for the unidirectional hoop plies, inducing an aggressive load redistribution when damage appears, thus, letting the material degradation grow through-the-thickness. The prediction of these cracks is additionally depicted in fig. 9.4 against microscopic observations of samples after pressurization up to 105 MPa. The microscopic images permit the identification of the extension of failure, also correlating well with the prediction of cracks rapidly developing through the whole group of circumferential plies.

Matrix damage in the cylindrical region appears last in the inner helical plies (50 to 55 MPa) where the meridional stress gradient through-the-thickness still leads to an earlier failure of the outer plies of the stack. At similar load stages at which damage progresses in the inner layers in the cylinder, it also develops in the outer plies in the dome region. In the meantime, the dome inner helical plies appear to remain pristine, which is reasoned on the deformational pattern introduced in section 7.3. The dome of the W1A stacking sequence is presented to swell between the cylinder-dome transition and the boss contact, introducing inward meridional bending that comparatively increases the outer surface tensile stress, safeguarding the inner dome surface from matrix degradation.

Experimental results on damage progression are qualitatively depicted by the channel file in fig. 9.5, which illustrates the amount and amplitude of the acoustic emissions recorded during pressurization. The analysis of these emissions is based on the sum beam-forming of air-borne acoustic events reported by Cesari [135], and permits to correlate the amplitude of the recording to the elastic energy released during brittle material fracture. This channel file depicts a region in the range of 20 to 50 MPa where high amplitude emissions take place, followed by subsequent unceasing smaller amplitude events until the vessel burst. Circumferential cracks can be confidently related to the recording of high amplitude AEs due to the absence of damage stoppers in the circumferential and through-the-thickness directions. Likewise, fractures in the helical plies are anticipated to generate low energy releases because of the complex material construction that limits crack propagation.

The range at which high amplitude emissions are recorded agrees with the progression of damage illustrated in fig. 9.4, where essentially matrix damage appears in the circumferential ply stack before it does in the inner helical ones and the upper dome. Withal, the earliest high amplitude AEs are recorded in the load range of 20 to 25 MPa, which thus, precede the damage progression prediction, at approximately 35 MPa. The discussion in section 8.3 reasons the discrepancy, because the high porosity outer circumferential layers experience a lower transverse tensile strength than the average material characteristics. Considering a homogeneous material definition disregards the influence of the material quality on nucleating cracks, which in the case of the low fracture toughness circumferential plies, may lead to relevant AEs.

The AEs localization in fig. 9.6 permits further identification of the damage progression from an experimental perspective. Together with the outer component surface observations, also allows benchmarking the harshness of the events that are being recorded. Mapping emissions to their sound pressure in fig. 9.6a shows that, in the range of 20 to 50 MPa, high amplitude events prevail in the cylindrical region together with other less intense in the upper dome and cylinder-dome transition. With increasing pressure, only low amplitude AEs are identified in both cylinder and dome. The impact of the damage progression on the outside of the tested components is visualized in fig. 9.6b by the outer surface perturbation when covered with chalk. Particularly at the pressure stage of 50 MPa, when matrix failure in the circumferential plies has occurred, no obvious disturbance of the chalked vessel exists. Nevertheless, this is apparent at the higher load states, of 90 and 105 MPa, by numerous dark specks where the composite bands fractured and detached. Correspondingly, some of the low amplitude emissions in the range of 50 to 105 MPa depicted in fig. 9.6a show to be directly correlated with the observed surface perturbations in fig. 9.6b, [135].

Damage in the outer helical layers is predicted significantly earlier than the visual observation of cracks in fig. 9.6b and their apparent AE recording. If material degradation indeed exists since an earlier stage, it implies that some non-linear behavior occurs before the development of macroscopic cracks, whereas a distinct stress state in the helical plies should exist otherwise. In this regard, the material is reported during the mechanical properties characterization in section 6.3 to experience a relevant ductile deformation when subjected to shear loading. A response compatible with the macroscopic crack observation would be possible if the interwoven band construction experienced some plasticity when loaded in combined transverse and shear. A more detailed investigation needs to be addressed

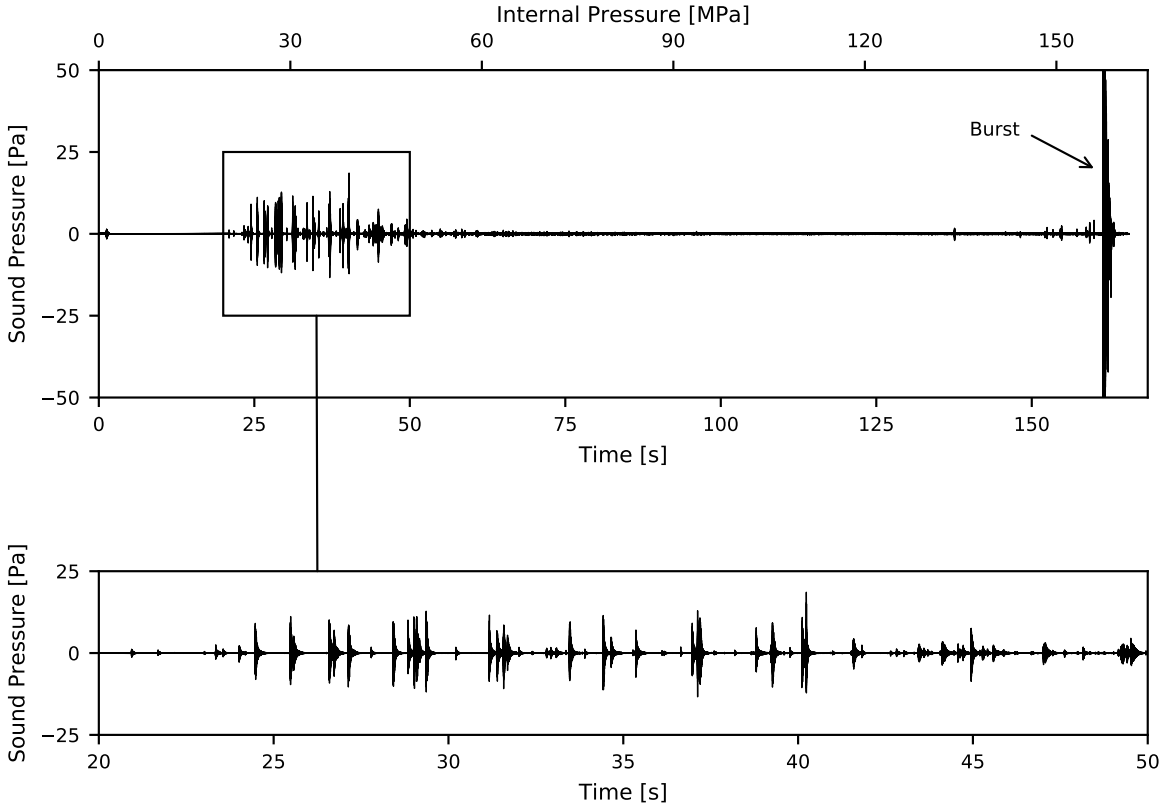


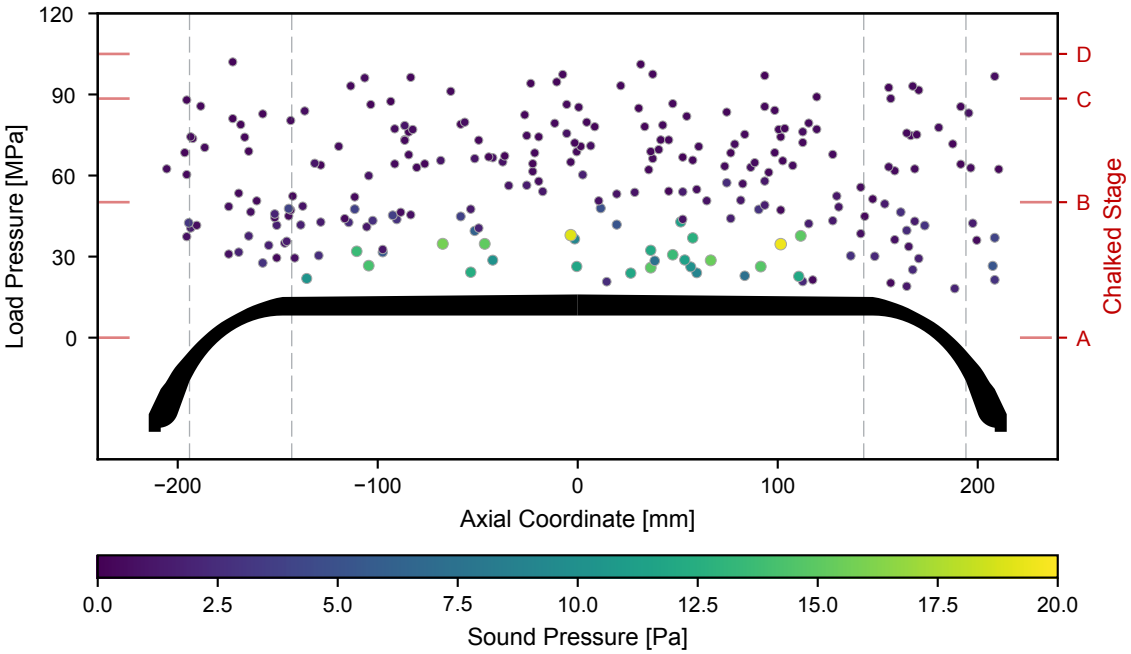
Figure 9.5: Acoustic emission channel file of a burst experiment of the 01-0077 | W1A stacking sequence

on the specific load state of an interwoven helical layer compared to the balanced sublply idealization presented in this work.

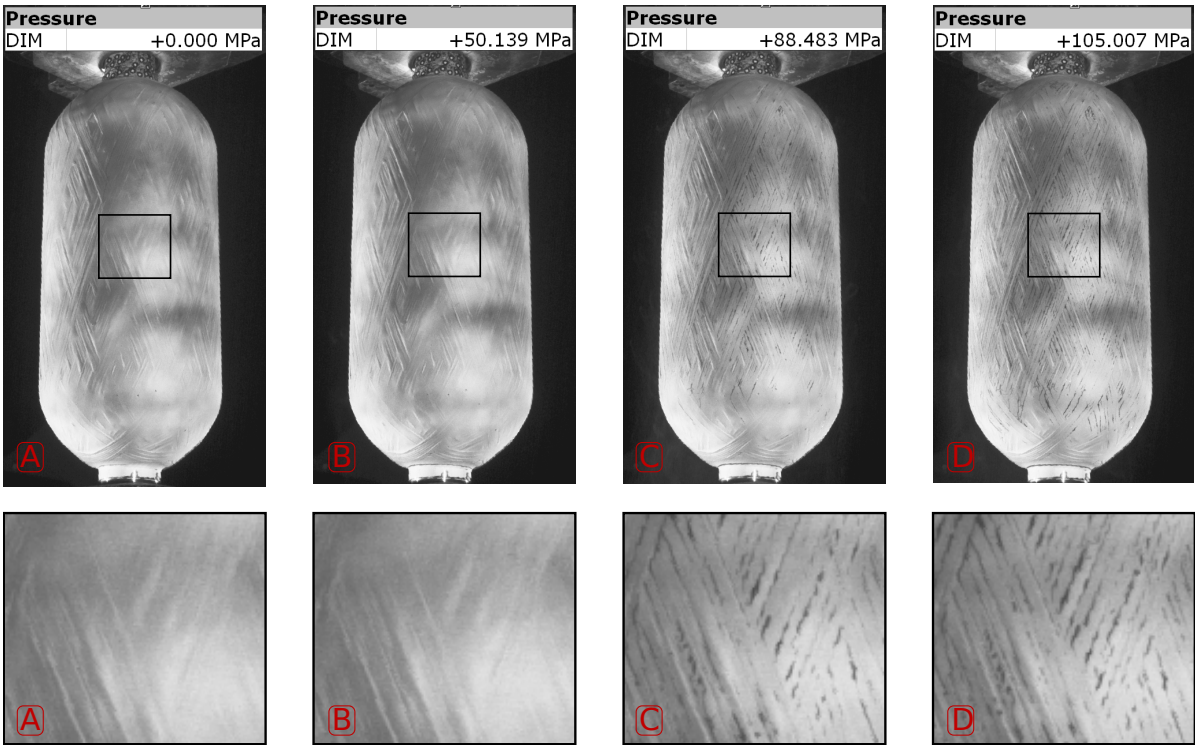
Another outcome of the prediction and experiment damage correlation is that the localization of events through-the-thickness is limited to the energy that is air-borne transmitted. Consequently, some of the events occurring vessel inside might be undetectable because of the emission attenuation when traveling through the material. Lower detection thresholds would ultimately permit to identify these sources, although being the low amplitude emissions inherently more numerous, a sufficiently low pressurization rate is needed to allow their rightful differentiation. In this context, it also appears that structure-borne emissions are better capable of identifying through-the-thickness sources because of the minimized traveling time and the no structure-air refraction surface. However, these are also subjected to relevant objections considering the heterogeneity of the composite material, the influence of voids and resin pockets on the acoustic emission transmission, and the curved surface of the component.

The structural instability introduced by the clustering of fiber breakages appear to lastly produce AEs at high-pressure stages, before the burst event. These emissions are correspondingly identified in fig. 9.5 before the final structural collapse, wherein a like manner to the work of Chou et al. [136], an increase in the AE hits precedes a sudden loss of bearing capacity. Crack density is expected to increase with the rising pressure, leading to accumulated damage of the type of fiber-matrix debonding and early fiber ruptures. Premature breakage of weak fibers, thus, causes load redistribution to the neighboring ones, ultimately prompting them to form failed clusters and generate AEs before final failure.

In the prediction results presented, no fiber damage is reached because of the numerical difficulty in applying high-pressure loads to the defined vessel configuration. Force equilibrium in the damaged elements requires convergence of the stress projection in the fracture surface defined in eq. (9.1). Withal, this appears to be hindered when mildly large strain exists in the elements of the dome end next to the boss. Relatively rigid boundary conditions exist here due to the low play for material deformation,



(a) Localization of AEs along the axial coordinate of the 01-0077 | W1A vessel geometry. Emissions are presented against the pressure stage at which they occur, whilst a higher sound amplitude is indicated by correspondingly larger markers. The right hand side indicates the pressure stages at which the damage state in the outer surface is portrayed



(b) Outer surface degradation on chalked 01-0178 | W1A vessel. Damage is shown by dark dots between the composite bands. This is apparent at the pressure stages of 88.5 and 105.0 MPa, whereas the at 50 MPa internal pressure no surface disruption is visible

Figure 9.6: Damage identification of the W1A stacking sequence after pressurization up to 105 MPa

while various contact interactions are also present between ply definitions of not fully coherent meshes. As a result, a distribution of load that ensures equilibrium in the damaged material is not found beside

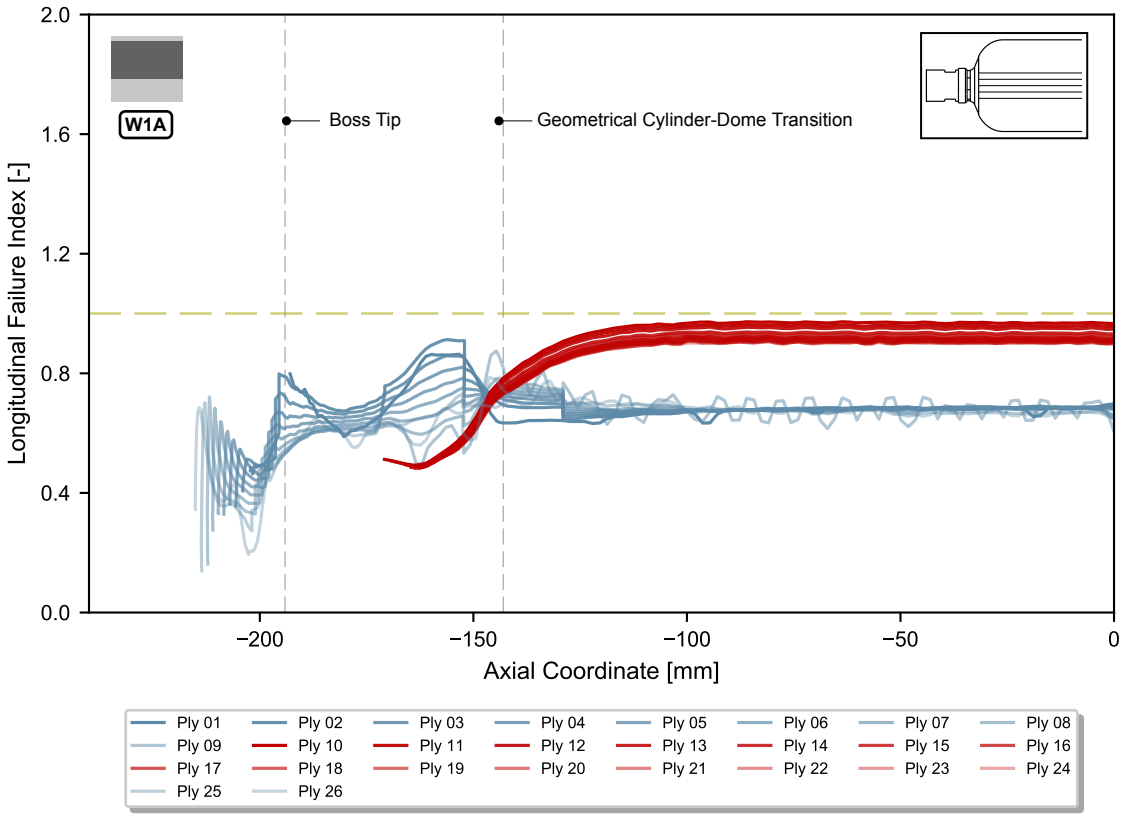


Figure 9.7: Fiber tensile failure criteria according to Puck, [87] at a load pressure of 1600 MPa

Table 9.1: Comparison of the damage onset prediction of the W1A stacking sequence with experimental data

Vessel	Exper.		No Damage				Damage			
	MF Cyl.	Burst	MF LaRC04	Diff. (%)	FF. Puck	Diff. (%)	MF CompDam	Diff. (%)	FF. CompDam	Diff. (%)
01 - 0128	25.2	165.3	36.1	43.3	169.5	2.5	35.0	38.0	165.8	0.3
01 - 0183	24.2	162.4	"	49.2	"	4.3	"	44.6	"	1.8
01 - 0184	24.5	162.4	"	47.3	"	3.2	"	42.9	"	1.8
01 - 0192	23.2	156.9	"	55.6	"	8.2	"	50.9	"	5.1

Stack. – stacking sequence; MF Cyl.– matrix failure pressure stage identified in the cylinder by means of AE; MF LaRC04 – matrix failure pressure stage in the circumferential group of plies according to LaRC04; FF Puck. – fibre failure pressure stage according to Puck; MF CompDam – matrix failure pressure stage in the circumferential group of plies according to CompDam; FF CompDam. – fibre failure pressure stage according to CompDam; Diff. (%) – percentual difference between experimental and simulation results

the fiber constituents still being capable of assimilating higher loading.

The presence of matrix damage until mildly high-pressure stages still permits comparatively realistic prediction of the failure of fibers and relates it to the burst event. It is estimated by the linear extrapolation of the failure index in the fiber direction for the last pressure stage at which results were obtained. The anticipated burst pressure is reported in table 9.1 together with the damage onset in the circumferential stack, where results are correlated with the burst experiments noted in table 8.2. A comparison with the prediction without the consideration of damage is accounted for, where only a minor difference exists in the predicted failure stage in the stack of hoop plies.

Concerning the burst event, the existence of load redistribution into the fibers in the damaged configuration is depicted for the failure criteria evaluation along a meridional path in fig. 9.7. It compares with the estimation of longitudinal failure of a constitutively elastic analysis in section 8.3, foretelling a

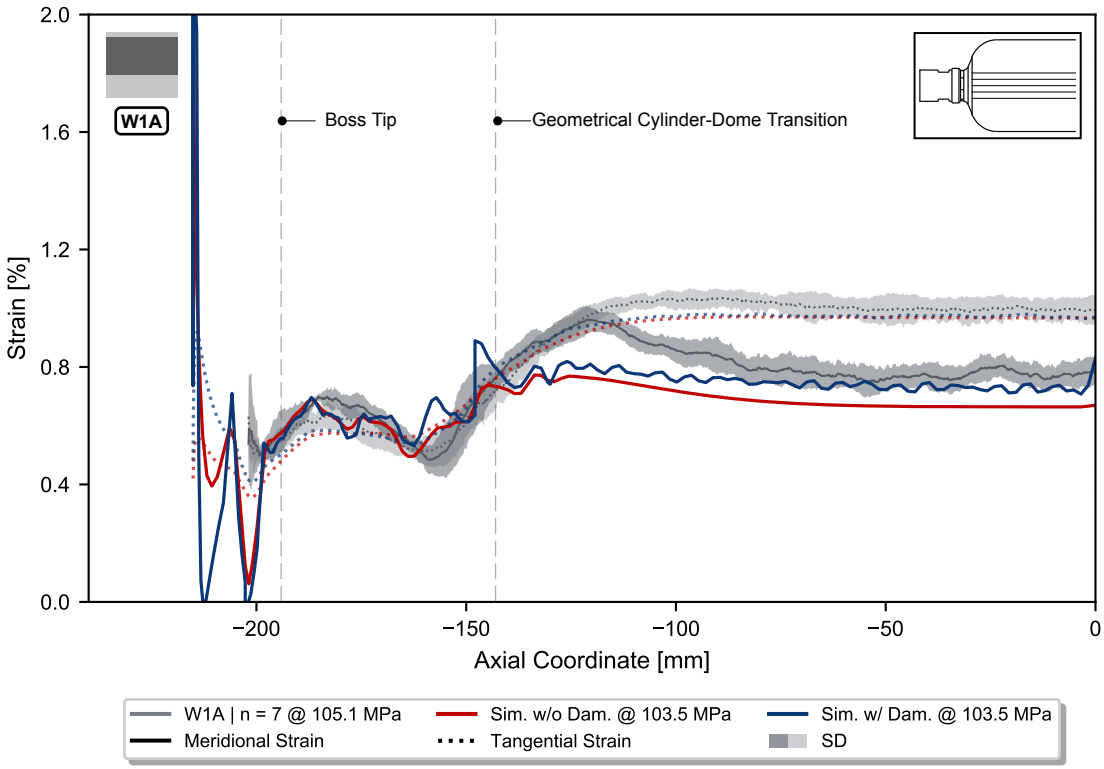


Figure 9.8: Comparison of the outer surface meridional and tangential strain of the W1A stacking sequence considering damage at a load pressure of 103.5 MPa. Numerical predictions are presented against average experimental results for a number of samples n, where their scatter is indicated by their standard deviation (SD)

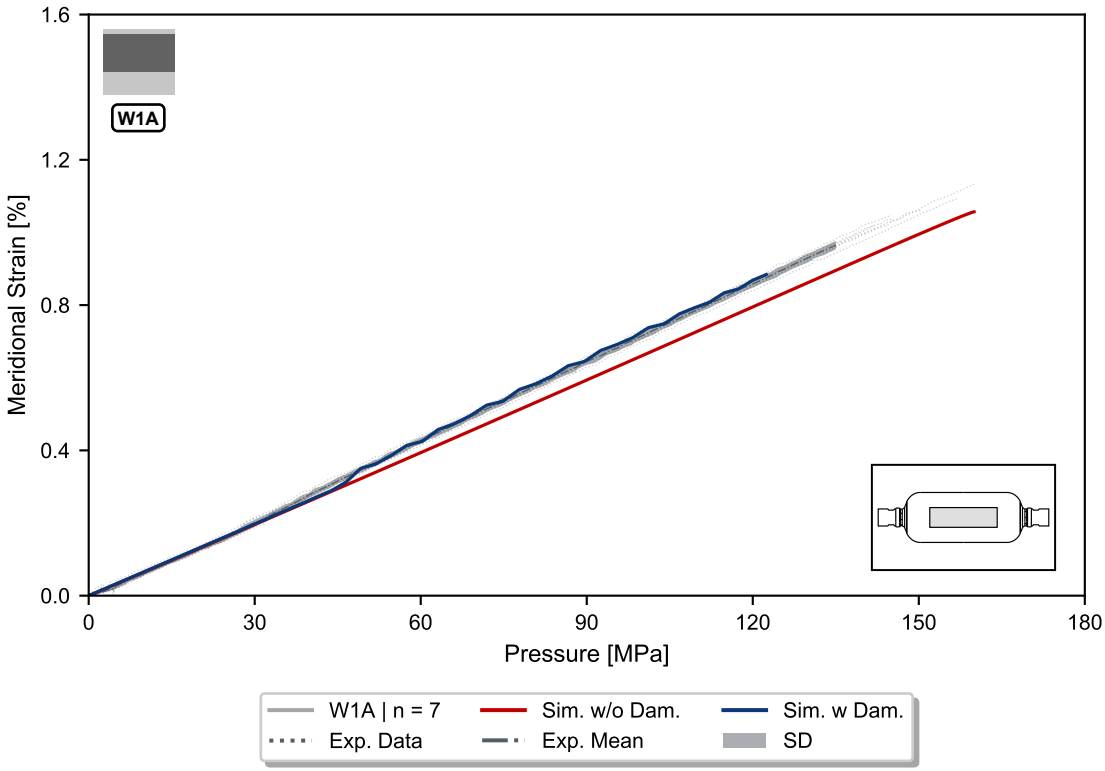
relatively earlier fiber breakage and comparatively reducing the discrepancy with the burst experiments.

9.2.2. Prediction on the Deformational Behavior of the W1A Stacking Sequence

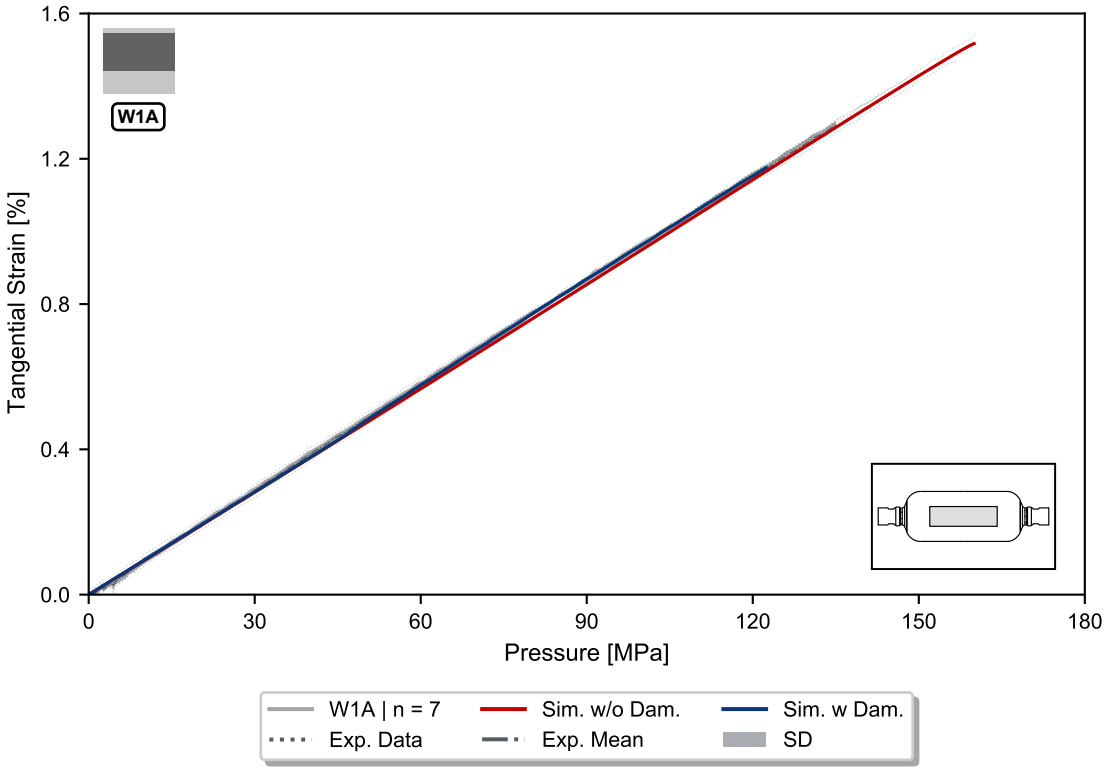
The influence of matrix damage on the deformational behavior of the W1A stacking sequence is noticeable from the correlation of prediction results with the available experimental data. To this purpose, outer surface strain data and boss axial displacement are comparatively presented for the damaged configuration and the constitutively elastic results introduced in chapter 7.

Meridional and tangential outer surface strain components along a meridional path are illustrated at a pressure stage of 103.5 MPa in fig. 9.8, whereas the maximum predicted and measured values at multiple applied loads are comparatively reported in table 9.2. Overall, the predicted meridional strain component in the damaged configuration is shown to increase concerning the undamaged reference modestly. Such behavior is expected from the increased compliance introduced with the material stiffness degradation, transferring the load to the fibers, which, besides a corresponding stress increase, report a marginal strain variation. Additionally, it is noted that the meridional strain in the cylinder becomes relevantly uneven with the progression of matrix damage. As shown in fig. 9.4, interfiber cracks grow there through-the-thickness in the stack of hoop plies, thus allowing a larger meridional displacement where they exist, and generating the presented irregular meridional strain profile. Accounting for damage is shown in table 9.2 to relatively decreasing the discrepancy with experimental results, whereas this mismatch also becomes correspondingly less severe at the higher load states.

Withal, the correlation with experimental results appears to be better in the cylindrical and dome regions than in the cylinder-dome transition. In this case, the defined material thickness profile is argued to limit the local vessel deformation, whereas additional contributors exist on the approach for modeling damage. On the one side, damage progression in the idealized helical $[+\alpha/-\alpha/-\alpha/+\alpha]$ subplies disregards the growth of delaminations between the consecutive detaching bands, also showing lower compliance than reality. On the other side, relatively high fracture toughness is considered in the helical



(a) Meridional strain



(b) Tangential strain

Figure 9.9: Comparison of the outer surface meridional and tangential strain of the W1A stacking sequence considering damage. Numerical predictions are presented against average experimental results for a number of samples n

Table 9.2: Results of the maximum meridional and tangential strain of the W1A stacking sequence considering damage

	Pressure [MPa]		Max. Mer. Strain [%]				Max. Tan. Strain [%]			
	Exper.	Simul.	Exper.	Simul.	Diff.	Diff. (%)	Exper.	Simul.	Diff.	Diff. (%)
No Damage	34.6	35.1	0.37 ± 0.02	0.27	−0.10	−27.34	0.36 ± 0.02	0.33	−0.04	−11.02
	69.9	71.0	0.68 ± 0.02	0.53	−0.14	−21.15	0.70 ± 0.02	0.67	−0.03	−5.00
	105.1	103.5	0.96 ± 0.05	0.77	−0.19	−19.66	1.04 ± 0.03	0.98	−0.06	−6.25
	130.0	127.2	1.15 ± 0.05	0.94	−0.21	−18.26	1.27 ± 0.04	1.22	−0.05	−3.93
	155.6	160.0	1.28 ± 0.05	1.17	−0.10	−8.02	1.47 ± 0.08	1.52	0.05	3.20
Damage	34.6	35.1	0.37 ± 0.02	0.27	−0.10	−26.63	0.36 ± 0.02	0.33	−0.04	−0.83
	69.9	71.0	0.68 ± 0.02	0.58	−0.10	−14.19	0.70 ± 0.02	0.67	−0.03	0.95
	105.1	103.5	0.96 ± 0.05	0.84	−0.12	−12.71	1.04 ± 0.03	0.98	−0.06	0.93
	130.0	127.2	1.15 ± 0.05	1.04	−0.12	−10.34	1.27 ± 0.04	1.22	−0.06	−0.53
	155.6	160.0	1.28 ± 0.05	–	–	–	1.47 ± 0.08	–	–	–

Stack. – stacking sequence; Max. Mer. Strain – maximum meridional strain; Max. Tan. Strain – maximum tangential strain; Exper. – Experimental data; Simul. – Simulation results; Diff. – absolute difference between Experimental data and Simulation results Diff. (%) – percentual difference between Experimental and Simulation results
Note 1: The pressure stages at which Experimental and Simulation results are presented slightly differs because of the unequal frequencies of the recording of results

plies in table 7.1, which limits the relative displacement of the cracked surfaces upon onset. This value of fracture toughness is deemed necessary to achieve numerical stability during damage growth and intends to model the hampered crack growth in these plies during material degradation. However, the representative definition of the fracture toughness in the helical plies needs a more detailed correlation between testing specimens and numerical predictions, as already mentioned in section 9.2.1.

The average strain components in the cylindrical region for increased applied pressure appear as a complementary perspective on the depicted mechanical response along a vessel meridional path. These are presented in fig. 9.9, where a deviation from the constitutively linear response is clearly observed in the meridional component after failure is triggered at 35 MPa. Following, the predicted meridional strain of the damaged configuration closely matches the experimental data, even though a larger discrepancy was already apparent in the results along a meridional path in fig. 9.8. The predicted and experimental results mismatch is reported in table 9.3, where the disparity is comparatively small. The average meridional strain components in the cylinder are impacted by the natural irregularity of the crack growth in the circumferential stack. Therefore, a larger scatter is expected in the strain compo-

Table 9.3: Results of the average meridional and tangential strain in the cylinder of the W1A stacking sequence considering damage. Numerical predictions are presented against average experimental results for a number of samples n

	Pressure [MPa]		Max. Mer. Strain [%]				Max. Tan. Strain [%]			
	Exper.	Simul.	Exper.	Simul.	Diff.	Diff. (%)	Exper.	Simul.	Diff.	Diff. (%)
No Damage	35.4	35.1	0.24 ± 0.01	0.24	0.00	−0.68	0.33 ± 0.01	0.35	0.01	2.07
	70.1	71.0	0.50 ± 0.01	0.48	−0.03	−5.29	0.68 ± 0.01	0.69	0.01	1.10
	105.1	103.5	0.76 ± 0.02	0.71	−0.04	−6.06	1.01 ± 0.01	1.02	0.01	0.85
	130.0	128.0	0.93 ± 0.02	0.85	−0.08	−8.80	1.25 ± 0.01	1.27	0.02	1.61
	155.6	160.0	1.09 ± 0.02	1.06	−0.03	−2.71	1.46 ± 0.01	1.52	0.05	3.67
Damage	35.4	35.1	0.24 ± 0.01	0.24	0.39	0.29	0.33 ± 0.01	0.34	0.01	1.94
	70.1	71.0	0.50 ± 0.01	0.52	5.13	0.16	0.68 ± 0.01	0.69	0.01	2.25
	105.1	103.5	0.76 ± 0.02	0.77	3.34	2.72	1.01 ± 0.01	1.03	0.02	1.60
	130.0	128.0	0.93 ± 0.02	0.93	0.43	8.37	1.25 ± 0.01	1.23	−0.02	−1.36
	155.6	160.0	1.09 ± 0.02	–	–	–	1.46 ± 0.01	–	–	–

Stack. – stacking sequence; Max. Mer. Strain – maximum meridional strain; Max. Tan. Strain – maximum tangential strain; Exper. – Experimental data; Simul. – Simulation results; Diff. – absolute difference between Experimental data and Simulation results Diff. (%) – percentual difference between Experimental and Simulation results
Note 1: The pressure stages at which Experimental and Simulation results are presented slightly differs because of the unequal frequencies of the recording of results

nents along a meridional path than in the corresponding surface average, resulting from the variability in the axial position of the cracks in the hoop plies. When calculating the surface average, these effects are avoided by balancing discrepancies with neighboring positions along the circumference.

Concerning the tangential strain in the cylinder, a minor influence of damage is reported in table 9.3 on the increased loading response. This small effect is reasoned on the minor fiber stress increment experienced by the circumferential plies that, correspondingly, leads to a marginal tangential strain raise. The prevailing hoop stiffness difference between helical and circumferential layers causes the latter to carry the greater part of the expansion loading, thus not being so deeply impacted when the matrix degrades in the helical plies.

In the case of the boss axial displacement, the existence of damage is illustrated in fig. 9.10 to have a significant impact on the aggregated vessel behavior. First, transverse damage in the circumferential ply stack requires the meridional loading to be carried by the neighboring helical layers. The fibers in the helical layers are not aligned with the principal meridional loading direction. This means that as matrix damage also progresses, this has to be transferred to the fibers, inducing more significant meridional strain components in the cylinder and dome transition region. Second, the stiffness reduction in the upper dome region allows the component to flare compared with the undamaged configuration, allowing the boss to displace axially because of the geometric shape change. Such a tendency is anticipated to increase the inner dome surface strain components while the outer remains approximately equal. Third, damage develops in the dome end next to the boss since the early pressurization stages, increasing the propensity of this region to deform because of the existing through-the-thickness shear. Therefore, the boss is allowed to displace axially without a major increase in the outer surface strain because the deformation is inherently taking place within the bulk material.

The experimental measurement of the boss axial displacement depicted in fig. 9.10 corresponds to the offset result of performing a linear regression in the range of 10 to 25 MPa. According to this, the non-linearity reported in the early pressurization stages in section 7.6 is removed, and the actual composite reinforcement response is compared with the predicted results. Notwithstanding, the boss

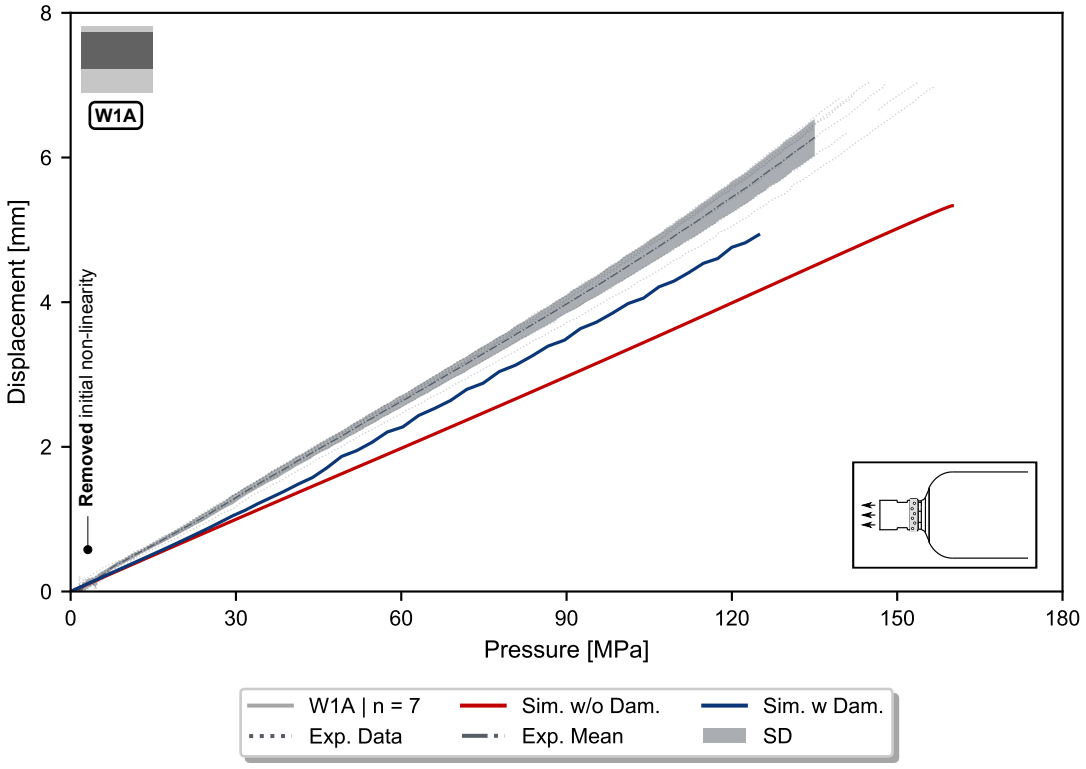


Figure 9.10: Comparison of the axial boss displacement of the W1A stacking sequence considering damage

axial displacement is presented to be less compliant than the experimental data since the early pressurization stages. Such an effect is reasoned on the geometrical depiction and the average material property definition implemented along with the studied vessel configuration. The first results from the tapering shape of the circumferential ply group, hence limiting the tangential expansion of the dome transition region and the change in a dome shape that allows the boss to displace. The second arises from the diminished stiffness and strength in the material because of the higher porosity and lower fiber volume contents in the dome transition region. Ahead of the circumferential ply drop location, the vessel stacking sequence is integrated solely of helical plies, which because of their low angle orientation, it also experiences a low consolidation level. Then, the dome is more likely to change shape and allow a larger boss axial displacement because of the generally less stiff response.

The boss axial displacement results are reported in table 9.4, considering the raw measured data and the offset results that eliminate the initial non-linearity. The discrepancy between damaged prediction and measurement is presented to decrease comparatively with the increasing pressure load, even though the absolute mismatch still broadens slightly. Such a diverging tendency indicates that additional non-linear deformation effects occur with the increasing loading besides the mentioned inaccuracy in the material property definition. These entail the non-linear geometrical deformation encompassing the heterogeneous material property definition and the increased load application because of the expanding enclosed volume during expansion.

Table 9.4: Results of the boss axial displacement of the W1A stacking sequence considering damage

	Pressure [MPa]		Boss Displ. [mm]				Boss Displ. Trunc. [mm]			
	Exper.	Simul.	Exper.	Simul.	Diff.	Diff. (%)	Exper.	Simul.	Diff.	Diff. (%)
No Damage	35.5	35.1	1.72 ± 0.07	1.22	−0.50	−28.92	1.55 ± 0.07	1.22	−0.33	−21.42
	69.1	71.0	3.26 ± 0.12	2.39	−0.87	−26.61	3.10 ± 0.12	2.39	−0.70	−22.72
	104.1	103.5	4.87 ± 0.19	3.56	−1.31	−26.93	4.71 ± 0.19	3.56	−1.15	−24.39
	130.0	128.0	6.19 ± 0.28	4.26	−1.92	−31.10	5.99 ± 0.25	4.26	−1.73	−28.91
	155.6	160.0	7.13 ± 0.28	5.33	−1.80	−25.15	6.93 ± 0.28	5.33	−1.60	−23.06
Damage	35.5	35.1	1.72 ± 0.07	1.29	−0.42	−24.40	1.55 ± 0.07	1.29	−0.22	−15.05
	69.1	71.0	3.26 ± 0.12	2.79	−0.47	−14.30	3.10 ± 0.12	2.79	−0.28	−9.00
	104.1	103.5	4.87 ± 0.19	3.98	−0.89	−18.38	4.71 ± 0.19	3.98	−0.70	−15.07
	130.0	128.0	6.19 ± 0.28	5.03	−1.16	−18.74	5.99 ± 0.25	5.03	−0.96	−16.03
	155.6	160.0	7.13 ± 0.28	–	–	–	6.93 ± 0.28	–	–	–

Stack. – stacking sequence; Boss Displ. – boss displacement; Boss Displ. Trunc. – boss displacement truncated at a pressure of 10 MPa; Exper. – Experimental data; Simul. – Simulation results; Diff. – absolute difference between Experimental data and Simulation results Diff. (%) – percentual difference between Experimental and Simulation results
Note 1: The pressure stages at which Experimental and Simulation results are presented slightly differs because of the unequal frequencies of the recording of results

9.2.3. Prediction on the Damage Progression of the B* Stacking Sequence

The deformational behavior of the B* stacking sequence is presented to influence its progression of damage relevantly. This is depicted in fig. 9.11 for pressure stages ranging from 35 to 70 MPa by illustrating its transverse damage variable. In a similar manner to the W1A configuration, failure occurs first in the dome end next to the boss, albeit degradation also happens in the dome transition region because of a protrusion growth (20 to 25 MPa). As the upper dome quarter tends to expand tangentially and forces the dome shape to stretch, failure in the dome end next to the boss appears at the contact between the composite reinforcement and the boss brim. The sudden stiffness mismatch at this location generates a stress concentration that is already reported in section 8.3, hence prompting the appearance of damage.

With the increased loading, transverse damage generally extends within the helical plies in the cylinder and dome regions. Failure in these plies develops from the outer to the inner ones, following the decreasing meridional stress gradient through-the-thickness. Eventually, interfiber cracks appear in the circumferential ply stack (47 MPa), developing rapidly through the whole group. The existence of continuous cracks through-the-thickness is analogous to the observations made for the W1A layup, being their correlation with microscopic observations also portrayed in fig. 9.11. After pressurization up

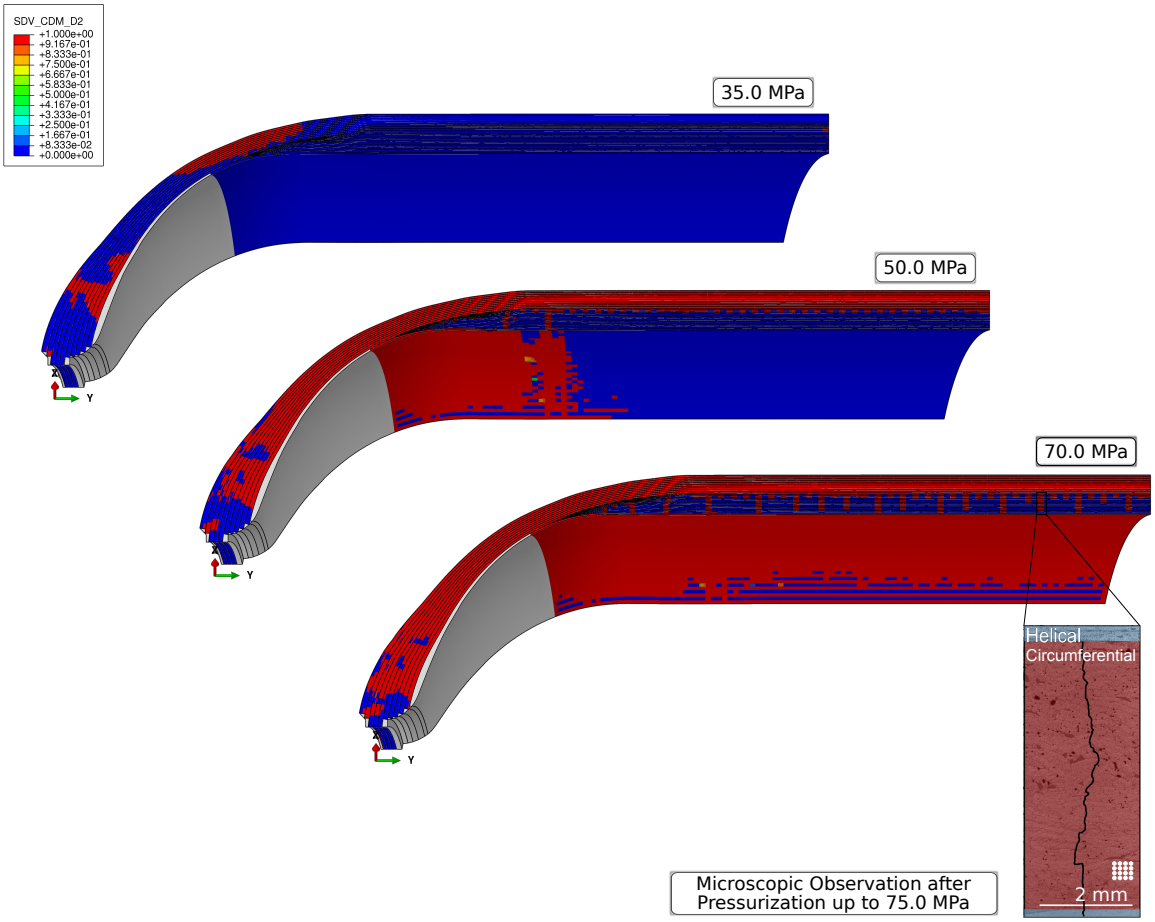


Figure 9.11: Predicted transverse damage of the Bx stacking sequence at load pressures of 35, 50 and 70 MPa. The predicted cracks through-the-thickness in the circumferential ply stack are additionally compared with microscopic observations of samples after pressurization up to 75 MPa

to 75 MPa, cracks are presented to extend throughout the whole stack while connecting the existing pores.

Interfiber fracture in the circumferential stack appears relatively later for the B* case than for the W1A configuration. Two reasons principally appear; first, the B* configuration experiences lower tangential expansion because of the high hoop stiffness of the innermost circumferential plies, and coupled with it, also a lower meridional strain; whereas second, the meridional stress reduces toward the inside, which is also the location of the circumferential stack. The pressure range within which these cracks are predicted can be correlated with the recording of acoustic emissions. These are shown in fig. 9.12 on the channel file during a burst experiment. In this case, a region of relatively higher AEs is depicted in the range of 35 to 50 MPa, which reasonably compares with the high amplitude acoustic events that are expected from cracks appearing in the circumferential group. Yet, the pressure at which these emissions start is modestly lower than the damage progression prediction. The considered material definition disregards the lower transverse strength of the outer circumferential plies, which because of their relatively higher porosity, are expected to develop cracks comparatively earlier. This trend coincides with the observations made for the W1A stacking sequence, where a similar trend in the porosity content is expected through-the-thickness.

However, identifying the onset of interfiber cracks in the circumferential ply stack is not categorical. On the one hand, this can be determined by the first AE that surpasses a pressure threshold, as reported for the prediction and experimental results correlation in table 9.5. Withal, this is biased by local failures generating an emission unrelated to actual cracking in the group. On the other hand, failure is already predicted in the outer helical layers when cracks appear in the circumferential group. Their existence implies that emissions because of failures in both layers might overlap and, consequently, hinder their

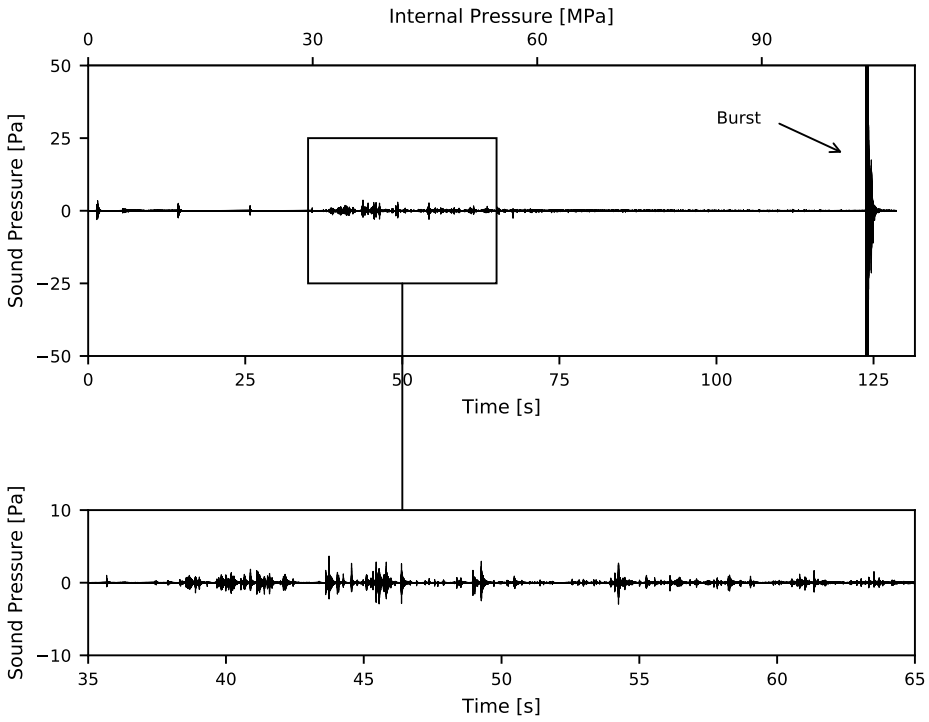


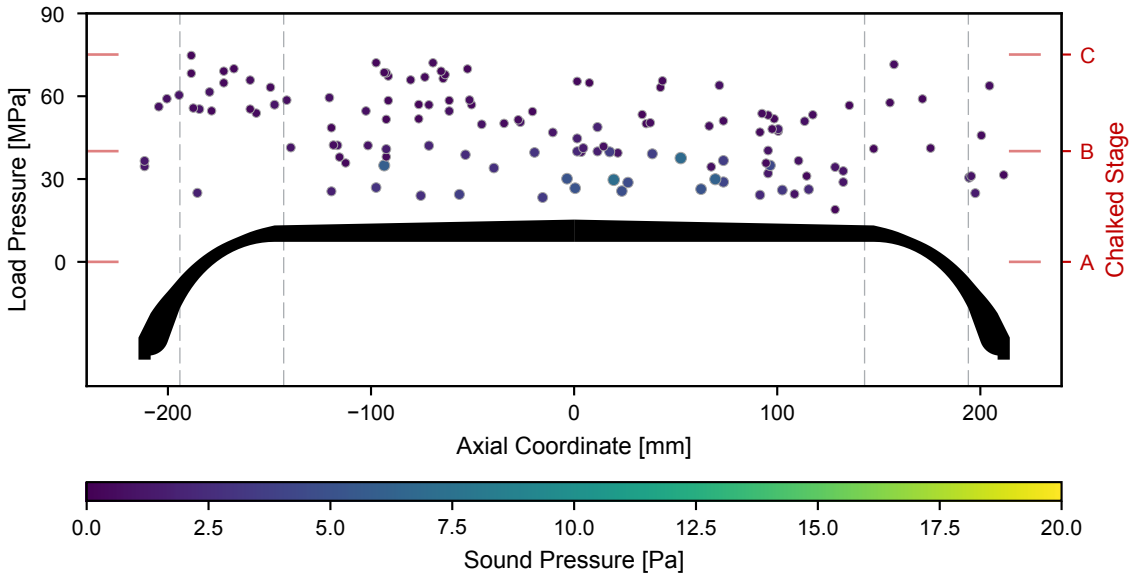
Figure 9.12: Acoustic emission channel file of a burst experiment of the 01-0243 | B* stacking sequence

interpretation. Particularly to the case where the hoop layers are on the inside, the emission magnitude does not unequivocally differentiate the layer where it occurs.

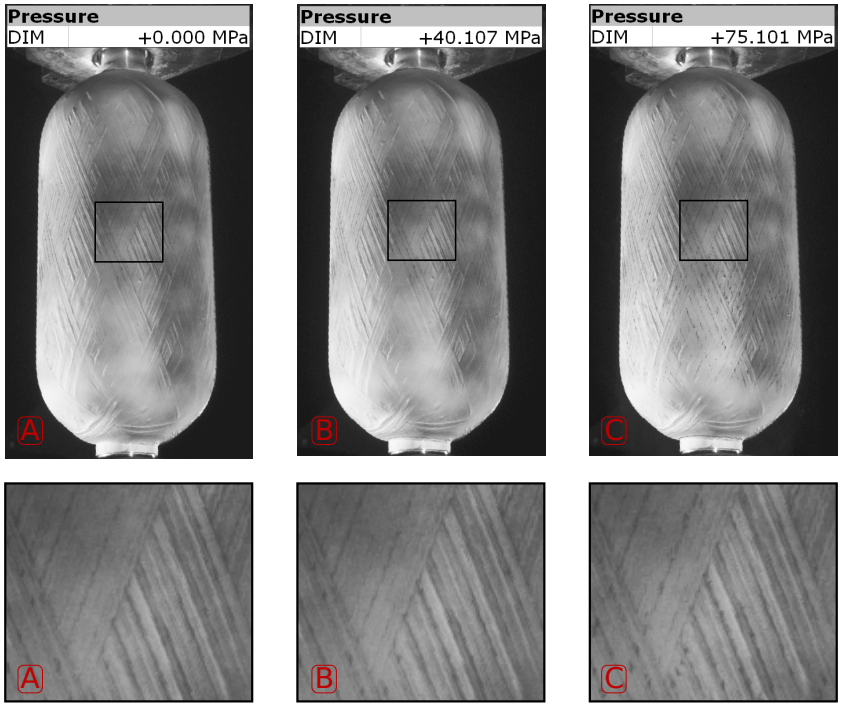
Besides, significant amounts of elastic energy are released during cracking of the circumferential group, the amount of layers above them attenuates this. As depicted in fig. 9.12, the emissions in the range where cracks in the hoop layers are expected, only modestly stand above the following ones, related instead with degradation in the outer helical group. Low amplitude emissions are presented in fig. 9.12 to occur until mildly high-pressure stages after the likely cracking in the circumferential ply stack. Therefore, the gradual degradation of the helical layers is depicted, besides failure in the transverse direction being expected relatively earlier. Acoustic events are generated with the successive interfiber cracking and detaching of bands, which require increased loading to overcome the multiple crack growth arrests of the interwoven band architecture.

These layers progressive degradation is illustrated from the identification of damage in fig. 9.13, where the AEs localization and the outer surface visible degradation are shown. Emissions in fig. 9.13a are mostly localized first in the cylindrical region, including those of marginally higher amplitude, while at higher pressure stages, additional events are reported in the dome transition regions. Acoustic events in the dome transition occur considerably later than the damage onset prediction, hence suggesting that the onset of damage and the production of acoustic events is not unequivocally connected. Related to the B* stacking sequence, relevant tangential expansion develops in the dome transition region, which also reasonably leads to premature material degradation in the transverse direction. However, the presented AEs show the most of these events after degradation in the cylinder that, comparatively, experiences a less severe stress state. As a result, it appears that material degradation in the helical layers might exist before emissions occur, which needs to be correlated more precisely with the actual band construction.

In fig. 9.13b, the vessel outer surface is presented when covered with chalk during pressurization. Degradation is only visible at the stage of 75 MPa by black dots at the intersections of the multiple bands, whereas this is not clearly noticeable at the 45 MPa pressure stage. Furthermore, the outer surface degradation of the B* configuration is overall less apparent than the damage encountered in the W1A case. The less noticeable surface cracking is related to the magnitude of the transverse strain through-the-thickness, being it lower for the B* case than for the W1A layup. The lower reported strain



(a) Localization of AEs along the axial coordinate of the 01-0190 | B* vessel geometry. Emissions are presented against the pressure stage at which they occur, whilst a higher sound amplitude is indicated by correspondingly larger markers. The right hand side indicates the pressure stages at which the damage state in the outer surface is portrayed



(b) Outer surface degradation on chalked 01-0190 | B* vessel. Damage is shown by dark dots between the composite bands. This is slightly visible at the pressure stage of 75.0 MPa, whereas at 45 MPa internal pressure no clear surface disruption is noticed

Figure 9.13: Damage identification of the B* stacking sequence after pressurization up to 75 MPa

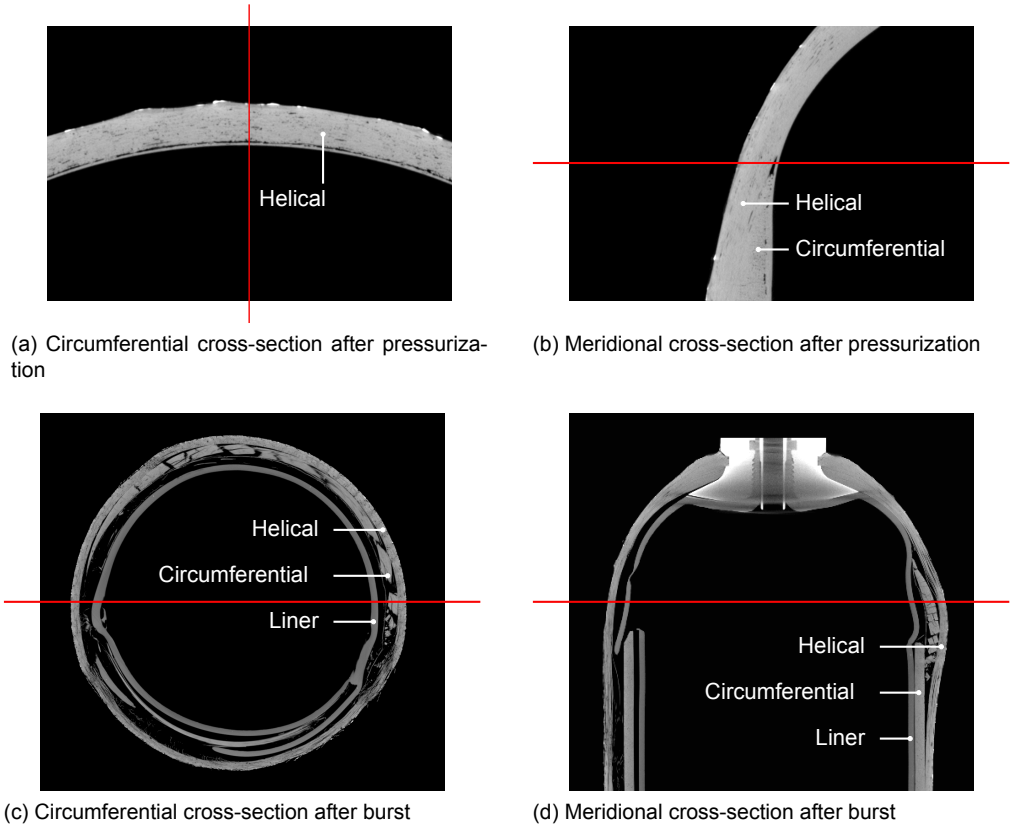
components result from the high tangential stiffness of the inner circumferential plies of the B* stacking sequence. Additionally, cracks in this stack tend not to open so severely because the meridional stress component is minimum in the inner layers, and hence, it is the released elastic energy during fracture. Furthermore, the chalked vessel in fig. 9.13b does not clearly show surface degradation in the dome transition region; it relates to the complex damage progression in the helical layers and its limited crack

opening besides the material experiencing significant strain values.

The final collapse manifests by the fiber breakage in the adjacent circumferential ply stack, resulting from the growth of a protrusion in the dome transition region. This type of failure is local to the cylinder end and derived from a highly specialized load path. Therefore, the load-bearing capacity is lost when fibers break at the tip of the circumferential ply stack, and further load redistribution is not allowed. This effect contrasts with the W1A configuration, where preliminary fiber breakages occur in the cylindrical region before the final collapse. Longitudinal damage is present in light of the uniformly loaded cylinder, where the circumferential plies are close to the maximum stress, and preliminary damage may occur because of initially weaker fibers. As a result, the AE channel file of the B* configuration in fig. 9.12 shows no events related to fiber breakage before burst, while this is regarded in fig. 9.5 for W1A.

A failure mode in the dome transition region is clearly illustrated from the CT images in fig. 9.14 after pressurization and burst. In the first place, figs. 9.14a and 9.14b show that a flawed bond exists between the tip of the circumferential ply group and the overlying helical layers. It is anticipated that this has a stress concentration effect, inducing the growth of a delamination at the interface between circumferential and helical plies, and causing a load path deviation while also detrimentally impacting the strength of the hoop stack. However, if the CT images are taken after pressurization, the existence of a delaminated interface cannot be assured because of the vessel depressurized state, thus requiring a closer microscope observation of the region. Secondly, fiber breakage in the circumferential stack after burst is apparent in figs. 9.14c and 9.14d. Fibers in the hoop plies are made into pieces nearby the dome transition region, whereas they remain relatively intact in the cylinder. Likewise, the helical layers at this location are shattered, although not annihilated, suggesting a local failure mode and less energetic than corresponding in W1A.

The tendency toward a vessel collapse in the dome transition region is additionally depicted in fig. 9.15 for the longitudinal failure criteria evaluation along a meridional path. When compared with



(a) Circumferential cross-section after pressurization

(b) Meridional cross-section after pressurization

(c) Circumferential cross-section after burst

(d) Meridional cross-section after burst

Figure 9.14: CT image of the dome transition of the 01-0176| B* stacking sequence after pressurization up to 75 MPa and of the 01-0194 | B* after the burst event. The solid red lines indicate the position of the corresponding circumferential and meridional cross-sections

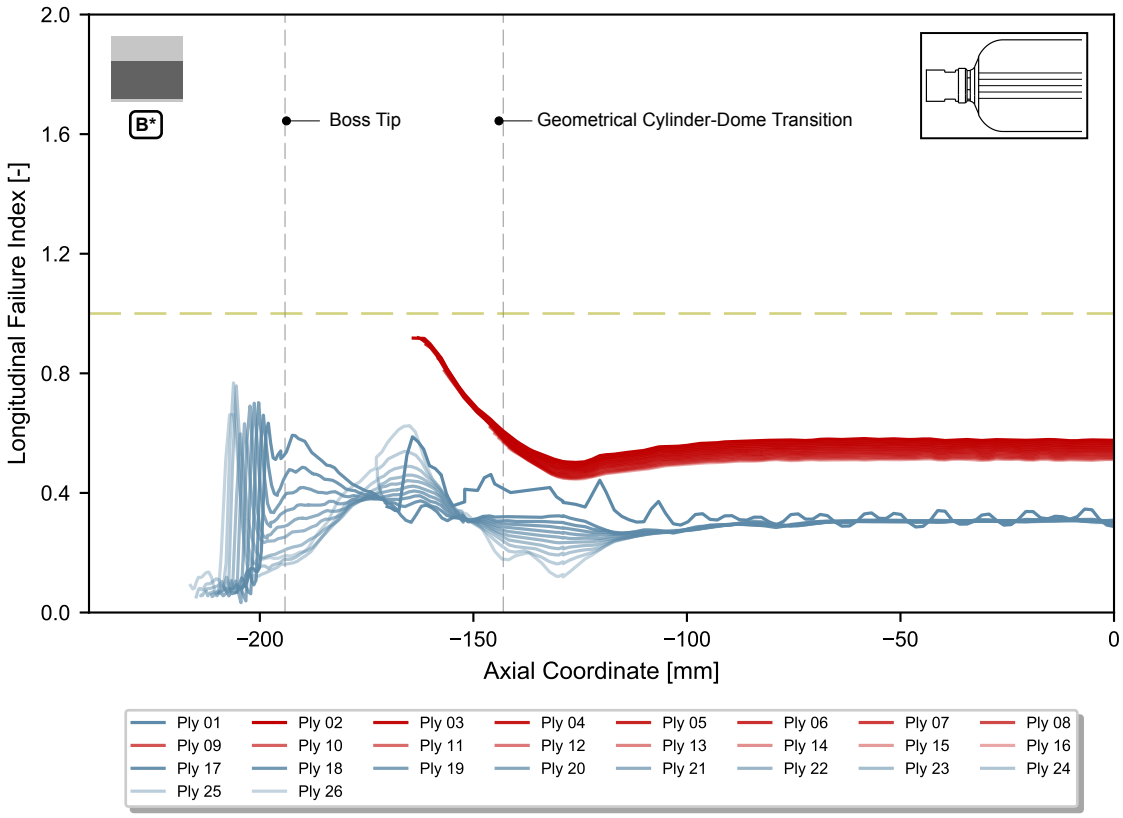


Figure 9.15: Fiber tensile failure criteria according to Puck, [87] at a load pressure of 980 MPa

the prediction of a constitutively elastic analysis in section 8.3, the likelihood of failure at the tip of the circumferential ply stack relevantly increases. This response relates to the load redistribution to the hoop plies when the tangential stiffness drops in the helical layers, therefore also relevantly impacting the burst pressure estimation.

In a similar manner to the W1A case, the damage progression prediction for the B* stacking sequence is unable to find a solution at mildly high-pressure stages. Therefore, the pressure level of the burst event is ultimately estimated by linearly extrapolating the longitudinal failure criteria evaluation at the last converged increment. The predicted stage of final collapse is compared with experimental data in table 9.5, where the correlation with the onset of interfiber cracks in the circumferential ply stack is additionally reported. The latter is identified by the first AE that exceeds a threshold of 0.3 MPa.

Table 9.5: Comparison of the damage onset prediction of the B* stacking sequence with experimental data

Vessel	Exper.		No Damage				Damage			
	MF Cyl.	Burst	MF LaRC04	Diff. (%)	FF. Puck	Diff. (%)	MF CompDam	Diff. (%)	FF. CompDam	Diff. (%)
01 - 0190	23.3	101.2	46.2	98.3	132.6	31.0	47.0	101.7	116.4	15.0
01 - 0243	22.3	110.5	"	107.2	"	20.0	"	110.8	"	5.3
01 - 0257	24.8	91.4	"	86.3	"	44.9	"	89.5	"	27.4
01 - 0281	21.7	119.7	"	112.9	"	10.7	"	116.6	"	−2.8
01 - 0282	20.4	98.9	"	126.5	"	34.1	"	130.4	"	17.7

Stack. – stacking sequence; MF Cyl.– matrix failure pressure stage identified in the cylinder by means of AE; MF LaRC04 – matrix failure pressure stage in the circumferential group of plies according to LaRC04; FF Puck. – fibre failure pressure stage according to Puck; MF CompDam – matrix failure pressure stage in the circumferential group of plies according to CompDam; FF CompDam. – fibre failure pressure stage according to CompDam; Diff. (%) – percentual difference between experimental and simulation results

Load redistribution during damage shows to relevantly decrease the discrepancy between prediction and experimental results, although a modest mismatch still exists. On the one hand, modeling damage progression does not account for delaminations connecting cracks in the helical layers, limiting the increased compliance of the damaged regions. On the other hand, the prediction of the burst event is particularly sensitive to the longitudinal strength definition, thus depending on the porosity and fiber volume contents at the tip of the circumferential ply group. Concerning the correlation with the crack growth in the circumferential ply stack, a substantial discrepancy exists in both elastic and damaged configurations. This mismatch arises from the distorted onset identification derived from the first recorded emission, and which is not necessarily produced by the extensive cracking within this stack. Instead, identifying the onset of cracking from the analysis of the emission channel files appears as a more robust approach.

9.2.4. Prediction on the Deformational Behavior of the B* Stacking Sequence

The impact of accounting for damage in the deformational behavior of the B* stacking sequence is presented by probing the surface strain components and the boss axial displacement. These are compared for configurations assuming elastic material properties and the progression of damage, which are, additionally, benchmarked with the measurements obtained through DIC. Opposite to the W1A configuration, where the modeling of damage depicts a more realistic deformational behavior, the damaged response of B* appears to deviate further from the experimental results. Such an effect contrasts with the plausible progression of damage depicted and is ultimately related to the limitations of modeling the material degradation through a CDM approach.

The outer surface strain components are illustrated in fig. 9.16 at a pressure stage of 85.0 MPa. Particularly, the tangential strain is presented to increase significantly compared with the constitutively elastic result in the dome transition region, where a protrusion grows. The damaged material expe-

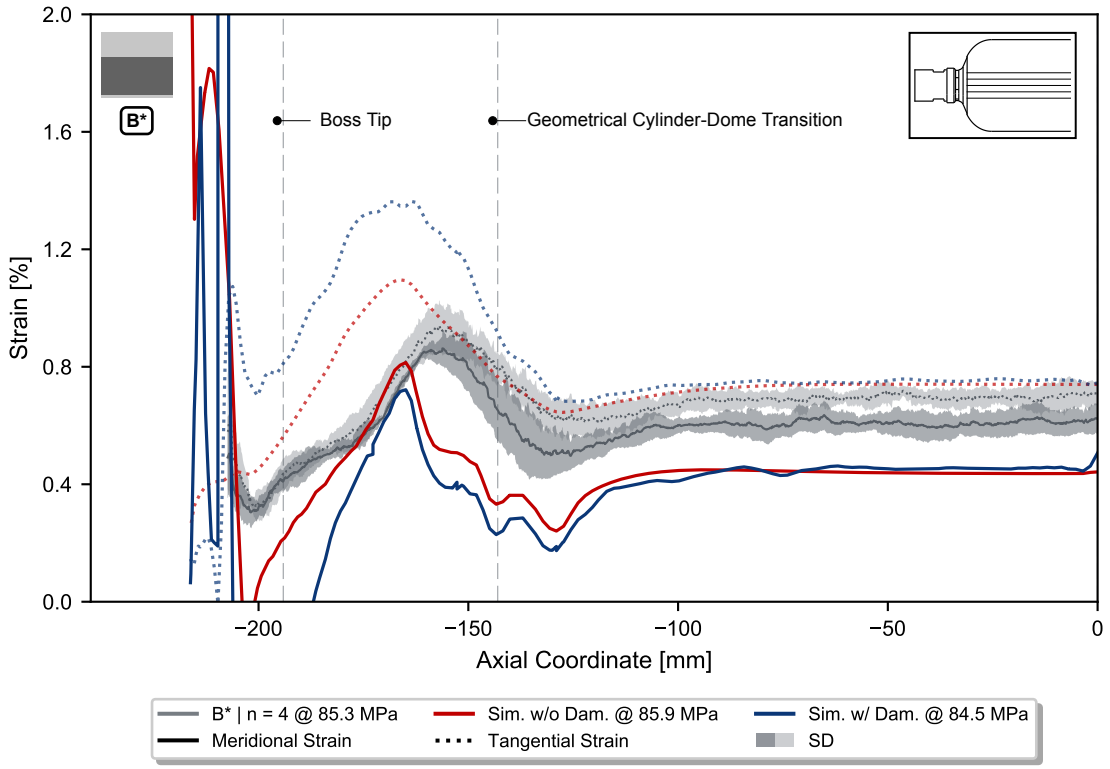
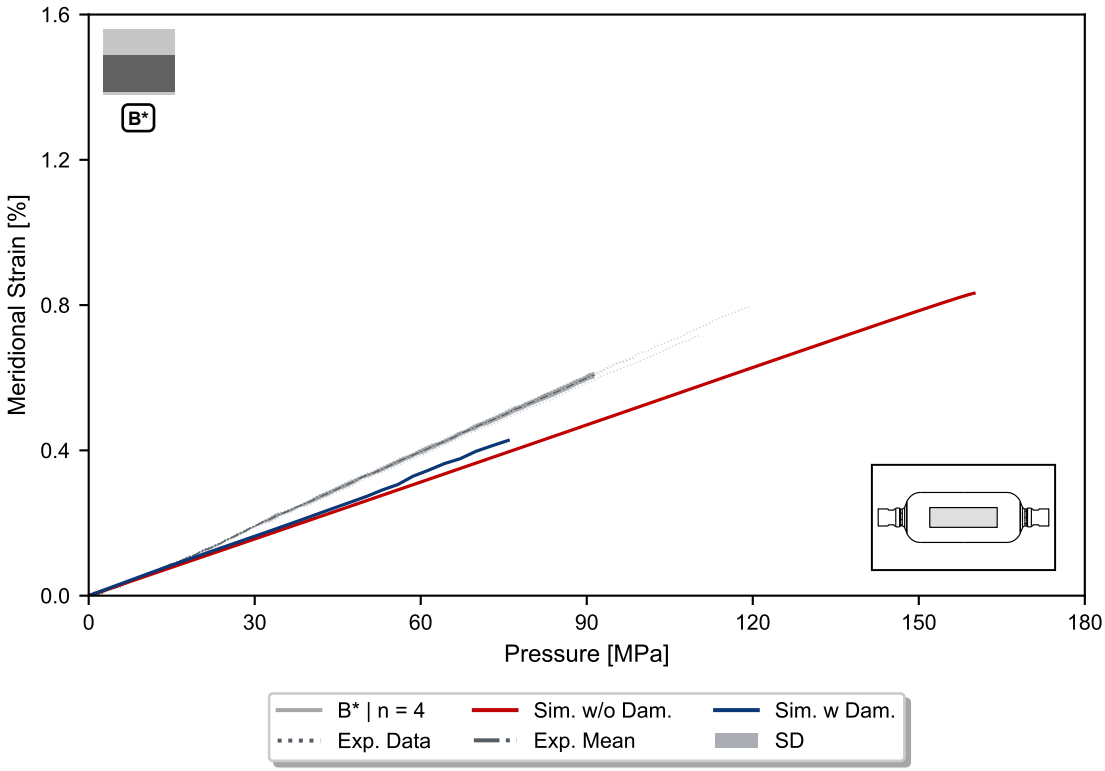
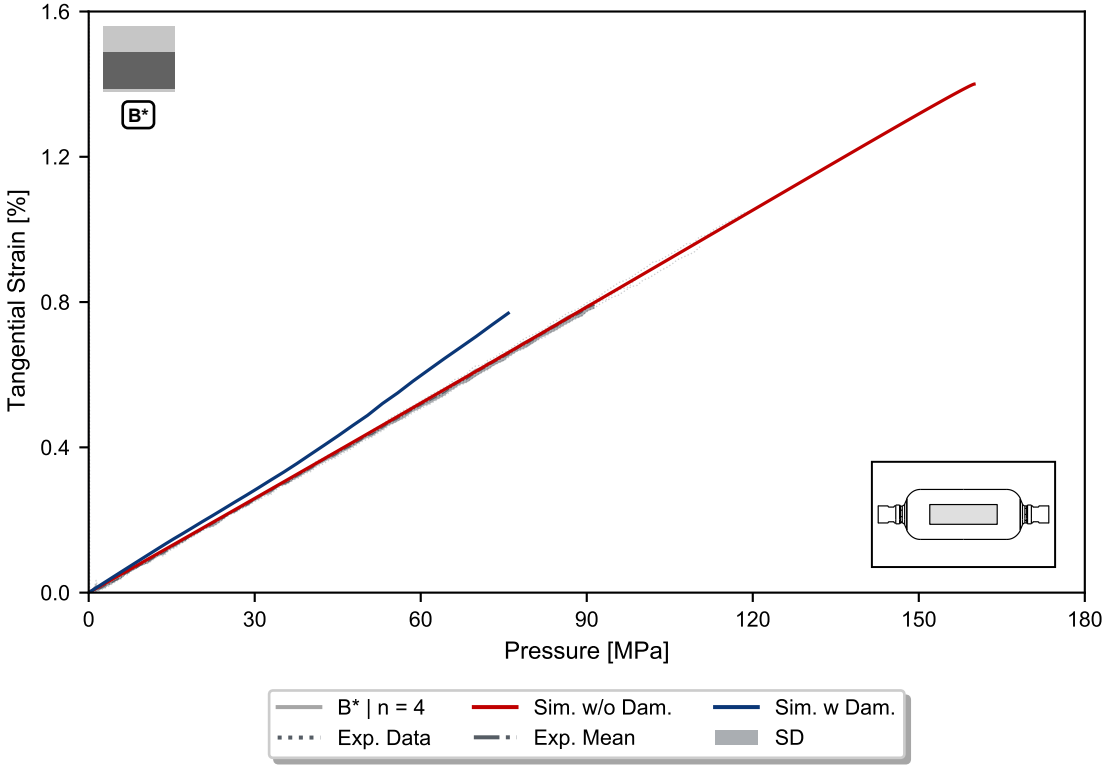


Figure 9.16: Comparison of the outer surface meridional and tangential strain of the B* stacking sequence considering damage at a load pressure of 85.0 MPa. Numerical predictions are presented against average experimental results for a number of samples n, where their scatter is indicated by their standard deviation (SD)



(a) Meridional strain



(b) Tangential strain

Figure 9.17: Comparison of the outer surface meridional and tangential strain of the B* stacking sequence considering damage. Numerical predictions are presented against average experimental results for a number of samples n

riences increased compliance, although, as a result of it, the magnitude of the tangential strain component substantially overpasses the experimental measurement. Comparatively, the predicted strain in the meridional direction only marginally increases compared to the elastic solution in the cylindrical region, whereas it decreases in the dome and dome transition regions. This effect deviates from the experimental response, and also, disagrees with the expected behavior upon the existence of failure.

Concerning the average cylinder strain components in the outer surface, similar tendencies to the ones observed along the meridional path are depicted in fig. 9.17. The meridional strain result slightly increases over the constitutively elastic solution, yet not sufficiently matched with the experimental measurement. Likewise, the tangential component appears to be more compliant than in the burst tests, as it is driven by the relevant expansion in the dome transition region. Therefore, the prediction of the tangential expansion in the cylinder, which is presented as very accurate for a constitutively elastic analysis, deviates significantly when considering the existence of damage.

A subsequent representation of the disagreeing deformational response in the dome region is illustrated in fig. 9.18 for the boss axial displacement. In this case, the triggering of failure prompts a relevant increase in the compliance of the lower dome quarter. It culminates with a boss displacement duplicating the magnitude of the elastic result and unrealistically exceeding the displacement reported during tests.

The excessive boss axial displacement predicted with the modeling of damage progression suggests that a local deformational effect might occur in the lower dome quarter. This is depicted in fig. 9.19 through the transverse strain component in the elastic configuration and under the damage progression assumption. The deformed shape in the dome is illustrated at pressure stages of 35 and 85 MPa, where a through-the-thickness shear-off effect of the composite reinforcement is depicted at the location of the boss brim tip. This tendency is noticed by the locally high transverse strain component, which aggravates the increased loading. A local effect of this type appears to allow the relevant axial displacement of the boss while limiting the crack opening in the cylinder and upper dome regions. The shearing plane in the lower dome quarter dissipates the elastic energy that would otherwise be invested

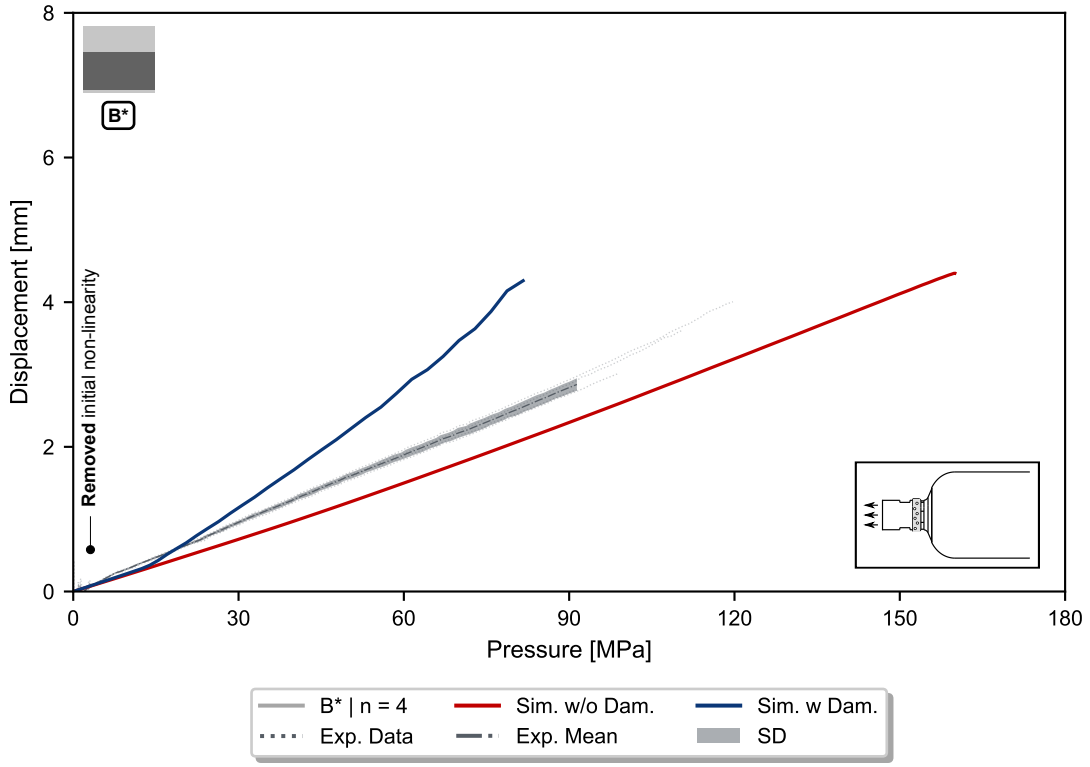


Figure 9.18: Comparison of the axial boss displacement of the W1A stacking sequence considering damage

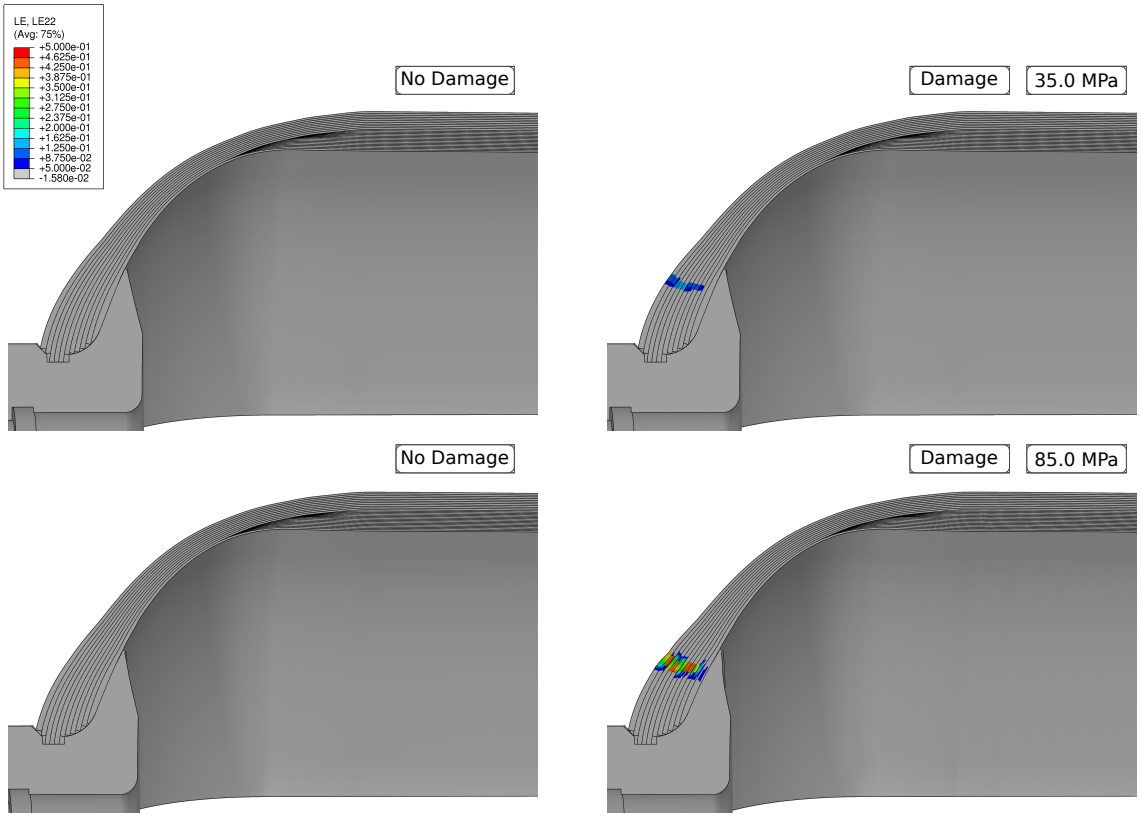


Figure 9.19: Comparison of the dome transverse strain for the undamaged and damaged configurations at load pressure of 35.0 and 85.0 MPa

in opening cracks in the cylinder and the upper dome.

The generation of a shearing load state is a consequence of the prediction of transverse damage through the helical layers. Its prediction is idealized by the stiffness degradation in the transverse direction, which eventually permits the free relative displacement of the two confronting sides. However, cracks through-the-thickness in the helical layers do not allow a free relative displacement in reality. In this case, sliding is limited by the fibers shear strength and the friction generated by the engagement of the uneven crack growth. When damage is depicted through a CDM idealization, cracks are allowed to grow perpendicular to the fibers, even though the fracture toughness, in this case, is substantially larger than if they grow parallel.

Considering the growth of cracks through-the-thickness in the stack of helical layers, the B* vessel is more prone to show the limitations of the CDM idealization than its counterparts. It derives from its deformational behavior, where the upper dome quarter expands relevantly tangentially, and the dome shape tends to stretch as a result. The stress concentration generated at this location is the most relevant among the studied vessel configurations, hence inducing the relevant material degradation illustrated in fig. 9.11. The illustrated shearing effect occurs as the axial component of the pressure load is applied in combination with this localized material degradation.

9.3. Concluding Remarks

During material degradation, load redistribution is observed to follow a physically sound pattern when the mechanical response of the vessel is modeled. Failure is expected first in the dome region next to the boss, followed by degradation in the cylindrical and upper dome quarter. In the cylinder of the considered W1A and B* layups, damage is initially predicted in the outer helical layers, before through-the-thickness cracks develop in the circumferential ply stack inner helical layers start degrading. This pattern is noted to be generally compatible with recorded AEs, and vessel observations during pressurization, albeit shortfalls, exist both in the numerical and experimental determination of damage.

On the one side, the modeling of damage in the helical plies requires a more thorough calibration of how the stiffness degrades within the existing interwoven bands. The variability of material quality through the vessel geometry aggravates this difficulty, overlooking the triggering of failure where large amounts of resin and pores exist. Coherent with the FPF prediction in section 8.3, damage onset is overestimated in the circumferential ply stack, where the diminished strength in the outer plies results in earlier AE recordings than the numerical prediction.

On the other side, acoustic events taking place in the inner layers of the vessel cannot be reliably discerned because of their low amplitude emissions. A reduced detection threshold would ultimately allow this, although at the expense of decreasing the pressurization rate to avoid the coupling of multiple simultaneous events. Besides, the correlation of damage onset with the visual observation of outer surface cracks shows to diverge from the numerical prediction. Macroscopic cracks are distinguished only at considerably later stages than their prediction, hence suggesting that either non-visible cracks exist but are not identified, that the material mechanical characteristics are insufficiently accurate, or that the load transfer to the outer helical plies is not modeled correctly.

Accounting for matrix damage is also presented to impact the prediction of the deformational behavior compared with the constitutively elastic solution. It becomes more realistic for the W1A stacking sequence, whereas it is limited by the prediction of cracks perpendicular to the fibers in the B* case. In the W1A configuration, the general stiffness degradation leads to an increase in the meridional strain components and the boss axial displacements. The load is redistributed to the fibers, which mildly increase their stress state and predict a vessel burst pressure that becomes more similar to the experimentally obtained ones.

However, the concentration of stress in the lower dome quarter of the B* stacking sequence results in a local through-the-thickness shearing effect that disregards the substantial fracture toughness required. This deformation pattern distorts the strain state in the dome while limiting the meridional strain in the cylinder and dome transition. Still, a burst pressure that approximates the experimental measurement better than the elastic solution is obtained. The burst pressure is controlled by the increased compliance in the upper dome quarter, which is not influenced by the deformational pattern near the boss.

Lastly, the modeling of damage stands as a task of germane complexity, where numerical difficulties are encountered while reproducing the material behavior at high-pressure stages. The high-loading condition causes numerical solutions to terminate prematurely because of divergence, therefore hindering the unequivocal estimation of vessel burst pressures.

10

Modeling Heterogeneous Material Properties

The detailed geometrical configuration of a CPV is presented in chapter 5 to depend on the normal forces applied on the winding surface. This pre-curing loading state induces various consolidation levels in the uncured composite material that, because of resin outflow, tends to reduce the final thickness magnitude. Withal, this process has other direct consequences in the material quality, such as the relative increase in the fiber volume content and the diminishing porosity because of the percolation of the resin. The sensitivity of the latter is discussed in chapter 6 concerning the variability of the mechanical characteristics of the composite material with various porosity contents. Matrix dominated properties show to be relevantly influenced by this feature, which correspondingly indicates that the stiffness and strength of the CPV generally differ from a homogeneous simplification.

This chapter accounts for the heterogeneity of material properties relative to the position in the vessel and discusses the applicability of this definition in the determination of the vessel burst pressure. To this purpose, an analysis of the CPV laminate is first introduced in section 10.1, framing the variability of the material quality. This effect is presented from the influence of the stacking sequence and the vessel position in the fiber volume and porosity contents. Moreover, the origin and type of voids in the material are identified and connected with the failure modes that they might trigger. Following, a variable material definition is implemented in the FE model of section 7.2 and their results discussed in section 10.2 regarding their response upon damage progression.

10.1. Experimental Analysis of the Vessel Material Characteristics

Material quality is evaluated in this project context from the specimen chemical digestion, according to the standard DIN EN 2564:2019-08 [137], and their CT scan. Chemical digestion permits to determine fiber volume and porosity contents, although these results are subjected to the accuracy and representativeness with which weight and volume measurements are made. Likewise, the use of CT images allows computing void volumes from their surface recognition but are subject to the numerical sensitivity of the unevenly interpolated cavity surfaces.

The material characteristics vary through-the-thickness direction according to the constructed stacking sequence presented in fig. 10.1 for the cylindrical region of the W1A, E+ and B* layups according to the standardized chemical digestion test, [137]. These results are presented for the full stacking sequence in all three cases, whereas the material quality of the helical and circumferential layer groups is additionally determined for the W1A and B* vessels.

On the one hand, it is observed that the full stack fiber volume content is noticeably similar for the three configurations, whereas porosity reduces in the case of E+. The fiber volume content appears to remain constant because resin flowing out during consolidation simply accumulates at the outer group surface and is still measured during the standard test. Concerning the lower void content of E+, it is argued that the alternating winding of helical and circumferential layers in this layup minimizes large voids at layer interfaces, where winding of the upper hoop plies forces lower group boundaries to shut tight.

On the other hand, a clear difference in the quality of the helical and circumferential stacks exists between the W1A and B* cases. The W1A stacking sequence locates the stack of helical layers on the bottom, being these greatly compacted by the subsequent circumferential plies. Correspondingly, the outer circumferential plies are lightly compacted because there is no significant outer pressure. In the case of B*, it is the circumferential layer group located on the inside, which, as a result of the low radial pressure applied by the outer helical layers, only experienced light consolidation. Likewise, the helical plies in this layup are barely compacted as they are also located on the outside. This trend is visible for both the porosity and fiber volume contents illustrated in fig. 10.1. The contents in the circumferential stacks are similar in both cases because they are subjected to similar consolidation levels. In the helical layers, the fiber volume content reduces for the B* layup, while the porosity also increases compared with the W1A case.

It is noted that the average of the porosity and fiber volume contents for the individual stacks does not match the result for the full stack. Withal, this occurs because the full stack includes the resin layer that accumulates on the outer surface during consolidation. When extracting the samples for the individual group testing, this layer is removed, therefore distorting the comparison. The fiber volume content of the full stacking sequence is lower than the average of the individual groups, whereas the porosity of these also increases due to the entrapped gas in the stock of resin.

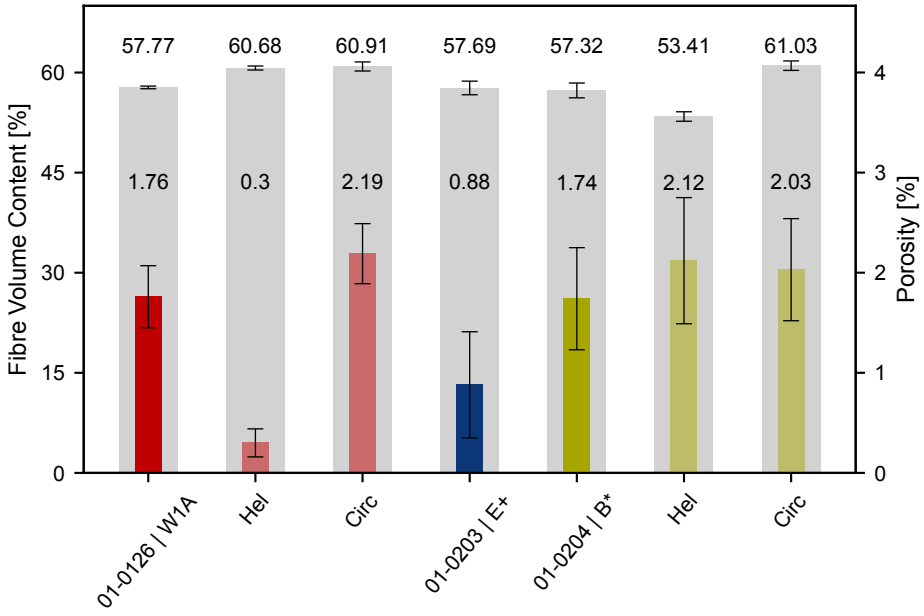


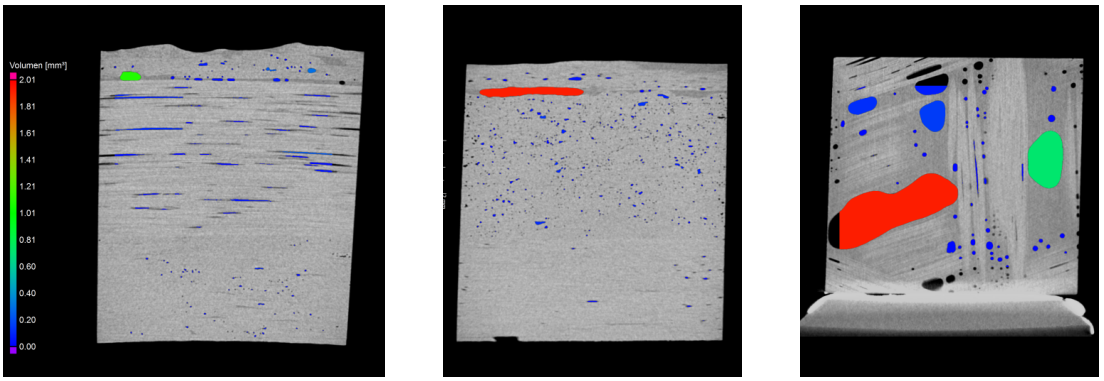
Figure 10.1: Results of the fiber volume and porosity contents in the cylindrical region of the W1A, E+ and B* stacking sequences characterized by chemical digestion

Fiber volume and porosity determination through standardized chemical digestion tests provide a general overview of the quality of the material investigated. However, no information exists on the type and distribution of voids within the stacking sequence. This shortcoming is overcome with the estimation of porosity contents from the void surface analysis of CT scans, which, hence, also allows illustrating how the winding manufacturing process impacts this variable.

In this regard, transverse, meridional, and through-the-thickness sections of a W1A vessel are presented in fig. 10.2 by referencing the relative volumes of the cavities identified. Two types of voids are observed and alternatively regarded as entrapped air between layers of the same type, and gas bubbles at the group interface where resin accumulates during consolidation. The first characterize by being elongated and of relatively low volume. These are shown in fig. 10.2 in the helical and circumferential layer groups, where the cavities amount decreases towards the inside because of the higher consolidation. These needle-shaped voids are noticeably aligned with the fiber orientation, forming between the filament wound tows. Therefore, a clear distinction exists between porosity in the circumferential plies, where voids penetrate straightforward, and the helical layers, where cavities intercalate

as a result of the band construction.

In the second, circumferential group consolidation leads to a layer of the resin forming outside the hoop layer stack. Resin outflow from circumferential groups is generally halted by the lower permeability of the overlying helical plies, hence forming resin-rich regions at the interface. Relatively large air bubbles form at this location because of the lower viscosity of the constituent and the entrapped air during winding, detrimentally impacting the strength and possibly leading to the premature failure of the group interface.



(a) View parallel to the circumferential plane of the vessel

(b) View parallel to the axial plane of the vessel

(c) View parallel to the through-the-thickness direction

Figure 10.2: Type and magnitude of voids in the 01-0126 | W1A stacking sequence obtained from CT images

An interpolation of the porosity content through-the-thickness direction of CT scan samples is depicted in fig. 10.3 for the W1A, E+ and B* stacking sequences. Furthermore, their average porosity magnitudes are reported in table 10.1 and compared against the results of chemical digestion. The porosity calculations are the mean outcome of three different 10×10 mm^2 specimens while whole laminate and group results are obtained from the weighted average through-the-thickness.

It is observed that the results of CT void surface identification follow a similar trend to the determination from sample digestion. The W1A layup shows lower porosity on the inner helical layers than on the outer circumferential plies Above, relevantly large bubbles are identified in the form of a very high porosity value. The E+ case presents a rather uniform void distribution with slightly lower contents on the inner layer groups. Likewise, the B* configuration rapidly increases in void content from the inner circumferential ply group to the outer helical stack, showing relatively large entrapped air cavities between plies. Nonetheless, if the tendency concerning the void content distribution of CT scans agrees with the chemical digestion results, their measured magnitudes appear to be relevantly overestimated. The origin of this discrepancy is argued to rely on the void surface interpolation factor and which also controls the useful volume enclosed within. Following the modeling of the heterogeneous material properties of the vessel, the chemical digestion results are used as the reference parameter. These are obtained from the same standard as the material property characterization in chapter 6, thence permitting to correlate their results consistently.

In addition to the material quality determination in the cylindrical region, specimens are also extracted at various locations along the meridional direction of the W1A vessel layup. These are depicted in fig. 10.4 against the sample position to illustrate the fiber volume and porosity variation toward the domes. The reported results for the helical and circumferential ply stacks are also presented to show the qualitative comparison of these parameters variation.

Helical plies generate a larger surface pressure towards the dome poles, where their winding angle tends to be orthogonal to the meridional direction. Consequently, results show that fiber volume content is maximum, just as porosity is minimum at the dome end next to the boss, while these appear to respectively decrease and increase in the upper quarter of the dome. From the tested samples it cannot be concluded whether the upper dome quarter features lower material quality (lower fiber volume content and higher porosity) than the cylinder region. This being the case, can only be expected right after the circumferential ply drop location, where surface pressure applied by the helical layers during winding is the least. Moreover, despite defining the dome material quality for the W1A stacking

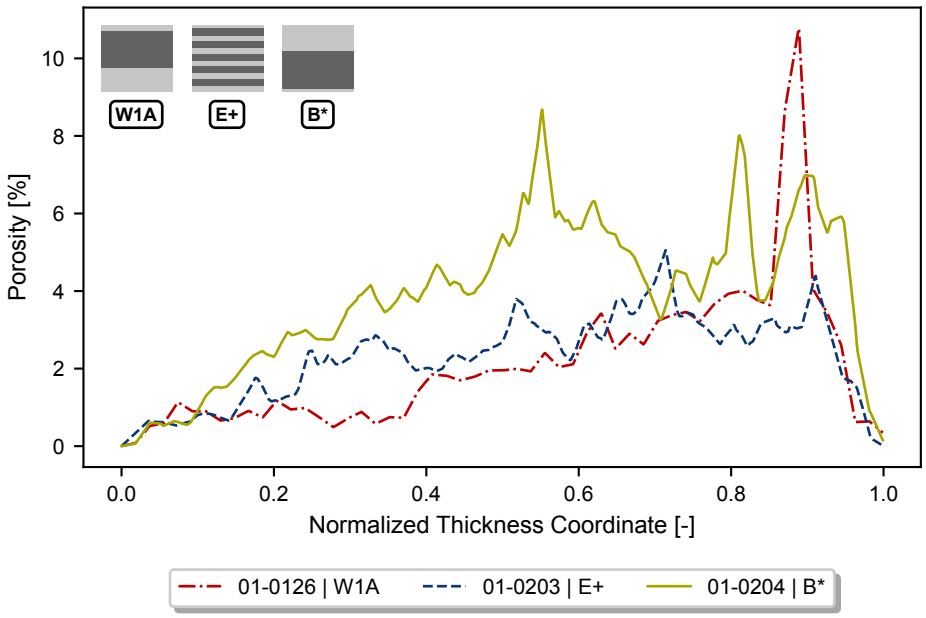


Figure 10.3: Results of the porosity content in the cylindrical region of the W1A, E+ and B* stacking sequences characterized from CT images

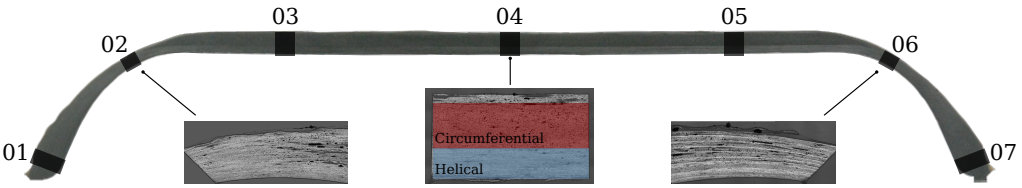
Table 10.1: Results of the porosity determination of the W1A, E+ and B* stacking sequences

Stack.	Vessel ID	Group	Por. EN 2564 [%]	Por. CT [%]	Diff. [%]
W1A	01 - 0126	Whole	1.76 ± 0.31	2.84 ± 2.06	61.36
		Hel.	0.31 ± 0.14	0.96 ± 0.38	209.68
		Circ.	2.19 ± 0.30	3.65 ± 1.99	66.67
E+	01 - 0203	Whole	0.88 ± 0.53	2.69 ± 0.97	205.68
B*	01 - 0204	Whole	1.74 ± 0.51	4.61 ± 1.67	164.94
		Hel.	2.12 ± 0.63	4.44 ± 1.53	109.43
		Circ.	2.03 ± 0.51	4.77 ± 1.64	134.98

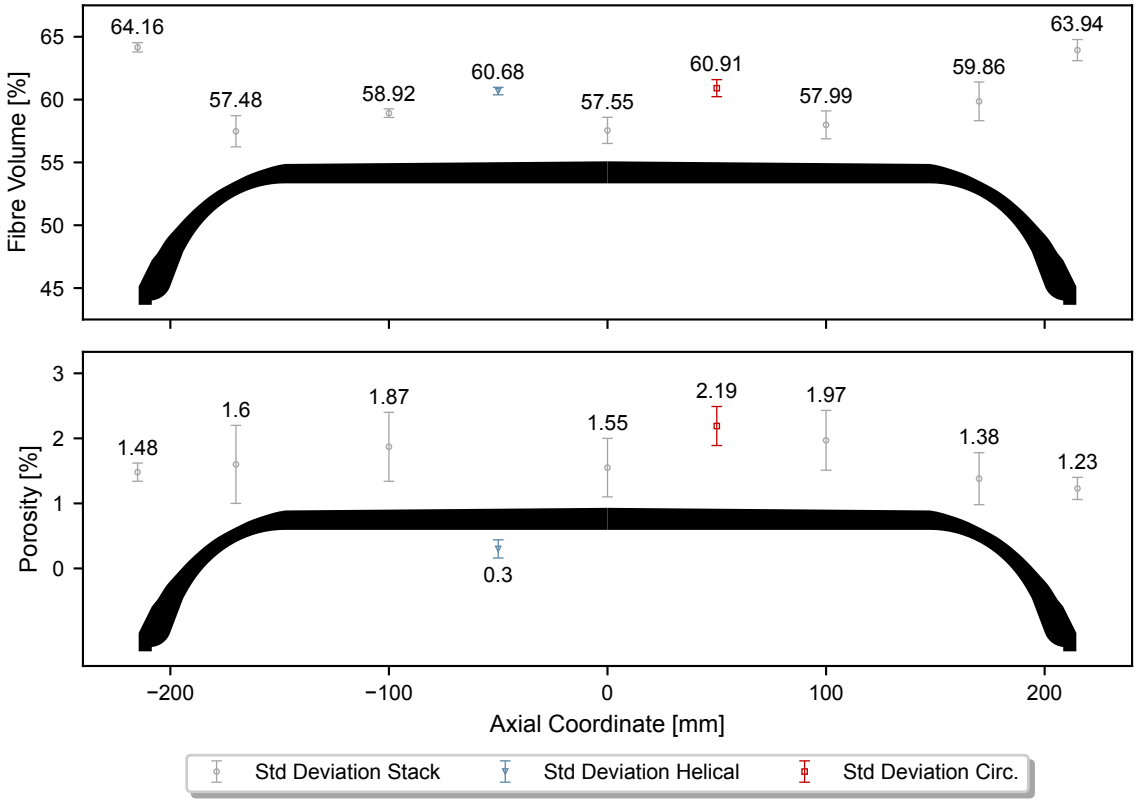
Stack. – stacking sequence; Por. EN 2564 – porosity content obtained from acid digestion tests, [137]; Por. CT – porosity content obtained from CT scans analysis; Diff. – percentual difference between the acid digestion and the CT scan porosity results; Hel. – stack of helical plies; Circ. – stack of circumferential plies

sequence, it is assumed that a minimal discrepancy exists with the E+ and B* configurations as the dome region stackup is equivalent for all three vessel architectures.

The geometry of the vessel is divided into sections along the meridional direction, as depicted in fig. 10.5, where material properties are defined according to the determined sample porosity values in fig. 10.4. These, are interpolated with respect to the material characterization porosity results of section 6.3 and reported in table 10.2. Material properties are varied along the axial coordinate for the helical layers, whereas an alternative gradient through-the-thickness is implemented in the case of circumferential plies. This variation through-the-thickness is based on the relevant porosity gradient depicted in fig. 10.3, which consequently impacts the prediction of damage onset. Therefore, a more realistic representation of the damage process and a better correlation with the measured AEs are expected. The porosity contents referenced for the through-the-thickness variation of material properties are inferred from the analysis of CT images in fig. 10.3. Nevertheless, as the average values determined through CT images differ from the results from the acid digestion tests in table 10.1, the variation through-the-thickness is scaled correspondingly against the porosity contents determined through acid



(a) Reference location of the specimen extraction



(b) fiber volume and porosity content

Figure 10.4: Results of the porosity content along the axial coordinate of the W1A stacking sequence

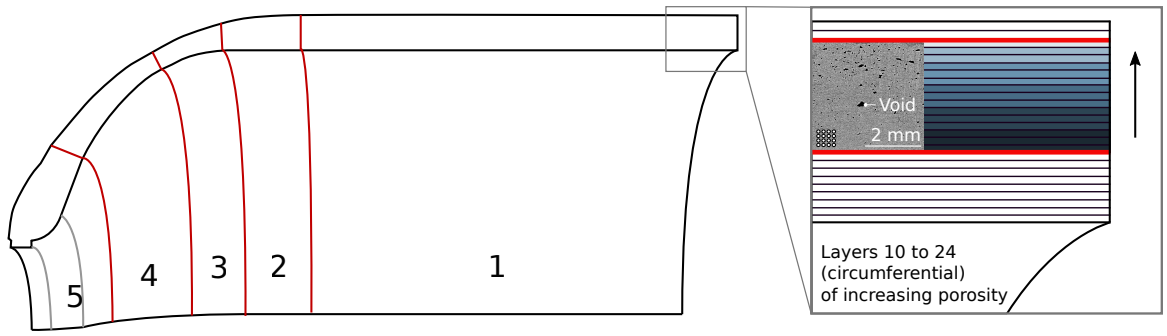


Figure 10.5: Region diagram with the heterogeneous material property definition

digestion.

The result of interpolating the porosity and fiber volume contents on the results of the experimental characterization in section 6.3 shows some relevant deviation compared with the previously assumed

Table 10.2: Heterogeneous material property definition for the various regions of the W1A stacking sequence

Group	k	Ref. FV [%]	Ref. Por. [%]	E_{11} [GPa]	X^T [MPa]	E_{22} [GPa]	Y^T [MPa]	G_{12} [GPa]	S^L [MPa]
Hel.	1	60.68	0.30	133.92	2477.85	8.96	47.08	4.08	51.78
	2	59.50	1.00	131.71	2328.23	8.72	44.74	4.07	51.64
	3	58.00	1.70	128.89	2138.04	8.49	42.39	4.05	51.50
	4	58.67	1.49	130.15	2222.99	8.56	43.10	4.06	51.54
	5	64.05	1.35	140.24	2905.14	8.61	43.57	4.06	51.53
Group	Layer	Ref. FV [%]	Ref. Por. [%]	E_{11} [GPa]	X^T [MPa]	E_{22} [GPa]	Y^T [MPa]	G_{12} [GPa]	S^L [MPa]
Circ.	10 – 12	60.91	1.80	134.35	2507.01	8.46	42.00	4.03	51.44
	13 – 15	60.91	2.00	134.35	2507.01	8.39	41.33	4.02	51.38
	16 – 18	60.91	2.19	134.35	2507.01	8.32	40.75	4.02	51.25
	19 – 21	60.41	2.60	133.41	2443.61	8.19	39.38	3.98	50.85
	22 – 23	59.91	3.40	132.47	2380.22	7.92	36.64	3.79	48.13
	24	59.91	8.00	132.47	2380.22	6.37	21.24	3.10	38.30

k – region along the axial coordinate where material properties of the helical layers are varied; Layer – layer number on which the material properties of the circumferential plies are varied, corresponding layer 1 with the inner surface of the vessel; Ref. FV – reference fibre volume content in the given vessel region; Ref. Por. – reference porosity content in the given vessel region; Hel. – stack of helical plies; Circ. – stack of circumferential plies

material properties in table 7.1. This mismatch is particularly presented for the transverse tensile strength, which, after the detailed characterization for plates of various porosity contents, derives in the identification of a modestly higher value for this material variable. As a result, a generally slightly delayed damage onset and progression are anticipated. In terms of stiffness, the heterogeneous material property identification appears to be ultimately compared to the average property definition in table 7.1, where the upper dome quarter appears as an area of more substantial compliance because of the identified lower consolidation level.

10.2. Results of Vessel Behavior with a Heterogeneous Material Definition

10.2.1. Prediction on the Damage Progression of the W1A Stacking Sequence

The definition of heterogeneous material properties induces a progression of damage that, even though not deviating fundamentally from the homogeneous solution, still shows some relevant disparities. Therefore, the sequence with which transverse damage develops in the composite reinforcement is presented in fig. 10.6 for pressure stages from 35 to 103.5 MPa. Results are presented back-to-back between the depiction of homogeneous material properties discussed in section 9.2 and the current approach with a heterogeneous definition.

Similarly to the homogeneous case, material degradation is predicted first in the lower half of the dome (approximately at 30 MPa). At this location, a high level of consolidation is induced by the local high angle fiber orientation, which, thereupon, results in a relatively high transverse strength. Still, there is also relevant transverse stress because of the existing through-the-thickness shear, eventually leading to failure at the connection with the boss. As the material strength with the heterogeneous material definition is here slightly higher than the homogeneous case, a relatively lesser damage extension is observed in the lower dome region throughout pressure stages 35 to 70 MPa. With the higher applied loading, this discrepancy is less apparent, derived from the general proliferation of damage throughout the geometry.

Matrix failure in the outer circumferential plies is predicted next (30 to 35 MPa), where a relevantly low material strength is reported in table 10.2. Withal, the circumferential plies depict a relevant gradient of their material properties through-the-thickness, being the transverse strength under tension on the innermost ply approximately twice of the outer one. Besides this, the low fracture toughness of the unidirectional material appears to develop a sufficiently sudden release of energy upon failure that still allows cracks to develop through the whole stack fully. Crack growth is not immediate, depicting a necessary applied pressure increase until the corresponding failure criteria are fulfilled.

Predicting a slight delay in the through-the-thickness crack growth identification in the circumferen-

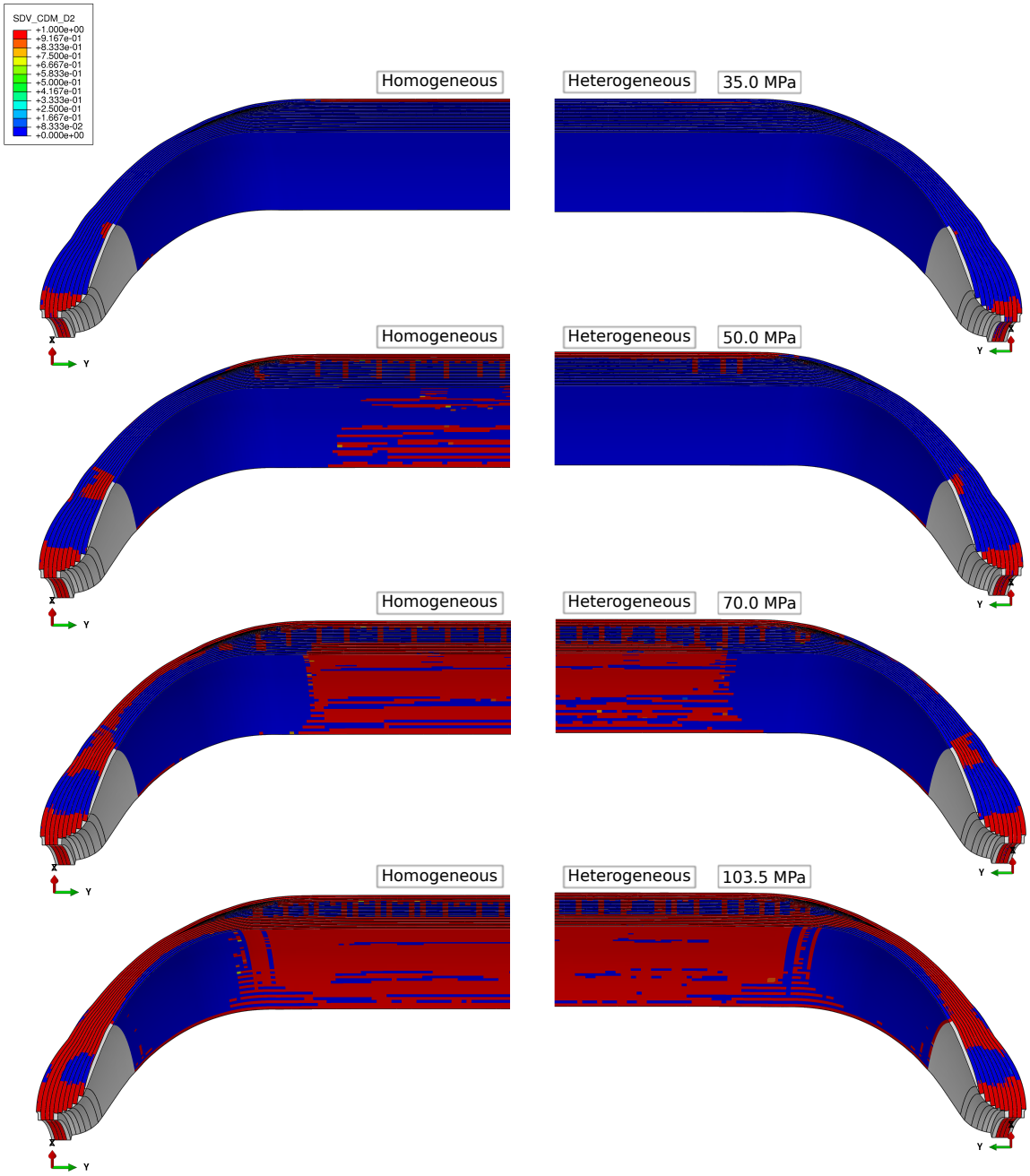


Figure 10.6: Comparison of the prediction of transverse damage of the W1A stacking sequence for homogeneous and heterogeneous material properties. Results are presented at load pressures of 35, 50, 70 and 103.5 MPa

tial ply stack suggests that the definition of the corresponding fracture toughness in section 6.4 might not be fully representative of the real vessel. This identification disregards the influence of more copious amounts of pores in the resistance towards crack growth, which can well considerably decrease the material toughness. However, testing for Mode I delamination in the presence of high porosities might still be challenging, because of the discontinuous crack growth that possibly results from it.

Successive to the material degradation in the circumferential group, the outer helical plies show the onset of damage (45 to 50 MPa). Compared with the homogeneous case, this happens at a higher applied loading that directly correlates with the material property definition. Particularly, the prediction of failure in the outer plies at this stage is coherent with the visual observations of damage on the outer surface, happening after the transverse failure of the circumferential plies. Both the localization of AE

in fig. 9.6a and the observation of damage on the chalked specimens in fig. 9.6b show no apparent surface degradation before the threshold of 50 MPa. Instead, this is noticeable when observations are made at pressure stages of 90 and 105 MPa. Defining heterogeneous material properties shows a similar sequence of events concerning damage progression, which permits to establish a more robust correlation with the results of experiments. Furthermore, this appears to result besides any non-linear mechanical response related to the helical layer construction, which is not inherently modeled in the subply discretization presented in section 7.2.

Meridional stress is discussed in section 8.3 to be higher in the outer plies than in the inner ones, accordingly causing the inner helical layers to fail last in the cylinder (60 to 65 MPa). Likewise, at the time damage extends on the inner side of the cylinder, it also develops in the outer plies of the upper dome quarter. A swelling shape appears because of the stiffness distribution of the W1A layup, ultimately causing the outer layers to fail first. As loading is increased, transverse damage extends to almost the entirety of the vessel. Withal, being the transverse strength higher in the heterogeneous case, the extension to which it progresses is presented in fig. 10.6 to be generally lesser than the homogeneous simplification.

The progression of damage when accounting for heterogeneous material properties is presented to alter the sequence with which damage onsets slightly. The load is redistributed to the fibers throughout material degradation, hence experiencing a modest increase in stress. Nevertheless, this increase occurs in the elastic regime, meaning that the order in which this is transferred is anticipated to have a marginal impact on the final mechanical state. For an equivalent progression of damage in the transverse direction, the prediction of burst pressure is shown ultimately in table 10.3 to be comparable in both homogeneous and heterogeneous cases. One the one hand, as a gradient of material properties, exists through-the-thickness in the circumferential ply stack, the stage at which cracks grow at this location is considerably better approximated. One the other hand, the relatively higher tangential stiffness of the inner circumferential plies redistributes a higher load on them, leading to a marginally earlier prediction of burst when the variability of material properties is accounted.

In a similar manner to the prediction for homogeneous material properties presented in section 9.2, numerical difficulties are encountered when applying high-pressure loads in the presence of damage. As a result, burst pressure is ultimately estimated by extrapolating linearly the failure criteria in the fibers from the last pressure stage where convergence of the damage model is achieved.

Table 10.3: Comparison of the damage onset prediction of the W1A stacking sequence with experimental data

Vessel	Exper.		Homogeneous				Heterogeneous			
	MF Cyl.	Burst	MF LaRC04	Diff. (%)	FF. Puck	Diff. (%)	MF CompDam	Diff. (%)	FF. CompDam	Diff. (%)
01 - 0128	25.2	165.3	35.0	38.0	165.8	0.3	30.5	21.0	165.2	0.1
01 - 0183	24.2	162.4	"	44.6	"	1.8	"	26.0	"	1.7
01 - 0184	24.5	162.4	"	42.9	"	1.8	"	24.5	"	1.7
01 - 0192	23.2	156.9	"	50.9	"	5.1	"	31.4	"	5.0

Stack. – stacking sequence; MF Cyl.– matrix failure pressure stage identified in the cylinder by means of AE; MF LaRC04 – matrix failure pressure stage in the circumferential group of plies according to LaRC04; FF Puck. – fibre failure pressure stage according to Puck; MF CompDam – matrix failure pressure stage in the circumferential group of plies according to CompDam; FF CompDam. – fibre failure pressure stage according to CompDam; Diff. (%) – percentual difference between experimental and simulation results

10.2.2. Prediction on the Deformational Behavior of the W1A Stacking Sequence

Accounting for heterogeneous material properties influences the deformational behavior of the vessel by correspondingly changing the stiffness and strength distribution compared with the homogeneous case. This effect is apparent in the upper dome quarter, where the lower consolidation of the material results in generally lower transverse stiffness. Simultaneously, the material in the dome end next to the boss is highly compacted, whereas in the cylinder, a gradient exists through the circumferential ply stack. Accordingly, the sequence with which failure is triggered is predicted to be different in the case heterogeneous properties exist, therefore impacting the compliance of the vessel with the increased applied pressure.

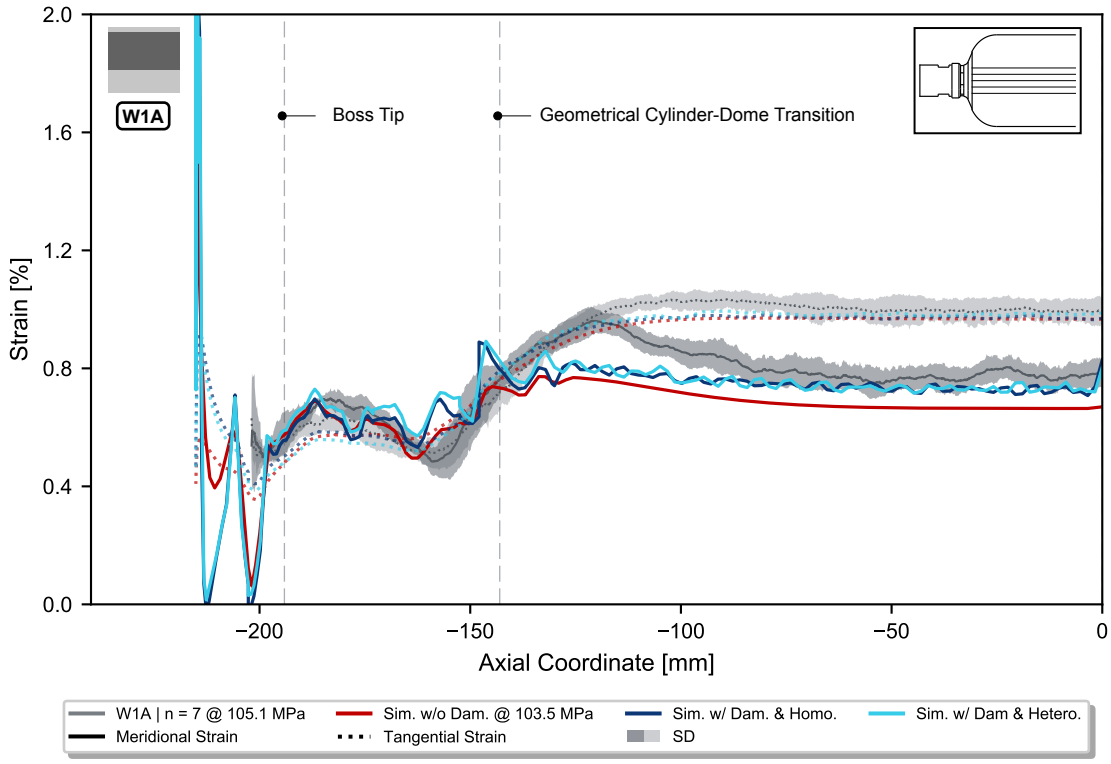


Figure 10.7: Comparison of the outer surface meridional and tangential strain of the W1A stacking sequence considering homogeneous and heterogeneous material properties at a load pressure of 103.5 MPa. Numerical predictions are presented against average experimental results for a number of samples n, where their scatter is indicated by their standard deviation (SD)

This variability is presented in fig. 10.7 against the outer surface strain components along a meridional path. Results are depicted at a pressure stage of 103.5 MPa for the reference configuration without damage, and the solutions with homogeneous and heterogeneous material properties. At this relatively high load, transverse damage is generally present in the whole vessel, making the existing deviations between the two material definitions to depend mostly on their stiffness distribution. This variation is more apparent in the dome than in the cylindrical region. In the former, larger compliance is illustrated in the upper dome quarter for the heterogeneous case, where the least consolidation is expected, and a swelled region is predicted to appear. In the later, a nearly equivalent solution is predicted for both material definitions, being the modeled gradient of properties in the circumferential ply stack as compliant as the average property definition in the homogeneous case.

The average and varying material properties in the circumferential stack show similar responses, both in meridional and tangential strain components. Such an effect is reasoned by the counteracting result of the relatively stiffer inner plies compared with the more flexible outer ones. This variation exists principally in the transverse direction, although it is also reported on a smaller scale, in the longitudinal one. As the inner plies comparatively carry more load, their fiber stress gently increases, hence slightly impacting the burst pressure prediction.

Being the sequence with which damage progresses altered with the consideration of the variable material properties, the magnitude of the maximum reported strain components is accordingly mildly impacted. This influence is reported in table 10.4 for the maximum predicted strain components at various load stages. Until transverse damage has generally developed in the vessel, the compliance when accounting for the heterogeneity of the material is lower than in the homogeneous case. However, this eventually equalizes when the extent of transverse damage is comparable, as detailed for pressure stages above 103.5 MPa.

The magnitude of this maximum strain result still appears to underestimate the maximum meridional strain measured during pressurization experiments, which happens in the cylindrical region abaft

Table 10.4: Results of the maximum meridional and tangential strain of the W1A stacking sequence considering homogeneous and heterogeneous material properties

	Pressure [MPa]		Max. Mer. Strain [%]				Max. Tan. Strain [%]			
	Exper.	Simul.	Exper.	Simul.	Diff.	Diff. (%)	Exper.	Simul.	Diff.	Diff. (%)
Homogeneous	34.6	35.1	0.37 ± 0.02	0.27	−0.10	−26.63	0.36 ± 0.02	0.33	−0.04	−11.02
	69.9	71.0	0.68 ± 0.02	0.58	−0.10	−14.19	0.70 ± 0.02	0.67	−0.03	−4.05
	105.1	103.5	0.96 ± 0.05	0.84	−0.12	−12.71	1.04 ± 0.03	0.98	−0.06	−5.32
	130.0	127.2	1.15 ± 0.05	1.04	−0.12	−10.34	1.27 ± 0.04	1.22	−0.06	−4.46
Heterogeneous	34.6	35.1	0.37 ± 0.02	0.28	−0.09	−24.19	0.36 ± 0.02	0.32	−0.04	−11.84
	69.9	71.0	0.68 ± 0.02	0.61	−0.06	−9.46	0.70 ± 0.02	0.68	−0.02	−2.16
	105.1	103.5	0.96 ± 0.05	0.87	−0.10	−9.90	1.04 ± 0.03	1.00	−0.04	−3.91
	120.3	120.6	1.07 ± 0.05	1.01	−0.06	−6.00	1.18 ± 0.03	1.16	−0.02	−2.10

Stack. – stacking sequence; Max. Mer. Strain – maximum meridional strain; Max. Tan. Strain – maximum tangential strain; Exper. – Experimental data; Simul. – Simulation results; Diff. – absolute difference between Experimental data and Simulation results Diff. (%) – percentual difference between Experimental and Simulation results

Note 1: The pressure stages at which Experimental and Simulation results are presented slightly differs because of the unequal frequencies of the recording of results

of the dome transition. The measured porosity and fiber volume contents at this location do not anticipate a relevant decrease in the material quality, hence conveying that the origin of the discrepancy is likely related to an alternatively incorrect depiction of stiffness. Similar to the reasoning in section 7.6, the excessive stiffness in the dome transition region is argued to result from the geometry definition, relating to the circumferential ply group tapering slope the helical ply fiber angle orientation. In order to

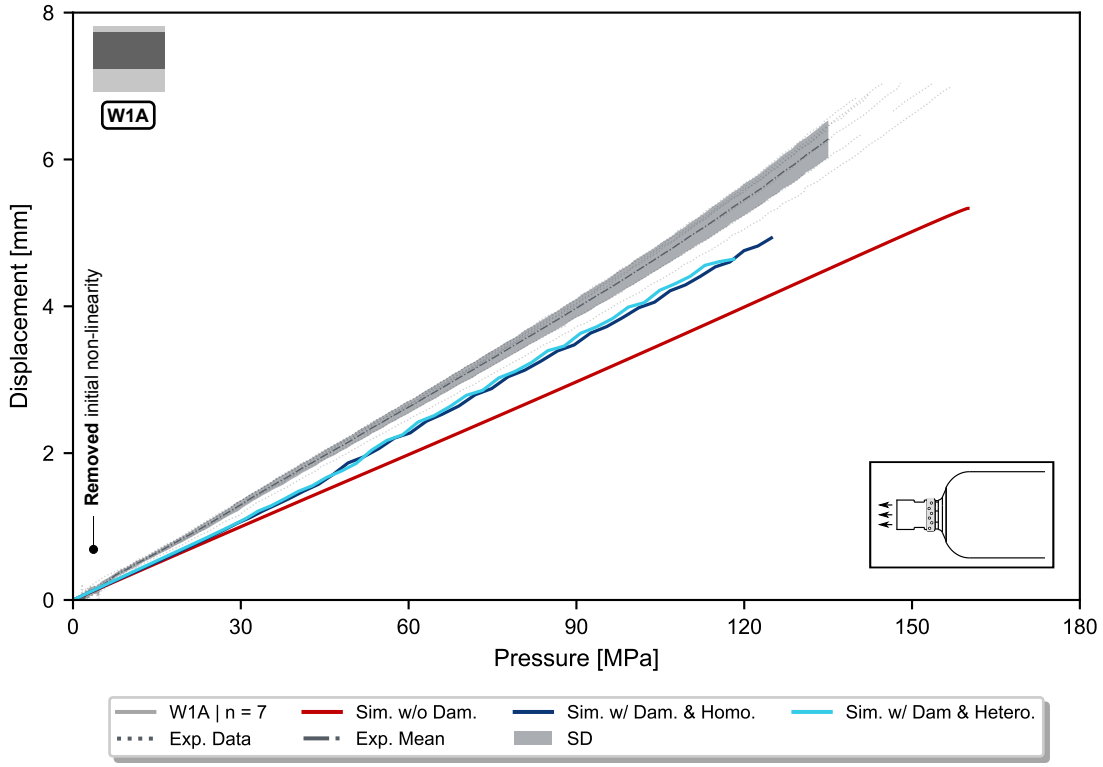


Figure 10.8: Comparison of the axial boss displacements of the W1A stacking sequence considering homogeneous and heterogeneous material properties

overcome discrepancies in the representation of the mechanical response, experimentally correlating the geometry of the vessel with the configuration modeled appears as a crucial element. This permits to ensure that the referred stiffness distribution, which fundamentally determines the deformational behavior of the vessel, is representative of the reality.

Earlier onset of damage in the circumferential ply stack derived from the heterogeneous material definition is presented in fig. 10.8 to prompt an earlier non-linear deviation of the boss axial displacement. This happens at the pressure stage of approximately 30 MPa, while it was predicted at 35 MPa for the homogeneous case. Still, the deviation between the two predictions is practically not discernible because of the gradual material degradation taking place at this stage. Ultimately, the heterogeneous configuration results in a marginally larger predicted displacement attributed to the marginally larger compliance definition in the upper dome quarter. The consideration of damage for both the heterogeneous and homogeneous material configurations is shown in fig. 10.8 to improve the prediction compared with an undamaged case. However, a mismatch in the modeled stiffness is still apparent in the pressure stages until the onset of transverse damage. This discrepancy prevails besides the larger compliance considered in the upper dome quarter with the heterogeneous approach, hence justifying that a principal underlying source of disparity remains. In this regard, the already mentioned geometrical setup is argued to relate to this effect.

The prediction concerning the boss axial displacement is ultimately complemented with the correlation with experimental results in table 10.5. In this case, the small variability between the modeled stiffness distribution of the two approaches is presented as a minor deviation. The absolute and relative improvements in the predicted boss axial displacement are insufficient to correlate the simulation and experimental results adequately. Such an effect indicates that, even if the modeling of changing material properties along the vessel geometry has a relatively significant impact on the pressure stages for damage onset, the deformational behavior of the vessel is not sensitively influenced by them.

Table 10.5: Results of the boss axial displacement of the W1A stacking sequence considering homogeneous and heterogeneous material properties

	Pressure [MPa]		Boss Displ. [mm]				Boss Displ. Trunc. [mm]			
	Exper.	Simul.	Exper.	Simul.	Diff.	Diff. (%)	Exper.	Simul.	Diff.	Diff. (%)
Homogeneous	35.5	35.1	1.72 ± 0.07	1.29	−0.42	−24.40	1.55 ± 0.07	1.29	−0.22	−15.05
	69.1	71.0	3.26 ± 0.12	2.79	−0.47	−14.30	3.10 ± 0.12	2.79	−0.28	−9.00
	104.1	103.5	4.87 ± 0.19	3.98	−0.89	−18.38	4.71 ± 0.19	3.98	−0.70	−15.07
	130.0	128.0	6.19 ± 0.28	5.03	−1.16	−18.74	5.99 ± 0.25	5.03	−0.96	−16.03
Heterogeneous	35.5	35.4	1.72 ± 0.07	1.28	−0.43	−25.00	1.55 ± 0.07	1.28	−0.23	−15.84
	69.1	70.3	3.26 ± 0.12	2.79	−0.47	−14.41	3.10 ± 0.12	2.79	−0.28	−9.03
	104.1	104.9	4.87 ± 0.19	4.22	−0.65	−13.34	4.71 ± 0.19	4.22	−0.49	−10.40
	120.0	118.1	5.45 ± 0.21	4.64	−0.81	−14.86	5.27 ± 0.20	4.64	−0.63	−11.96

Stack. – stacking sequence; Boss Displ. – boss displacement; Boss Displ. Trunc. – boss displacement truncated at a pressure of 10 MPa; Exper. – Experimental data; Simul. – Simulation results; Diff. – absolute difference between Experimental data and Simulation results Diff. (%) – percentual difference between Experimental and Simulation results

Note 1: The pressure stages at which Experimental and Simulation results are presented slightly differs because of the unequal frequencies of the recording of results

10.3. Concluding Remarks

The consideration of variable material properties in the geometry of the CPV stands as an instrument for depicting the progression of damage in the real component with higher accuracy, thus identifying the regions of inferior strength and predicting their timely stage of damage onset. This variability appears to be founded on the deviating level of consolidation of the wound layers, influencing the porosity and fiber volume contents and, as a result, also the stiffness and strength.

Correlating the material porosity and fiber volume contents with the results of the material characterization in chapter 6 permits to define varying material properties along the axial and the through-the-thickness coordinates. Therefore, stiffness and strength are varied for the cylinder, dome transition, and lower dome regions. Particularly to the W1A stacking sequence, the upper dome quarter shows

the most modest characteristics because of the least compaction generated by the winding of low angle helical layers. Similarly, the transverse stiffness and strength of the circumferential plies decrease relevantly towards the outside due to their increased porosity.

The onset of damage shows that, compared with a homogeneous material definition, the sequence with which failure is triggered agrees better with the observations made during experiments. In this regard, the growth of cracks in the circumferential ply stack is predicted before the material degradation in the outer helical layers, in a similar sequence to the recording of high amplitude AEs and the visual observation of degradation on the outer surface. However, disparities of approximately 5 MPa exist in these estimations, which are likely influenced by the actual fracture toughness for high porosity values after the nucleation of cracks and the real stress state of the interwoven helical layers in comparison to their subply idealization.

In terms of the deformational response, the definition of variable material properties appears to have a minor impact on the predicted strain and displacement components. Besides a gradient of transverse stiffness existing in the circumferential ply stack, the higher inner layers appear to compensate the larger compliance of the outer ones. Likewise, as a the inner circumferential plies concentrate a slightly higher amount of load, the burst pressure prediction marginally decrease compared with a case where only homogeneous properties are considered.

Additionally, showing the upper dome quarter a scarcely higher compliance, its predicted deformation appears to increase locally. However, this change of shape in the dome region, appears to neither impact the maximum of the meridional strain component nor increase the compliance with which the boss displaces axially in the early pressurization stages. Such a discrepancy is argued on an incorrect definition of stiffness in this region, related to an insufficiently accurate geometry representation in the dome transition region.

11

Conclusions

The current work explores the opportunities of virtual simulations as a tool for modeling representatively the mechanical response of CPVs under internal pressure. The focus is set on bridging the gap between the vessel design (layer stacking sequence, circumferential ply taper, filament path orientation, and winding pattern) and the result of the manufacturing (thickness profile and variability of material properties), hence permitting to predict the vessel burst pressure in a comprehensive and reliable manner. Strategies are proposed to fundamentally account for the factors driving the mechanical response, principally identified as their geometrical configuration and material properties. Correspondingly, the generality of the framework is demonstrated by analyzing and experimentally correlating three stacking sequence designs of distinct expected behavior. These, feature two extreme asymmetric layups of low angle helical and circumferential layers, and an intercalated, quasi-symmetric version of the former.

The mechanical response of the studied CPVs is illustrated by their analysis through three-dimensional FE models, presenting their constitutively elastic response, the prediction of FPF and the modeling of damage progression. Therefore, depicting the deformational behavior with increased loading and predicting the burst event with various degrees of complexity. The reliability of results is ascertained by correlating the predicted responses with strain and displacement fields obtained using DIC, whereas recorded AEs during pressurization tests are used equivalently to validate the sequence of damage progression. Likewise, the description of the vessel geometries is supported by the measurement of outer contours and wall thickness according to stripe-light projections and CT scans. Material properties are determined from a characterization campaign considering the variability of stiffness and strength for various consolidation levels of the composite reinforcement.

Definition of the Geometric Configuration as a Result of the Manufacturing Process

Characterizing the geometry of a CPV resulting from the manufacturing process is recognized as the thickness increase result during the consecutive winding of layers. However, being the adequate computation of robot motions not generally sufficient to depict correctly the final geometry, a methodology is proposed to readjust their original geometry prediction. A conforming thickness profile is resolved by redefining the tapering slope of each individual ply, accounting for a manufacturing gap between the liner and the composite reinforcement, correcting the ply thickness decrease because of consolidation, and reformulating the ply ends in the dome next to the boss. The adjustment is compelled by experimental measurements of the geometry with stripe-light projections and CT scans, thus permitting to quantify the deformation of the reinforcement during winding and curing.

The vessel geometry adjustments result shows proper similitude with the investigated components, including the layer group boundaries, and the outer and inner contours. However, no direct correlation is made on the tapering slope of the stacks of circumferential plies. Concerning these, the circumferential ply stack location through-the-thickness is presented to relate with the drop position along the axial coordinate. The outer the location of the stack, the further into the dome it is predicted to extend. First, the earlier winding of low angle helical layers induces liner shortening and the relative displacement toward the dome pole of the overlying plies; second, the lesser constrained the group is, the more likely

the stack is going to shift towards the pole, because of the radial stress resulting from the winding and the low viscosity regime curing.

Identification and Representativeness of the Material Properties

The material description is regarded as a crucial aspect dictating the vessel deformational behavior, the onset of damage, the subsequent load redistribution, and, ultimately, the prediction of the burst pressure. Acid digestion tests and CT observations show that the porosity and fiber volume contents of the filament wound material depend on the axial and through-the-thickness positions. These result from the varying consolidation levels because of the stacking sequence definition, thereupon correlating with changing stiffness and strength characteristics.

Producing flat plates with equivalent winding parameters to the CPV manufacturing permits to identify a reducing stiffness and strength with the lower level of consolidation. This effect is found for unidirectional specimens in the longitudinal and transverse directions, and helically wound counterparts in in-plane shear. Thus, consolidation in the material is presented to influence the matrix-dominated characteristics (transverse and shear failure) and impact the fiber-controlled longitudinal strength. The winding of flat plates for specimen testing appears as a convenient solution for material characterization because of the simplicity of the standard test setup. However, results are influenced by the relatively thin tested specimens and the disruption of the pure stress states because of the existence of free edges. Moreover, yet the correlation is direct for the unidirectionally wound circumferential plies, its application to helically wound layers disregards the load path disruption induced by the interlacing of bands.

Fracture toughness of the unidirectional filament wound material is additionally determined in Modes I and II to describe the subsequent progression of failure. Withal, these results are not represented within the helical layer architecture because of the continuous crack arrests induced by the changing fiber orientation, requiring the definition of arbitrarily higher values.

Modeling the Onset of Damage and the Burst Event

Failure in CPVs is triggered by the degradation of the matrix constituent that, happening since relatively early pressure stages (20 to 30 MPa), leads to a progressive redistribution of load to the fibers. With the increased loading, transverse damage develops broadly within the vessel geometry until the fibers start breaking, that because of their large accumulated elastic energy, rapidly cascade into the burst event. Damage onset is predicted from the evaluation of failure criteria, therefore, permitting to identify the pressure stages at which material degradation starts in the matrix and fiber constituents.

In the most fundamental approximation, the burst is estimated by the stage at which the longitudinal failure criteria are fulfilled in a constitutively elastic analysis. The sole use of failure criteria disregards load redistribution because of damage in the matrix, thus consistently resulting in an overestimation of the burst pressure. Nevertheless, the stage at which failure is triggered in the matrix can still be reasonably estimated. In the three-dimensional stress evaluation of the current analysis, this is evaluated accordingly concerning Puck and LaRC04, which conclusively show small relative disparities ($< 5\ \%$).

Alternatively, damage is represented in the composite material in the context of the CDM model implementation of Leone et al. [1]. Matrix cracks are considered embedded within the continuum element, evaluated according to a cohesive failure criterion, and following a linear stiffness degradation law. This approach permits to gradually redistribute load to the fiber constituent until breakage is predicted there through a maximum stress criterion. The fracture toughness definition controls the degradation of stiffness in the matrix, being it in the helical layers relevantly higher than in the circumferential plies because of the corresponding crack arrest of the interwoven band construction.

Nevertheless, the solution of the damaged state in the composite material appears as a task of relevant numerical complexity. The relative displacements at the existing cracks are found iteratively by minimizing the residual difference between the stress vector in the fractured surface and projection of the bulk stress tensor in that plane. However, stress states are deceived by the existence of boundary conditions and mesh constraints, consequently frustrating solution convergence at mildly high-pressure stages (120 to 130 MPa). However, these stages are sufficiently advanced to depict the broad development of transverse damage and consequent load redistribution. The evaluation of failure criteria ultimately estimates burst pressure at this last converged step.

Influence of the Stacking Sequence in the Mechanical Response

Analyzing the deformational behavior of vessels with distinctive stacking sequences shows a compelling connection between their stiffness distribution and their response in the cylinder, the dome transition region, and boss axial displacement. The gradient of directional stiffness in the cylinder relates closely with the load distribution in the thick wall assumptions, depicting tangential stress components in the inner layers that are comparatively larger than in the outer ones. Therefore, locating high tangential stiffness layers on the outside is found to generate a milder tangential stress gradient through-the-thickness, shifting the load path toward the higher stiffness positions. The maximum longitudinal stress in the high angle layers reduces, besides allowing more substantial compliance and, comparatively, increasing loading in the transverse direction. When layers of high and low tangential stiffness are intercalated, this effect is not achieved because the inner highly stiff ones intrinsically draw a proper amount of the loading. The high tangential stiffness of the inner layers prevents the expansion of the cylinder, developing tangential stress states that are the most detrimental while hindering load transferring toward the outside.

The geometrical description of the vessel is also presented to relate closely to the stacking sequence definition in the cylinder with the circumferential ply drop location in the dome transition region. Coupled with the fiber orientation change of the helical layers, the circumferential ply stack on the outside, which extends far into the dome, also generates a gradual change of directional stiffness in this region. Accordingly, tangential expansion in the dome transition is shown to be largely inhibited, while critical loading in the fibers swiftly changes from the circumferential to the helical plies.

Being the through-the-thickness position of the circumferential plies toward the inside, the group end locates comparatively abaft. A sudden change in tangential stiffness is generated, where low angle helical layers ahead are highly compliant. As a consequence, a region of relevant tangential expansion develops in the form of a bulge. The growth of this protrusion is restrained by the tangential stiffness of the adjacent circumferential plies that, correspondingly, generates a high longitudinal stress state at the tip of the layer group. Besides, a growing delamination is noticed at the interface between the two, striping the outer helical layers from the circumferential ply stack. Such an effect is argued to concentrate locally on the transfer of tangential load and impact the subsequent prediction of the burst.

Considering that burst occurs when failure in the fibers is triggered, a gradual stiffness change in the dome transition region predicts, for the investigated stacking sequences, that final collapse occurs in the cylindrical region. It occurs when the innermost ply of high tangential stiffness reaches its maximum longitudinal stress state, thereupon failing in the entire cylinder at approximately the same time. However, when a bulge forms in the dome transition, an earlier burst event might occur because of the circumferential plies failing locally nearby the existing protrusion. In this regard, a shift in the collapse mode is expected if the magnitude of the tangential expansion is sufficient to exceed the longitudinal stress state in the cylinder. This effect is predicted in a configuration that locates its circumferential plies on the bottom of the layup, but it is not when high tangential stiffness groups are staggered through-the-thickness. Correspondingly, the dome transition region appears to be critical for the investigated configurations because the dome poles are strengthened sufficiently to prevent their collapse. Their reinforcement is achieved through the sufficient stack of material that prevents the local shearing of the laminate and the flaring of the lower dome quarter.

In addition to the axial position of the circumferential ply drop, the extreme asymmetry of the group location through-the-thickness appears to influence the response in the dome transition region further. Extensional-bending coupling of the asymmetric layup induces additional meridional bending, hence revealing ahead of the circumferential group end, where tangential stiffness is minimum, and the vessel is allowed to deform proportionally. A circumferential ply stack on the outside encourages outward meridional bending, whereas when located on the inside, it promotes the meridional bending to go inward. As a result, the circumferential ply stack on the outside prevents the dome transition region tangential expansion, while this effect is benefited, also aggravating the formation of a bulge, when the group is located on the inside.

The boss axial displacement ultimately emerges as the aggregated response on which the influence of the stacking sequence in the cylinder, dome transition, and dome are projected. Such effects are portrayed in the deformation of the dome transition region, alternatively inducing flaring or crimping of the dome end next to the boss. A stacking sequence depicting a gradual change of directional stiffness in the dome transition region is comparatively constrained tangentially at this location. Therefore, a concavity tends to form at the position of most considerable restraint, which, in light of the continuity in

the deformed shape, is matched by the lower dome quarter being encouraged to move outward. If a sudden drop of tangential stiffness exists in the dome transition region, the formation of a bulge has a comparatively opposite effect. As the bulge is expanding tangentially, it stretches the lower dome with it, while also hindering the boss from displacing in the positive axial direction.

Influence of the Progression of Damage in the Mechanical Response

Considering material degradation during the applied loading results in more significant compliance of the CPV upon the triggering of failure. The effect of damage is observed in the vessel response with the circumferential ply stack toward the outside, which consolidates in a boss axial displacement of magnitude relevantly higher than in a constitutively elastic solution (+18.1 %). Likewise, the meridional strain component is reported to increase modestly in the cylindrical region, resulting from the through-the-thickness crack growth in the circumferential ply stack. These fractures aggregate to the corresponding degradation of the helical layers in the cylindrical and dome regions, ultimately leading to a general load redistribution to the fiber constituents. Withal, only a marginal variation is reported in the corresponding strain component that, nevertheless, duly impacts the burst pressure estimation.

Nevertheless, the prediction of the deformational behavior upon the progression of damage shows to be also impacted by the growth of a protrusion, as in the configuration with the circumferential ply stack toward the inside. Its dome shape tends significantly to stretch, concentrating stress at the contact between the laminate and the boss brim, and developing a local shearing effect through-the-thickness. Withal, the CDM implementation may unrealistically predict cracks growing through-the-thickness in the circumferential ply stack, disregarding the shearing strength of the fibers. The deformed shape of the lower dome quarter gets distorted, limiting the crack opening in the cylindrical region.

The tangential strain increase is marginal when considering the progression of damage because of the high elastic stiffness of the fiber constituents. The stacking sequences investigated feature a high number of circumferential layers which, aligned with the principal direction of loading in the cylinder, do not experience a significant load path deviation with the degradation of the matrix. However, should a more significant number of high angle helical layers be defined in the stacking sequence, the influence of damage progression is anticipated to have a more profound influence in the response of the cylindrical region.

In the case a final collapse is predicted in the cylindrical region, the estimated burst event appears to be only altered slightly as compared with the constitutively elastic solution (-2.1 %). This is the case of a configuration that locates its circumferential plies toward the outside, where the higher fiber stress causing burst results from a uniform redistribution of loading throughout the whole cylindrical region. However, if the formation of a bulge prompts a premature burst, damage progression shows to impact the final collapse more significantly (-13.4 %). A burst event triggered in the dome transition region is forecast for the stacking sequence configuration that locates its circumferential plies toward the inside. Here, the stress escalation at the tip of the circumferential ply group is directly related to the magnitude of the bulge. Therefore, the limitation of the load-bearing capability of the helical layers is shown to concentrate loading further in the circumferential plies.

Influence of the Material Variability in the Mechanical Response

Material variability deems the changing stiffness and strength of the composite reinforcement through the vessel axial coordinate and thickness position. Testing samples at multiple locations permits the determination of porosity and fiber volume contents, consequently allowing the estimation of the material properties. These are determined from the experimental analysis of the material concerning its sensitivity to various levels of consolidation. Results are particularized for a vessel with the circumferential ply stack toward the outside, where the disparity against the average longitudinal and transverse stiffness shows respective maximum values of 3.4 and 11.6 %. Likewise, maximum deviations in material strength are presented to be 12.0 and 49.7 % for the longitudinal and transverse cases.

Concerning the deformational response, only minor deviations are reported when comparing heterogeneous and homogeneous material definitions. A slightly larger compliance is presented in the upper dome for the heterogeneous case, coinciding with the region of least consolidation, and leading to a minor increase in the most sensitive boss axial displacement prediction (+4.7 %). In the cylinder, the disparity in the maximum meridional strain is additionally limited (+2.0 %), being the stiffer inner layers presented to compensate for the more substantial compliance of the outer ones.

In terms of damage progression, the more realistic depiction of strength through-the-thickness with a

heterogeneous material definition comparatively influences the sequence with which failure is triggered in the outer layers. Being the transverse strength of the highly porous outer circumferential plies lower than the one of a wrapping outer helical layer, failure is predicted first in the former. The failure sequence prediction flips compared with the series reported for a homogeneous material description, yet at mildly high loads, the extension of transverse damage is sufficiently broad, so the deformational response coalesces for both approaches.

Validation of Results

The trends presented by the real vessel deformational response are well reproduced by the numerical predictions in all three stacking sequences considered. These, include the succession of bending responses shown by the variation of the meridional strain in the outer surface along a meridional path, the variation of tangential stiffness in the dome transition region illustrated by the formation of a protrusion or the absence of it, and the relative magnitude between the three depicted configurations for the average cylinder strain components and the boss axial displacement. The axial coordinate at which the peak of any formed bulge is predicted appears to be shifted slightly with respect to the experimental data.

Comparing the magnitude of the predicted and measured strain components, it is observed that the analyses are generally accurate for the tangential case (< 7 %), even for the assumption of a constitutively elastic behavior. In the case of meridional strain, a general underestimation exists under the elastic material consideration (10 to 20 %). For the analyzed vessel with circumferential layers toward the outside, the average strain prediction in the cylindrical region shows to improve with the consideration of damage significantly (< 3 %). However, the maximum meridional strain along a vessel meridional path is presented to only improve modestly when damage progression and homogeneous material properties are regarded (∼10 %) and when heterogeneity is modeled (∼6 %).

The boss axial displacement is also relevantly underestimated for elastic material definitions (20 to 30 %), even though fair improvements are achieved with the consideration of damage. In the configuration with circumferential layers toward the outside this is reported for homogeneous (∼16 %) and heterogeneous material definitions (∼12 %).The origin of these discrepancies is argued on the insufficiently accurate description of the stiffness distribution in the dome transition region. The vessel geometry is only strictly validated concerning its outer contour, which, therefore, concedes the circumferential group start and end locations to deviate from the real vessels slightly.

Regarding the progression of damage, it is possible to predict the growth of cracks in the circumferential plies in the same pressure range at which AE are recorded. Additionally, these cracks are also presented to rapidly grow through-the-thickness, in the same trend reported from CT images and microscopic observations of pressurized vessels. The pressure stage of damage onset in the circumferential plies is overestimated with the definition of homogeneous material properties (+10 MPa), although the prediction is improved considering heterogeneity (+5 MPa). In a like manner, triggering of failure on the outer surface is relevantly underestimated when compared to the observation of macroscopic damage. The prediction improves by shifting from a homogeneous material definition (-25 MPa) to the consideration of heterogeneous material properties (-10 MPa). This discrepancy is argued on the questionable representativity of a subply idealization in reproducing the real stress state of an interwoven helical ply, thus fundamentally impacting its damage onset and subsequent progression.

Lastly, the burst pressure correlation shows various levels of agreement according to the depicted vessel deformational response. Assuming a constitutively elastic response, discrepancy within the experimental scatter is minimum if the burst is predicted unequivocally in the cylinder (∼4.8 %), moderate if a bulge develops in the dome transition region. However, it does not determine the component integrity (∼8.9 %)), and substantial if the burst is decidedly controlled by the growth of a protrusion (∼27.1 %). If accounting for damage progression the prediction relevantly improves for a final collapse in the cylindrical region (∼2.2 %), and for a failure in the dome transition (∼12.3 %).

Generalization of the Analysis Methodology for the Design of CPVs

The strategy for the analysis of CPVs presented in this work is implemented to compile the steps ranging from the vessel stacking sequence design to the burst pressure estimation. Its prediction capabilities are demonstrated for the type and stage of the expected burst events, ultimately presenting the approach as an application framework for the investigation of any arbitrary stacking sequence. Still, the methodology holds a modest dependence on experimental results concerning the material

characterization, the liner deformation during winding, and the material consolidation level, for which the development of analytical or numerical models falls outside scope.

Being the CPV stiffness and strength closely connected with the geometrical and material description, the realistic representation of these stands as the foundation of a reliable burst pressure estimation. It depends on the methodology sophistication with which the produced vessel configuration is predicted and the consistency with which it is manufactured. A process that is highly controllable inherently results in lesser variations in the material quality, allowing the generalization of designs and increasing the reliability with which the predictions are made.

Besides, the general structural response is also shown to relate with the accuracy with which deformation and failure are anticipated. Stacking sequences that depict sudden changes in stiffness are also presented to form protruding deformed shapes, triggering failure at earlier stages, inducing the growth of delaminations at the group interfaces, and lowering the burst pressures. Accordingly, an inherent deviation from the real vessel happens, not only because of the more complex representation of reality but also because of the larger scatter in the corresponding experimental response. In this regard, burst pressures can be reasonably estimated from a constitutively elastic approximation if failure occurs in the cylinder, and a high number of elastically deforming circumferential plies exist. Material degradation becomes more relevant the larger the number of angle plies, leading to the most acute deviations when collapse shifts toward the dome.

A sufficiently gradual variation of the directional stiffness in the dome shape is presented to avoid the growth of protruding shapes. Withal, the needed stiffness is a direct result of the dome shape, through which the pressure loading shifts from radial to axial dominated. The milder the dome slope, the more gradual this change is, and the less sensitive it appears to the slight fiber misalignments, the adjustments in the ply drop location, and the local thickness increase. However, a milder dome slope also implies that the dome region is cornered, then reducing the useful storage volume for its enclosing casket and lessening the fuel storage capability.

Additional consequences of the stacking sequence definition are the result in laminate quality and the deformational behavior in the cylindrical region. Locating high angle layers on the outside generates significant compaction forces during winding, thus ensuring low porosity and notable fiber volume contents. Stiffness and strength tend to increase under these conditions, while scatter in the material mechanical characteristics also decreases accordingly. As a result, the vessel mechanical response may be more confidently determined. However, a configuration that locates high angle layers toward the outside also deviates the load path from the location of maximum tangential stress on the inner surface. This configuration implies that higher strain components exist, resulting in a higher number of cracks developing in the inner layers, inducing load redistribution to the fibers, and hampering the unequivocal burst estimation.

Conclusively, the veracity of a numerical estimation is strongly connected with the looseness of the CPV design, where the high sensitivity to the small variations during the manufacturing hinders their rightful prognosis. Premature burst events are identified by incorrect stiffness definitions for the applied loading, whereas the variation of this is the acutest with the smallest curvature of the dome region. Hence, a vessel design should feature a sufficiently mild dome shape to minimize uncertainty concerning the manufacturing process and the failure prediction, while being steepest to maximize enclosed volume.

Note for Completeness. A perspective on weight minimization is also derived from the stacking sequence analysis presented in this investigation. On the one side, locating high angle plies in the cylindrical region toward the outside levels the gradient of the generated tangential stress. Therefore, a relatively uniform distribution of fiber stress is achieved through-the-thickness, hence preventing the premature failure of the generally critically loaded inner plies. On the other side, the steeper the dome slope, the larger the number of low angle helical plies needed to bear the axial load component. However, their contribution to the strength in the cylindrical region is the least, requiring there further reinforcement and a relative weight increase. Featuring a milder slope in the dome requires the winding of high angle helical layers, thus simultaneously reinforcing the cylindrical region.

12

Future Work

The analyses of CPVs conducted thus far show that a significant influence exists on the mechanical response of the component derived from the manufacturing process. However, several challenges still need to be addressed to achieve a fully generalizable methodology while still accurately depicting the final vessel collapse.

Prediction of Uncured Material Deformation during Winding and Curing

The generalization of a vessel geometry for any arbitrary stacking sequence is dependent on the estimation of tow readjustments, the viscous material deformation during winding and curing, and the distortion of the liner. These effects are currently accounted through experimental measurements, which, as a consequence, are bounded to the tested configurations. The deformational behavior of the CPV is presented to be tightly bounded to its geometrical definition, determining the relative tangential expansion and axial displacement, and defining the extent to which results may be correlated with experimental data.

An alternative consists of the implementation of analytical and numerical models that represent the uncured material compliance. The defined filament tension generates radial pressure on the liner and the previously wound layers, hence inducing their deformation. This readjustment is further influenced by the addition of the thermal and kinetics of curing processes, which, by impacting the viscosity of the resin constituent, also permit its associated flow. It is expected that the combination of these effects can reasonably approximate the influence of the stacking sequence in the final vessel geometry.

Modeling of Failure and Damage Progression in the Helical Layers

The interwoven band construction of helical layers is idealized in the presented implementation as a set of laminated subplies of alternative fiber orientations. The general layer mechanical response is represented with a reasonable computational cost, albeit the real stress state in the bands is not explicitly modeled. Therefore, the representativeness of this idealization in predicting failure is not assured. A better depiction can be achieved by correlating failure predictions with experimental observations of specimens where the failure stages are clearly defined.

Concerning the progression of damage, arbitrarily high fracture toughness values are considered to account for the multiple crack arrests due to the changing fiber orientation. Withal, no standard procedures are known to identify the magnitude of such a resistance to damage progression, appearing connected to the relative size of the mesh discretization to the woven bands. The implementation of multiscale models appears to diminish this limitation by identifying, at the representative magnitude of the macroscale elements, the type, and extent of the material degradation within. It requires representing the actual construction of the helical ply bands and modeling the corresponding interfiber failure, connecting delaminations, and fiber orientation change with the increased loading.

Furthermore, cracks through-the-thickness in a stack of helical layers may predict growth perpendicular to the fiber direction. This effect disregards the residual strength in the fibers against shearing and appears as an intrinsic limitation of the modeling of damage through CDM. A convenient solution within this framework is the definition of distinct fracture toughness values for the crack growth parallel and perpendicular to the fibers.

Accounting for Bridging Delaminations between Plies

Modeling of damage progression is overall limited to interfiber failure modes, thus disregarding the influence of delaminating plies in increasing the corresponding vessel compliance. Such an effect can be considered with the modeling of cohesive elements between the individually discretized plies of the three-dimensional FE construction. Yet, an open question exists on whether the coupling of both delamination and failure modes is sufficiently representative of the real damage process while still dependent on the mesh discretization.

Improving the Numerical Robustness during Damage Progression

Numerical difficulties during the progression of damage are encountered when reaching relatively high-pressure stages. The definition of hourglass control stiffness to limit the spread of zero-energy deformation modes is found to connect with the robustness of the numerical setup. Furthermore, a detailed analysis of the sensitivity of damage progression variables to the mesh refinement needs to be established. Their benchmarking requires the benchmarking of various mesh configurations, which therefore influence the progression of damage. A finer mesh description depicts smoother stress gradients, also expected to feature a higher number of elements that can progressively degrade.

Establishing a Framework for Layup Optimization

A subsequent step to the detailed analysis of a CPV is the eventual determination of the stacking sequence that optimally distributes stiffness and strength for a given liner shape. Direct usage of the current methodology requires the generation of a detailed geometry for each optimization candidate, hence involving its meshing per ply and the definition of the corresponding individual layer constraints. The number of variables of the optimization problem also appears remarkable, including stacking sequence, ply drop location, non-geodesy, and winding pattern. As a consequence, the solution to this optimization problem appears to be mathematically challenging while also impractical considering the involved computational cost.

Alternatively, an approach for this task can divide the optimization process into three stages. First, determining the optimum lamination parameters of the full stackup according to the structural requirements (stiffness and strength); second, particularizing the lamination parameters at each discretization point into a sequence through-the-thickness of fiber orientations; and third, converting the discrete stacking sequences into fiber paths and winding patterns that indeed feasible to be manufactured.

A

Vessel Stacking Sequence Description

This appendix reviews the geometrical characteristics of the vessels involved in this investigation. This assessment is done to present a concise image of the distinct stacking configurations considered, which appears to be necessary in light of the discussion on their respective mechanical responses.

To this purpose, index cards are arranged for each layup of the vessels where experimental data and geometrical predictions are comparatively depicted. The first involves cross-section views of cut components, outer contour measurements using stripe-light projections, and CT images of through-the-thickness specimens. Likewise, the second concerns the vessel thickness profile estimated from the filament winding software ComposiCAD™ and FE model construction. This filament winding software defines a preliminary geometrical configuration from the winding robot motion computation, which is subsequently adjusted in a systematic form with the methodology presented in chapter 5.

Burst pressures of various vessel components are reported in a tabular format, together with some of their relevant geometrical measurements. In this regard, the vessel boss-to-boss lengths are introduced for the post-winding and post-curing states, as they provide an insight on the deformation experienced by the liner during the winding process. This information is complemented with the detailing of the vessel diameters in the cylindrical region for the various available measurements. Lastly, the relative thickness of the groups forming the vessel stacking sequence is accounted for from the corresponding CT scan analysis.

W1A

Stacking Sequence Definition
(from bottom to top)



Name	Type	Number	Ori. (deg)	W. Pattern
H1	Helical	9	19.9	Non-geo.
C1	Circ.	30	88.8	–
H2	Helical	2	19.9	Non-geo.

Ori. – filament orientation in the cylindrical region; W. Pattern – winding pattern; Non-geo. – non-geodesic winding pattern; Circ. – circumferential

Description

Composite pressure vessel wound with two layer types, low angle helicals and circumferentials. Plies are grouped in stacks of same type defining a clearly unbalanced stacking sequence. In the circumferential region, low angle helicals are placed on the bottom, while circumferentials are located on top.

Geometrical Measurements

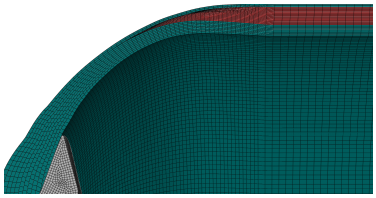
Vessel ID	B. Pres. [MPa]	L. Wind. [mm]	L. Tot. [mm]	Mea. Dia. W. [mm]	Mea. Dia.[mm]
01 - 0126	–	–	−5.8	–	192.2 ± 0.2
01 - 0128	165.3	–	−4.8	–	192.7 ± 0.3
01 - 0183	162.4	–	–	–	–
01 - 0192	156.9	−3.5	0.4	191.1 ± 0.2	192.9 ± 0.4

B. Pres. – burst pressure; L. Wind. – measured boss-to-boss length difference between before and after winding; L. Tot. – measured boss-to-boss length difference between before winding and after curing; Mea. Dia. W. – measured diameter after winding; Mea. Dia. – measured diameter after curing

Specimen Cut 01 - 0192



Specimen Mesh



Geometrical Measurements (cont.)

Vessel ID	Weight [kg]	SP Dia. [mm]	SP STD. Vess. [mm]	CT Dia. [mm]	CT Thick. [mm]	CT Thick. H1 [mm]	CT Thick. C1 [mm]	CT Thick. H2 [mm]	CT Gap [mm]
01 - 0126	3.638	–	–	192.02 ± 0.29	10.49 ± 0.09	3.85 ± 0.06	5.42 ± 0.14	1.22 ± 0.10	0.90
01 - 0183	3.587	190.98 ± 0.09	0.35	–	–	–	–	–	–

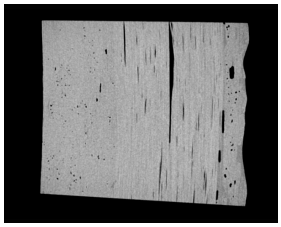
SP Dia. – stripe-light projection diameter; SP STD Vess. – stripe-light projection vessel average standard deviation; CT Dia. – CT scan diameter; CT Thick. – CT scan thickness; CT Thick. H1 – CT scan thickness first helical layer group; CT Thick. C1 – CT scan thickness first circumferential layer group; CT Thick. H2 – CT scan thickness second helical layer group; CT Gap – CT scan gap between liner and composite reinforcement

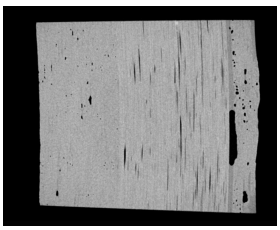
Note 1: The diameter, thickness and gap measurements refer to the cylindrical section of the vessel

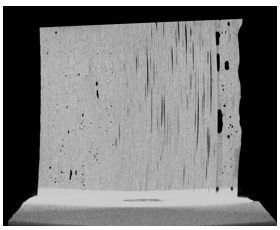
Note 2: The stripe-light projection measurements are calculated from six equidistant longitudinal sections of the vessel

Note 3: CT scan thickness measurements are calculated from three $10x10$ mm^2 specimens

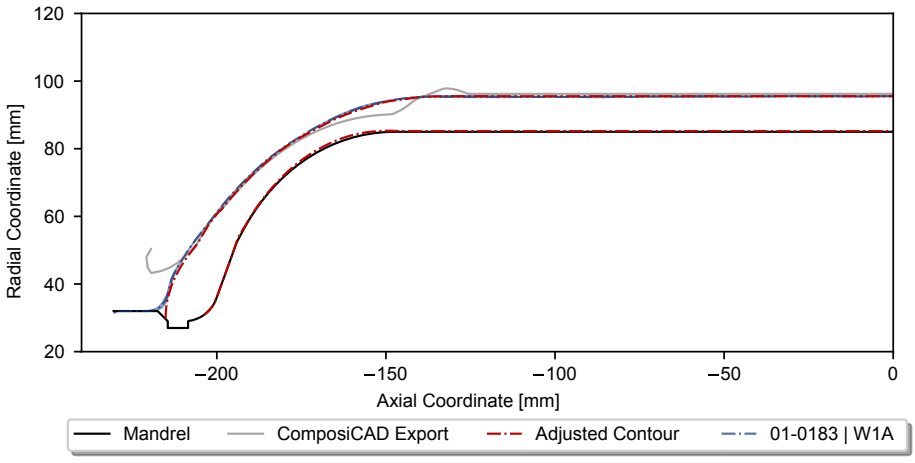
CT Scans 01 - 0126







Specimen Contour Simulation



E+

Stacking Sequence Definition
(from bottom to top)



Gr. Num.	Name	Type	Number	Ori. (deg)	W. Pattern
5	H1	Helical	2	19.90	Non-geo.
	C1	Circ.	6	88.80	–
1	H2	Helical	1	19.90	Non-geo.

Gr. Num. – number of groups; Ori. – filament orientation in the cylindrical region; W. Pattern – winding pattern; Non-geo. – non-geodesic winding pattern; Circ. – circumferential

Description

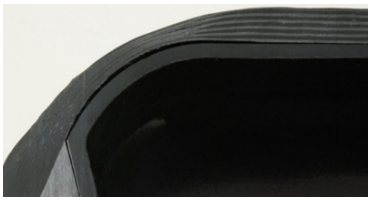
Composite pressure vessel wound with two layer types, low angle helicals and circumferentials. Plies are grouped in stacks of same type and staggered through the stacking sequence. In total, there are five of these groups of helical and circumferential layers

Geometrical Measurements

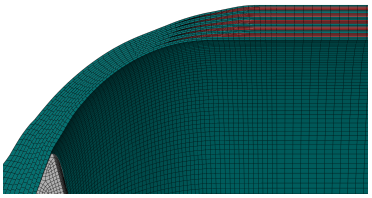
Vessel ID	B. Pres. [MPa]	L. Wind. [mm]	L. Tot. [mm]	Mea. Dia. W. [mm]	Mea. Dia.[mm]
01 - 0197	–	–	−3.7	–	192.5 ± 0.3
01 - 0201	149.4	−3.3	−3.5	191.8 ± 0.5	192.5 ± 0.3
01 - 0268	147.5	−3.5	−3.2	192.0 ± 0.5	192.9 ± 0.7
01 - 0271	144.4	−2.8	−2.2	191.9 ± 0.3	192.8 ± 0.6

B. Pres. – burst pressure; L. Wind. – measured boss-to-boss length difference between before and after winding; L. Tot. – measured boss-to-boss length difference between before winding and after curing; Mea. Dia. W. – measured diameter after winding; Mea. Dia. – measured diameter after curing

Specimen Cut 01 - 0197



Specimen Mesh



Geometrical Measurements (cont.)

Vessel ID	Weigth [kg]	SP Dia. [mm]	SP STD. Vess. [mm]	CT Dia. [mm]	CT Thick. [mm]	CT Thick. G1 [mm]	CT Thick. G3 [mm]	CT Thick. G5 [mm]	CT Gap [mm]
01 - 0197	3.649	190.67 ± 0.05	0.49	–	–	–	–	–	–
01 - 0271	–	–	–	–	–	–	–	–	–

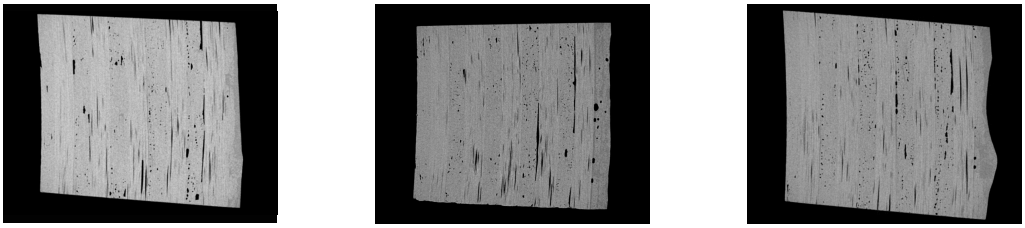
SP Dia. – stripe-light projection diameter; SP STD Vess. – stripe-light projection vessel average standard deviation; CT Dia. – CT scan diameter; CT Thick. – CT scan thickness; CT Thick. H1 – CT scan thickness first helical layer group; CT Thick. C1 – CT scan thickness first circumferential layer group; CT Thick. H2 – CT scan thickness second helical layer group; CT Gap – CT scan gap between liner and composite reinforcement

Note 1: The diameter, thickness and gap measurements refer to the cylindrical section of the vessel

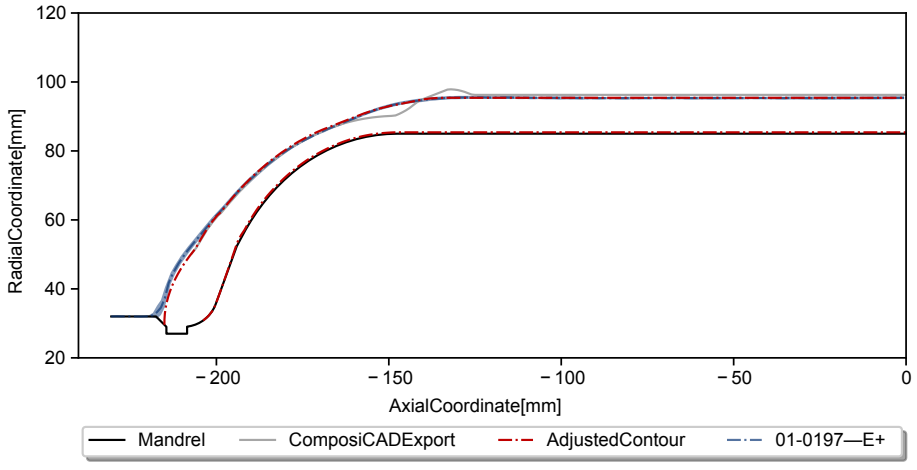
Note 2: The stripe-light projection measurements are calculated from six equidistant longitudinal sections of the vessel

Note 3: CT scan thickness measurements are calculated from three $10x10$ mm^2 specimens

CT Scans 01 - 0271



Specimen Contour Simulation



B*

Stacking Sequence Definition
(from bottom to top)



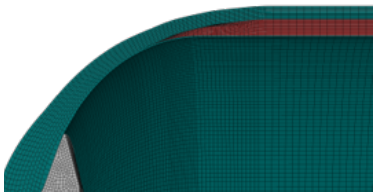
Name	Type	Number	Ori. (deg)	W. Pattern
H1	Helical	1	19.90	Non-geo.
C1	Circ.	30	88.80	–
H2	Helical	10	19.90	Non-geo.

Ori. – filament orientation in the cylindrical region; W. Pattern – winding pattern; Non-geo. – non-geodesic winding pattern; Circ. – circumferential

Specimen Cut 01 - 0190



Specimen Mesh



Description

Composite pressure vessel wound with two layer types, low angle helicals and circumferentials. Plies are grouped in stacks of same type defining a clearly unbalanced stacking sequence. In the circumferential region, low angle helicals are placed on top while circumferentials are located on the bottom.

Geometrical Measurements

Vessel ID	B. Pres. [MPa]	L. Wind. [mm]	L. Tot. [mm]	Mea. Dia. W. [mm]	Mea. Dia.[mm]
01 - 0190	–	–	−2.9	–	192.2 ± 0.3
01 - 0204	149.4	−2.5	−2.2	191.2 ± 0.3	192.4 ± 0.5
01 - 0243	110.5	−3.4	−2.9	191.4 ± 0.4	191.4 ± 0.6
01 - 0282	–	−3.8	−2.9	191.6 ± 0.8	192.3 ± 0.2

B. Pres. – burst pressure; L. Wind. – measured boss-to-boss length difference between before and after winding; L. Tot. – measured boss-to-boss length difference between before winding and after curing; Mea. Dia. W. – measured diameter after winding; Mea. Dia. – measured diameter after curing

Geometrical Measurements (cont.)

Vessel ID	Weight [kg]	SP Dia. [mm]	SP STD. Vess. [mm]	CT Dia. [mm]	CT Thick. [mm]	CT Thick. H1 + C1 [mm]	CT Thick. H2 [mm]	CT Gap [mm]
01 - 0190	3.615	190.07 ± 0.11	0.36	–	–	–	–	–
01 - 0204	3.631	–	–	–	10.89 ± 0.23	5.95 ± 0.13	4.94 ± 0.16	–

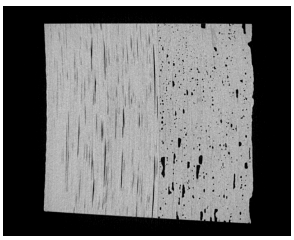
SP Dia. – stripe-light projection diameter; SP STD Vess. – stripe-light projection vessel average standard deviation; CT Dia. – CT scan diameter; CT Thick. – CT scan thickness; CT Thick. H1 – CT scan thickness first helical layer group; CT Thick. C1 – CT scan thickness first circumferential layer group; CT Thick. H2 – CT scan thickness second helical layer group; CT Gap – CT scan gap between liner and composite reinforcement

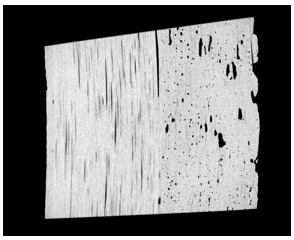
Note 1: The diameter, thickness and gap measurements refer to the cylindrical section of the vessel

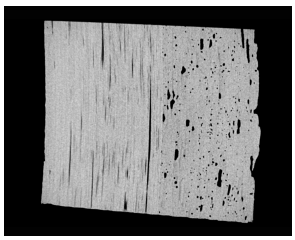
Note 2: The stripe-light projection measurements are calculated from six equidistant longitudinal sections of the vessel

Note 3: CT scan thickness measurements are calculated from three $10x10$ mm^2 specimens

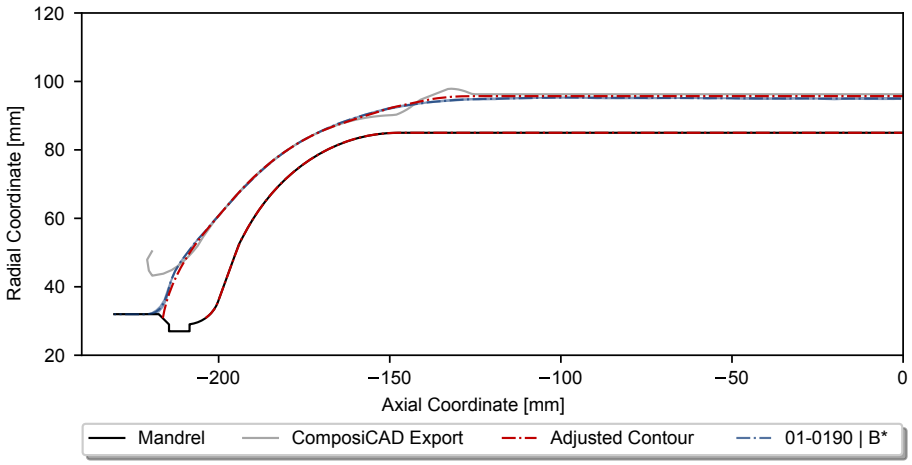
CT Scans 01 - 0204







Specimen Contour Simulation



B

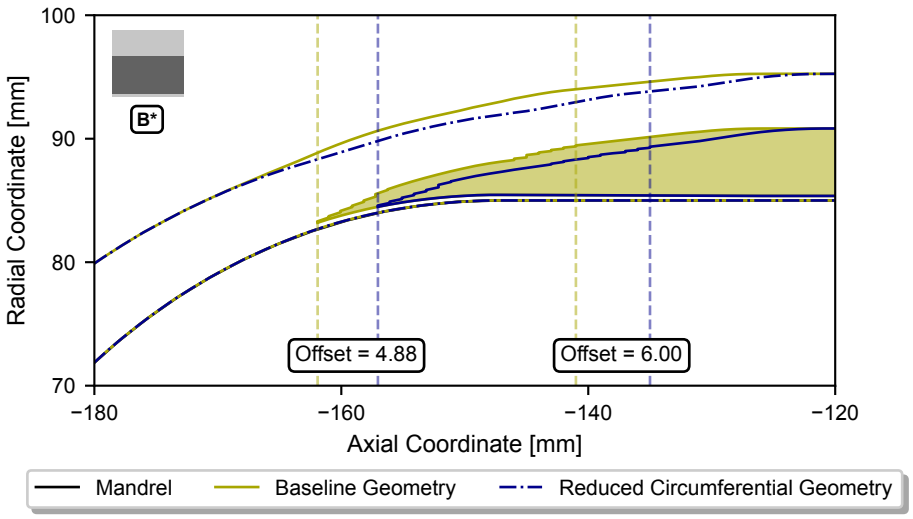
Influence of the Circumferential Ply Drop Location on the B* Stacking Sequence Deformation

In this appendix, the length of the circumferential layer stack of the B* stacking sequence is alternatively extended and reduced compared with the baseline geometry depicted in fig. 5.10. This side investigation permits the presentation of the extent to which the formation of a bulge in the dome transition region can be avoided, while also showing how its magnitude changes with the internal pressure component at the circumferential ply drop location. Thus, the boundaries of the circumferential layer groups are offset with respect to the baseline geometry about 5 mm in the axial direction as illustrated in fig. B.1. The tapering offset implies a change of the start and end coordinates of the tapering section and intends to reproduce the effect of reducing the circumferential ply length realistically.

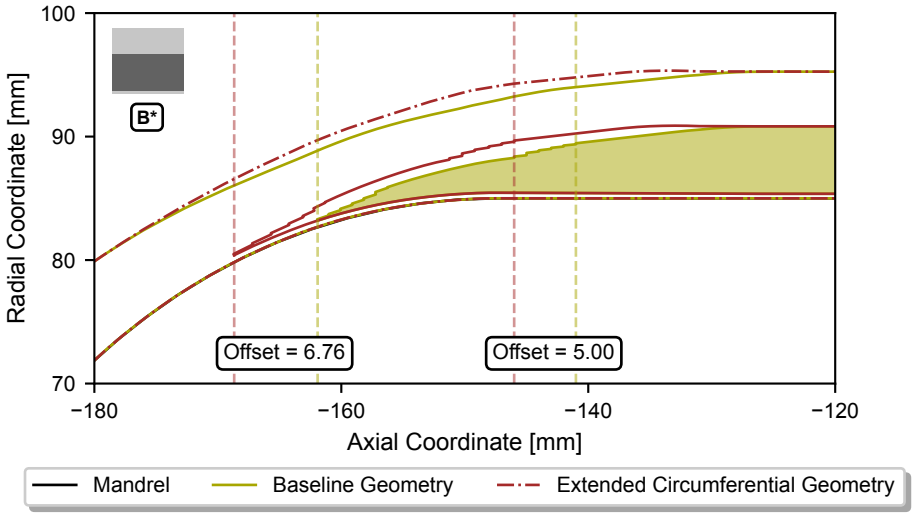
The deformed shapes of the geometries depicted in fig. B.1 are presented in fig. B.2 with their meridional strain fields at a load pressure of 160 MPa. This comparison shows the sensitivity of the mechanical response of the B* layup qualitatively, indicating how the reduction of the circumferential group length bolsters the formation of a bulge in the dome transition region. Likewise, extending the circumferential group length appears to hinder the local tangential expansion, although it does not eliminate the formation of a bulge for the defined circumferential length.

A more detailed illustration of the varying deformational behavior of these configurations is presented in fig. B.3 for the outer surface strain components along a longitudinal vessel path. Here, the meridional and tangential strain components are presented for each of the defined circumferential group lengths at a load pressure of 103.5 MPa, compared against the experimental data of the baseline configuration acquired using DIC. It is observed that the general tendency concerning meridional bending and tangential expansion introduced with the baseline geometry is maintained for the alternative configurations. In this regard, the reduced circumferential length configuration shows a bulge formation closer to the cylindrical region than that of the baseline. It results in an earlier peak in the tangential strain and correspondingly also an earlier local maximum in the meridional component. The expansion in the dome transition region is comparatively larger than the one experienced by the reference geometry because of the dominant radial pressure component and its diminished hoop stiffness. Consequently, this significant radial expansion displaces the cylinder edge radially, generating outward meridional bending nearby the dome transition region, which shows in the meridional strain component as a local minimum.

In the case of the extended circumferential length configuration, a region of significant tangential expansion still appears ahead of the circumferential ply drop location. However, the increased hoop stiffness in the dome transition region develops in two effects. First, the tangential strain is predicted to decrease in the cylindrical region nearby the dome transition, while second, the meridional strain shows a slight tendency to increase at this location, followed by an observed local minimum in the upper quarter of the dome. This pattern develops abaft the bulge formation and indicates an evolution towards a deformational behavior comparable to the orthotropic configuration. In this case, the dome



(a) Reduced circumferential stack length against baseline configuration



(b) Extended circumferential stack length against baseline configuration

Figure B.1: Group boundary definition of the B* stacking sequence by extending and reducing the length of the circumferential stack

transition region is effectively restrained in the tangential direction, and this creates an edge effect in the cylinder expansion, thus inducing respective outward and inward meridional bending responses.

Nevertheless, the stacking sequence definition with the helical group on top still stimulates the protrusion ahead of the circumferential ply drop because of its meridional inward bending. This effect shows ahead of the group end despite being generated only where the circumferential group exists. It happens because the dome region still features low tangential stiffness after the circumferential ply drop, hence permitting the unconstrained material to deform and preserve load equilibrium.

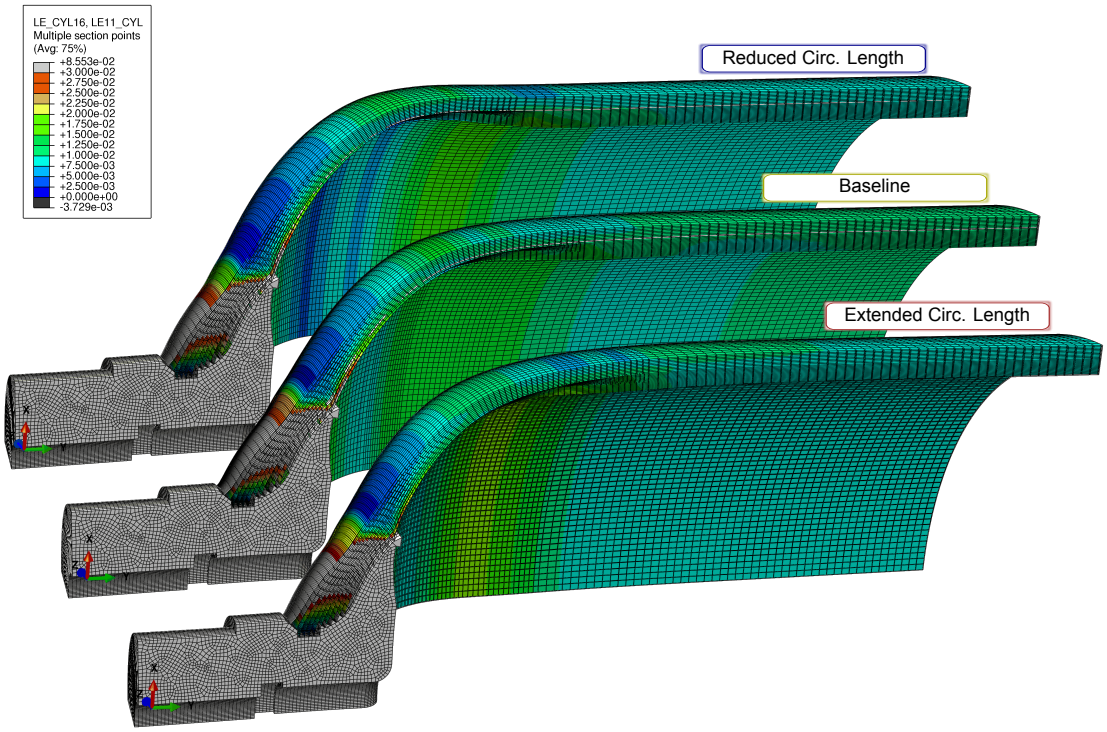


Figure B.2: Comparison of the deformed shape and the meridional strain field of the B* stacking sequence at a load pressure of 160 MPa by extending and reducing the length of the circumferential stack

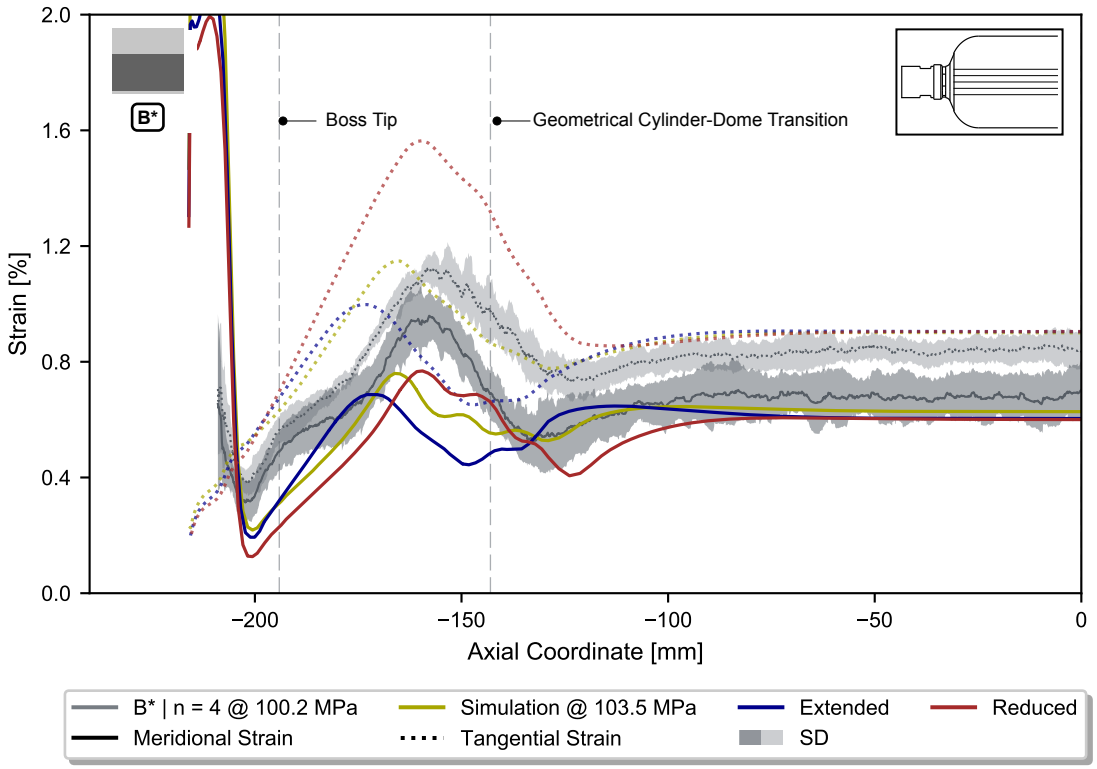


Figure B.3: Comparison of the outer surface meridional and tangential strain of the B* stacking sequence at a load pressure of 103.5 MPa by extending and reducing the length of the circumferential stack. Numerical predictions are presented against average experimental results for a number of samples n, where their scatter is indicated by their standard deviation (SD)

Overall, it is noted that extending the length of the circumferential layer group promotes a mechanical response of the orthotropic type in the dome transition region. Instead of eliminating the formation of a bulge, this is comparatively displaced further into the dome, where the extensional-bending coupling of the B* stacking sequence promotes an inward meridional bending response and, as a result, the growth of a swelling. This effect can generate a stress concentration in the circumferential group tip because of the restraining effect on the tangential expansion of the bulge. Such an overstressed region can lead to premature failures that correspond to a low robustness design.

C

Sensitivity of the Deformational Behavior to the Numerical Setup

The implementation of the explicit dynamic FE model described in section 7.2 requires the definition of various numerical variables that control the structural solution. The numerical results are susceptible to this configuration and, therefore, require their calibration. This appendix reports the sensitivity of the structural response of the W1A vessel to the mesh density, the simulation time, the mass scaling factor, the hourglass control stiffness. These are presented for a constitutively elastic material configuration, serving as a reference for the analysis setup considering the progression of damage. The elastic material properties permit a timely solution of the mechanical response, hence, also allowing the quick variable sensitivity identification.

Results are presented for the outer surface strain components in the meridional and tangential directions, reported at a pressure stage of 103.5 MPa, and compared with the average experimental results obtained using DIC. The baseline configuration coincides with the configuration analyzed in chapters chapter 7 through chapter 10. The mesh density is sufficiently fine to depict the geometric definition realistically, as illustrated in fig. C.1. The simulation lasts for 0.025 s, while the mass scaling factor ensures a stable time increment of $1 \cdot 10^{-7}$ s. Hourglass control stiffness is used to prevent the development of zero energetic deformation modes during material degradation. To this purpose, a pure stiffness Kelvin-type approach is used, with a scaling factor of 10. Lastly, the selected elements are solid with reduced integration.

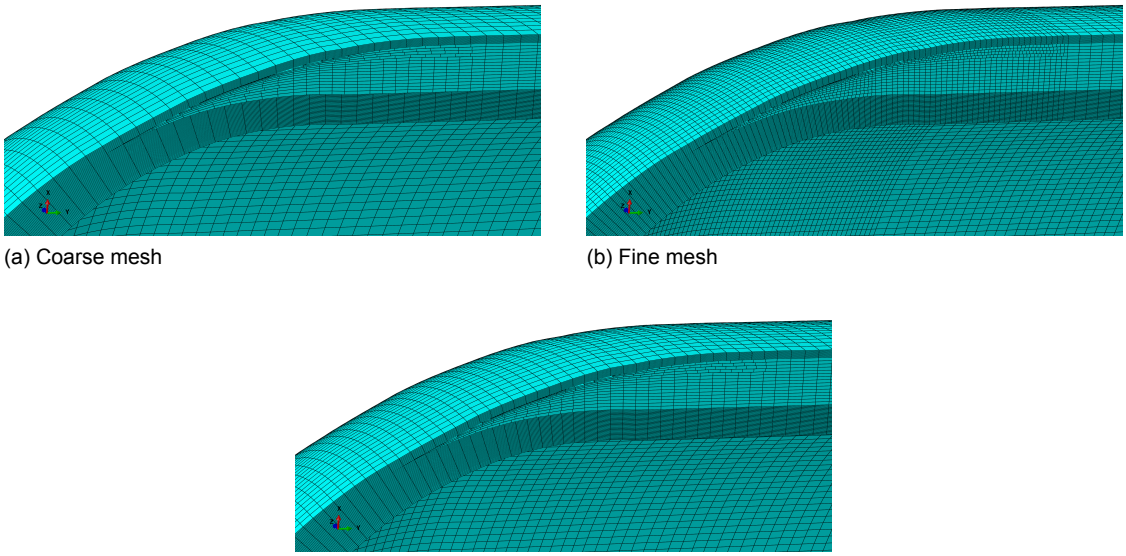
Sensitivity to the Mesh Density

Various mesh densities are defined as depicted in fig. C.1. These show various levels of refinement in the dome and dome transition regions, thus illustrating the sensitivity of the meridional bending response to the discretization along the meridional direction. The strain fields presented in fig. C.2 indicate that there is no relevant differences in the deformational behavior of the vessel investigated. Therefore, the mesh discretization is sufficient to reproduce the meridional bending response by considering reduced integration elements, which feature a limited response regarding bending loading.

However, a mesh finer than necessary for an adequate deformational behavior is defined for the analysis considering damage progression. Snap-backs in the stress-strain relation are to be mitigated through this description, eq. (9.18), where the material properties in table 7.1 determine a minimum element length of 0.11 mm. Even though the average element size in the baseline mesh definition is 1.28 mm, this mesh refinement is used for the modeling of damage. It is presented in section 9.2 that the progression of damage is physically sound, whereas the coarser mesh implementation significantly reduces the related computational cost.

Sensitivity to the Simulation Time

The simulation time relates to the amount of kinetic energy introduced during loading, thus ensuring that a quasi-static condition exists in the result prediction. In fig. C.3 the sensitivity of the deformational behavior is depicted for simulation times of 0.01, 0.025 and 0.05 s. These show that the variation in



(a) Coarse mesh

(b) Fine mesh

(c) Baseline mesh

Figure C.1: Comparison of the mesh density definitions for the sensitivity analysis

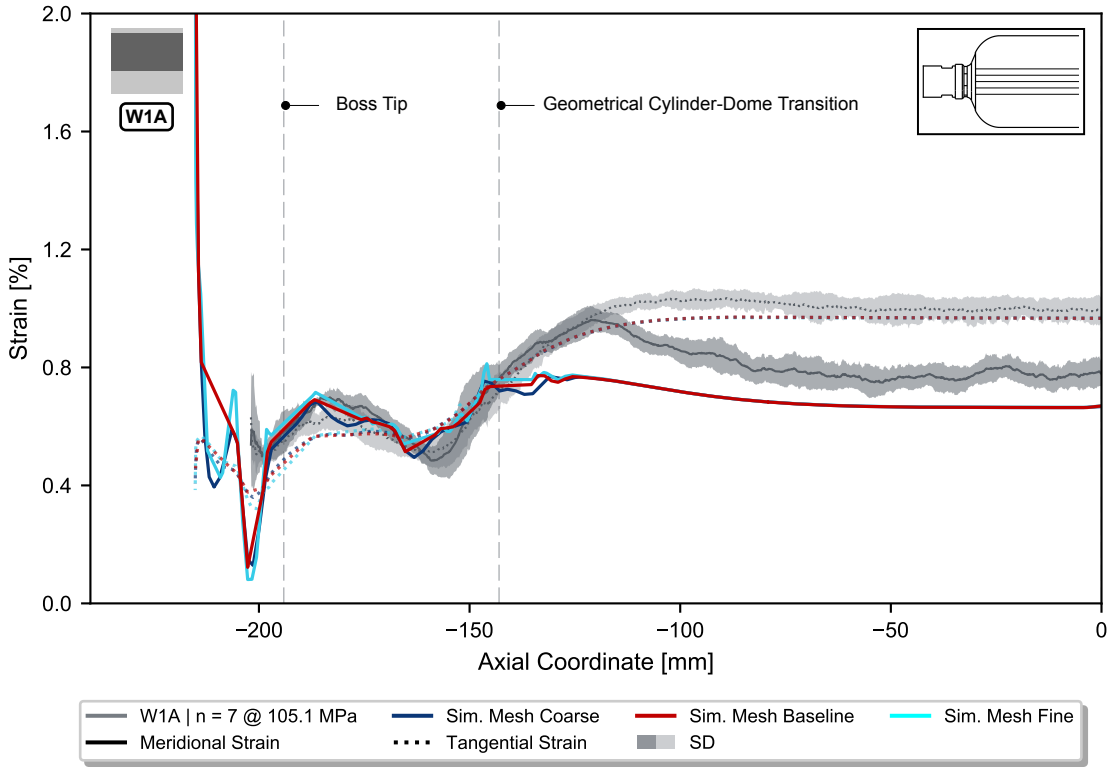


Figure C.2: Comparison of the outer surface meridional and tangential strain of the W1A stacking sequence considering three different **mesh** densities. Numerical predictions are presented against average experimental results for a number of samples n, where their scatter is indicated by their standard deviation (SD)

the response is almost negligible, being the maximum kinetic energy developed approximately three orders of magnitude lower than the internal energy result for all three cases.

Withal, the configuration with a simulation time of 0.025 s is ultimately selected as a baseline to prevent undesirable dynamic loading effects during the progression of damage. The sufficiently low

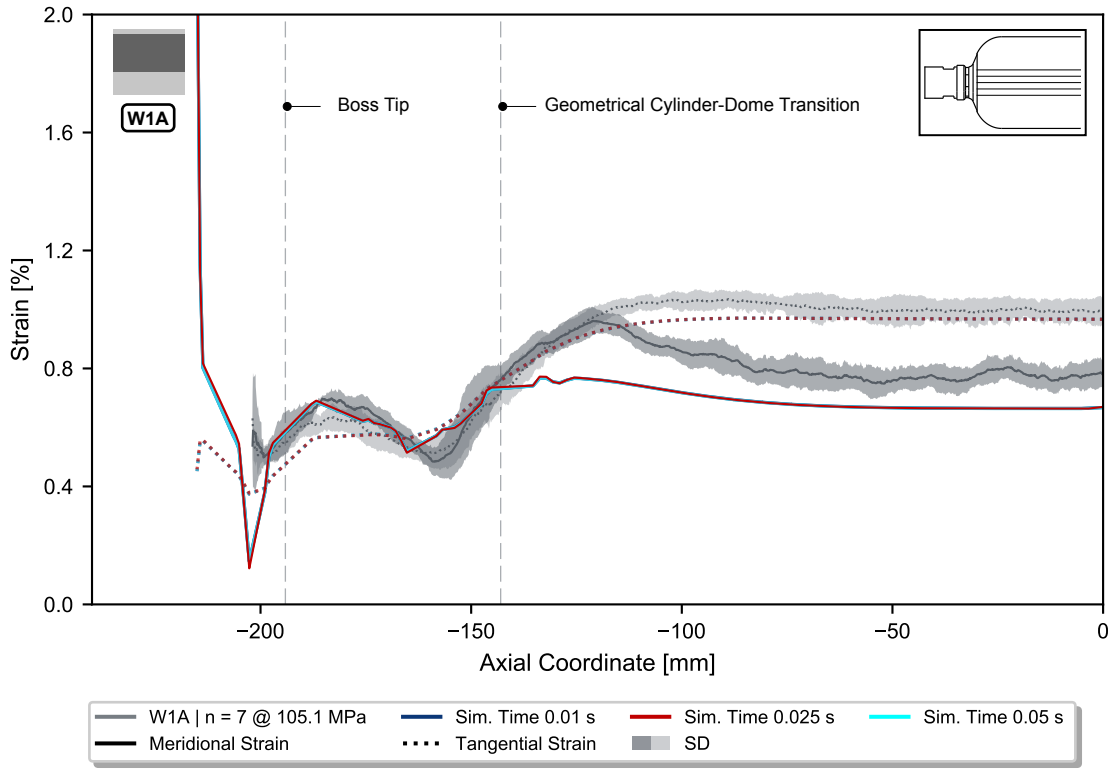


Figure C.3: Comparison of the outer surface meridional and tangential strain of the W1A stacking sequence considering three different **simulation time** definitions. Numerical predictions are presented against average experimental results for a number of samples n, where their scatter is indicated by their standard deviation (SD)

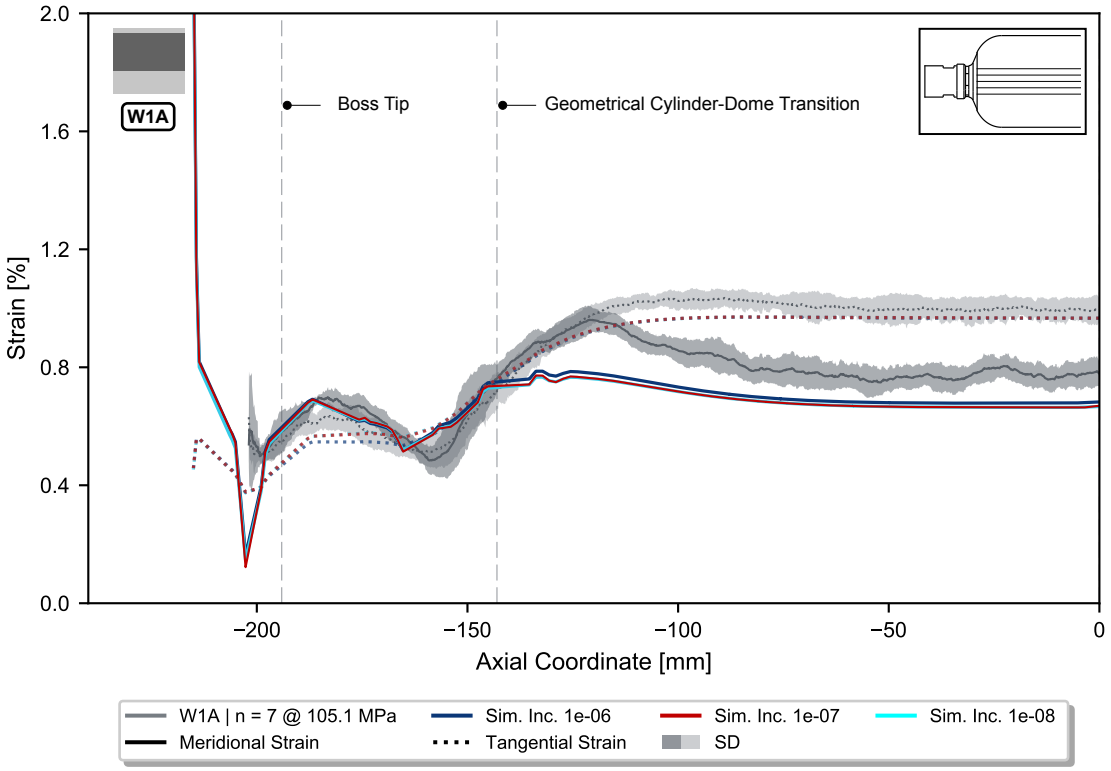


Figure C.4: Comparison of the outer surface meridional and tangential strain of the W1A stacking sequence considering three different **mass scaling** factors. Numerical predictions are presented against average experimental results for a number of samples n, where their scatter is indicated by their standard deviation (SD)

loading rate permits that the load redistribution upon fracture does not couple with the subsequent applied internal pressure, therefore avoiding the alteration of the results because of an excessively detrimental loading condition.

Sensitivity to the Mass Scaling Factor

Mass scaling factors artificially increase the stable time increment of the explicit FE solution in exchange for larger inertial effects. The kinetic energy developed by the deforming vessel increase with the higher scaling factor, although this is not observed to impact the solution in fig. C.4 severely. Configurations on which mass scaling is added to reach stable time increments of $1 \cdot 10^{-6}$, $1 \cdot 10^{-7}$ and $1 \cdot 10^{-8}$ s are defined. The baseline configuration used for the analysis adds a mass scaling factor to a $1 \cdot 10^{-7}$ s stable time increment. This intermediate point does not intend to minimizing inertial effects while still being computationally tractable, which considering damage progression appears as more relevant than regarding the deformational behavior.

Sensitivity to the Hourglass Control Stiffness Factor

The selection of reduced integration solid elements introduces the possibility of hourglass deformation modes appearing as a result of the load application. This numerical instability arises from the mesh density and stiffness distribution, which can be ultimately controlled by the addition of a corresponding stiffness value. This supplementary stiffness prevents elements from deforming in non-energetic modes, yet also influencing the elastic solution.

In the comparison presented in fig. C.5 a marginal variation in the deformational behavior exists when introducing section control stiffness with factors 2, 10 and 20. Scaling these factors, the hourglass control stiffness according to the material characteristics. Hourglass modes do not appear as a limitation in the deformational behavior of the vessel under constitutive elastic material properties, yet a mild factor is defined considering the subsequent material degradation.

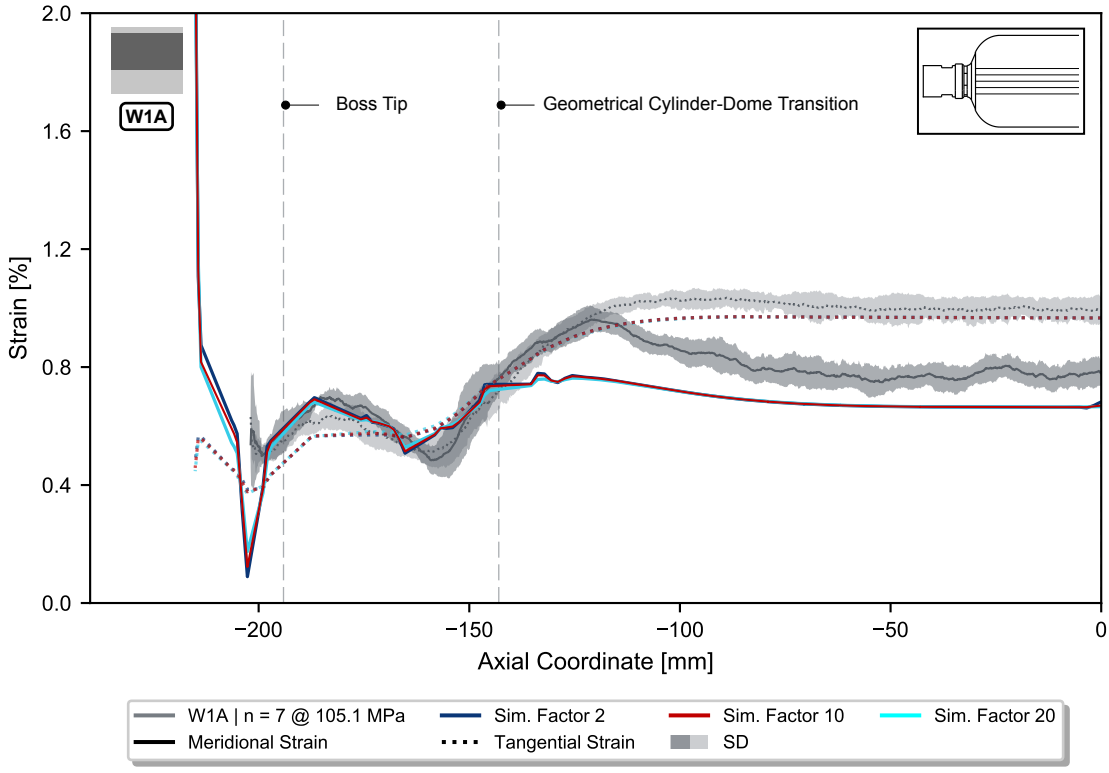


Figure C.5: Comparison of the outer surface meridional and tangential strain of the W1A stacking sequence considering three different **hourglass control stiffness** factors. Numerical predictions are presented against average experimental results for a number of samples n, where their scatter is indicated by their standard deviation (SD)

Bibliography

[1] F.A. Leone, A.C. Bergan, and C.G. Dávila. CompDam - Deformation Gradient Decomposition (DGD), v2.5.0, 2019. https://github.com/nasa/CompDam_DGD.

[2] M. Ehsani, Y. Gao, and A. Emadi. *Modern Electric, Hybrid Electric, and Fuel Cell Vehicles*. CRC Press, Boca Raton, 2017.

[3] J. D. Holladay, J. Hu, D. L. King, and Y. Wang. An overview of hydrogen production technologies. *Catalysis Today*, 139(4):244–260, 2009. doi: 10.1016/j.cattod.2008.08.039.

[4] J. Chi and H. Yu. Water electrolysis based on renewable energy for hydrogen production. *Cuihua Xuebao/Chinese Journal of Catalysis*, 39(3):390–394, 2018. doi: 10.1016/S1872-2067(17)62949-8.

[5] Economic Commission for Europe of the United Nations (UN/ECE). Regulation No 134 - Uniform provisions concerning the approval of motor vehicles and their components with regard to the safety-related performance of hydrogen fuelled vehicles (HFCV), 2015.

[6] The Official Blog of Toyota GB. blog.toyota.co.uk/toyota-mirai-safety-facts/toyotablog-h2-safety-pict-n2. Accessed: 2019-12-11.

[7] K. O'Malley, G. Ordaz, J. Adams, K. Randolph, C. C. Ahn, and N. T. Stetson. Applied hydrogen storage research and development: A perspective from the U.S. Department of Energy. *Journal of Alloys and Compounds*, 645:419–422, 2015. doi: 10.1016/j.jallcom.2014.12.090.

[8] D. Leh, P. Saffré, P. Francescato, and R. Arrieux. Multi-sequence dome lay-up simulations for hydrogen hyper-bar composite pressure vessels. *Composites Part A: Applied Science and Manufacturing*, 52:106–117, 2013. doi: 10.1016/j.compositesa.2013.05.007.

[9] H. S. Roh, T. Q. Hua, and R. K. Ahluwalia. Optimization of carbon fiber usage in Type 4 hydrogen storage tanks for fuel cell automobiles. *International Journal of Hydrogen Energy*, 38(29):12795–12802, 2013. doi: 10.1016/j.ijhydene.2013.07.016.

[10] J. P. Berro Ramirez, D. Halm, J. C. Grandidier, S. Villalonga, and F. Nony. 700 bar type IV high pressure hydrogen storage vessel burst - Simulation and experimental validation. *International Journal of Hydrogen Energy*, 40(38):13183–13192, 2015. doi: 10.1016/j.ijhydene.2015.05.126.

[11] V. Alcántar, S. M. Aceves, E. Ledesma, S. Ledesma, and E. Aguilera. Optimization of Type 4 composite pressure vessels using genetic algorithms and simulated annealing. *International Journal of Hydrogen Energy*, 42(24):15770–15781, 2017. doi: 10.1016/j.ijhydene.2017.03.032.

[12] M. Nebe, D. Maraite, C. Braun, D. Hülsbusch, and F. Walther. Experimental Characterization of the Structural Deformation of Type IV Pressure Vessels Subjected to Internal Pressure. *Key Engineering Materials*, 809:47–52, 2019. doi: 10.4028/www.scientific.net/kem.809.47.

[13] ISO 19881. *Gaseous hydrogen - Land vehicle fuel containers*. International Standards Organization. Geneva, Switzerland, 2018.

[14] ISO 11439. *Gas cylinders – High pressure cylinders for the on-board storage of natural gas as a fuel for automotive vehicles*. International Standards Organization. Geneva, Switzerland, 2013.

[15] C. P. Fowler, A. C. Orifici, and C. H. Wang. A review of toroidal composite pressure vessel optimisation and damage tolerant design for high pressure gaseous fuel storage. *International Journal of Hydrogen Energy*, 41(47):22067–22089, 2016. doi: 10.1016/j.ijhydene.2016.10.039.

[16] J. Błachut and K. Magnucki. Strength, stability, and optimization of pressure vessels: Review of selected problems. *Applied Mechanics Reviews*, 61:1–6, 2008. doi: 10.1115/1.2978080.

[17] V. V. Vasiliev, A. A. Krikanov, and A. F. Razin. New generation of filament-wound composite pressure vessels for commercial applications. *Composite Structures*, 62(3–4):449–459, 2003. doi: 10.1016/j.compstruct.2003.09.019.

[18] D. K. Roylance. Netting Analysis for Filament-Wound Pressure Vessels. Technical Report AMMRC TN 76-3, Composites Division Army Materials and Mechanics Research Center, 1976.

[19] H. Fukunaga and M. Uemura. Optimum design of helically wound composite pressure vessels. *Composite Structures*, 1(1):31–49, 1983. doi: 10.1016/0263-8223(83)90015-6.

[20] M. Hojjati, V. Safavi Ardebili, and S.V. Hoa. Design of domes for polymeric composite pressure vessels. *Composites Engineering*, 5(1):51 – 59, 1995. doi: 10.1016/0961-9526(95)93979-6.

[21] C. C. Liang, H. W. Chen, and C. H. Wang. Optimum design of dome contour for filament-wound composite pressure vessels based on a shape factor. *Composite Structures*, 58(4):469–482, 2002. doi: 10.1016/S0263-8223(02)00136-8.

[22] D. Leh, B. Magneville, P. Saffré, P. Francescato, R. Arrieux, and S. Villalonga. Optimisation of 700 bar type IV hydrogen pressure vessel considering composite damage and dome multi-sequencing. *International Journal of Hydrogen Energy*, 40(38):13215–13230, 2015. doi: 10.1016/j.ijhydene.2015.06.156.

[23] F. C. Shen. A filament-wound structure technology overview. *Materials Chemistry and Physics*, 42(2):96–100, 1995. doi: 10.1016/0254-0584(95)01554-X.

[24] R. Wang, W. Jiao, W. Liu, F. Yang, and X. He. Slippage coefficient measurement for non-geodesic filament-winding process. *Composites Part A: Applied Science and Manufacturing*, 42(3):303–309, 2011. doi: 10.1016/j.compositesa.2010.12.002.

[25] S.T. Peters. *Composite filament winding*. ASM International, 2011.

[26] D. Cohen, S. C. Mantell, and L. Zhao. The effect of fiber volume fraction on filament wound composite pressure vessel strength. *Composites Part B:Engineering*, 28(12):1035–1047, 2001. doi: 10.1016/S1359-8368(01)00009-9.

[27] L. Zu, S. Koussios, and A. Beukers. Design of filament–wound domes based on continuum theory and non-geodesic roving trajectories. *Composites Part A: Applied Science and Manufacturing*, 41(9):1312–1320, 2010. doi: 10.1016/j.compositesa.2010.05.015.

[28] L. Zu, H. Xu, H. Wang, B. Zhang, and B. Zi. Design and analysis of filament-wound composite pressure vessels based on non-geodesic winding. *Composite Structures*, 207:41–52, 2019. doi: 10.1016/j.compstruct.2018.09.007.

[29] J. T. Hofeditz. Structural design considerations for glass pressure vessels. In *18th Annual Meeting of the Reinforced Plastics Division*, 1963.

[30] T. De Jong. *A theory of filament wound pressure vessels*. PhD Thesis. Faculty of Aerospace Engineering, Delft University of Technology. Delft, 1983.

[31] S. Koussios, O. K. Bergsma, and A. Beukers. Filament winding. Part 1: Determination of the wound body related parameters. *Composites Part A: Applied Science and Manufacturing*, 35(2): 181–195, 2004. doi: 10.1016/j.compositesa.2003.10.003.

[32] L. Zu, S. Koussios, and A. Beukers. Design of filament-wound isotensoid pressure vessels with unequal polar openings. *Composite Structures*, 92(9):2307–2313, 2010. doi: 10.1016/j.compstruct.2009.07.013.

[33] J. S. Park, C. S. Hong, C. G. Kim, and C. U. Kim. Analysis of filament wound composite structures considering the change of winding angles through the thickness direction. *Composite Structures*, 55(1):63–71, 2002. doi: 10.1016/S0263-8223(01)00137-4.

[34] J. Zhou, J. Chen, Y. Zheng, Z. Wang, and Q. An. Dome shape optimization of filament-wound composite pressure vessels based on hyperelliptic functions considering both geodesic and non-geodesic winding patterns. *Journal of Composite Materials*, 51(14):1961–1969, 2017. doi: 10.1177/0021998316662512.

[35] P. Baličević, D. Kozak, and T. Mrčela. Strength of pressure vessels with ellipsoidal heads. *Strojniski Vestnik/Journal of Mechanical Engineering*, 54(10):685–692, 2008.

[36] S. Koussios. *Filament winding: a unified approach*. PhD Thesis. Faculty of Aerospace Engineering, Delft University of Technology. Delft, 2004.

[37] *Wound Composite Modeler for ABAQUS 6.17 User's Manual*. Dassault Systèmes, 2017.

[38] *ABAQUS 6.17 Documentation*. Dassault Systèmes, 2017.

[39] A. C. Knoell. Structural design and stress analysis program for advanced composite filament-wound axisymmetric pressure vessels (COMTANK). *Computer-Aided Design*, 1973. doi: 10.1016/0010-4485(73)90309-6.

[40] K. C. Gramoll, B. Namiki, and S. Onoda. Dome Thickness of Filament Wound Pressure Vessels. *Transactions of the Japan Society for Aeronautical and Space Sciences*, 33(100):66–79, 1990.

[41] R. Wang, W. Jiao, W. Liu, and F. Yang. A new method for predicting dome thickness of composite pressure vessels. *Journal of Reinforced Plastics and Composites*, 29(22):3345–3352, 2010. doi: 10.1177/0731684410376330.

[42] R. Wang, W. Jiao, W. Liu, and F. Yang. Dome thickness prediction of composite pressure vessels by a cubic spline function and finite element analysis. *Polymers and Polymer Composites*, 19 (2–3):227–234, 2011.

[43] J. De Carvalho, M. Lossie, D. Vandepitte, and H. Van Brussel. Optimization of filament-wound parts based on non-geodesic winding. *Composites Manufacturing*, 6(2):79–84, 1995. doi: 10.1016/0956-7143(95)99647-B.

[44] B. W. Tew. Preliminary design of tubular composite structures using netting theory and composite degradation factors. *Journal of Pressure Vessel Technology*, 117:390–394, 1995. doi: 10.1115/1.2842141.

[45] R. M. Jones. *Mechanics of Composite Materials*. CRC Press, Virginia, 1999.

[46] M. Xia, H. Takayanagi, and K. Kemmochi. Analysis of multi-layered filament-wound composite pipes under internal pressure. *Composite Structures*, 53(4):483–491, 2001. doi: 10.1016/S0263-8223(01)00061-7.

[47] L. Zu, J. Wang, and S. Li. Analysis of multi-layered thick-walled filament-wound hydrogen storage vessels. *International Journal of Hydrogen Energy*, 39(36):21083–21096, 2014. doi: 10.1016/j.ijhydene.2014.10.075.

[48] E. Asadi, W. Wang, and M. S. Qatu. Static and vibration analyses of thick deep laminated cylindrical shells using 3D and various shear deformation theories. *Composite Structures*, 94(2): 494–500, 2012. doi: 10.1016/j.compstruct.2011.08.011.

[49] L. Parnas and N. Katirci. Design of fiber-reinforced composite pressure vessels under various loading conditions. *Composite Structures*, 58(1):83–95, 2000. doi: 10.1016/S0263-8223(02)00037-5.

[50] I. Ramos, Y. Ho Park, and J. Ulibarri-Sanchez. Analytical and Numerical Studies of a Thick Anisotropic Multilayered Fiber-Reinforced Composite Pressure Vessel. *Journal of Pressure Vessel Technology, Transactions of the ASME*, 141(1):011203, 2019. doi: 10.1115/1.4041887.

[51] P. Mertiny, F. Ellyin, and A. Hothan. Stacking sequence effect of multi-angle filament wound tubular composite structures. *Journal of Composite Materials*, 38(12):1095–1113, 2004. doi: 10.1177/0021998304042077.

[52] Vinson, J. R. *Derivation of the Governing Equations for Thin Shells*. Springer, Dordrecht, 1993.

[53] S. Koussios, A. Beukers, O. K. Bergsma, and H. E.N. Bersee. Isotensoid related composite structures. In *Technical Conference of the American Society for Composites*, 2006.

[54] B. Solomon and A. Gray. Modern Differential Geometry of Curves and Surfaces. *The American Mathematical Monthly*, 102(10):937–942, 1995. doi: 10.1080/00029890.1995.12004690.

[55] M. Madhavi, K. V. J. Rao, and K. N. Rao. Design and analysis of filament wound composite pressure vessel with integrated-end domes. *Defence Science Journal*, 59(1):73–81, 2009. doi: 10.14429/dsj.59.1488.

[56] M. Musthak, P. Madar Valli, S. Narayanarao, and M. Madhavi. Prediction of Structural Behavior of FRP Pressure Vessel by Using Shear Deformation Theories. *Materials Today: Proceedings*, 4(2):872–882, 2017. doi: 10.1016/j.matpr.2017.01.098.

[57] A. C. Knoell. Structural design and stress analysis program for advanced composite filament wound axisymmetric pressure vessel (CLMTRANK). Technical Report JPL Technical Report 32-1521, NASA Jet Propulsion Laboratory, 1971.

[58] A. K. Roy and T. N. Massard. A Design Study of Thick Multilayered Composite Spherical Pressure Vessels. *Journal of Reinforced Plastics and Composites*, 2:479–493, 1992. doi: 10.1177/073168449201100502.

[59] J. N. Reddy. *Computer Implementation*. McGraw-Hill Education, 2005.

[60] Ever J. Barbero. *Finite element analysis of composite materials using Abaqus™*. CRC Press, 2013.

[61] D. S. Son and S. H. Chang. Evaluation of modeling techniques for a type III hydrogen pressure vessel (70 MPa) made of an aluminum liner and a thick carbon/epoxy composite for fuel cell vehicles. *International Journal of Hydrogen Energy*, 37(3):2353–2369, 2012. doi: 10.1016/j.ijhydene.2011.11.001.

[62] D. Leh, P. Saffré, P. Francescato, R. Arrieux, and S. Villalonga. A progressive failure analysis of a 700-bar type IV hydrogen composite pressure vessel. *International Journal of Hydrogen Energy*, 40(38):13206–13214, 2015. doi: 10.1016/j.ijhydene.2015.05.061.

[63] Z. Hashin. Fatigue failure criteria for unidirectional fiber composites. *Journal of Applied Mechanics, Transactions ASME*, 1981. doi: 10.1115/1.3157744.

[64] J. P. Berro Ramirez, D. Halm, J. C. Grandidier, and S. Villalonga. A fixed directions damage model for composite materials dedicated to hyperbaric type IV hydrogen storage vessel – Part I: Model formulation and identification. *International Journal of Hydrogen Energy*, 40(38):13165–13173, 2015.

[65] J. P. Berro Ramirez, D. Halm, J. C. Grandidier, and S. Villalonga. A fixed directions damage model for composite materials dedicated to hyperbaric type IV hydrogen storage vessel - Part II: Validation on notched structures. *International Journal of Hydrogen Energy*, 40(38):13174–13182, 2015. doi: 10.1016/j.ijhydene.2015.06.014.

[66] J. P. Berro Ramirez, D. Halm, J. C. Grandidier, S. Villalonga, and F. Nony. Experimental study of the thermomechanical behavior of wound notched structures. *International Journal of Hydrogen Energy*, 40(38):13148–13159, 2015. doi: 10.1016/j.ijhydene.2015.05.156.

[67] B. Magneville, B. Gentilleau, S. Villalonga, F. Nony, and H. Galiano. Modeling, parameters identification and experimental validation of composite materials behavior law used in 700 bar type IV hydrogen high pressure storage vessel. *International Journal of Hydrogen Energy*, 40(38):13193–13205, 2015. doi: 10.1016/j.ijhydene.2015.06.121.

[68] P. Ladeveze and E. Le Dantec. Damage modelling of the elementary ply for laminated composites. *Composites Science and Technology*, 43(3):257–267, 1992. doi: 10.1016/0266-3538(92)90097-M.

[69] B. Gentilleau, F. Touchard, and J. C. Grandidier. Numerical study of influence of temperature and matrix cracking on type IV hydrogen high pressure storage vessel behavior. *Composite Structures*, 111:98–110, 2014. doi: 10.1016/j.compstruct.2013.12.034.

[70] L. Wang, C. Zheng, H. Luo, S. Wei, and Z. Wei. Continuum damage modeling and progressive failure analysis of carbon fiber/epoxy composite pressure vessel. *Composite Structures*, 134: 475–482, 2015. doi: 10.1016/j.compstruct.2015.08.107.

[71] C. A. Rose, C. G. Dávila, and F. A. Leone. Analysis Methods for Progressive Damage of Composite Structures. Technical Report NASA/TM–2013-218024, NASA Langley Research Center, 2013.

[72] L. Wang, C. Zheng, S. Wei, and Z. Wei. Micromechanics-based progressive failure analysis of carbon fiber/epoxy composite vessel under combined internal pressure and thermomechanical loading. *Composites Part B: Engineering*, 89:77–84, 2016. doi: 10.1016/j.compositesb.2015.11.018.

[73] P. F. Liu, J. K. Chu, S. J. Hou, and J. Y. Zheng. Micromechanical damage modeling and multiscale progressive failure analysis of composite pressure vessel. *Computational Materials Science*, 60: 137–148, 2012. doi: 10.1016/j.commatsci.2012.03.015.

[74] B. Gentilleau, S. Villalonga, F. Nony, and H. Galiano. A probabilistic damage behavior law for composite material dedicated to composite pressure vessel. *International Journal of Hydrogen Energy*, 40(38):13193–13205, 2015. doi: 10.1016/j.ijhydene.2015.04.043.

[75] S. Harada, Y. Arai, W. Araki, T. Iijima, A. Kurosawa, T. Ohbuchi, and N. Sasaki. A simplified method for predicting burst pressure of type III filament-wound CFRP composite vessels considering the inhomogeneity of fiber packing. *Composite Structures*, 190:79–90, 2018. doi: 10.1016/j.compstruct.2018.02.011.

[76] R. Rafiee and M. A. Torabi. Stochastic prediction of burst pressure in composite pressure vessels. *Composite Structures*, 185:573–583, 2018. doi: 10.1016/j.compstruct.2017.11.068.

[77] B. Ellul and D. Camilleri. The influence of manufacturing variances on the progressive failure of filament wound cylindrical pressure vessels. *Composite Structures*, 133:853–862, 2015. doi: 10.1016/j.compstruct.2015.07.059.

[78] P. Gasior, M. Malesa, J. Kaleta, M. Kujawińska, K. Malowany, and R. Rybczyński. Application of complementary optical methods for strain investigation in composite high pressure vessel. *Composite Structures*, 203:718–724, 2018. doi: 10.1016/j.compstruct.2018.07.060.

[79] F. Dahmene, S. Yaacoubi, and M. E. Mountassir. Acoustic emission of composites structures: Story, success, and challenges. *Physics Procedia*, 70:599–603, 2015. doi: 10.1016/j.phpro.2015.08.031.

[80] ATOS - Industrial 3D Scanning Technology. gom.com/metrology-systems/atos.html. Accessed: 2020-03-24.

[81] F. Aymerich and S. Meili. Ultrasonic evaluation of matrix damage in impacted composite laminates. *Composites Part B: Engineering*, 31(1):1–6, 2000. doi: 10.1016/S1359-8368(99)00067-0.

[82] A. E. Scott, M. Mavrogordato, P. Wright, I. Sinclair, and S. M. Spearing. In situ fibre fracture measurement in carbon-epoxy laminates using high resolution computed tomography. *Composites Science and Technology*, 71(12):1471–1477, 2011. doi: 10.1016/j.compscitech.2011.06.004.

[83] Z. Cai, T. Gutowski, and S. Allen. Winding and Consolidation Analysis for Cylindrical Composite Structures. *Journal of Composite Materials*, 26(9):1374–1399, 1992. doi: 10.1177/002199839202600908.

[84] A. Banerjee, L. Sun, S. C. Mantell, and D. Cohen. Model and experimental study of fiber motion in wet filament winding. *Composites Part A: Applied Science and Manufacturing*, 29(3):251–263, 1998. doi: 10.1016/S1359-835X(97)00091-2.

[85] D. Cohen. Influence of filament winding parameters on composite vessel quality and strength. *Composites Part A: Applied Science and Manufacturing*, 1997. doi: 10.1016/S1359-835X(97)00073-0.

[86] M. J. Hinton and P. D. Soden. Predicting failure in composite laminates: the background to the exercise. *Composites Science and Technology*, 58(7):1001–1010, 1998. doi: 10.1016/S0266-3538(98)00074-8.

[87] M. Knops. *Analysis of failure in fiber polymer laminates: The theory of Alfred Puck*. Springer, Berlin, 2008. doi: 10.1007/978-3-540-75765-8.

[88] N. Perry, J. C. Wahl, C. Bois, A. Pilato, and A. Bernard. Thick composite design for hydrogen vessels: A contribution to composite design method. *CIRP Annals - Manufacturing Technology*, 62(1):139–142, 2013. doi: 10.1016/j.cirp.2013.03.108.

[89] ISO 1268-5:2001. *Fibre-reinforced plastics - Methods of producing test plates - Part 5: Filament winding*. ISO/TC 61/SC 13 Composites and reinforcement fibres, 2001.

[90] ISO 527-4:1997. *Plastics - Determination of tensile properties - Part 4: Test conditions for isotropic and orthotropic fibre-reinforced plastic composites*. ISO/TC 61/SC 13 Composites and reinforcement fibres, 1997.

[91] ISO 14129:1997. *Fibre-reinforced plastic composites - Determination of the in-plane shear stress/shear strain response, including the in-plane shear modulus and strength, by the plus or minus 45 degree tension test method*. ISO/TC 61/SC 13 Composites and reinforcement fibres, 1997.

[92] A. Pilato. *Caractérisation des structures composites bobinées épaisses, application à l'étude du comportement de réservoirs de stockage d'hydrogène (in french)*. PhD Thesis. Universite Bordeaux. Bordeaux, 2011.

[93] T. K. Christ. *Rechnerische und experimentelle Untersuchungen zum Versagensverhalten CFK-umwickelter Kryo-Druckbehälter (in german)*. PhD Thesis. Department of Mechanical Engineering. Technical University of Munich. Munich, 2017.

[94] MIL-HDBK-17-1F. Composite Materials Handbook Volume 1: Polymer Matrix Composites - Guidelines for Characterisation of Structural Materials. Technical report, US Department of Defense, 2002.

[95] ASTM D5448 / ASTM D5448M-16. *Standard Test Method for Inplane Shear Properties of Hoop Wound Polymer Matrix Composite Cylinders*. ASTM International, West Conshohocken, PA, 2016.

[96] ASTM D5450 / ASTM D5450M-16. *Standard Test Method for Transverse Tensile Properties of Hoop Wound Polymer Matrix Composite Cylinders*. ASTM International, West Conshohocken, PA, 2016.

[97] ASTM D 2290-00. *Standard Test Method for Apparent Hoop Tensile Strength of Plastic or Reinforced Plastic Pipe by Split Disk Method*. ASTM Book of Standards, 2003.

[98] E. J. Walsh and D. O. Adams. Development and evaluation of the quadrant ring test method. *Experimental Mechanics*, 48(3):319–326, 2008. doi: 10.1007/s11340-007-9089-x.

[99] C. Bois, A. Pilato, J. C. Wahl, and N. Perry. Proposal for a smart pressurised ring test to study thick composite produced by filament winding. *Composites Part B: Engineering*, 53:382–390, 2013. doi: 10.1016/j.compositesb.2013.06.001.

[100] J. Cain, S. Case, and J. Lesko. Testing of hygrothermally aged e-glass/epoxy cylindrical laminates using a novel fixture for simulating internal pressure. *Journal of Composites for Construction*, 13(4):325–331, 2009. doi: 10.1061/(ASCE)1090-0268(2009)13:4(325).

[101] W. R. Broughton. Dissemination, standardization and reviews. Thick composites. Technical Report Project CPD5 - Report 5, NPL Materials Centre, 2001.

[102] ASTM D5379 / ASTM D5379M-19. *Standard Test Method for Shear Properties in Composite Materials by the V-Notched Beam Test Method*. ASTM International, West Conshohocken, PA, 2019.

[103] ASTM D3171. *Standard test methods for constituent content of composite materials*. ASTM International, West Conshohocken, PA, 1999.

[104] ASTM D2734. *Standard test methods for void content of reinforced plastics*. ASTM International, West Conshohocken, PA, 1994.

[105] ASTM D5528-13. *Standard test method for mode I interlaminar fracture toughness of unidirectional fiber-reinforced polymer matrix composites*. ASTM International, West Conshohocken, PA, 2013.

[106] ASTM D7905 / D7905M-19e1. *Standard test method for determination of the mode II interlaminar fracture toughness of unidirectional fiber-reinforced polymer matrix composites*. ASTM International, West Conshohocken, PA, 2014.

[107] J. Kellas, S.and Morton. Scaling Effects in Angle-Ply Laminates. Technical Report NASA Contractor Report 4423, NASA Langley Research Center, 1992.

[108] P. P. Camanho, C. G. Dávila, S. T. Pinho, L. Iannucci, and P. Robinson. Prediction of in situ strengths and matrix cracking in composites under transverse tension and in-plane shear. *Composites Part A: Applied Science and Manufacturing*, 37(2):165–176, 2006. doi: 10.1016/j.compositesa.2005.04.023.

[109] S.T. Pinho, L. Iannucci, and P. Robinson. Physically-based failure models and criteria for laminated fibre-reinforced composites with emphasis on fibre kinking: Part I: Development. *Composites Part A: Applied Science and Manufacturing*, 37(1):63–73, 2006. doi: 10.1016/j.compositesa.2005.04.016.

[110] D. H. Kang, C. U. Kim, and C. G. Kim. The embedment of fiber Bragg grating sensors into filament wound pressure tanks considering multiplexing. *NDT and E International*, 39(2):109–116, 2006. doi: 10.1016/j.ndteint.2005.07.013.

[111] R. Brault, A. Germaneau, J. C. Dupré, P. Doumalin, S. Mistou, and M. Fazzini. In-situ Analysis of Laminated Composite Materials by X-ray Micro-Computed Tomography and Digital Volume Correlation. *Experimental Mechanics*, 53(7):1143–1151, 2013. doi: 10.1007/s11340-013-9730-9.

[112] A. I. Torres. *Experimental and Analytical Determination of Interfiber Fracture Mechanisms and Patterns in Type IV Composite Pressure Vessels*. MSc Thesis. Faculty of Aerospace Engineering, Delft University of Technology. Delft, 2019.

[113] E. V. Morozov. Application of the boundary-layer theory to the analysis of composite shells of revolution. *Composite Structures*, 54(2–3):261–265, 2001. doi: 10.1016/S0263-8223(01)00096-4.

[114] P. P. Camanho, P. Maimí, and C. G. Dávila. Prediction of size effects in notched laminates using continuum damage mechanics. *Composites Science and Technology*, 67:2715–2727, 2007. doi: 10.1016/j.compscitech.2007.02.005.

[115] C. G. Dávila, C. A. Rose, and P. Camanho, P. A procedure for superposing linear cohesive laws to represent multiple damage mechanisms in the fracture of composites. *International Journal of Fracture*, 158(2):211–223, 2009. doi: 10.1007/s10704-009-9366-z.

[116] MIL-HDBK-5J. Metallic Materials and Elements for Aerospace Vehicle Structures. Technical report, US Department of Defense, 2003.

[117] A. P. Boresi and R. J. Schmidt. *The Thick- Wall Cylinder*. John Wiley & Sons, 2003.

[118] F. P. Van Der Meer, C. Oliver, and L. J. Sluys. Computational analysis of progressive failure in a notched laminate including shear nonlinearity and fiber failure. *Composites Science and Technology*, 70(4):692–700, 2010. doi: 10.1016/j.compscitech.2010.01.003.

[119] P. P. Camanho, M. A. Bessa, G. Catalanotti, M. Vogler, and R. Rolfes. Modeling the inelastic deformation and fracture of polymer composites-Part II: Smeared crack model. *Mechanics of Materials*, 59:36–49, 2013. doi: 10.1016/j.mechmat.2012.12.001.

[120] K. J. Saeger, P. A. Lagace, and D. J. Shim. Interlaminar stresses due to in-plane gradient stress fields. *Journal of Composite Materials*, 36(2):211–227, 2002. doi: 10.1177/0021998302036002548.

[121] S. W. Tsai and E. M. Wu. A General Theory of Strength for Anisotropic Materials. *Journal of Composite Materials*, 5:58–80, 1971. doi: 10.1177/002199837100500106.

[122] C. G. Dávila, P. P. Camanho, and C. A. Rose. Failure Criteria for FRP Laminates. *Journal of Composite Materials*, 39(4):323–345, 2005. doi: 10.1177/0021998305046452.

[123] G. Catalanotti, P. P. Camanho, and A. T. Marques. Three-dimensional failure criteria for fiber-reinforced laminates. *Composite Structures*, 95:63–79, 2013. doi: 10.1016/j.compstruct.2012.07.016.

[124] W. Ramberg and W. Osgood. Description of stress-strain curves by three parameters. Technical Report Technical Note No. 902, National Advisory Committee For Aeronautics, 1943.

[125] A. Soriano and J. Díaz. Failure analysis of variable stiffness composite plates using continuum damage mechanics models. *Composite Structures*, 184:1071–1080, 2018. doi: 10.1016/j.compstruct.2017.10.065.

[126] F.P. Van Der Meer and L.J. Sluys. Continuum Models for the Analysis of Progressive Failure in Composite Laminates. *Journal of Composite Materials*, 43(20):2131–2156, 2009.

[127] F. A. Leone. Deformation gradient tensor decomposition for representing matrix cracks in fiber-reinforced materials. *Composites Part A: Applied Science and Manufacturing*, 76:334–341, 2015. doi: 10.1016/j.compositesa.2015.06.014.

[128] A. Turon, P. P. Camanho, J. Costa, and C. G. Dávila. A damage model for the simulation of delamination in advanced composites under variable-mode loading. *Mechanics of Materials*, 38 (11):1072–1089, 2006.

[129] A. Turon, P. P. Camanho, J. Costa, and J. Renart. Accurate simulation of delamination growth under mixed-mode loading using cohesive elements: Definition of interlaminar strengths and elastic stiffness. *Composite Structures*, 92(8):1857–1864, 2010.

[130] M. L. Benzeggagh and M. Kenane. Measurement of mixed-mode delamination fracture toughness of unidirectional glass/epoxy composites with mixed-mode bending apparatus. *Composites Science and Technology*, 56(4):439–449, 1996. doi: 10.1016/0266-3538(96)00005-X.

[131] E.V. González, P. Maimí, A. Turon, P. P. Camanho, and J Renart. Simulation of delamination by means of cohesive elements using an explicit finite element code. *Computers, Materials and Continua*, 9(1):51–92, 2009.

[132] P. Maimí, P. P. Camanho, J. A. Mayugo, and C. G. Dávila. A continuum damage model for composite laminates: Part I - Constitutive model. *Mechanics of Materials*, 39(10):897–908, 2007. doi: 10.1016/j.mechmat.2007.03.005.

[133] P. Maimí, P. P. Camanho, J. A. Mayugo, and C. G. Dávila. A continuum damage model for composite laminates: Part II - Computational implementation and validation. *Mechanics of Materials*, 39(10):909–919, 2007. doi: 10.1016/j.mechmat.2007.03.006.

[134] Zdeněk P. Bažant and B. H. Oh. Crack band theory for fracture of concrete. *Matériaux et Constructions*, 16:155–177, 1983. doi: 10.1007/BF02486267.

[135] E. Cesari. *Combined Acoustic and Optic Characterization of Damage Mechanisms in Internally Pressurized Composite Pressure Vessels*. MSc Thesis. Faculty of Aerospace Engineering, Delft University of Technology. Delft, 2020.

[136] H. Y. Chou, A. P. Mouritz, M. K. Bannister, and A. R. Bunsell. Acoustic emission analysis of composite pressure vessels under constant and cyclic pressure. *Composites Part A: Applied Science and Manufacturing*, 70:111–120, 2015. doi: 10.1016/j.compositesa.2014.11.027.

[137] DIN EN 2564:2019-08. *Aerospace series - Carbon fibre laminates - Determination of the fibre, resin and void contents; German and English version EN 2564:2018*. Deutsches Institut für Normung, Berlin, Germany, 2019. doi: 10.1520/D6671_D6671M-19.